Inaugural - Dissertation

Submitted to the

Combined Faculty of Mathematics, Engineering and Natural Sciences

of the Ruperto-Carola University Heidelberg

for the degree of

Doctor of Natural Sciences (Dr. rer. nat.)

Presented by

Elke Völkle (Nee Evgrafov)

Born in Belebei, Russia

Oral Examination: 13.02.2025

Advancing Glaucoma Research:

Investigating a Hyaluronan-Based Drainage Device

and a Model for Ocular Calcification

Referees:

Prof. Dr. Joachim P. Spatz

Institute for Molecular Systems Engineering and Advanced Materials

Ruperto-Carola University Heidelberg

Max Planck Institute for Medical Research, Heidelberg

Prof. Dr. Peer Fischer

Institute for Molecular Systems Engineering and Advanced Materials,

Ruperto-Carola University Heidelberg

Max Planck Institute for Medical Research, Heidelberg

"A Scientist in his laboratory is not a mere technician: he is also a child confronting natural phenomena that impress him as though they were fairy tales"

Marie Curie

- Für meine Familie -

Eidesstattliche Versicherung

Gemäß §8 der Promotionsordnung der für die Gesamtfakultät für Mathematik, Ingenieur- und Naturwissenschaften der Universität Heidelberg

1. Bei der eingereichten Dissertation zu dem Thema **„Advancing Glaucoma Research: Investigating a Hyaluronan-Based Drainage Device and a Model for Ocular Calcification"** handelt es sich um eigenständige erbrachte Leistung.

2. Ich habe nur die angegebenen Quellen und Hilfsmittel benutzt und mich keiner unzulässigen Hilfe Dritter bedient. Insbesondere habe ich wörtlich oder sinngemäß aus anderen Werken übernommene Inhalte als solche kenntlich gemacht.

3. Die Arbeit oder Teile davon habe ich bislang nicht an einer Hochschule des In- oder Auslands als Bestandteil einer Prüfungs- oder Qualifikationsleistung vorgelegt.

4. Die Richtigkeit der vorstehenden Erklärungen bestätige ich.

5. Die Bedeutung der eidesstattlichen Versicherung und die strafrechtlichen Folgen einer unrichtigen oder unvollständigen eidesstattlichen Versicherung sind mir bekannt.

Ich versichere an Eides statt, dass ich nach bestem Wissen die reine Wahrheit erklärt und nichts verschwiegen habe

Stuttgart, den 13. Dezember 2024

Elke Völkle

Contents

Danksagung

Diese Arbeit wäre ohne die Unterstützung und Hilfe vieler Menschen nicht möglich gewesen und dafür bin ich allen sehr dankbar.

Zuallererst bedanken möchte ich mich bei Prof. Joachim Spatz für die Möglichkeit in seiner Gruppe und an diesem interessanten Projekt zu arbeiten, und für die wertvollen Anregungen und Unterstützung während der gesamten Zeit.

Für die Zweitkorrektur meiner Arbeit möchte ich mich bei Prof. Dr. Peer Fischer bedanken.

Meine tiefste Anerkennung und Dankbarkeit gelten meiner Betreuerin Dr. Fania Geiger. Danke für die großartige Betreuung und deine Unterstützung während meiner Master- und Doktorarbeit. Wenn nichts mehr funktionierte (was nicht selten vorkam), ich nicht mehr weiterwusste oder zu verzweifeln begann, konnte ich mich zu jeder Zeit auf dein offenes Ohr und deine Hilfe verlassen, obwohl du meist selbst alle Hände voll zu tun hattest mit deinen Kindern und in deinem neuen Job. Du hast mich stets motiviert neue Wege zu finden und weiterzumachen und dadurch maßgeblich zum Erfolg dieser Arbeit beigetragen.

Weiterhin bedanken möchte ich mich bei Dr. Johannes Feierfeil, Dr. Helge Menz und Dr. Melanie Lievenbrück von der Pharmpur GmbH für die sehr gute Zusammenarbeit im Rahmen des Glaukom Projekts und die produktiven Projekttreffen. Besonderer Dank gilt vor allem Dr. Johannes Feierfeil für die Herstellung und Bereitstellung der thiolierten Hyaluronsäure, für die Analytik der Syntheseprodukte, sowie für die Erarbeitung eines Augenmodels und die vielen wertvollen Diskussionen.

Bedanken möchte ich mich auch bei den Mitarbeitern der Glas-Werkstatt des Max-Planck-Instituts für Intelligente Systeme für die stets zuverlässige und schnelle Herstellung der Model-Röhrchen.

Mein Dank gilt auch Dr. Günther Majer für die NMR-Analyse und Auswertung der Syntheseprodukte.

Danke auch an Joannis Grigoridis für die Hilfestellung beim REM und Plasma und die vielen lustigen Gespräche die mich immer wieder abgelenkt und aufgebaut haben.

Dr. Lucia Benk und Dr. Christoph Frey danke ich für die Einführung in die Mikrofluidik, sowie das Entwerfen und die Herstellung der Si-wafer-Designs für die Mikrofluidik-Chips.

Danke auch an Ruben Werbke vom Max-Planck-Institut für Intelligente Systeme, sowie Clara Vazquez-Martel vom Institut für Molekulare Systemtechnik und Fortschrittliche Werkstoffe, für das Drucken der 3D Designs.

Ein großer Dank gilt auch meinen KollegInnen Nina Conzelmann, Darya (Dascha) Freimann, Manuel (Mischa) Baumann, Pascal (Kalle) Jeschenko und Jonathan (Rantanplan) Bodenschatz. Ihr habt mir nach der Elternzeit den Wieder-Einstieg in vielerlei Hinsicht erleichtert, sei es im Labor oder durch eure stets hilfsbereite Art, wertvollen Ratschläge, aufbauenden Worte und immer lustigen Kaffeepausen.

In diesem Zusammenhang, danke Kalle für den täglich frisch von Hand gemahlenen Kaffee und für die Korrektur der Chemie-Teile meiner Arbeit. Nina, auch dir vielen Dank, dass du dir ebenfalls

die Zeit genommen hast Teile meiner Arbeit zu lesen und zu korrigieren und natürlich for showing me BioRender :-). Ich bedanke mich auch bei allen anderen Mitarbeitern und Kollegen aus der Spatz-Gruppe, für die sehr gute Arbeitsatmosphäre und die immer lustigen Stammtische.

Mein Größter Dank allerdings gebührt meiner Familie, die mich während meines Studiums, meiner Doktorarbeit und in allen Lebenslagen begleitet und immer unterstützt und bestärkt hat.
Liebe Oma, lieber Leo, danke für eure stets aufmunternden Worte und dass ihr immer stolz auf mich seid, egal was ich tue.
Lieber Artur, liebe Sarah, auch Euch möchte ich danken für eure Zuversicht in den Erfolg dieser Arbeit und für die Kinderbetreuung, besonders in der letzten stressigen Phase.
Liebe Mama, ich danke dir von Herzen für deine Unterstützung all die Jahre, dass du mich immer in allen meinen Entscheidungen bestärkt hast und dafür, dass du so oft kurzfristig eingesprungen bist für die Betreuung, wenn die Kita geschlossen hatte oder auch an den Wochenenden, wenn ich mal eine Auszeit brauchte.
Mein lieber Sohn Milan, auch dir gebührt ein ganz besonderer Dank. Du kannst zwar noch nicht lesen, aber durch dich habe ich gelernt alles etwas gelassener zu nehmen und dein Lachen am Ende eines jeden Tages hat mich immer wieder aufgebaut und den Stress des Alltags vergessen lassen.
Mein letzter und tiefster Dank gilt schließlich dir lieber Martin. Seit über 15 Jahren gehst du mit mir durch alle Höhen und Tiefen. Ohne dich, dein grenzenloses Vertrauen und deine Zuversicht, dass ich alles schaffen kann was ich mir vornehme, wäre ich jetzt nicht da wo ich heute bin. Dein Rückhalt und deine Liebe haben mich durch viele stressige und anstrengende Tage getragen. Dafür und für so viel mehr bin ich dir unendlich dankbar!

Abstract

Glaucoma is a prevalent eye disease and one of the leading causes of blindness worldwide. Among various risk factors like genetics or age, elevated intraocular pressure (IOP) remains the only modifiable variable to slow down the disease progression. In all types of glaucoma, IOP elevation results from obstructions in aqueous outflow, caused by changes in the extracellular matrix (ECM) of the ocular outflow structures, primarily the trabecular meshwork (TM). One such alteration is the precipitation of calcium phosphate (CaP), in form of hydroxyapatite (HAp), which stiffens the TM and increases outflow resistance. The artificial drainage of excess fluid is the only way to reduce the IOP and preserve eyesight. Glaucoma drainage devices (GDDs) are common treatment options, but until today current implants are neither completely reliable nor long lasting and prone to issues like hypotony, implant occlusion, fibrosis or poor biocompatibility. This thesis investigates the glaucoma disease from two complementary perspectives: treatment development (part I) and the underlying pathological mechanisms (part II).

The first part of this thesis focused on the development and evaluation of a new type of GDD designed to address key issues of existing implants for controlling IOP. The core innovation of this device is a hyaluronan (HA) hydrogel, aiming to prevent hypotony, cell occlusion and providing pressure-depending drainage to reduce elevated IOP. The main concept of the new GDD was established by Michael Thaller, PhD student in the team of Joachim Spatz of the Max Planck Institute for Medical Research (MPI-MR), which included the conceptualization and fabrication of large model prototypes with valve functionality. This thesis advances the design through miniaturization to dimensions comparable to those of real glaucoma implants (ID=0.5-1 mm, l=3-6 mm) and the exploration of various hydrogel compositions including a combination with polyethylene glycol (PEG). HA-PEG hydrogels, when immobilized within the implants, demonstrated superior enzymatic stability, making them promising for long-term use. Moreover, a new microfluidic measurement setup was developed to assess the pressure regulation capabilities of model tubes under realistic physiological conditions. The model implants demonstrated consistent pressure regulation under conventional flowrates and daily IOP fluctuations, albeit with the need for further optimizations to align with physiological IOP levels. In a last approach, iterative design and testing of 3D-printed patterns enhanced the reproducibility of model implant fabrication. These advancements, provide a solid foundation for scalable, biocompatible GDDs capable of effective long-term personalized IOP management, though further refinement of hydrogel compositions and *in vivo* validation remain necessary.

In the second part, the picture is extended by another aspect: the occurrence of calcification processes in glaucomatous eyes and the design of a new biomimetic model for biomineralization studies of CaP. A droplet-based system was developed to mimic early stages of mineral formation within matrix vesicles (MVs), including ion accumulation and crystal formation. Mineralized particles formed within droplets revealed needle-like structures indicative of HAp, which differed

significantly from those observed in bulk systems. This finding suggests a distinct mineralization pathway in the droplet-based model that could provide new insights into mineralization in MVs.
Further exploration addressed the anti-calcification properties of matrix gla protein (MGP), a known inhibitor of tissue calcification. Peptides, derived from MGP, with varying amount and position of gamma-carboxyglutamic acid (gla) residues, were tested for their effects on mineralization. Although, no significant reduction in mineral formation was observed, peptides containing gla residues altered crystal morphology, forming fiber-like bundles and nano-spherical aggregates similar to HAp. These findings highlight the potential of the droplet-based approach for investigating CaP mineralization and crystal morphology.
This new droplet-based mineralization model combines simplicity with controllability, by bridging the gap between simple bulk systems and the confined, controllable environment of MVs. This enhances control over mineralization conditions and minimizes side reactions and influences from the external environment by isolating the reaction components within a confined space. In addition, the high-throughput analysis of uniform droplets enables reproducible and efficient analysis of mineralization processes.
Future efforts should focus on reducing droplet size, incorporating peptides at a later stage of mineralization and fusion of droplets, to better mimic natural MVs and extracellular processes. Furthermore, a characterization of the mineralized particles via x-ray diffraction (XRD) will be necessary.

Together, both experimental parts contribute to the development of improved GDDs and enhance the understanding of glaucomatous calcification processes, offering valuable insights for both glaucoma management and biomimetic material design.

Zusammenfassung

Das Glaukom (grüner Star) ist eine weit verbreitete Augenkrankheit und eine der Hauptursachen für Erblindung weltweit. Neben verschiedenen Risikofaktoren wie genetische Veranlagung oder Alter, ist ein erhöhter Augeninnendruck (engl. intraocular pressure, IOP) die einzige veränderbare Variable, um das Fortschreiten der Krankheit zu verlangsamen. Bei allen Glaukom-Arten resultiert der erhöhte IOP daraus, dass durch strukturelle Veränderungen der extrazellulären Matrix (engl. extracellular matrix, ECM) der Abflussstrukturen, vor allem des Trabekelwerks, der Abfluss des Kammerwassers verhindert wird. Eine dieser Veränderungen ist die Ausfällung von Calciumphosphat (CaP), in Form von Hydroxylapatit (HAp) die zu einer Versteifung des Trabekelwerks und einem erhöhten Abflusswiderstand führt. Die überschüssige Flüssigkeit künstlich abzuleiten ist die einzige Möglichkeit, den IOP zu senken und das Sehvermögen zu erhalten. Glaukom-Implantate sind gängige Behandlungsoptionen, aber bis heute sind diese weder absolut zuverlässig noch langlebig und anfällig für Probleme wie Hypotonie, Implantat Verschluss, Fibrosen oder schlechte Biokompatibilität. Diese Arbeit untersucht die Glaukom-Erkrankung aus zwei unterschiedlichen und dennoch sich ergänzenden Perspektiven: der Entwicklung einer Behandlungsmethode (1. Teil) und den zugrunde liegenden pathologischen Mechanismen (2. Teil).

Der erste Teil dieser Arbeit konzentriert sich auf die Entwicklung eines neuartigen Glaukom-Drainage-Implantats (engl. glaucoma drainage device, GDD), welches die wichtigsten Probleme bestehender Implantate zur Kontrolle des IOP lösen soll. Kernstück dieses Implantats ist ein druckempfindliches Hyaluronsäure (HA)-Hydrogel, das eine gezielte Regulation des IOP ermöglicht und gleichzeitig Hypotonie und Implantat Verschluss verhindern soll. Das Hauptkonzept des neuen GDD wurde von Michael Thaller aus dem Team von Joachim Spatz vom Max-Planck-Institut für medizinische Forschung (MPI-MF) entwickelt und umfasste die Konzeption und Herstellung großer Modellprototypen.

Diese hier vorliegende Arbeit verbessert das Design und die Funktion durch Miniaturisierung auf Abmessungen, die mit echten GDDs vergleichbar sind (ID=0,5-1 mm, l=3-6 mm), sowie durch die Erforschung verschiedener Hydrogel Zusammensetzungen inklusive Hybridgelen mit einem Polyethylenglykol-Anteil (PEG). Die HA-PEG Hydrogele wiesen, nach ihrer Immobilisierung in den Implantaten, eine hohe Stabilität gegen enzymatischen Abbau auf, was sie als vielversprechende Kandidaten für eine langfristige Anwendung auszeichnet. Desweiteren wurde ein neuartiger mikrofluidischer Messaufbau entwickelt, um die Druckregulierungsfähigkeiten der Modell Implantate unter realistischen physiologischen Bedingungen zu untersuchen. Die Messungen zeigten eine konsistente reproduzierbare Druckregulierung bei natürlichen Flussraten und täglichen IOP-Schwankungen, erfordern jedoch weitere Optimierungen zur vollständigen Anpassung an physiologische IOP-Werte. Die Reproduzierbarkeit und Herstellung größerer Stückzahlen der Modell-Implantate wurde durch iteratives Design und Testen von 3D-gedruckten Mustern verbessert. Diese Ergebnisse bilden eine solide Grundlage für skalierbare, biokompatible GDDs, zur personalisierten und langfristigen IOP-Kontrolle, wenngleich weitere Optimierungen

der Hydrogel Zusammensetzung, sowie eine Validierung unter *in vivo* Bedingungen erforderlich bleiben.

Im zweiten Teil dieser Arbeit wird ein weiterer Aspekt beleuchtet: das Auftreten von Verkalkungsprozessen in glaukomatösen Augen und die Entwicklung eines neuen biomimetischen Modells zur Untersuchung der Biomineralisation von CaP. Hierzu wurde ein tröpfchenbasiertes System entwickelt, das die frühen Stadien der Mineralbildung innerhalb von Matrixvesikeln (MVs) nachahmt, einschließlich der Ionenakkumulation und Kristallbildung. Die in den Tröpfchen gebildeten mineralisierten Partikel wiesen nadelartige Strukturen auf, die auf HAp hindeuteten und sich deutlich von den Ergebnissen in Bulk-Experimenten unterschieden. Dies lässt einen alternativen Mineralisierungsweg im tröpfchenbasierten Modell vermuten, der neue Erkenntnisse über die Mineralisation in MVs eröffnen kann.

Weitere Untersuchungen befassten sich mit den anti-kalzifizierenden Eigenschaften des Matrix-Gla-Proteins (MGP), einem bekannten Inhibitor der Gewebekalzifizierung. Hierfür wurden MGP-abgeleitete Peptide mit unterschiedlichen Positionen und Anzahl an Gamma-Carboxyglutaminsäure (gla) Resten getestet. Obwohl keine signifikante Verringerung der Mineralbildung festgestellt wurde, führten Peptide, die gla-Reste enthielten, zu veränderten Kristallmorphologien, darunter faserartige Bündel und nanosphärische Aggregate, die HAp ähnelten. Diese Ergebnisse verdeutlichen das Potenzial des tröpfchenbasierten Modells für die Untersuchung der CaP-Mineralisierung und der Kristallmorphologie.

Dieser neue Ansatz kombiniert die Einfachheit von Bulk-Experimenten mit der diskreten Umgebung von MVs. Das verbessert zum einen die Kontrolle über Mineralisierungsbedingungen und verringert Nebenreaktion, sowie äußere Einflüsse, durch die Isolierung der Reaktionskomponenten in geschlossene Reaktionsräume. Zudem lassen sich die Tröpfchen kontrolliert und reproduzierbar in Massen herstellen, was eine effiziente Hochdurchsatz-Analyse von Mineralisierungsprozessen ermöglicht.

Zukünftige Studien sollten sich auf die Verringerung der Tröpfchengröße und die Einbindung von Peptiden in einem späteren Stadium der Mineralisierung sowie der Fusion von Tröpfchen konzentrieren, um natürliche MVs und extrazelluläre Prozesse besser nachzuahmen. Darüber hinaus sollte eine detaillierte Charakterisierung der Mineralphasen durch Röntgendiffraktionsspektroskopie (engl. x-ray diffraction, XRD) durchgeführt werden.

Zusammen tragen die beiden Teile dieser Arbeit zur Entwicklung verbesserter GDDs bei und fördern das Verständnis glaukomatöser Verkalkungsprozesse sowie der Biomineralisation. Damit liefern sie wertvolle Erkenntnisse sowohl für das Glaukom-Management als auch für die Entwicklung biomimetischer Materialien.

Abbreviations

(O/W)	Oil-in-water
(W/O)	Water-in-oil
(W/O/W)	Water-in-oil-in-water
4arm-PEG-ACLT	4-arm polyethylene glycol acrylate
4arm-PEG-VS	4-arm polyethylene glycol vinylsulfon
AC	Anterior chamber
ACG	Angle-closure glaucoma
ACLT-PEG-ACLT	Poly(ethylene glycol) bisacrylate
ACP	Amorphous calcium phosphate
AGV	Achmed glaucoma valve
ALT	Argon laser trabeculoplasty
AP	Alkaline phosphatase
ATP	Adenosine triphosphate
BAK	Benzalkonium chloride
BMP2	Bone morphogenetic protein 2
CaP	Calcium phosphate
CMC	Critical micellar concentration
DTNB	5,5'-Dithiobis(2-nitrobenzoic acid)
DTPA	Dithiodipropionic acid
DTPH	3,3'-dithiobis(propionic hydrazide)
DTT	Dithiothreitol
ECM	Extracellular matrix
EDC	*N*-(3-dimethylaminopropyl)-*N*-ethylcarbodiimide hydrochloride
EtOAc	Ethyl acetate
EtOH	Ethanol
FA	Fluoresceinamine or 5-aminofluorescein
FTIR	Fourier transform infrared spectroscopy
GAG	Glycosaminoglycan
GDD	Glaucoma drainage device
GGCX	Gamma-glutamyl carboxylase
Gla or γ-E	Gamma carboxy glutamic acid
GPI	Glycosylphosphatidylinositol
GPS	(3-glycidyloxypropyl)trimethoxysilane or (3-(2,3-epoxypropoxy)propyltrimethoxysilane
HA	Hyaluronic acid, hyaluronan
HAp	Hydroxyapatite
HCEC	Human corneal endothelia cells

HEPES	*N*-(2-hydroxylethyl)piperazine-*N*'-ethane sulfonic acid
HS-HA	Thiolated Hyaluronan
HS-HA-FA	Thiolated fluorescently labeled hyaluronan
HTM	Human trabecular meshwork
ID	Inner diameter
IOP	Intraocular pressure
LGN	Lateral geniculate nucleus
LSM	Light scanning microscopy
MBAA	*N*,*N*'-methylene(bisacrylamide)
MG	Malignant glaucoma
MGP	Matrix gla protein
MIGS	Minimal invasive glaucoma surgery
MPI-MR	Max Planck Institute for Medical Research
MPS	(3-mercaptopropyl)trimethoxysilane or 3-(trimethoxysilyl)-1-propanethiol
MV	Matrix vesicle
MWCO	Molecular weigth cut off
NaAc	Sodium acetate
NMR	Nuclear magnetic resonance spectroscopy
NPP-1	Nucleotide pyrophosphatase-1
NTG	Normal-tension glaucoma
OA	Osteoarthritis
OCP	Octacalcium phosphate
OD	Outer diameter
OSD	Ocular surface disease
PAMAM	Polyamidoamine
PBS	Phosphate buffered saline
PC	Posterior chamber
PDMS	Polydimethoxysilane
PEA	Phosphoethanolamine
PEG	Polyethylene glycol
PEGDA	Polyethylene glycol diacrylate
PFPE	Perfluoropolyether
PLA	Poly(lactico-glycolic acid)
PMV	Platelet membrane vesicle
PNIPAM	Poly(*N*-isopropylacrylamide)
POAG	Primary open-angle glaucoma
POC	Point-of-care
Re	Reynolds number
SC	Schlemm's canal, canal of Schlemm

SEM	Scanning electron microscopy
SLT	Selective laser trabeculoplasty
TG	Thiolation grade
TM	Trabecular meshwork
TNAP	Tissue non-specific alkaline phosphatase
TNB^{2-}	2-Nitro-5-thiobenzoate
TPH	Thio(propanoic hydrazide)
TRIS	Tris(hydroxymethyl)aminomethane
WHO	World health organization
XRD	X-ray diffraction
α-CD	α-cyclodextrin
β-GP	β glycerophosphate

1 Introduction

1.1 The Glaucoma Disease

The glaucoma disease is a prevalent eye disease and a significant global health problem due to the fact that it is one of the leading causes of blindness in the world [1, 2]. The disease comes in different variations, but all of them share the common symptom of a gradual and irreversible degeneration of the visual nerve [3, 4]. Early diagnosis and treatment can significantly slow down the progressing of the disease, preserving vision for an extended period [1, 5]. Every year, the number of people suffering from glaucoma is growing due to an increasing aging society [2]. In 2010, the world health organization (WHO) estimated that over 60 million people were globally affected, with 57 million suffering from vision impairment or loss as a result of glaucoma [6, 7]. In previous studies from Tham et al., the numbers of glaucoma cases in 2013 were estimated around 64 million, and the prognosis for 2020 and 2040 were 76 million and around 112 million cases [2]. Newer studies by the WHO confirm these previous estimations in their "world report on vision" published in 2019 [8].

The estimated cases are based on calculations from several available studies [2, 6, 8], but in fact the real number of people with glaucoma is probably much larger than expected. Indeed, a high number of people are unaware that they have glaucoma, since the progression of the disease is sneaky and pain free and, in many cases, remains undiagnosed and gets only detected in the late course, when eyesight is already impaired [1, 5, 9]. Moreover, with growing population age, the prevalence of glaucoma increases and the problem will magnify [5].

For that reason, it is important to gain a deeper knowledge of the disease progression, to further improve current therapies and to explore new treatment options, to cure or slow down the progression of the disease.

1.1.1 The Pathophysiology of Glaucoma

The glaucoma disease encompasses a group of progressive optic neuropathies, such as normal-tension glaucoma (NTG), angle-closure glaucoma (ACG) or malignant glaucoma (MG). Of the different glaucoma variations, which vary among countries and races [2], the primary open-angle glaucoma (POAG) is the most common manifestation in the western hemisphere [8, 9], with up to 85 % of diagnosed glaucoma cases [10]. Studies by Zhang et al. in 2021 estimated about 68.6 million adult people (+40) that are globally suffering from POAG [11].

In detail, the pathophysiology of neurodegeneration in the glaucomatous eye is not yet fully understood [12]. What we know so far is, that the level of intraocular pressure (IOP) above the normal values (over 21 mmHg) is related to retinal ganglion cell death and degeneration of optic nerve fibers [5, 12].

Eye Anatomy & Glaucomatous Neurodegeneration

The innermost layer of the retina is the retinal nerve fiber layer, containing the axons of the ganglion cells, which converge on the optic disk, forming the optic nerve [5] (figure 1a). After traversing the lamina cribrosa, the fibers exit the eye and synapse in the lateral geniculate nucleus (LGN) of the thalamus, essential for visual processing [5]. By the convergence of the axons, a small central deepening in the optic disk, called cup, is formed [5] (figure 1b, left). The optic nerve and retinal vessels surround this cup [5].

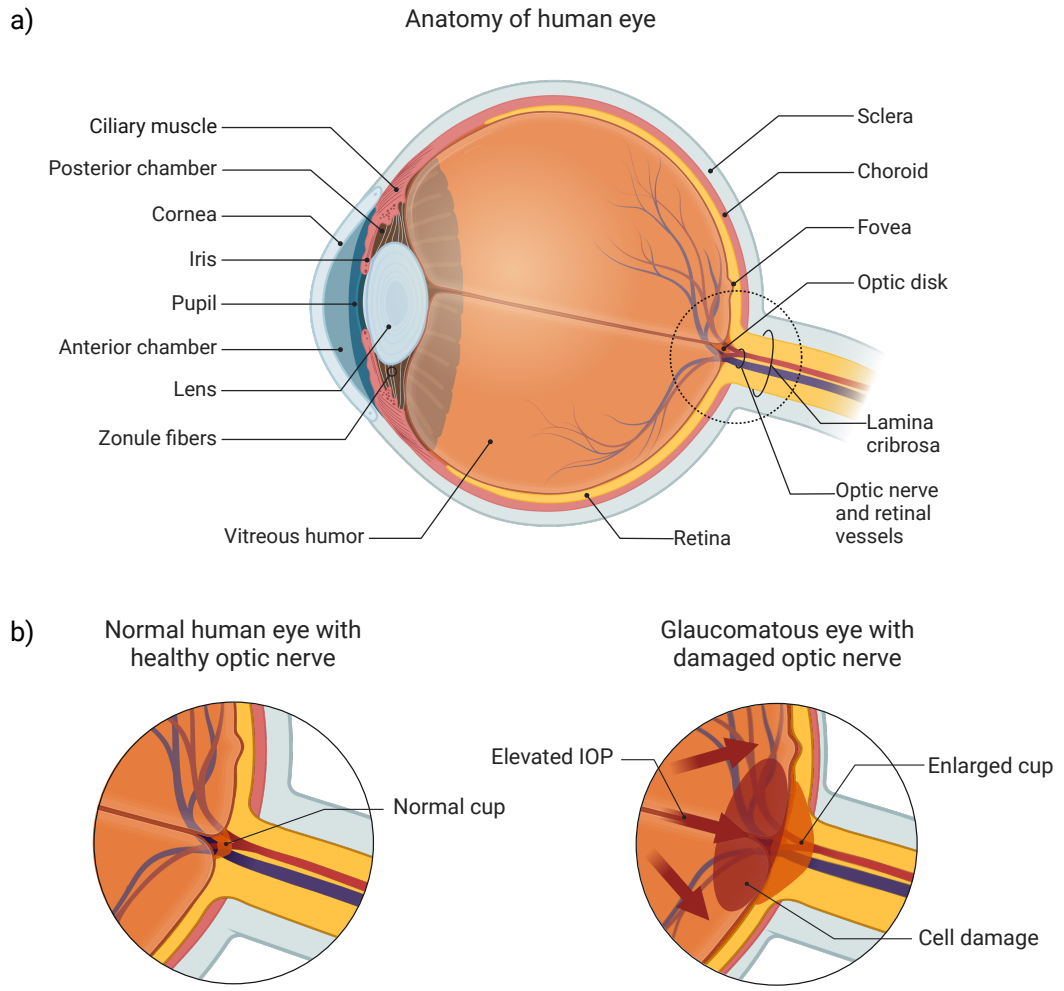

Figure 1: Eye anatomy and comparison of healthy and glaucomatous eye. Structures and parts of normal human eye (a) with magnified region (circle) in (b) showing the comparison of a healthy eye with normal cup (left) and glaucomatous eye with enlarged cup and damaged optic nerve as a result of elevated IOP (right). The anatomy and structures were adapted from the literature [13] and created with BioRender.com.

Elevated IOP leads to compression, deformation and mechanical stress of the optic disc, lamina cribrosa and retinal ganglion cells [5, 12, 14, 15] (figure 1b, right). This leads subsequently to a significant and visible enlargement of the optic disc cup and thinning of the retinal nerve fiber layer [5]. As a result of the pressure-induced compression the axonal transport of retinal ganglion cells is disturbed [12, 16], as well as the blood supply of e.g. the retina and optic nerve [12, 17] which collectively contributes to a gradual apoptosis of retinal ganglion cells and damage of optic nerve fibers [5].

1.1.2 Risk Factor for Glaucoma: Intraocular Pressure (IOP)

In the common knowledge, elevated IOP is causatively connected to glaucoma development and progression [9, 18, 19]. Whereby statistically, normal IOP does not exclude the presence of glaucoma, as in the variant of NTG, and conversely, not every person with elevated IOP is suffering from glaucoma disease [18].
However, the likelihood of developing glaucoma increases with higher IOP [5, 9, 20] and furthermore, among different other risk factors, as gender [21], increasing age or genetic predisposition, elevated IOP is currently the only truly modifiable variable to prevent or slow down the progression of the disease [1, 5, 9].

Factors Causing IOP Fluctuations

In the normal human eye, the IOP is a dynamic value between 10-21 mmHg. Influenced by various internal and external factors, the IOP in normal persons can vary between 2-6 mmHg in one eye over the day [18, 22].
One factor is the circadian variation of aqueous humor production which is twice higher at day as at night [18, 22, 23]. Besides diurnal/nocturnal variations, the season is influencing the ocular pressure with higher IOP values in winter in contrast to summer or autumn [23].
The position of the person is another factor that influences the IOP variation: the pressure is higher in supine position compared to a seated position, resulting from an increased episcleral venous pressure [18, 22, 24, 25]. Studies measuring the IOP over 24 h showed significantly higher values during the nocturnal period, with IOP peaks in the early morning before awaking, due to the supine position [24, 25]. This leads to the conclusion that the position of the person has a greater impact on IOP, than the circadian aqueous humor production, since the nocturnal slowdown of aqueous secretion is not sufficient to counterbalance the IOP elevation caused by the supine position [24].
Further examples influencing IOP are physical exercise, fluid intake [10], systemic drugs like corticosteroids [18] and even the tightness of a necktie [26].

1.1.3 IOP Regulation - Production & Outflow of Aqueous Humor

The IOP is regulated by a balance between the secretion and drainage of aqueous humor [5]. Modifying the Goldmann equation [19], the IOP can be formulated as a function of aqueous humor production and outflow [18]:

$$IOP = \frac{F}{C} + P_v - U$$

With ‘F’ being the formation rate of aqueous humor in µl/min, ‘C’ being the outflow facility in µl/min/mmHg, ‘P_v’ being the episcleral venous pressure in mmHg and ‘U’ being the aqueous humor outflow rate in µl/min.

Route of Aqueous Humor

The aqueous humor is a complex mixture of organic solutes, growth factors, electrolytes, oxygen and other components that are important to nourish all parts of the eye, as the iris, lens, cornea or the trabecular meshwork (TM) and additionally, it serves to drain metabolic waste products out of the eye [5, 27]. Figure 2 displays the route of aqueous humor.

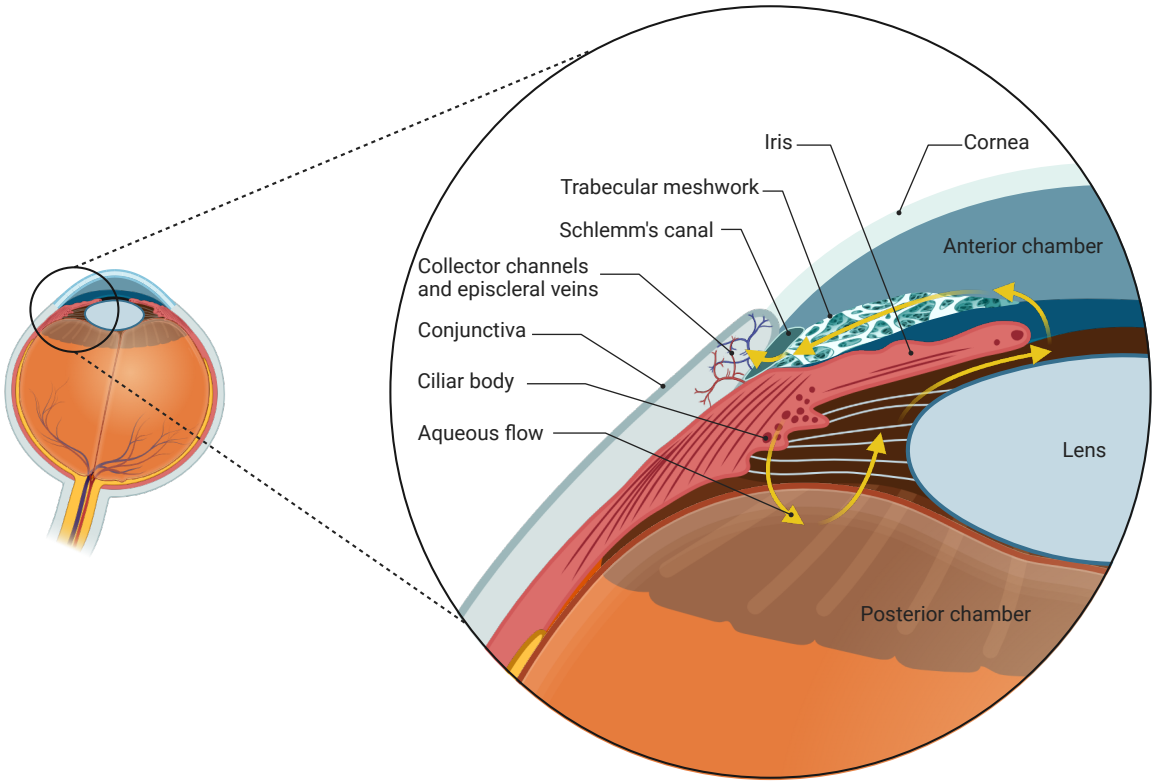

Figure 2: Anatomy of limbus area of the human eye and flow of aqueous humor. Within the ciliar body the aqueous is produced and flows from the posterior chamber (PC), through the pupil in the anterior chamber (AC) where the outflow structures are located: the trabecular meshwork (TM) and the adjacent Schlemm's canal (SC). The anatomy and structures were adapted from the literature [27, 28] and created with BioRender.

Within the non-pigmented epithelium of the ciliar body, the aqueous is produced with a rate of 2-3 µl/min [10, 27]. From the posterior chamber (PC), which holds about 60 µl of aqueous, it flows through the pupil in the anterior chamber (AC), containing an aqueous volume of approximately 250 µl [27]. After entering the AC the aqueous exits the eye through two pathways: a pressure-dependent route through the TM and the adjacent Schlemm's canal (TM-SC pathway), where 85-90 % of the aqueous passes through, and a pressure-independent pathway through the uveoscleral venous system [9, 10, 27], which accounts the remaining 10-15 % of aqueous outflow. During the day the aqueous humor is replenished about every 2 h [27].

1.1.4 Structure & Maintenance of the Ocular Outflow System

In the healthy human eye, the TM and several components in the extracellular matrix (ECM) play an important role for the maintenance of aqueous humor outflow and IOP regulation [29, 30]. This chapter gives an overview of the main outflow structures and highlights the main components which are important for TM integrity and their alterations under glaucomatous conditions.

The Trabecular Meshwork – Schlemm's Canal (TM-SC) Outflow Pathway

The conventional ocular outflow system is located in the anterior part of the eye in the iridocorneal angle and consists of the TM and the SC [10] (figure 3a). The TM is located prior to the AC and is a three-dimensional, soft, spongiform tissue with a size of about 350 x 50-150 µm [10]. It is divided in the uveal meshwork, the deeper corneoscleral meshwork and the juxtacanalicular region (or cribriform region) [10, 31].

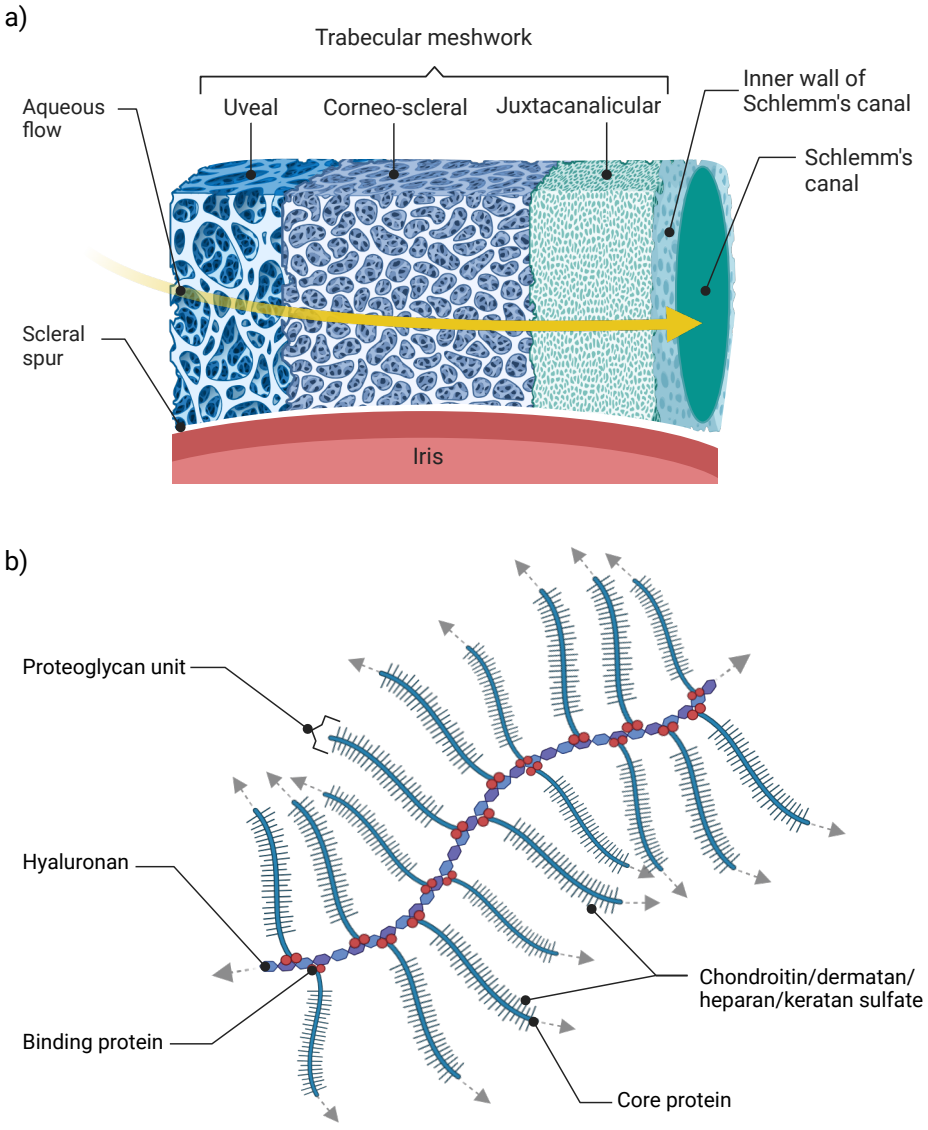

Figure 3: Schematic drawing and structure of the trabecular-Schlemm's canal (TM-SC) outflow pathway (a) and a proteoglycan aggregate as major component of the extracellular matrix (ECM) of trabecular meshwork (TM) (b). The drawing was adapted from Buffault et al. [28] (a) and Lennarz et al. [32] (b) and created with BioRender.com.

The uveal and corneoscleral meshwork consist of a network of densely packed collagen and elastin "bundles" or lamellae wrapped with flat confluent TM cells [10, 31, 33] and large "free spaces" [34], which become smaller in size when getting closer to the SC [10, 31]. In the uveal meshwork the intertrabecular spaces are about 25-27 μm, in the corneoscleral meshwork the space sizes are 2-15 μm [10].
The JCT region is the thinnest part of the TM (2-20 μm), containing TM cells embedded in a ECM of collagen, fibronectin and laminin [33] and exhibit a bridging connection between the TM lamellae and the inner wall endothelium of the SC, which has a length of about 25 mm and a diameter of 300 μm [10, 35]. After percolating in the TM and entering the SC the aqueous exits through the ~35 collector channels to the venous drainage system [10].
The TM possess several unique functions which all contribute to a normal structure and maintenance of the outflow system. In summary, TM cells have a phagocytic, self-cleaning mechanism, contractile properties, they respond to biomechanical and mechanical stress by changes in gene expression and morphology, and they secrete various enzymes and proteins, which are important for the formation of the ECM [36].

The Extracellular Matrix (ECM) of Trabecular Meshwork (TM) Cells

The intertrabecular spaces are the pathways taken by the aqueous humor on their way to SC, therefore the ECM surrounding the TM plays an important role, also for the maintenance of TM integrity [37]. The ECM composition varies depending on the location within the TM tissue [37]. One major class of macromolecules in the ECM of the corneal and uveoscleral meshwork are proteoglycans, which consist of glycosaminoglycan (GAG)-chains of chondroitin, dermatan, keratan and heparan sulfate, attached to a core protein [29, 30, 32, 37] (figure 3b).
Each proteoglycan unit is covalently connected to a hyaluronic acid (HA) chain, building together a gel-like network in the TM tissue which serves as a gel-filtration-system [29]. The major GAG constituents in these TM tissues are hyaluronan and chondroitin-dermatan sulfate, whereas heparan and keratan sulfate are only present in small amounts [29, 38].
Further important ECM components are collagens or cell-binding glycoproteins like laminin and fibronectin which are present in different levels in all TM regions [37] and also contribute to normal aqueous humor resistance and outflow [29].

Trabecular Meshwork (TM) & Glaucoma Development

In virtually all forms of glaucoma, the IOP elevation is caused by obstructions of the aqueous outflow [39], while aqueous production remains unchanged [10]. Several studies suggest, that the blockage is mainly attributed to abnormal accumulations or decreases of ECM components in the TM [29, 40-43], resulting in a stiffening of the TM tissue, which is – similar to the glaucoma disease itself – progressive and irreversible [44].
The ECM alterations mainly affecting the GAGs, as for example, an accumulation of chondroitin sulfate and simultaneous depletion of hyaluronan in the ECM of TM cells are associated with increased outflow resistance and POAG [38]. The overexpression of further components that may

cause resistance to aqueous outflow are laminin and collagen type IV, as shown in previous studies by Tane et al. [45].

Another process contributing to TM stiffening and increased outflow resistance is the precipitation of mineralized particles of calcium phosphate in the drainage zone, mainly in the ECM of TM cells. This mineralization processes in the outflow structures of glaucoma patients are in focus of several studies and also in the second part of this thesis. This is introduced and discussed in detail in chapter 1.2. Regardless of how the outflow of aqueous is obstructed, the current treatment options focus on improving aqueous outflow to slow down glaucomatous development. All treatment options are summarized in the following.

1.1.5 Current Glaucoma Treatments

There are different ways to treat glaucoma but they all have the same goal: a consistent reduction of the patients IOP, even when the values are at normal levels [27]. Overall, glaucoma treatment begins with medical therapy, followed by laser trabeculoplasty and filtration surgery, as trabeculectomy or glaucoma drainage devices (GDDs) [46] (figure 4).

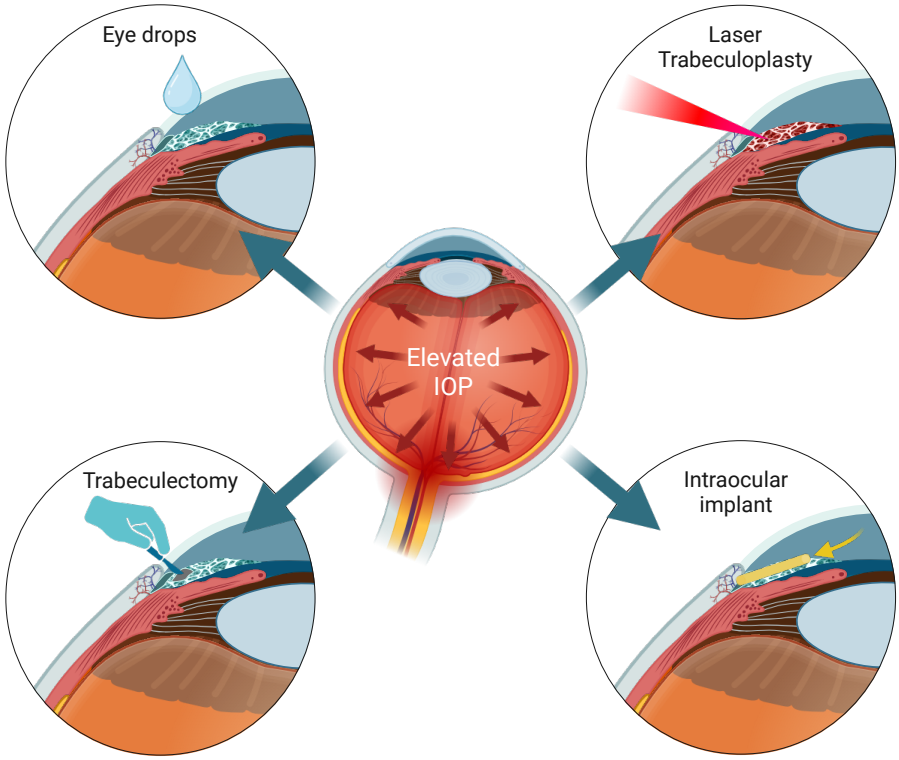

Figure 4: Overview of current glaucoma treatments to lower elevated IOP and prevent cell damage of the visual nerve. Generally, the first line of glaucoma treatment is medical therapy using eyedrops, followed by laser trabeculoplasty and filtration surgery (trabeculectomy and intraocular implants) for lowering the outflow resistance. The drawings were created with Biorender.com.

Each glaucoma therapy is as individual as each patient, depending on different parameters, as the status of nerve degeneration, the type of glaucoma or initial IOP value. However, the initial IOP determination is not that easy, due to the dynamic variation of the pressure value, as outlined before

(see section 1.1.2). Thereby, a single measurement at 'office hours' for the determination of initial IOP is not very meaningful and a correct characterization would require multiple measurements over days, weeks or even months and that makes it both consuming and costly [26]. Another challenge in the management of glaucoma is that not all patients respond equally to the same therapy and an exact prediction of IOP reduction is impossible [26]. For that reason often a target pressure range is defined at which no glaucoma progression is expected to occur, which is in general at least 30 % lowering of initial IOP [5, 18].

Medical Therapy: Eyedrops

The medications for glaucoma therapy reduce elevated IOP by either decreasing aqueous humor production (beta-blockers), or by increasing the TM-SC-mediated outflow of aqueous [5, 27, 46] or the outflow through the uveoscleral pathway, both is induced by prostaglandins [47-49].
The majority of glaucoma medications are eyedrops [27]. Applied on the eyes' surface, the eyedrop is becoming part of the tear film and over time diffusing into the cornea and conjunctiva and finally into the aqueous humor [27]. Actually, the drug penetration through the multilayered cornea is not that easy and limited by the tight junctions in the corneal cell layers [27]. Most medications contain preservatives such as benzalkonium chloride (BAK), which act as detergents and break up the tight junctions, enhancing the passage of substances through these layers [27]. Since the effects of BAK are non-selective and cumulative, it can adversly affect the health of various ocular tissues, resulting in ocular surface disease (OSD), as dry eyes or leading to chronic inflammations of the conjunctiva [27, 50].
In contrast to other treatments, the application of eyedrops is though relatively cheap and easy to perform. In recent years, especially the prostaglandin-containing eyedrops, like latanoprost, travoprost or bimatoprost, became very popular, since they provide an excellent IOP reduction around 30 % from initial IOP and have only minimal side-effects [46]. However, for latanoprost an unusual side-effect was observed, especially in patients with hazel irises: an irreversible darkening of the iris as a result of an increase of melanosomes and upregulation of tyrosinase [51, 52].
Overall, in most cases a single eyedrop-agent is not sufficient for a permanent IOP reduction since it loses its effectiveness over time and thereby many glaucoma patients require adjunctive medications with different classes of compounds to achieve the same result as at the beginning of the therapy [46]. And that leads to another recurring problem, that more than a half of glaucoma patients only show low willingness following their prescribed medication schedule [53], especially with a complex schedule with three or four medications [46].

Laser Therapy: Trabeculoplasty

When medications lose their effectiveness in IOP reduction the most common procedure afterwards include laser trabeculoplasty, such as argon laser trabeculoplasty (ALT) or selective laser trabeculoplasty (SLT) [46]. Depending on the instrument and laser beam, the different types are classified in either continuous, pulse or micropulse diode laser system [54]. During the laser

treatment the TM is burned, causing damage and expanding of the meshwork and leading to IOP reduction by increasing the outflow of aqueous humor [46].
The trabeculoplasty is an effective and beneficial method, yet not for all types of open-angle glaucoma [54]. Some exclusion criteria for laser trabeculoplasty are: patients with POAG and extreme IOP values above 35 mmHg despite medical treatment, or serious and advanced optic nerve damage [54]. Some frequent postoperative complications of laser treatment are marked inflammation of the tissue, encapsulated blebs or AC bleeding [54, 55]. Another disadvantage is the relatively high failure rate with about 30-50 % of patients regaining elevated IOP within 5 years and require additional surgical therapy [55-57].

Incisional Surgery: Trabeculectomy

The incisional surgery is in general the next step, when medications and laser approaches for glaucoma therapy fail [46]. The trabeculectomy is a standard method, used since several decades [57] and widely considered to be the gold standard in glaucoma surgery [58]. By this, a small part of the TM and adjacent tissue is removed to enhance the outflow of fluid from the AC [57, 59].
The trabeculectomy is a relatively simple procedure and easy to learn [35] and in 70-80 % of cases it is successful in reducing IOP and preserving eye sight and furthermore reduces the need for medications and ocular side effects [57]. But conversely, in 20-30 % of cases the surgery can fail and lead to significant postoperative complications like fibrosis [35], infections, uncontrolled leackage - resulting in hypotony [60] - or cataract formation [57, 61]. Summarized, this procedure is not only fraught with short-term risk but also potentially life-time risks which can lead to devastating consequences for eye sight [35]. However, among other treatments, trabeculectomy still offers the best the best option and is therefore also referred to as the gold standard [58]. Nonetheless, GDDs would probably be a better alternative, if the main issues are solved which are currently limiting their long-term applicability.

Glaucoma Drainage Devices (GDDs)

In the late 1960s Dr. Anthony Molteno introduced the first intraocular implant for glaucoma treatment [62]. The concept of this implant relied on an episcleral plate, positioned in the equatorial region, and a silicon tube, connected to the plate to drain the fluid from the AC to the limbus area [62, 63]. Since then, a variety of GDDs emerged and followed which can broadly be classified into valved and non-valved drainage devices [64].
Valved glaucoma implants, as the Krupin pressure-sensitive valve [64, 65], or the Ahmed glaucoma valve (AGV) [35, 64], are flow-restrictive and prevent hypotony [64]. The Molteno implant [66] and the Baerveldt implant (Iovision, Inc, Irvine, California) are open-tube devices and examples for non-valved glaucoma implants (shunts) [64, 67]. Another example for a newer GDD is the Ex-PRESS shunt (Optonol Ltd., Neve Ilan, Israel), existing in four designs with different lengths, plate shapes and lumen sizes [35]. All these devices vary in material (silicone, polypropylene) but generally are designed similar to the first developed implant by Molteno: a tube attached to a plate, which is fixed to the post-equatorial sclera and divert the aqueous humor from the AC to the

subconjunctival space, forming a filtering 'bleb' [35, 64]. In multiple short- and long-term studies, these implant options demonstrate a good and effective IOP control [35, 64]. However, there are still several complications occuring after implant surgery, such as hypotony, tube retraction and erosion, motility disturbance, valve malfunction, tube kink and occlusion, fibrosis or 'bleb infections' - due to the non-physiologic nature of aqueous filtration - which all ultimately result in failed IOP control and increased pressure [35, 64].

In the last decades the surgery options further developed and improved opening a new field in glaucoma surgery: the minimal invasive glaucoma surgery (MIGS) [28]. MIGS devices are divided into Schlemm's canal devices, subconjunctival devices and suprachoroidal devices [68].

Devices that use an *ab interno* approach to access Schlemm's canal directly are for example the Hydrus Microstent® with 8 mm in length (Ivantis Inc., Irvine, CA) or the trabecular micro-bypass iStent® (GlaukosCorp., Laguna Hills, CA), with a length of 1 mm and a diameter of 250 µm [35, 69, 70]. Due to the very small size of the iStent® the implantation of several stents (up to fife) in one eye is possible to achieve the desired IOP [69]. On the other hand the very small size offers an increased risk of lumen occlusion and mispositioning [69].

The 6.35 mm long CyPass micro-stent (Alcon, USA) with an inner diameter of 300 µm is an example for a suprachoroidal device, using the uveoscleral pathway to reduce elevated IOP [68].

Further implants, belonging to the MIGS-device group are the XEN45 gel implant with l=6 mm and ID=63 µm (Allergan Inc., Irvine, CA) and the InnFocus MicroShunt® with a length of 8.5 mm (InnFocus Inc., Miami, FL), which use the pathway to the subconjunctival space, similar to the traditional GDDs (Ahmed valve, Baerveldt, …) [70, 71].

The advantages of these MIGS are that they avoid major alterations in eye anatomy and by this lower the risk of complications, e.g. bleb infections [35]. Furthermore, only small incisions are necessary, due to the very small sizes of the GDDs, and minimal postoperative management [35]. Previous studies reported low complication rates and reliable IOP decrease in the mid-tens without the occurrence of hypotony [69]. However, the studies for these newer drainage devices are ongoing and especially the evidences of long-term success, reliability and safety are still lacking [35, 68]. Furthermore, MIGS are currently not useful for all types of glaucoma or for patients with very high IOP values, but only target patients with mild to moderate glaucoma [72].

Overall, the number of GDD implantations significantly increased in the last decades [73]. Whereas, in the past, glaucoma implants were mainly used as last option when other treatments failed, today, the implantation of GDDs is often considered as primary treatment option as well [73, 74], especially with the appearance of MIGS. Unfortunately, despite safer surgical techniques and distinct improvement of GDDs, we are still far away from a long-term reliable treatment of glaucoma. Indeed, the failure rate of an implant is about 10 % per year and 33-53 % at 5 years [73, 75, 76]. Furthermore, not only early post-operative complications can occur, as already outlined, but also (or especially) long-term complications are notably prevalent. Within five year, 34-69 % of cases reported implant-specific complications as tube erosions, plate exposures and significant endothelial cell loss (ECL) [70, 73, 75, 77-79]. In these cases, the only options are rectification or removal of the implant and reimplantation of a new GDD in a different area of the eye [73, 80].

1.2 Matrix Calcification in Glaucomatous Eyes

In the human body, there are two faces of calcification: the physiological and pathological. The physiological calcification is an important and desired function for the formation of hard components as human skeleton (bones and cartilage) or teeth, whereby the ectopic calcification of soft tissue, as lung, arteries or eyes, is considered as pathological and can have serious impact on health [81].

1.2.1 Biomineralization of Calcium Phosphate (CaP)

The physiological mineralization of calcium phosphate (CaP) is a highly regulated and complex process under cellular control, which is still not yet fully understood [82, 83].
The most thermodynamically stable phase of CaP is hydroxyapatite (HAp) [84] (figure 5). It serves as the primary inorganic constituent of natural hard tissues (bones, dental enamel) in vertebrate animals and humans [84]. Other CaP phases, such as amorphous calcium phosphate (ACP) or octacalcium phosphate (OCP) are precursors, or sub-precursors, that transform into HAp *in vivo* or in aqueous environments with elevated pH [85-87]. All phases of CaP are summarized in table 1.

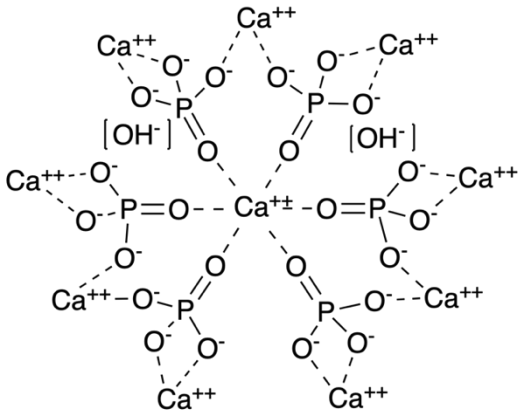

Figure 5: Chemical structure of hydroxyapatite (HAp), the most stable form of calcium phosphate (CaP).

In the late 1960s Anderson [83] and Bonucci [88] discovered - independently from each other - the presence of spherical nanostructures at initial sites of mineral formation in growth plate cartilage, today known as matrix vesicles (MVs) [89]. Since then, there are different assumptions of how the calcification starts and mineral formation takes place. However, there is one general aspect, the majority agrees: the initial crystal formation in mineralizing tissues as cartilage or bone starts in form of ACP precursors, then develops to HAp. The whole process is influenced by and takes place in MVs, originated by budding and pinching off from the plasma membrane of the corresponding mineral forming cells (e.g. osteoblasts or chondrocytes) [82, 90].

Table 1: Overview of calcium phosphate (CaP) minerals/phases. The table was adapted from the literature [87, 91].

Name	Symbol	Formula	Ca/P
Monocalcium phosphate monohydrate	MCPM/MCPH	$Ca(H_2PO_4)_2*H_2O$	0.5
Monocalcium phosphate anhydrous	MCPA/MCP	$Ca(H_2PO_4)_2$	0.5
Dicalcium phosphate dihydrate (Brushite)	DCPD	$CaHPO_4*2H_2O$	1.0
Dicalcium phosphate anhydrous (Monetite)	DCPA/DCP	$CaHPO_4$	1.0
Octacalcium phosphate	OCP	$Ca_8(HPO_4)_2(PO_4)_4*5H_2O$	1.33
α-Tricalcium phosphate	α-TCP	α-$Ca_3(PO_4)_2$	1.5
β-Tricalcium phosphate	β-TCP	β-$Ca_3(PO_4)_2$	1.5
Tetracalciumphosphate	TTCP	$Ca_4(PO_4)_2O$	2.0
Amorphous calcium phosphate	ACP	$Ca_xH_y(PO_4)_z*nH_2O$, n=3-4.5	1.2-2.2
Hydroxyapatite	HAp	$Ca_{10}(PO_4)_6(OH)_2$	1.67

The Mineralization Mechanism in Matrix Vesicles (MVs)

Simplified, the whole biomineralization process is divided into two phases: the intake and accumulation of Ca^{2+} and PO_4^{3-} (Pi) in the MVs and the formation of first HAp crystals within the vesicles (phase I), followed by MV disruption, crystal release and mineral propagation on collagen fibrils in the ECM (phase II) [90] (figure 6a). The structure and main components of MVs are summarized in figure 6b.

The membrane structure of MVs is a lipid bilayer and the sizes of MVs are ranging from 10 nm to 400 nm in diameter [90, 92-94]. The vesicles contain different mineralization supportive plasma membrane proteins, important for their function as initial sites of mineral formation [90]. Previous studies showed that the proteomic composition of MVs is diverse and manifold [95], therefore here we will only focus on the most important proteins, enzymes or channels which are referred to their function as initial sites of HAp mineralization.

One group of proteins in the membrane of MVs are the calcium-binding annexins (mainly annexin II, V & VI [92]), which serve as transmembrane Ca^{2+} ion channels [90]. Furthermore, the inner and outer membrane surface of the MVs is enriched in acidic calcium-binding phospholipids as phosphatidylserine (PS) [82], which can recruit surrounding Ca^{2+} to the MVs.

Another important group are phosphohydrolases in/on the MV membrane as the nucleotide pyrophosphatase-1 (NNP-1) and especially the enzyme alkaline phosphatase (AP), also known as tissue-non-specific alkaline phosphatase (TNAP) [92]. They promote the mineralization by hydrolysis of phosphate-containing substrates as adenosine triphosphate (ATP), ester phosphate or pyrophosphate (PPi) to Pi, and thereby increasing the concentration of phosphate required for the formation and growing of HAp [82, 90]. TNAP is a membrane ectoprotein with a glycosylphosphatidylinositol (GPI) anchor, which is connected to the C-terminus of the protein by an amide linkage and provides mobility of the protein in the membrane [96-98].

For initial crystal formation the Pi ions are channeled into the MVs via phosphate transporters [94]. In addition to the phosphatases in/on the MV membrane, the phosphatase Phospho-1 inside the vesicles produces Pi from phosphocholine (PC) or phosphoethanolamine (PEA) [99].

After initial mineral crystals are formed, first in form of ACP, then HAp, they disrupt the MV membrane and finally are released in the extravesicular fluid, where they deposit on and in collagen fibrils-the scaffolds for ECM calcification-and serve as templates for further mineral growth [82, 92, 100]. Furthermore, it was shown, that the MVs itself stimulate mineral precipitation by moving to and interacting with the collagen matrix via annexins and AP in the vesicle membrane [101]. However, the detailed interplay between MVs and collagen matrix is still largely unknown [101].

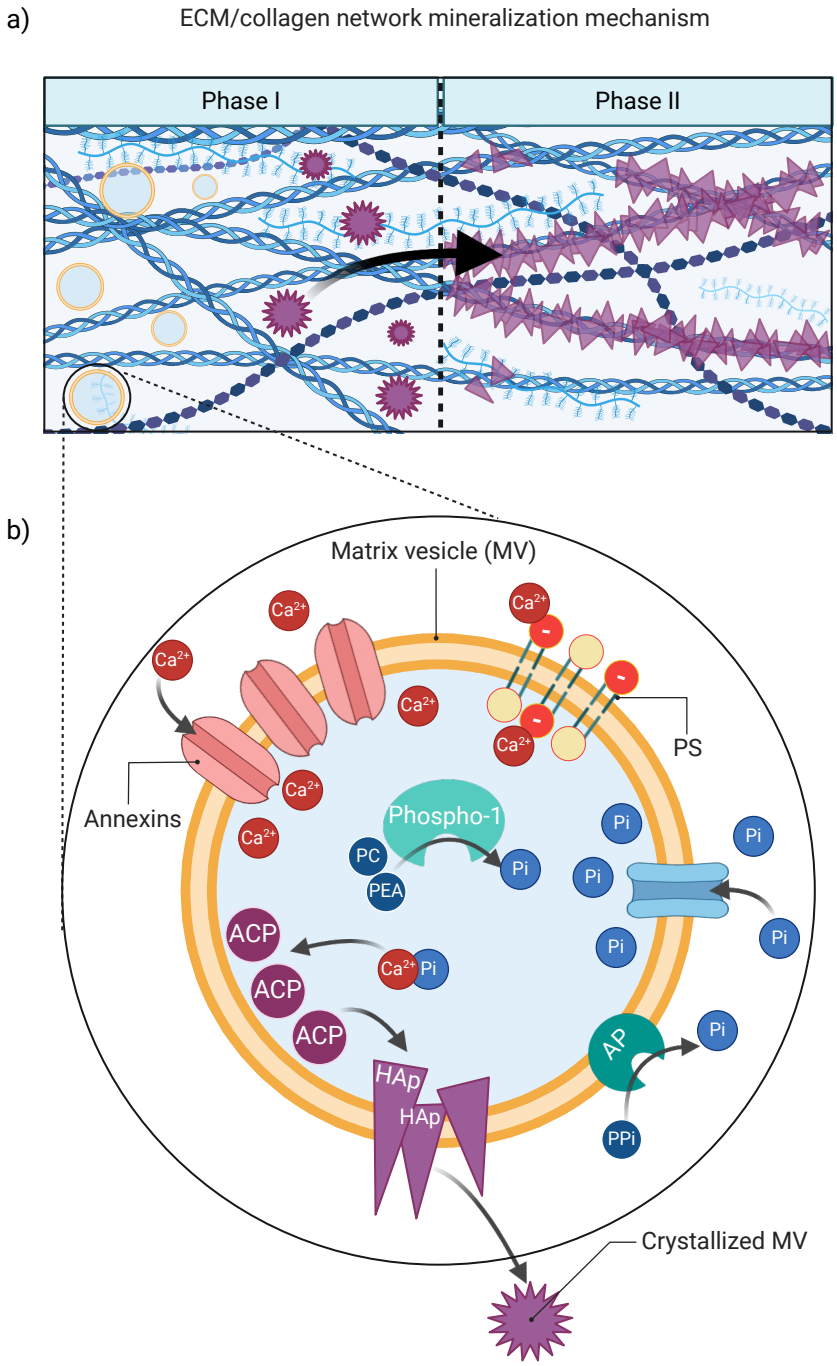

Figure 6: Schematic drawing of the ECM/collagen mineralization mechanism (a) and enlarged matrix vesicle (MV) with main components for hydroxyapatite (HAp) formation (b). AP, alkaline phosphatase; PS, phosphatidylserine; ACP, amorphous calcium phosphate. The drawing was adapted from the literature [94] and created with Biorender.com.

1.2.2 Ectopic Calcification of Ocular Outflow Structures

For a long time, it was thought that the ectopic mineralization of soft tissue is a passive process, occuring by the propensity of calcium and phosphate forming insoluble minerals [102]. In the early 1980s Rohen et al. analyzed TM tissues, obtained from trabeculectomies of more than 130 glaucoma patients, and firstly discovered the presence of MVs, AP and extracellular "plaque material" [103]. Since then, the view on ectopic calcification changed entirely, driven by further research and discoveries in the last decades, recognizing that these processes are dynamically regulated by different factors [102].

Over the years, several studies identified various calcification genes in the TM tissue, normally involved in bone and cartilage formation, and it was found that the expression of some of these genes is regulated by glaucomatous conditions as elevated IOP and mechanical stretching [36, 43, 100, 104-106]. The presence of these genes in the TM indicate a pathological calcification process in the ocular outflow structures which need to be counteracted [100].

Alkaline Phosphatase (AP) & Matrix Gla Protein (MGP) - The Key Player in Glaucomatous Calcification

As outlined before, one key player in CaP mineralization is the MV-associated enzyme AP (or TNAP), which is considered to be THE marker of calcification in the human body [100]. In the healthy human eye, AP is not expressed in the TM, or only in very small quantities [100], whereas in aged and glaucomatous eyes the AP expression and activity is significantly increased, leading to a hyperphosphatemia in the TM tissue [104, 105].

Another key player, found in the ECM of different tissues such as bone, cartilage [107], lung, or arterial vessels and which is also one of the most expressed genes in the TM [36], is the gene encoding the matrix gla protein (MGP), known as the matrix calcification inhibitor or protector (figure 7) [104, 108, 109].

MGP is an 84 amino acid protein with five γ-carboxy-glutamic acid (gla) residues, which are post-translationally activated by the vitamin K-dependent enzyme γ-glutamyl-carboxylase (GGCX) [107, 110]. The negatively charged gla residues provide the main function of MGP: the binding of calcium ions and crystals and thereby inhibiting calcium deposition in the human body, especially in soft tissues [102].

Another post-translational modification of MGP is the phosphorylation of the serine residues 3, 6 and 9, which are also able to bind calcium and calcium ions [102, 111]. Beyond that, the main function of the phosphorylated serines is the regulation of the protein secretion into the ECM [112], since unphosphorylated MGP primarily appears in the cytosol and is only partially secreted [113]. Previous studies of MGP-knockout mice showed the dramatic effect when the protein is lacking: hypermineralization of cartilage, known as Keutel syndrome [114], and abnormal calcification of arteries, resulting in blood-vessel rupture and early death shortly after birth [81].

In the healthy TM it was shown, that the gene expression of GGCX and MGP is regulated and increased by increasing IOP [106] and mechanical stretching [43]. In aged and glaucomatous human trabecular meshwork (HTM) cells in culture [104] and TM tissue from long-term glaucoma

donors, the expression of MGP and its activator GGCX is significantly decreased [105], resulting in a Ca^{2+} accumulation (hypercalcemia) in the ECM.

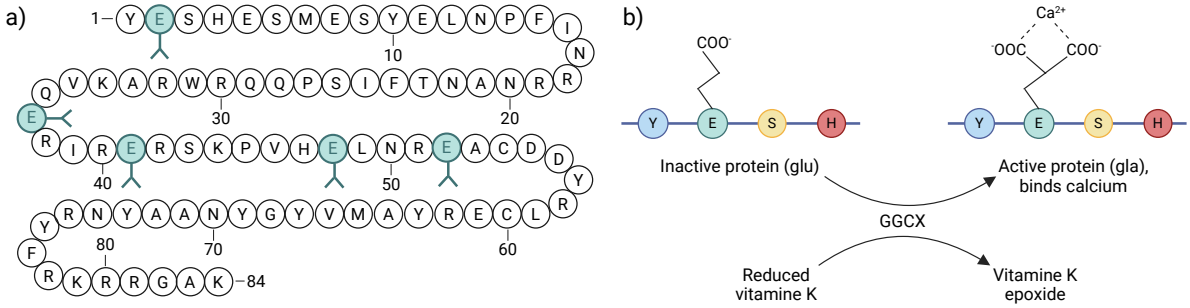

Figure 7: Amino acid sequence and activation mechanism of human MGP. MGP with five γ-carboxyglutamic acid (gla) residues (denoted by γ in light green) (a) and protein activation of MGP by vitamin K-dependent γ-glutamyl-carboxylase (GGCX) (b). The drawing was adapted from the literature [110] and created with BioRender.com.

It was also observed, that there is a correlation between MGP expression and AP activity: overexpression of MGP decreases AP activity [105], conversely increased AP activity was observed when silencing MGP [104]. In figure 8 the whole processes including gene expression and activity of MGP and AP are summarized comparing a normal and glaucomatous eye.

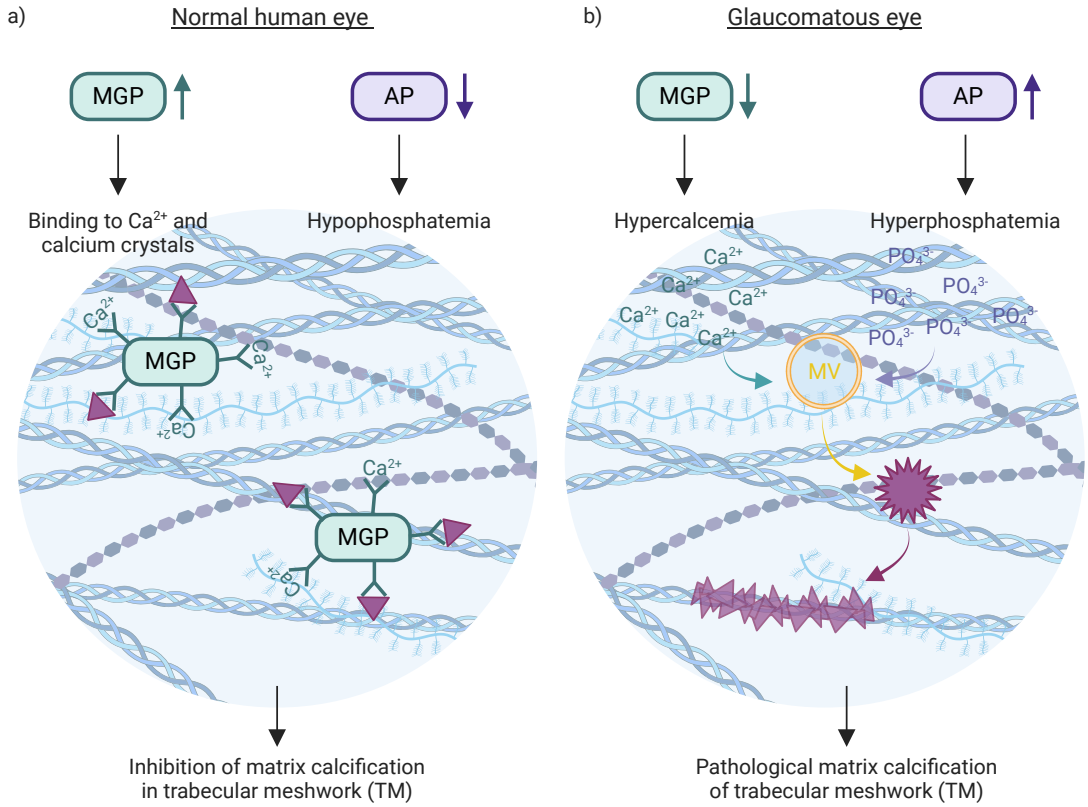

Figure 8: Schematic overview of gene expression and activity of matrix Gla protein (MGP) and alkaline phosphatase (AP) in normal (a) and glaucomatous eye (b). In normal human eye MGP is the most expressed gene and inhibits calcification by binding to calcium ions and crystals; AP is decreased (a). In glaucomatous eyes MGP expression is significantly decreased, leading to hypercalcemia; simultaneously hyperphosphatemia occurs by overexpression of AP. Both collectively results in a calcium phosphate (CaP) deposition in the ECM of trabecular meshwork (TM). Drawing was adapted from the literature [102] and created with BioRender.com.

Taken together, the fact that TM cells exhibit a variety of anti-calcific components in their ECM shows that the calcification process and its prevention are an important mechanism in the healthy TM to decrease the outflow resistance and enhance aqueous outflow [100]. A deeper knowledge of the calcification-preventing mechanism in the TM can be useful in order to influence the outflow resistance and provides a new approach to lower elevated IOP in glaucomatous eyes.

1.2.3 Mineralization Models of Calcium Phosphate (CaP)

The physiological and pathological mineralization of CaP, especially the role of MVs in the mineralization mechanism, is of growing interest in medical and scientific fields [94]. Over the years, several mineralization models and approaches were established in order to understand and unravel the mineralization processes in the human body.

The majority of studies focus on the isolation of MVs from osteoblasts, chondrocytes and odontoblasts, the characterization of their physical, biological and functional properties [101, 115-119] and their potential for therapeutic applications, as bone fracture healing [120, 121]. However, for the MV isolation live animals are required and the whole procedure is though laborious and time-consuming [122]. Instead of the extraction of cell-derived vesicles, various different mineralization models were established over the years, mainly focusing on the biomimetic engineering of MVs. This section gives an overview of the different approaches for, summarized in figure 9.

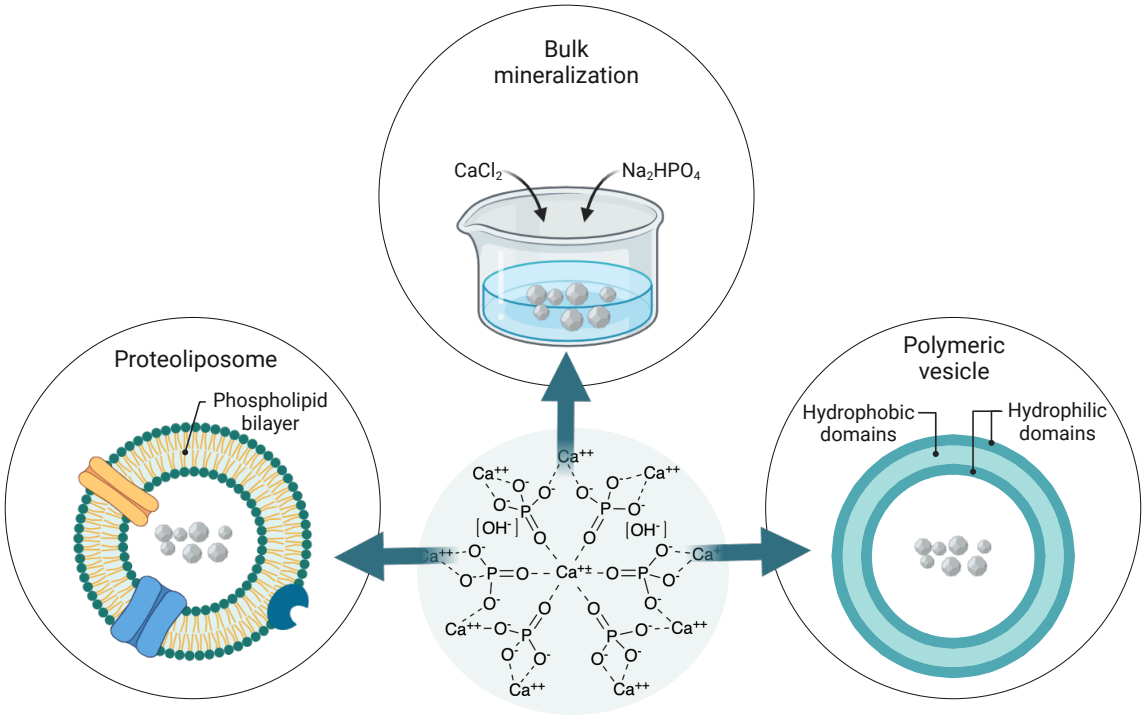

Figure 9: Overview of mineralization models for calcium phosphate (CaP)/hydroxyapatite (HAp). Bulk mineralization models are simple and widely used *in vitro* models using the corresponding ions for mineral formation (top). Other approaches for the functional mimicry of matrix vesicles (MVs) are proteoliposomes with a lipid bilayer, that can be modified with various proteins/enzymes (left), and polymeric vesicles composed of hydrophilic and hydrophobic domains. The drawing was created with BioRender.com.

Bulk Mineralization Models

A simple and widely used approach for biomineralization studies of different minerals as calcium carbonate, and also for CaP, is the mineralization in bulk systems [123-126]. Thereby, the desired mineral is created by using corresponding solutions which provide the ions for mineral formation. In general, such *in vitro* models involve also structure-directing additives as proteins and/or peptides which are artificially designed [123-126] or extracted from hard tissues of biological organisms as corals [127], mollusk shells [128] or sea urchins [126, 129, 130].

The major advantage of bulk systems for mineralization studies is attributed to its simplicity and they are useful model systems in order to investigate the influence of proteins/peptides on the mineral formation, as the nucleation, the formation rate, the polymorph or the morphology (size and shape) of the crystals [109, 123-126].

However, in bulk systems, parameters like pH or ion concentrations can be less precisely controlled and gradients that can form within the solution can lead to e.g. inhomogeneous mineral growth. The open nature of bulk systems makes them also prone to side reactions, which can influence the desired mineralization process and lead to impurities and undesired byproducts. Bulk systems also require large quantities of reagents, which increases costs and waste. Furthermore, as outlined before, the initial mineralization of HAp expires in MVs, for that reason the bulk mineralization model represents only partially the biological formation of hard tissues and ectopic mineralization processes.

Functional Mimicry of MVs by Proteoliposomes

One approach to mimic MVs for biomineralization studies are proteoliposomes, consisting of a lipid bilayer, similar to biological membranes [93, 94, 97, 122]. These lipid membranes composing of one lipid type or a mixture of different lipids [96, 131], can be modified with various enzyme and protein combinations, which are associated with MV-mediated mineralization, such as AP or annexin V [96, 97]. Typically, proteoliposomes are produced by mixing lipids with the desired membrane proteins, which can be either embedded within or associated with the lipid bilayer [132]. This MV-mimicking system is an excellent tool to examine for example the role and function of single components and lipid-protein interactions in general [133] and also during the MV-mediated mineralization process [93]. Furthermore, in medical fields the proteoliposome-based MV research is focused on the development of novel drug-transport-systems for the treatment of diseases as Osteoarthitis (OA) [93].

Another approach is a novel therapeutic strategy against pathological mineralization, with proteoliposomes which are designed to target soft tissues and prevent mineralization by inhibition or activation of MV enzymes [93, 96]. However, these therapeutic applications of MVs are "still in its infancies" [94], since they offer a major risk of unwanted mineralization when MVs reaching the wrong location in the human body [94]. It is known that the mechanisms of physiological bone formation are similar to vascular calcification [134, 135], therefore further investigations are necessary to increase the specifity of MVs before they can be considered for therapeutic applications [94].

Overall, proteoliposomes as biomimetic MVs are useful models for biomineralization studies of HAp. However, previous studies showed, the higher the complexity of the proteoliposome structure/composition, the lower the stability of the vesicles and the lower the activity of incorporated components, such as TNAP [136]. Furthermore, maintaining the stability of proteoliposomes over longer times can be difficult, which may compromise reproducibility of experiments [136]. Another aspect concerning the complex assembly of lipidic components of natural MVs, which normally are not randomly distributed, but organized in microdomains, and whose composition also changes during the mineralization process [136, 137]. Therefore, the proteoliposome systems require a methodological standardization for the insertion of each specific protein and verification of correct protein orientation and functionality [96]. Taken together, these challenges make proteoliposomes labor-intensive and less efficient compared to simpler models.

Polymeric Vesicles as Biomimetic MVs

Another way to mimic MVs are polymeric vesicles, composed of synthetic polymers instead of lipids. Similar to lipids they are amphiphilic, meaning they have hydrophilic and hydrophobic components, but they are chemically more complex and more robust than lipid membranes [132, 138]. The synthetic nature of polymeric vesicles allows greater flexibility in modifying their properties, such as size, charge and stability [138]. Polymeric vesicles are formed from amphiphilic block copolymers, which self-assemble into vesicles in aqueous environments [138, 139].

These vesicles are often used in technical and medical applications, particularly in drug delivery and nanomedicine [132, 140], and they are also useful models to investigate for example the second part of the mineralization process, the release of HAp from MVs and mineral propagation on collagen fibrils. In recent studies from Shen et al. a mineralization model of nanoparticles with polyethylene glycol (PEG) was established, equipped with ACP, which was stabilized with serine (S), forming together a PEG-S-ACP nanoparticle complex [141]. Adding these nanoparticles to a solution of polysorbate, micelles around the complex were formed, mimicking ACP-carrying MVs [141]. These biomimetic MV models were then introduced to collagen fibers, followed by the release of ACP from the vesicles and mineral propagation on and in collagen fibrils [141].

Another example for biomimetic polymeric MVs was established by Wang et al., which focused on targeting mineralization, showing that artificial MVs are able to promote new bone formation by regulating the mineralization process in cells [142]. The model MVs consisted of black phosphorous nanosheets encapsulated in nanoparticles made of poly(lactico-glycolic acid) (PLA) [142]. The nanoparticle surface was equipped with osteoblast-targeting aptamers, which enabled the binding of the MVs to osteoblasts [142]. The addition of black phosphorous to the system facilitated the *in vivo* mineralization by enhancing the local Pi concentration and by this promoted the formation of new hard tissue [142].

A new biomimetic inspiration and approach of hard tissue repair was shown for dentin using artificial MVs based on platelet membrane vesicles (PMVs) [143]. However, the platelet extraction for PMV preparation required living animals, since the platelets were isolated from the whole blood of rats [143].

Summarized, the applications of these polymeric vesicles are diverse: targeting mineralization, studying mineral propagation (phase II) including enzymatic defects occuring in bone diseases, and additionally they harbor the potential of therapeutic applications as hard tissue repair (fracture healing) [94, 144]. However, as already mentioned for proteoliposomes as artificial MVs, the therapeutical use of polymeric vesicles is also far away from reality and requires further investigations and characterizations of the MVs.

Moreover, for studying biomineralization processes using polymeric vesicles the opportunities are limited to the encapsulation of mineralized particles, while mineral formation cannot occur in these systems.

1.3 Motivation & Aim of the Thesis

More than 10 years ago my grandma got the diagnosis of glaucoma. At that point, her eyesight was already impaired, with minor vision field defects. To reduce the IOP and slow down the progress of her glaucoma she got eye drops, which helped for a few months, until she noticed a deterioration again. Since her diagnosis she got several laser trabeculoplasty, continued using eye drops and further surgical intervention is not excluded to preserve eyesight.
Besides my grandma, there are multiple cases of glaucoma disease in our family history, and everyone who has a genetic predisposition should definitely pay attention to prevent visual field impairment and blindness. Indeed, the risk to develop glaucoma is eight-fold higher for first-degree relatives, compared to the other population [5], and the fact, that in early stages of glaucoma most people are unaware of it and only notice it in the late course when eye sight is already impacted, is what makes it so mean and dangerous.
This circumstance and the direct relationship to glaucoma motivated me, to gain a deeper knowledge of the disease progression and to explore a new and reliable treatment option.

For that reason, this thesis aims to investigate the glaucoma disease from two different perspectives (figure 10). In the first part of my thesis a new type of glaucoma implant is investigated, focusing on its improvement, miniaturization and examination of its pressure regulation abilities to tackle the problems with current implants for controlling IOP. In the second part, I'm extending the picture of another aspect: the occurrence of calcification processes in glaucomatous eyes and the design of a new biomimetic model for biomineralization studies of CaP.

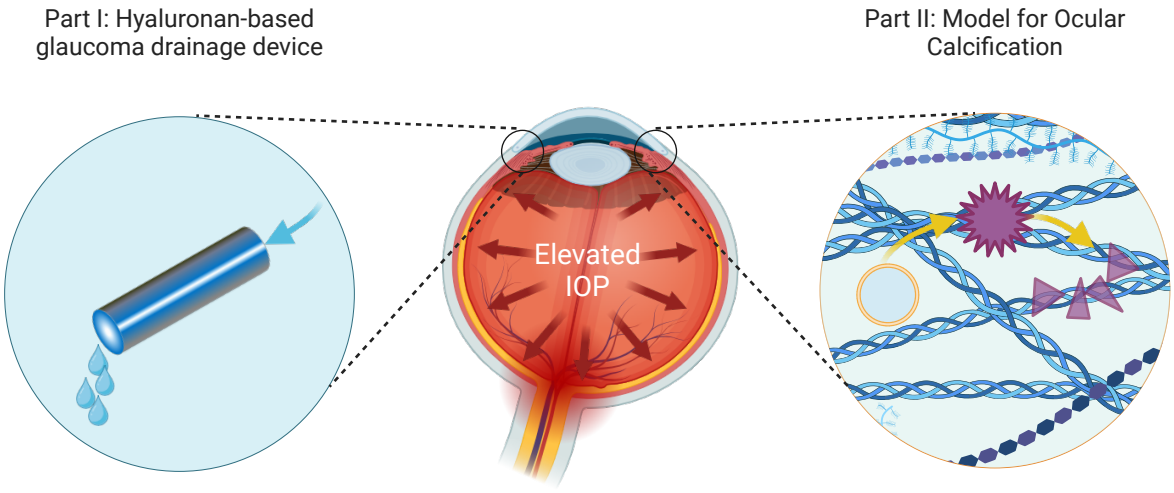

Figure 10: Experimental parts in this thesis. Design and investigation of a novel glaucoma drainage device (GDD) based on hyaluronan hydrogels (part I) and a model for ocular calcification (part II). The drawing was created with Biorender.com.

1.3.1 Part I: Hyaluronan-Based Glaucoma Drainage Device

The management of the glaucoma disease is a life-time burden for each patient, that requires an ongoing monitoring of the patient and adjustment or change of the treatment when deterioration occurs. Among several glaucoma risk factors that are out of everyone's control, as genetic predisposition or age, there's one modifiable factor: the IOP [5, 9]. All current treatments focus on IOP reduction to slow down the disease progression, and especially the number of GDD implantations markedly increased in the last decades. Unfortunately, despite distinct improvements of GDDs they are not completely reliable and the implant failure rate of 33-53 % in 5 years [73, 75, 76] is still too high and not acceptable. Therefore, further investigations are necessary to solve frequent implant issues like hypotony, implant occlusion, fibrosis or insufficient biocompatibility to finally reach a long lifespan of the implant and reduce post-operative management and complications for the patient.

The first part in this thesis focuses on investigations of a new type of glaucoma implant. Previous studies by Michael Thaller from the team of Joachim Spatz in the department of Cellular Biophysics at the Max Planck Institute for Medical Research (MPI-MR) established the main concept of the new GDD [145, 146]. The core innovation of this device is based on a small titanium implant, modified on its interior with a HA hydrogel. The requirements for this hydrogel modification are: 1. The hydrogel should possess valve properties to drain excess fluid and reduce elevated IOP; 2. The hydrogel should possess cell repellant properties to prevent clogging due to cell growth. Thaller created large implant "prototypes" (ID=5 mm and l=10 mm) and established the chemistry for their preparation, as the immobilization and formation of the HA hydrogels on the interior of large glass model tubes. Furthermore, he introduced a hydrostatic pressure setup for the measurement of the large model tubes. In my Master Thesis [147] Thallers' investigations and groundwork was extended by further aspects. In one of it, the pressure regulation abilities of the large hydrogel-modified glass model tubes were examined and it was shown that there is a correlation between HA hydrogels of different thiolation grades (TGs) and the final pressure measured, which was found to be in the normal pressure range of the healthy human eye.

In the first part of this thesis, the main focus lies on the miniaturization of the whole large model setup to a scale of a real future glaucoma implant (ID=0.5-1 mm, l=3-6 mm). Moreover, the investigations are focusing on further different hydrogel compositions for implant improvement by using HA of different molecular weigth (40 and 100 kDa), TGs (28-63 %) and mass concentrations of HA (β(HA)= 5, 10, 15 and 20 mg/ml), as well as different bi- and multifunctional crosslinker (MBAA, ACLT-PEG-ACLT, 4arm-PEG-ACLT, 4arm-PEG-VS). Another objective in this thesis is the characterization of the hydrogel compositions, specifically the swelling behaviour and the hydrogels' resistance against enzymatic degradation. For the miniaturized model implants a new and improved pressure measurement setup is established using microfluidics and different measurement modes are implemented to examine the pressure regulation abilities of the miniaturized model implants under realistic conditions as the pressure regulation at a physiological flowrate or during pressure fluctuations. Furthermore, the model implant production is improved by designing and testing different 3D printed patterns.

1.3.2 Part II: Model for Ocular Calcification

The pathological processes of glaucoma, the origin of IOP elevation and optic nerve degeneration are still only partially understood. Several studies suggest, that the blockage of aqueous outflow is the result of alterations/accumulations in the ECM of the ocular outflow structures, mainly in the soft, spongiform TM tissue [40, 41]. One form of ECM alteration is the precipitation of mineralized particles in form of CaP/HAp, which leads to a stiffening of the TM, increased outflow resistance and IOP elevation [37, 43, 45].

Furthermore, over the years, various calcification and anti-calcification genes were identified in the TM, normally involved in bone and cartilage formation [43]. The presence of these genes, and the fact that their expression is regulated by glaucomatous conditions, as elevated IOP and mechanical tension, indicates a pathological calcification process in the ocular outflow structures which need to be counteracted.

One of the most expressed genes in the TM is the gene encoding MGP, known as the matrix calcification inhibitor/protector [100]. In glaucomatous eyes the expression and activity of MGP is significantly decreased, resulting in a Ca^{2+} accumulation (hypercalcemia) in the TM, and simultaneously, it comes to a hyperphosphatemia by overexpression of the enzyme AP [100]. Both collectively results in a CaP precipitation in the TM and glaucoma progression.

Overall, there are still many unanswered questions regarding the entire mineralization process, as for example it is not yet clear, whether the calcification is a cause or the result of the glaucoma disease. Therefore, further investigations are necessary with appropriate models to unravel the complex interactions between the components, that play a role in this blinding disease.

In the second part of this thesis the picture of the glaucoma disease is extended by another aspect: the occurrence of calcified particles in the ocular outflow structures of glaucomatous eyes and the design of a new biomimetic approach for biomineralization studies of CaP. It is known that the pathological calcification in the TM takes place in small spherical structures, the MVs. Simplified, the whole mineralization process is divided into two phases: the initial mineral formation of HAp in MVs (phase I) followed by crystal release and subsequent mineral propagation on/in collagen fibrils in the ECM (phase II).

This experimental part focuses on phase I and the design of a new approach for mineralization studies, which mimics the biological mineral formation in MVs using a droplet-based system. Outgoing from previous CaP mineralization studies in bulk systems, this approach aims to further develop the existing bulk models by additionally reproducing the spherical geometry of MVs as individual controllable reaction chambers, which can provide further insights into the MV-mediated calcification.

Another aim of this second part is the investigation of the anti-calcification properties of MGP by using MGP peptides in the droplet-based mineralization model.

Part I:

Design and Investigation of a Hyaluronan-Based Glaucoma Drainage Device (GDD)

2 Introduction – Part I

2.1 Hydrogels

As biomaterials, hydrogels are employed in a wide range of applications [148], such as agents for wound dressings [149, 150] or as contact lenses [151] and the also build the core component of the novel GDD developed in this thesis. They can be synthesized from various natural and synthetic compounds, forming three-dimensional networks of interconnected hydrophilic polymer chains arranged in condensed coils of varying length and irregular structure [148] (figure 11). The crosslinks between the polymer chains within the network are either chemical (permanent) or physical (reversible) [148].

Naturally occuring polymer sources used for hydrogel formation are for example gelatin [152, 153], alginate [154] or HA [155-159]. Frequently used synthetic polymers are PEG [160-162] or poly(*N*-isopropylacrylamide) (PNIPAM) [163]. Hydrogels closely mimic natural tissue and due to their properties, such as flexibility, softness, biocompatibility and a high capacity for water uptake -termed swelling - they are used in various industrial and scientific applications [148, 149, 151, 164-168].

In biomedical fields hydrogels are used as scaffolds for tissue engineering [165, 169], as drug delivery systems [153, 166], agents for wound dressings [149, 150] or as contact lenses [151]. In biotechnology, hydrogel-modified surfaces are often employed as biosensors [170] or to manipulate cell adhesion [167]. Other potential hydrogel applications can be found in agriculture, for example as delivery systems for the controlled release of fertilizers [171] and/or water [168, 172] to crops. These examples represent only a small fraction of potential hydrogel applications, with numerous additional examples documented in literature [173-177].

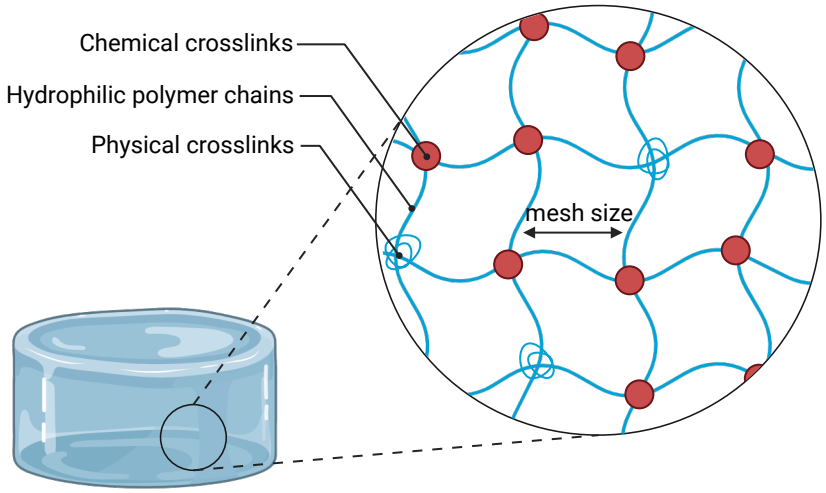

Figure 11: Schematic drawing of a hydrogels polymeric network structure with the two crosslinking mechanisms of the polymer chains inside a hydrogel. Chemical hydrogels are connected by covalent links resulting in permanent hydrogels; physical crosslinks are dynamic and can be dissolved. The picture was adapted from the literature [148, 178, 179] and created with BioRender.com.

2.1.1 Classification of Hydrogels

The classification of hydrogels is as diverse as their applications, depending for example on their source material (natural, synthetic), physical properties, type of crosslinking, degradability, ionic charge and more (figure 12) [148].

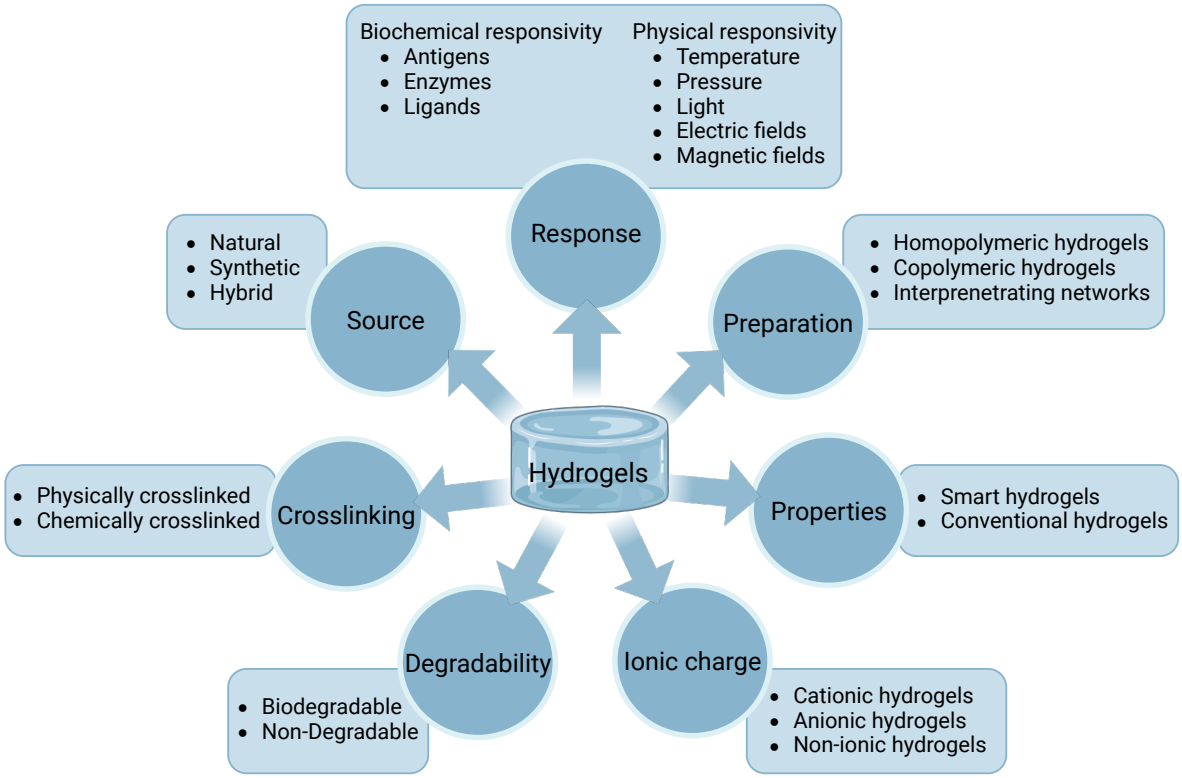

Figure 12: Overview of hydrogel classification and types according to different parameters. The picture was adapted from Ullah [148] and created with BioRender.com.

The most widely adopted classification categorizes hydrogels based on their crosslinking mechanism, distinguishing them as either chemical or physical hydrogels [180] (figure 13). The degree and type of crosslinking impacts different network characteristics, such as mesh size, swelling behavior or stiffness, which results in a wide spectrum of hydrogels with distinct properties, highlighting their versatility across various applications [148, 181].

In physical hydrogels the crosslinks between the polymer chains are driven by physical interactions such as H-bonding, ionic or hydrophobic/hydrophilic forces (figure 13a and b) [148]. As a result of these forces, the physical crosslinks are dynamical or reversible and can be dissolved by changes in temperature, pH or the addition of detergents [148]. For example, alginate chains can be crosslinked via ionic interactions using calcium ions [182], while polysaccharides of soft chitosan hydrogels are crosslinked by the hydrophobic effect and H-bonding [183].

In chemical or permanent hydrogels, the networks are formed by covalent links between polymers, or by the addition of bi-or multifunctional crosslinker (figure 13c and d), resulting in defined hydrogel networks with strong and permanent bonds [148]. The chemical reactions employed for hydrogel

synthesis are diverse and combinations of chemical and physical crosslinking methods are also feasible [148].

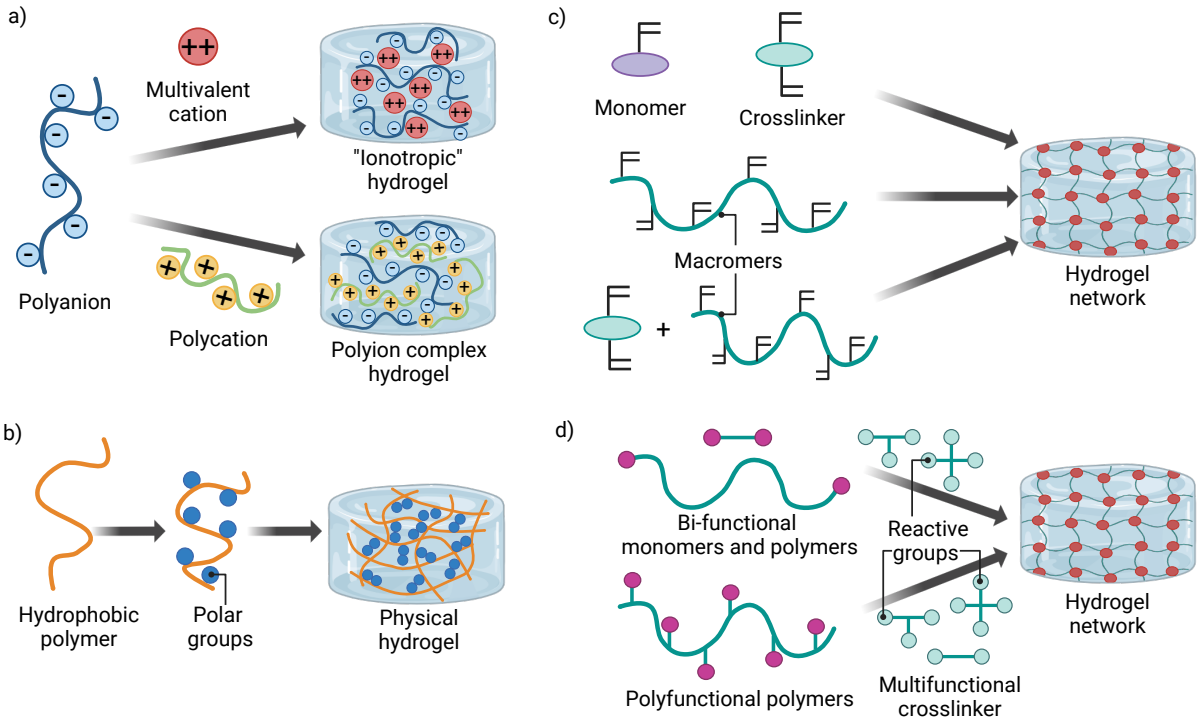

Figure 13: Schematic overview of different physical and chemical methods for hydrogel formation. Physically formed hydrogels use ionic interactions of charged polymers with oppositely charged ions or polymers (a); or hydrophilic interactions of a hydrophobic polymer functionalized with hydrophilic groups (b). A chemical hydrogel is formed via radical reactions involving monomers or polymers possessing functional groups capable of undergoing radical chain polymerization (c) or hydrogels are synthesized through chemical reactions such as Thio-Michael addition or Diels-Alder using polymers and multifunctional crosslinkers (d). Pictures were redrawn from Hoffman et al. [180] and created using Biorender.com.

The synthesis of chemically crosslinked hydrogels is commonly achieved through methods such as free radical polymerization, post-polymerization crosslinking or click-chemistry approaches, including Michael-type addition or Diels-Alder reactions [184-186].

2.1.2 Click Chemistry: The Thio-Michael Addition Reaction

Click chemistry has become a widely favored approach for the formation of hydrogels, due to its efficiency and versatility [187]. The reactions can be carried out in a single step under mild reaction conditions with no or only minimal byproducts, they are highly adaptable to various solvents and they have a strong thermodynamic driving force, leading to high yields [187, 188].

Additionally, a broad range of reactants and functional groups are available for click chemistry, making it highly customizable to suit specific requirements such as the desired crosslinking speed and other reaction conditions [187, 188].

One noticeable reaction pair in click-chemistry is thiol and ene, which exhibits many of the beneficial characteristics of click reactions [179]. First introduced by Arthur Michael in 1887, this reaction is commonly referred to as the Thio-Michael addition click reaction [189]. The thiol-ene-addition can occur under different conditions, including acid/base mediated, nucleophilic catalysis,

solvent-promoted reaction or radically initiated, whereby the latter is less common due to the disadvantage of byproducts [188, 190, 191].

The Thio-Michael addition mechanism describes a nucleophilic addition reaction in which a thiol reacts as a nucleophile with an α,β-unsaturated carbonyl compound (alkene), facilitated by the presence of a base or catalyst [192]. Thiols serves as strong nucleophiles (Michael-donors) and spontaneously react with alkenes next to electron withdrawing groups [192]. Common Michael-acceptors include electron-deficient groups as acrylates, acrylamides or vinyl sulfones since they facilitate the nucleophilic attack of the thiolate anion – often the rate-limiting step of the reaction [193]. The basic Thio-Michael addition reaction is outlined below (figure 14). For a more detailed crosslinking mechanism, specifically for our compounds, refer to section 2.2.1.

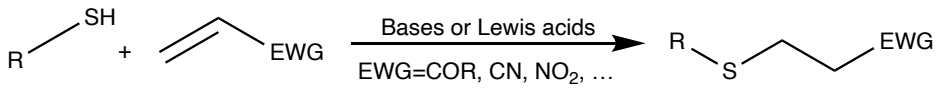

Figure 14: Basic thiol-Michael addition reaction. First the thiol is activated by a base (or nucleophilic) catalyst. The thiolate anion (Michael donor) attacks the β-position of the electrophilic double bond in the Michael acceptor (an α,β-unsaturated compound), forming an intermediate enolate anion. In a last step, the enolate anion is protonated, resulting in the final product: a β-thiol substituted carbonyl derivate. The reaction was adapted from the literature [191, 194]

2.1.3 Hyaluronan (HA) Hydrogels

HA is a polyanionic, non-sulfated glycosaminoglycan (GAG) consisting of unbranched, alternating chains of β-1,3- and β-1,4-linked units of glucoronic acid and *N*-acetyl-*D*-glucosamine (figure 15) [159, 195, 196]. Naturally occurring in the human body, HA serves as a major component of the ECM [195]. HA distinguishes itself from other GAGs in several key aspects. Notably, its synthesis occurs in the plasma membrane, rather than within the Golgi apparatus, as seen with other GAGs [195]. Additionally, HA forms significantly larger molecules, with molecular weights reaching up to $7 \cdot 10^6$ kDa, unlike other GAGs which are typically short (< 50 kDa) [195].

In addition, HA plays crucial roles in various biological processes, such as stabilization and organization of the ECM, regulation of cell adhesion and motility, and mediation of cell proliferation and differentation [195]. HA is predominantly found in skin and connective tissues [195, 197], as well as in the human eye, particularly in the aqueous humor [198] and in the ECM of the ocular outflow structures [39]. Within the TM, HA is a key component of the gel-filtration system and fulfills important regulatory functions for the maintenance of aqueous humor outflow and TM integrity [39].

HA is characterized by unique properties, including its remarkable capacity to bind large amounts of water up to 1,000 times of its own weigth [199]. This ability enables it to form highly viscous and elastic solutions even at low concentrations of <1 mg/ml [199]. Although the viscosity of HA solutions increases exponentially with concentration, solid gels are not formed [200, 201]. To enable the formation of stable HA-based hydrogel networks, chemical modifications are often required to introduce functional groups that enable crosslinking [202]. The three primary sites targeted for chemical modification of HA are highlighted in figure 15.

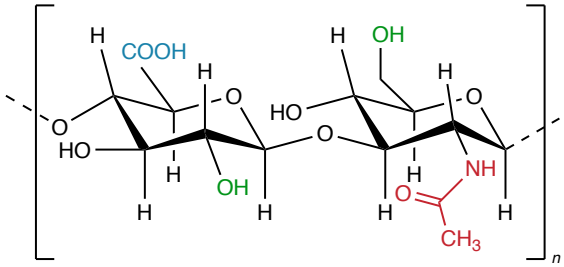

Figure 15: Chemical structure of hyaluronic acid (HA) with repeating units of glucoronic acid and *N*-acetyl-*D*-glucosamine. Functional moieties are colored, as the three most commonly used sites for covalent modifications: carboxylic group (blue), hydroxy group (green) and *N*-phenylacetamide ($NHCOCH_3$) (red) group.

In addition to its structural versatility for chemical modifications, HA possesses various unique properties which makes it an ideal candidate for the development of biomaterials [203]. These include its non-immunogenic nature, anti-inflammatory characteristics, and exceptional biocompatibility, all of which are critical for applications in tissue engineering or drug delivery systems [203]. For this reasons, HA and HA-based hydrogels are already employed in various biomedical applications: for the treatment of joint diseases [204], for the promotion of wound healing [205] or as scaffolds for bioactive agents, such as mitomycin C, to reduce postoperative complications [158].

In ophthalmology, HA products and hydrogels are also widespread [186, 206]. They are commonly used as main components of eyedrops to relieve dry eyes (Théa pharma), as protective agents during cataract surgery [207], or as ECM biomimetics for cell transplantation into the eye [208].

Considering these properties and various ophthalmological applications, HA-based hydrogels present themselves as excellent candidates for the development of a novel GDD. In addition, another polymer that was investigated in this thesis is PEG.

HA/PEG Hybrid Hydrogels

Hydrogels based on PEG are popular components in tissue engineering and biomedical applications due to their properties comparable to those of HA: excellent biocompatibility, non-immunogenicity and strong resistance to biofouling [209-211].

Several studies propose, that glaucoma therapy could significantly benefit from PEG-based hydrogels as ocular drug delivery systems in form of e.g. contact lenses or eye gels, to reduce elevated IOP [212]. Examples for such medical gelling systems are hybrid hydrogels of PEGDA/polyamidoamine (PAMAM) [213], 4arm-PEG/α-cyclodextrin (α-CD) [214] or the combination of PEG/PNIPAM, whereby the latter shows a thermoresponsive behavior for controlled drug release [215]. Another example for a PEG-based application is the ReSure® sealant (Ocular Therapeutix) [216], used as ocular adhesive in corneal wounds and incisions [217].

PEG-based hydrogel films also show promise for applications in the transplantation and regeneration of corneal endothelial cells (CEC), offering a supportive and biocompatible environment conductive to cellular growth and repair [218]. In addition to promoting cell adhesion, PEG hydrogels can also exhibit cell repellent properties [219]. Moreover, their behaviour can be

dynamically tuned to switch between cell adhesive and cell resistance by incorporating specific functional groups allowing for precise control over cellular interactions [220].
To design a novel GDD, a critical requirement is to prevent cell proliferation within the implant to avoid clogging caused by excessive cell growth - one of the main issues of current implants.
To address this, PEG was selected as a complementary material to HA. PEG is an extensively used polymer that can be functionalized with e.g. acrylate or vinyl sulfone groups [209]. These functional groups can act as Michael-acceptors in hydrogel formation through click-chemistry reaction (refer to section 2.1.2), enabling efficient and tunable crosslinking under mild conditions.
In summation, the combination of the two polymers HA and PEG creates a hybrid hydrogel with unique properties. Both polymers are highly biocompatible, non-toxic and non-immunogenic. They also exhibit anti-inflammatory characteristics, and a strong resistance to biofouling. Furthermore, the cell repellant properties of PEG address the issue of cell proliferation within the implants, a key challenge in current GDDs. Together HA and PEG result in a safe and long-lasting hydrogel combination for the development of a novel GDD.

2.1.4 Hydrogel Characteristics

As already outlined, hydrogels possess various characteristics that make them highly versatile materials for various applications. In the context of a new type of glaucoma implant two specific attributes of hydrogels are especially critical: the swelling behavior and the degradability of hydrogels. Therefore, in this thesis, these two aspects were examined more closely to optimize their performance and reliability for use in glaucoma implants.

Swelling Behavior

In polymer science, hydrogels are classified as a hydrophilic subgroup of polymeric gels, which tend to swell when immersed in a solvent that is thermodynamically compatible [221]. Swelling is defined as the uptake of the solvent into the polymer network, resulting in an expansion of the gel's overall volume [221, 222] (figure 16).

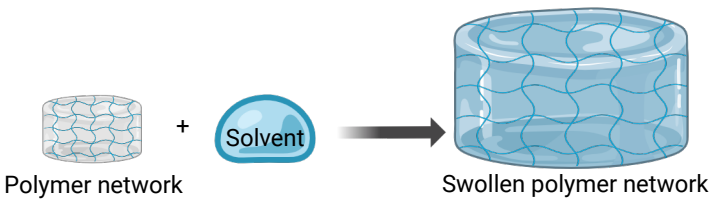

Figure 16: Schematic illustration of the volume expansion of a polymer network during swelling. The picture was adapted from Kreuz [178] and redrawn with BioRender.com.

The swelling kinetics of hydrogels can be complex and depend on their specific properties and structure [222]. The Flory-Rehner theory is often employed to describe and understand this behavior. According to this theory, the swelling occurs in a series of steps, driven by the balance of thermodynamic forces [223]. Initially, hydrophilic groups within the polymer network attract

water molecules resulting in the absorption of primary bound water [223]. As swelling progresses, hydrophobic groups become exposed and interact with water by hydrophobic interactions, leading to the incorporation of secondary bound water [223]. Subsequently, osmotic forces drive the infiltration of additional water molecules into the network, which are not bound and move freely, referred to as free water or bulk water, causing further swelling [223]. Swelling continues until a dynamic equilibrium is established, where osmotic forces are counterbalanced by the physical retractive force of the polymer chains [223]. At that point, the hydrogel maintains a steady size. However, if the hydrogel is degradable, prolonged swelling may eventually result in disintegration [180].

The swelling kinetics of hydrogels are influenced by a range of factors, including intrinsic characteristics such as molecular weight, type and degree of crosslinking, ionic charge density, polymer chain length and mesh size [224, 225]. Additionally, external environmental conditions, like pH, temperature and ionic strength play a significant role in determining the swelling behavior [186, 225]. Swelling not only affects the size and hydration of the hydrogel, but also directly impacts other critical properties such as elasticity, pore size and the diffusion rate of small molecules within the polymer network [200]. These interdependent properties are essential for optimizing hydrogel performance in various applications.

In the context of developing a new type of GDD, understanding and controlling the swelling behavior of hydrogels is particularly important. Swelling dynamics influence the valve functionality of the implant, which is crucial for ensuring consistent fluid regulation and preventing implant failure. Consequently, a precise characterization and modulation of swelling properties are key to tailoring hydrogels for this specialized application.

(Non-)Degradability of HA Hydrogels

Hydrogels can be either degradable or non-degradable, each with distinct properties that determine its suitability for specific applications [186].

Degradable HA-hydrogels are designed to break down over time, typically through hydrolysis or enzymatically via hyaluronidase enzymes [186]. As already outlined, in the human body HA is a key component of the ECM and its natural degradation plays a pivotal role in physiological processes like wound healing [226]. Human cells secrete six different hyaluronidases, enzymes responsible for ECM remodeling and HA degradation [226]. Thereby, HA is cleaved at the β-1,4-glycosilic bond [226], as depicted in figure 17.

This degradability is advantageous and crucial for certain HA hydrogel applications, such as drug delivery systems, whereby the gradual degradation enables the controlled releases of therapeutic agents over extended periods, ranging from days to months [227]. Similarly, in tissue engineering and wound healing, the breakdown of HA hydrogels supports angiogenesis and promotes cell migration [186]. In summation, degradable hydrogels offer flexibility for applications requiring temporary scaffolds or time-sensitive material functionality.

When using HA as a hydrogel material for the new type of glaucoma implant, this property presents a challenge. Degradation of the hydrogel within the implant would severely comprise its

functionality, particularly the valve mechanism essential for regulating IOP by facilitating controlled fluid drainage. The loss of structural integrity would render the implant ineffective, compromising its long-term therapeutic purpose.

To overcome this, it is important to design a HA-based hydrogel that resist enzymatic degradation, to ensure a reliable and sustained functionality. One option to achieve this include crosslinking with a stable, non-degradable polymer such as PEG, which can enhance durability and resist breakdown, while maintaining its biocompatibility [228, 229]. Given these advantages, as well as other considerations outlined in section 2.1.3, the combination of HA and PEG has emerged as an attractive option for creating a hybrid hydrogel for this application.

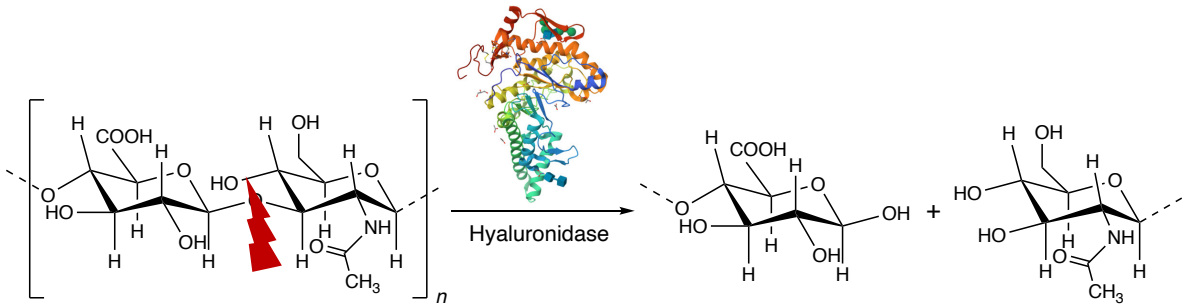

Figure 17: Schematic enzymatic degradation mechanism of HA by hyaluronidases. HA is cleaved at the β-1,4-glycosidic bond. The drawing was adapted from Hegger [179] and redrawn using BioRender.com. The structure of the enzyme represents hyaluronidase 1 (HYAL1) and was adapted from the protein data bank (PDB) RCBS.

2.2 The Implant Design

The proposed design for a novel GDD builds on a concept developed in a previous study [145]. The central innovation relies on a small titanium tube, modified on its interior with a HA hydrogel that can act as a valve to regulate IOP by facilitating controlled fluid drainage (figure 18a). This hydrogel-based implant addresses common issues of current implants such as hypotony (excessively low IOP) or clogging of the implant due to cell growth. In this context, the hydrogel should also possess cell repellant properties.

The valve mechanism is based on an artificial channel within the hydrogel (figure 18b), inserted prior to swelling. As the hydrogel absorbs fluid and swells, the channel closes and will only reopen when the IOP exceeds a certain threshold, ensuring that excess fluid is drained in a controlled manner due to the presence of the compressive channel, while maintaining the desired pressure levels.

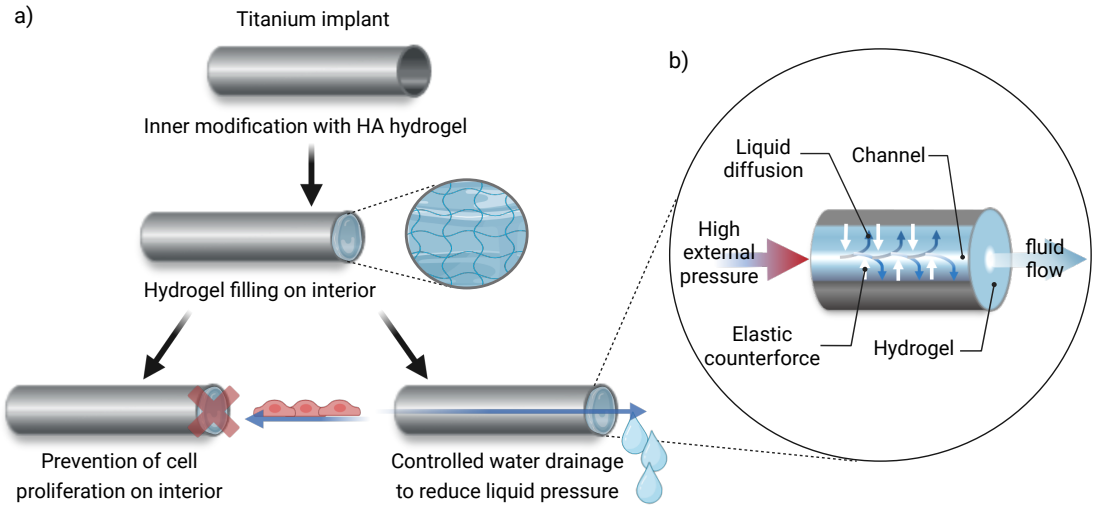

Figure 18: Concept for the novel glaucoma drainage device (GDD) investigated in this thesis. The basic design relies on a small titanium tube (ID=0.5-1 mm, l=6 mm) modified on its interior with a hyaluronan (HA) hydrogel, possessing cell repellant properties to prevent clogging due to cell growth and containing a valve functionality to for controlled water drainage to reduce elevated IOP (a). The valve mechanism is based on an artificial channel within the gel; at low external pressure the channel is closed, preventing hypotony – when external liquid pressure exceeds a certain threshold, the channel of the hydrogel is compressed and opens enabling fluid drainage (b). The picture was created using BioRender.com

2.2.1 Crosslinking and Immobilization of HA Hydrogels

As previously outlined in section 2.1.3, the formation of a HA hydrogel requires the introduction of functional groups to the HA structure through chemical modification, which enables crosslinking [202]. Therefore, the carboxylic (-COOH) groups of HA were functionalized with thiol groups, in accordance with the protocol of Vercruysee [230].

The common mechanism of HA functionalization involves the initial activation of the COOH-groups, mediated by *N*-(3-dimethylaminopropyl)-*N*'-ethylcarbodiimide hydrochloride (EDC) [230]. Subsequently, 3,3'-dithiobis(propionic hydrazide) (DTPH) is attached to the COOH-groups of HA, followed by the reduction of the disulfide bonds using dithiothreitol (DTT) [230]. For detailed thiolation mechanism refer to section 3.1.2.

The mechanism for HA-hydrogel formation based on the Thio-Michael addition reaction and is exemplary shown in figure 19 for crosslinking with *N*,*N*'-methylene(bisacrylamide) (MBAA).

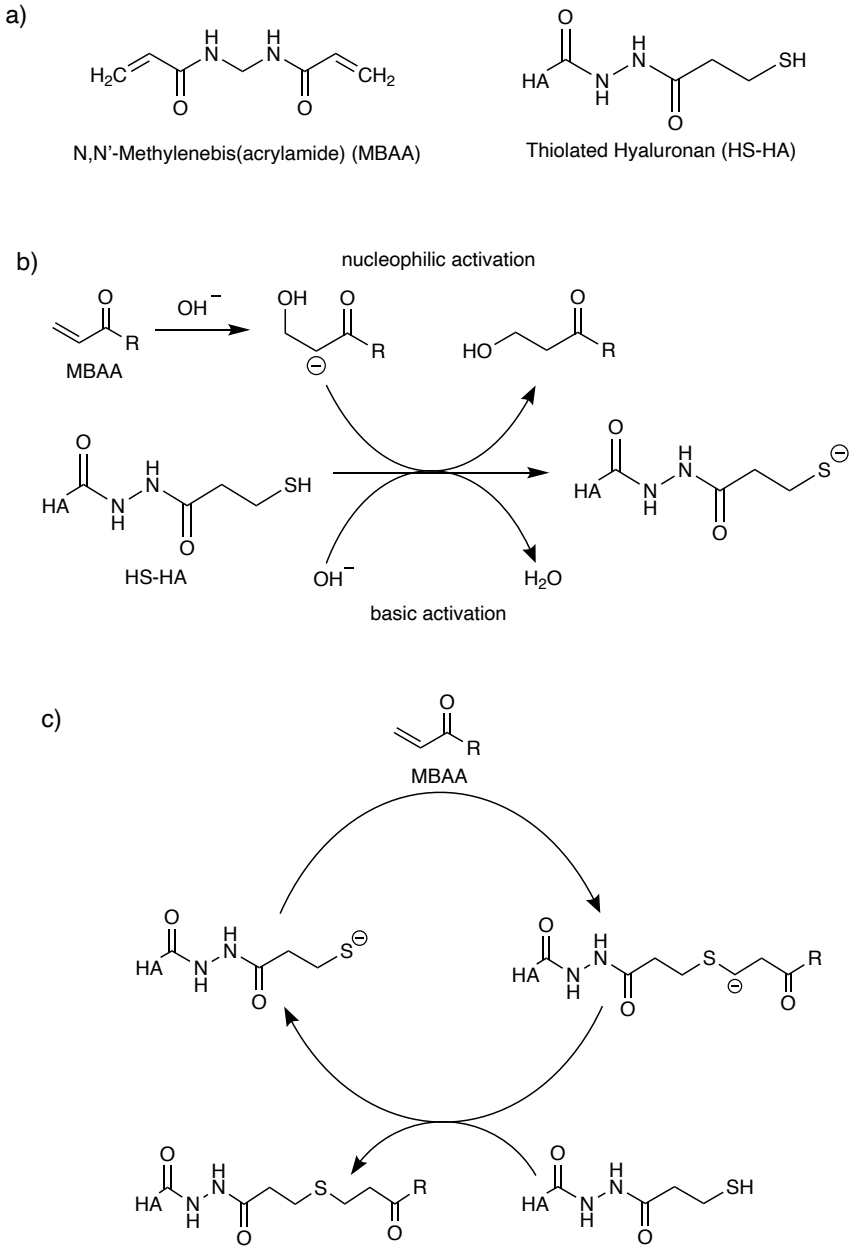

Figure 19: Schematic drawing of the Thio-Michael click-reaction used in this thesis for hydrogel formation. Crosslinking of thiolated HA (HS-HA) is exemplary shown for the bifunctional crosslinker *N*,*N*'-methylene(bisacrylamide) (MBAA) with acrylic groups (a). After nucleophilic activation of MBAA and basic activation of thiol-group of HS-HA (b), the nucleophile (Michael donor) was added to the unsaturated ß-carbon of the acrylic function (Michael acceptor). The mechanism was redrawn from the literature [145, 147, 192, 231].

Upon nucleophilic activation of MBAA and the base-catalyzed activation of the thiol group of thiolated HA (HS-HA) (figure 19b), the nucleophile (Michael donor) reacts with the unsaturated β-carbon in the acrylamide group (Michael acceptor), facilitating the formation of a stable crosslinked network [145].

Immobilization Strategy

One crucial requirement for the novel GDD is the sustained regulation of IOP over a long time period. To achieve this, it is essential to ensure that the hydrogel within the implant is permanently immobilized to the inner implant surface of the device, maintaining its position consistently without degradation or displacement.

The concept of permanently immobilizing HA hydrogels onto surface-bound epoxides was successfully established in a previous study and was adopted in this thesis [145]. The main concept involves the silanization of titanium model implants using (3-glycidyloxypropyl)trimethoxysilane (GPS). By this, surface-bound hydroxyl groups on the titanium react with alkoxysilane moieties of GPS, resulting in the grafting of epoxides onto the implant surface, which act as reactive sites for hydrogel attachment. The immobilization of the hydrogel is performed in a dual-action process with simultaneous crosslinking of the hydrogel, as depicted in figure 20.

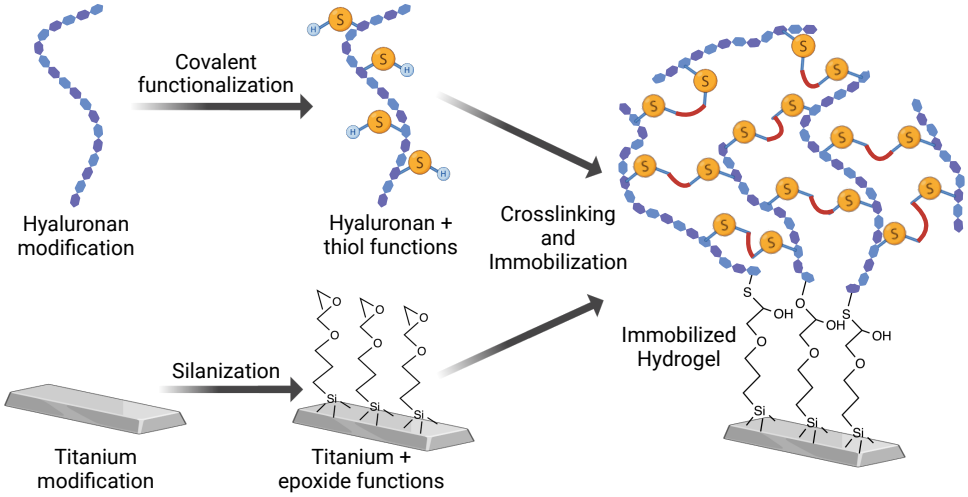

Figure 20: Schematic representation of the hyaluronan (HA) hydrogel-modified implant concept. In a two-step process, HA is first modified with thiol groups, while the titanium surface is functionalized with epoxides. Subsequently, crosslinking and immobilization occurs simultaneously in a single step. Hydrogel formation is achieved through Thio-Michael addition, and at the same time the hydrogel is immobilized onto the titanium surface via nucleophile ring-opening reaction of the epoxides.

In the final GDD, titanium is the material of choice, due to its frequent use as an implant material in medical fields [232]. However, in this thesis glass model implants are employed as model surfaces due to their transparency. For example, for the evaluation of hydrogel immobilization fluorescently labeled HA was used and therefore the tube interior had to be visible. Nevertheless, both materials, glass and titanium, exhibit comparable surface chemistry [233, 234]. Consequently, the epoxide grafting method utilizing silanes is analogous for both surfaces [233, 234] and can be applied with equal efficiency, as already confirmed by Thaller [145].

2.2.2 Customizable HA Hydrogel-Based GDD

Each glaucoma therapy is tailored to the individual patient, depending on different parameters, as the type of glaucoma or initial IOP value. Current implants are chosen based on specific pressure ranges, determined by their size and ID, which limits their applicability.

Since our implant concept relies on a hydrogel valve for pressure regulation, its pressure resistance can be tuned by varying HA hydrogel compositions, as demonstrated in previous studies [147]. This approach offers completely new opportunities for the customization of pressure resistances to individualize the pressure range for each patient.

For this, various HA hydrogel compositions were prepared and investigated, using HA of different molecular weigth (β(HA)=5, 10, 15 and 20 mg/ml), different TGs (28-63 %) and different bi- and multifunctional crosslinkers (MBAA, ACLT-PEG-ACLT, 4arm-PEG-ACLT, 4arm-PEG-VS).

Overall, the main concept behind the application of our implant is to insert it into the limbus area of the eye, after hydrogel swelling. Once in place, it is designed to replace the damaged outflow structures and divert excess fluid from the AC to the subconjunctival space forming a "bleb" directly under the conjunctiva, to reduce elevated IOP and slow down disease progression (figure 21).

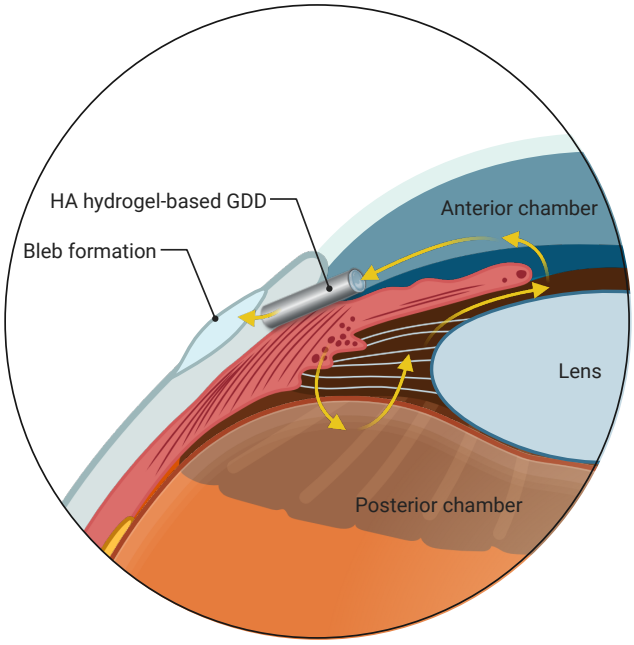

Figure 21: Concept for insertion area and fluid drainage mechanism of HA hydrogel-based GDD investigated in this thesis. The implant is inserted into the limbus area of the eye, where the main outflow structures are located, to divert excess fluid from the anterior chamber (AC) to the subconjunctival space forming a bleb directly under the conjunctiva. The drawing was created with BioRender.com.

3 Materials and Methods – Part I

3.1 Hyaluronic Acid (HA) Modification

HA hydrogels were used as main components of our new type of glaucoma implant. For crosslinking and immobilization of the hydrogel on the tube interior the HA was functionalized with thiol groups, using freshly synthesized DTPH as thiolation reagent. Furthermore, HS-HA was fluorescently labeled using fluorescineamine (FA).

3.1.1 Materials

Chemicals, reagents, solutions and equipment	**Source**
3,3'- Dithiodipropionic acid (DTPA)	Sigma-Aldrich, 109010
Concentrated ethanol (EtOH), ROTIPURAN® (≥ 99.8 %)	Carl Roth, 9065.1
Concentrated sulfuric acid (H_2SO_4)	Sigma-Aldrich, 258105
Ethyl-acetate (EtOAc)	Carl Roth, 7338.1
Magnesium sulfate ($MgSO_4$)	Sigma-Aldrich, 208094
Hydrazine monohydrate (N_2H_4), 64-65 % Hazards: GHS02, GHS05, GHS06, GHS08, GHS09	Sigma-Aldrich, 207942
Hexane ($CH_3(CH_2)_4CH_3$), mixture of isomers (95 %)	Sigma-Aldrich, 296090
Hyaluronic acid (HA), M_n= 40 kDa, 100 kDa	Lifecore-Biomedical
3,3'-Dithiobis (propanoic hydrazide) (DTPH)	Self-made, see section 1.1.2
N-(3-dimethylaminopropyl)-*N*'-ethylcarbodiimide-hydrochloride (EDC)	Sigma-Aldrich, E1769
Dithiothreitol (DTT)	Sigma-Aldrich, D0632
Hydrochloric acid (HCl)	Sigma-Aldrich, 320331
Sodium hydroxide (NaOH)	Sigma-Aldrich, S8045
Sodium chloride (NaCl)	Sigma-Aldrich,
Tris/HCl (TRIS), 1 M, pH 8.0	Sigma-Aldrich, T6791
5,5'-Dithiobis (2-nitrobenzoic acid) (DTNB)	Sigma-Aldrich, D8130
Sodium acetate (NaAc)	Sigma-Aldrich, W303406
pH universal indicator paper 1-14 roll	Merck, 1102320001
Dialysis membrane, MWCO 6-8 kDa	Carl Roth, E669.1
Polypropylene tubes (falcons), 15 ml	Sigma-Aldrich, 188271
Deuteriumoxid (D_2O)	Roth
NMR-tubes (178 x 4.97 mm)	Duran®
NMR spectrometer	JEOL (JNM-ECZ400s)
N-(2-hydroxyethyl)piperazine-*N*'-ethane sulfonic acid (HEPES)	Sigma Aldrich, #SLBP5730V
Fluoresceinamine (FA), 5-Aminofluorescein	Sigma Aldrich, #MKBH7059V
N-Hydroxysuccinimide (NHS)	Arcos Organics, A0355660

3.1.2 Functionalization of Hyaluronic Acid (HA) with Thiol-Groups

The following methods for functionalization of HA were already part of my Masterthesis *Pressure measurements and cell studies on hyaluronan hydrogel-modified implants for glaucoma treatment (2018)* [147]. For that reason, the following wording and formulations are similar to the previous work.

Synthesis of 3,3'-Dithiobis (Propanoic Hydrazide) (DTPH)

The synthesis of the thiolation reagent DTPH was carried out as adapted and modified by Thaller [145] according to a publication of Vercruysee et al. [230]. The chemical reaction for the synthesis of DTPH is shown in figure 22.

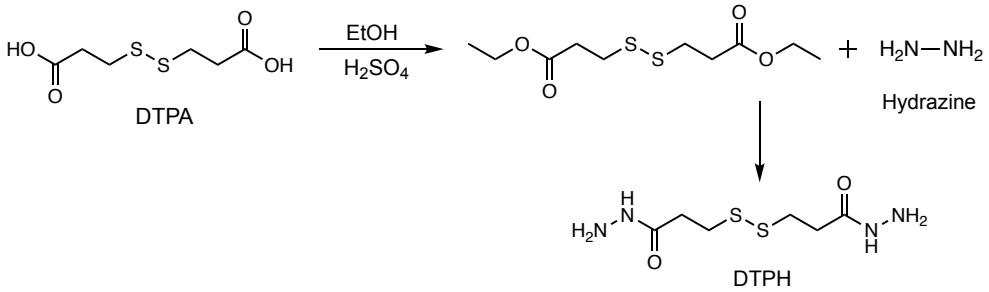

Figure 22: Chemical reaction for the synthesis of DTPH. After esterification DTPA with EtOH, the diester reacts with the hydrazine to form DTPH.

After complete dissolution of 10 g (48 mmol) 3,3'-dithiobis (propanoic acid) (DTPA) in 100 ml of EtOH, 3 drops of concentrated H_2SO_4 were added and the mixture was heated and stirred under reflux and oxygen exclusion for 1 h. Afterwards the mixture was concentrated under reduced pressure (40 °C, 110-150 mbar) to a volume of about 20 ml and transferred to a separatory funnel. 120 ml ethyl-acetate (EtOAc) were added, the aqueous phase was discarded and the organic phase was washed twice with 60 ml ddH_2O and dried over magnesium sulfate ($MgSO_4$). The solution was again concentrated under reduced pressure (40 °C, 150-200 mbar) until the intermediate product, an oily yellowish/brownish propanoic ester, was remaining. The ester was directly dissolved in 30 ml of EtOH and added dropwise into a stirred solution of 30 ml (480 mmol) hydrazine monohydrate (N_2H_4) in 10 ml EtOH. The reaction mixture was warmed (50-60 °C) and stirred under reflux for 1 h until the propanoic ester was fully consumed. The reaction product DTPH was sampled out by cooling down to room temperature (2 h), yielding a white crystalline solid. The filtered crystals were washed twice with 5 ml hexane and dried under vacuum for two days at room temperature.

Thiolation of Hyaluronic Acid (HA) with 3,3'-Dithiobis(Propanoic Hydrazide) (DTPH)

In corporation with the company Pharmpur (Königsbrunn, Germany), the thiolation of HA was introduced to Dr. Johannes Feierfeil, following a protocol from Shu et al. [159] and modified by Thaller [145]. HS-HA of different TGs were prepared by Dr. Johannes Feierfeil and provided to us. The main mechanism is shown in figure 23.

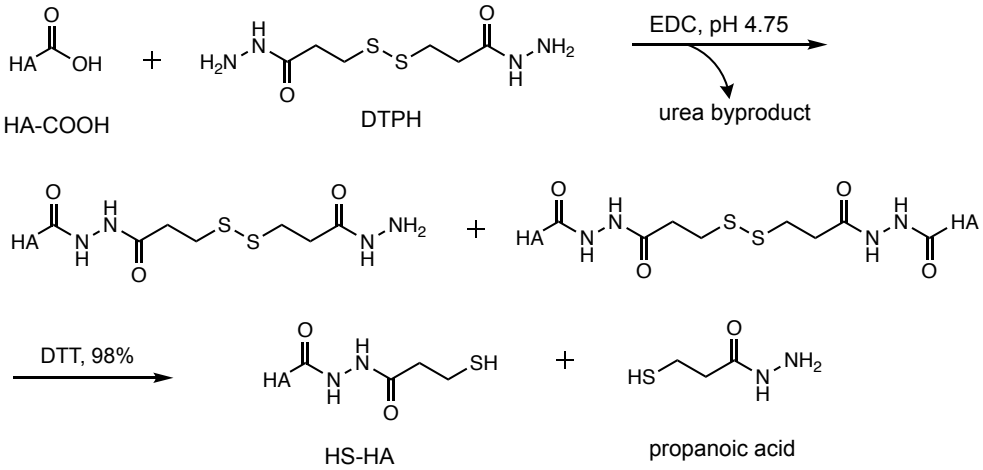

Figure 23: Thiolation of HA at COOH groups. Chemical reaction for HA thiolation: Two step reaction of HA thiolation using EDCl-mediated peptide coupling reaction of DTPH to COOH-groups of HA followed by a reduction of the disulfide bonds using DTT.

250 mg HA (M_n = 40 kDa and 100 kDa; n = 0.6 mmol) were dissolved in 250 ml ddH_2O and the pH was adjusted to 4.75 with 1 M HCl. While stirring, 142.8 mg of synthesized DTPH (0.6 mmol) were added, as well as 115.2 mg EDCl (0.6 mmol) to activate the carboxylic group of HA and initiate the reaction. The pH was constantly controlled and maintained at 4.75 during the thiolation reaction. In order to obtain specific TGs, the reaction was stopped at different time intervals (10 min – 2 h) by adding 1 M NaOH and adjusting the pH to 7.0. 924 mg DTT (6 mmol) were added to the reaction solution to break the disulfide bonds of the intermediate and dissolve the gel again that had occurred during the reaction. The pH of the solution was raised to 8.5 by adding NaOH (1 M) and the mixture was stirred for 24 h at room temperature.

Afterwards, the pH of the reaction mixture was lowered to pH 3.5 by adding HCl to prevent the regression of disulfide bonds. The HS-HA solutions were transferred to dialysis tubing (MWCO 6-8 kDa) and dialyzed against dilute HCl (pH 3.5) containing 0.1 M NaCl (30 g in 5 L ddH_2O). The solution was stirred overnight, followed by dialysis against dilute HCl (pH 3.5) without NaCl the next day. The dialysis solution was changed 6 times in total, until no more free thiols were detectable in the dialysis water. This was checked by adding 100 µl 1 M TRIS/HCl (pH 8.0) and 50 µl 5,5'-dithiobis(2-nitrobenzoic acid)-solution (50 mM NaAc and 2 mM DTNB in ddH_2O) to 850 µl of dialysis solution. If the solution was getting yellow, there were still free thiols in the solution. The purified HS-HA was aliquoted in 15 ml falcon tubes and lyophilized for 2 days, yielding HS-HA with a colorless solid foam-like appearance. The HS-HA products (figure 24) were stored under argon atmosphere at -20 °C in parafilm-sealed falcon tubes.

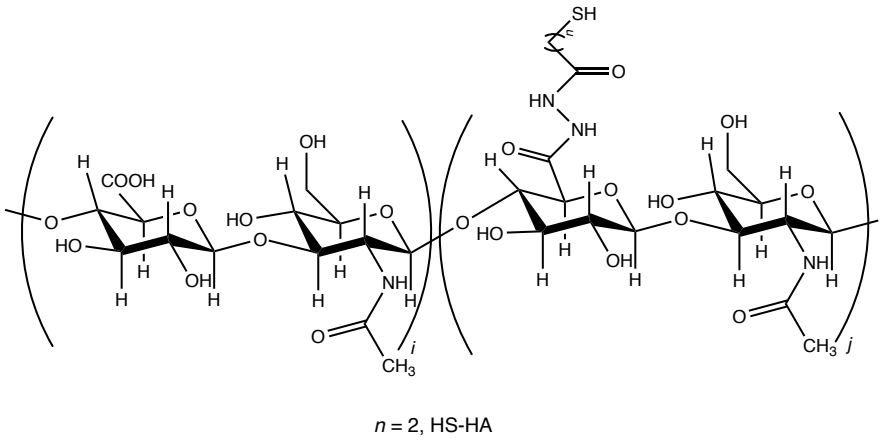

Figure 24: Chemical structure of thiolated hyaluronan (HS-HA).

3.1.3 Modification of HS-HA with Fluoresceinamine (FA)

HS-HA was fluorescently labeled using FA (figure 25) to visualize and analyze the immobilization of HS-HA to glass surfaces of small model implants. The protocol for the modification of HS-HA with FA was performed according to a protocol by Thaller [145].

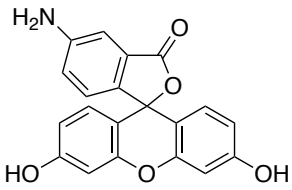

Figure 25: Chemical structure of 5-aminofluorescein/fluoresceinamine (FA).

A 10 mg/ml solution of HS-HA in ddH_2O was prepared and stirred for 2 h until complete dissolution. 595 mg HEPES (2.5 mmol) were added and the pH was adjusted to 7.0. In a separate vial, 160 mg FA (0.45 mmol) were dissolved in 10-12.5 ml ddH_2O and by the dropwise addition of NaOH (6 mol/L), ultra-sonication (240 W, 35 kHz) and manual shaking. Following complete dissolution the FA solution was added to the to the HA solution and stirred for 30 min. The reaction was initiated by the addition of 164 mg EDC (1.05 mmol) and 250 mg NHS (2.175 mmol) under further stirring for 5 h. To the resulting viscous and cloudy orange solution concentrated NaOH (6 mol/l) was added dropwise, until the solution became clear (pH 10-11). Dialysis was performed against NaOH (pH 10), with frequent changes of the dialysis medium until it remained colorless for an extended period of time (approx. one week and 25 changes of dialysis medium). Afterwards, the mixture was O_2 purged with Argon for 30 min, then 1.25 g DTT were added before adjusting the pH to 8.5, followed by stirring for another 24 h at room temperature. The pH was lowered to 3.5 and the solution was dialysed again against diluted HCl (pH 3.5) until a sample of the dialysis buffer remained colorless after the addition of a basic DTNB solution (50 mM NaAc and 2 mM DTNB in ddH_2O). The purified product was aliquoted in 2 ml Eppendorf tubes and lyophilized, resulting in the thiolated fluorescently labeled hyaluronan (HS-HA-FA) with a solid yellow/orange foam-like appearance.

3.2 Analysis of DTPH and HS-HA Products

General success of DTPH synthesis and HA thiolation was determined via ^{1}H-NMR spectroscopy. To determine the thiolation TG of functionalized HA a modified Ellman's assay was performed. Additionally, the TG was determined by ^{1}H-NMR spectroscopy and compared to the results obtained by Ellman's assay.

3.2.1 Materials

Chemicals, reagents, solutions and equipment	**Source**
Deuteriumoxid (D_2O)	Roth
NMR-tubes (178 x 4.97 mm)	Duran®
Dithiobis(propanoic hydrazide) (DTPH)	Self-made, see section 3.1.2
Thiolated hyaluronic acid (HS-HA), see section 3.1.2	Synthesized and provided by Dr. Johannes Feierfeil from the company Pharmpur (Königsbrunn, Germany)
NMR spectrometer	JEOL JNM-ECZ400s
Cystamine dihydrochloride, M_n=225.20 g/mol	Sigma-Aldrich, C8707
Tris/HCl (TRIS), 1 M, pH 8.0	Sigma-Aldrich, T6791
5,5'-dithiobis(2-nitrobenzoic acid) (DTNB)	Sigma-Aldrich, D8130
Sodium acetate (NaAc)	Sigma-Aldrich, W302406
96-well plates, Greiner CELLSTAR®	Sigma-Aldrich, M0687
Multi-well plate reader	TECAN Infinite® 200 PRO

3.2.2 ^{1}H-NMR Analysis of DTPH and HS-HA

The ^{1}H-NMR analysis of DTPH was performed by Dr. Günter Majer from the department of cellular biophysics of the Max Planck Institut for Medical Research in Stuttgart.
The ^{1}H-NMR spectroscopy of thiolated HA and the analysis and determination of the TGs were performed by Dr. Johannes Feierfeil from the company Pharmpur (Königsbrunn, Germany).
For the measurement, 3-5 mg of DTPH and HS-HA product were dissolved in 500 µl D_2O and transferred in NMR-tubes. NMR-spectra were recorded at 300 MHz and room temperature. The results of the NMR measurements were obtained from and discussed with Dr. Günter Majer and Dr. Johannes Feierfeil. For all NMR-spectra, characteristically chemical shifts (δ) in ppm were evaluated and compared to literature results.

3.2.3 Ellman's Assay for Thiolation Grade (TG) Determination

To determine the TG of thiolated HA a modified Ellman's assay was performed. The protocol from the literature was adapted and used in previous studies by Dr. Michael Thaller [145] and Dr. Patricia Hegger [179].
The main mechanism of the Ellman's assay is based on the reaction of a thiol with DTNB converted to 2-nitro-5-thiobenzoate (TNB^{2-}) (figure 26). The resulting yellow color of TNB^{2-} is

quantitative and can be detected (absorption maximum at 412 nm) and used in spectrophotometric analysis of thiol concentrations.

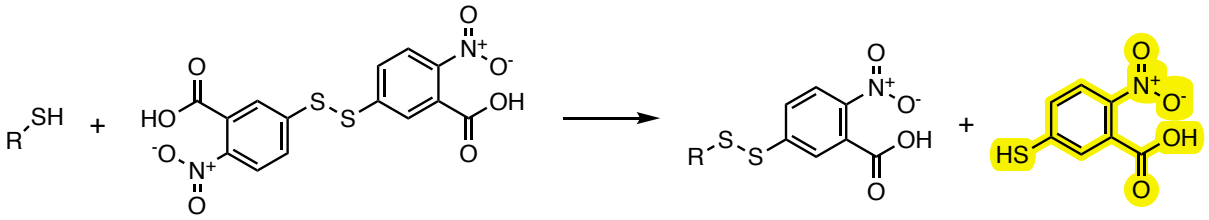

Figure 26: Chemical reaction of a thiol with DTNB. The conversion of DTNB yields 2-nitro-5-dithiobenzoat (TNB^{2-}), responsible for the yellow color of the sample and used for the analysis of thiol concentrations.

For the Ellman's assay, a serial dilution of cystamine dihydrochloride in 850 µl ddH_2O (ϵ_{SH}= 0.01 – 100 mM) was prepared from a stock solution of 2 mM cystamine hydrochloride. A 1 mg/ml stock solution of thiolated HA sample in ddH_2O was prepared and 20, 50 and 80 µl of this HA-dilutions were filled up with ddH_2O to a volume of 850 µl yielding three different concentrations of the HS-HA samples for the measurements (0.02 mg/ml, 0.05 mg/ml and 0.08 mg/ml). To all these samples of the standards and HA-dilutions, 100 µl Tris/HCl (1 M, pH 8.0) and 50 µl DTNB-solution (50 mM NaAc and 2 mM DTNB in ddH2O) were added and mixed together. 300 µl of each of the samples of the standard and the HA samples were pipetted in wells of a 96-well plate. The absorbance of each sample was directly measured at a wavelength of 420 nm with the plate reader TECAN Infinite® 200 PRO. Evaluation of the data was performed using 'Excel for Mac 2019' version 16.71. The calculations for TG determination were summarized in the appendix (see section 6.1.1). To determine the average TG with the standard deviation, the Ellman's assay was performed at least three times for each sample.

3.3 Preparation of Model Implants

The preparation of model implants was performed as described by Thaller [145] and included the formation and immobilization of different HA hydrogel compositions on the inner tube surface, as well as the introduction of an artificial channel inside the hydrogel.

3.3.1 Materials

Chemicals, reagents, solutions and equipment	**Source**
Glass tubes (borosilicate); Large model tubes: ID=5 mm, OD=7 mm, l=10 mm. Middle model tubes: ID=3 mm OD=4 mm and ID=2 mm, OD=3 mm; l=6 mm. Small model tubes: ID=1 mm, OD=2 mm and ID=0.5 mm, OD=1 mm, l=10, 8, 6, 5, 4, 3 mm.	Manufactured at the glass workshop of the MPI for Intelligent Systems, Stuttgart
Extran® MA01	Merck, L015023755520
(3-Glycidyloxypropyl)trimethoxysilane / (3-(2,3-epoxypropoxy)propyltrimethoxysilane (GPS)	Sigma Aldrich, #STBD1719V
(3-Mercaptopropyl)trimethoxysilane / 3-(Trimethoxysilyl)-1-propanethiol (MPS)	Sigma Aldrich, #MKCJ1613
Toluene, $C_6H_5CH_3$	Merck, K48040925629
Concentrated ethanol (EtOH) ROTIPURAN® (≥ 99.8 %)	Carl Roth, 9065.1
Ultrasonicator, 60/240 W; 35 kHz	Bandelin electronic, Berlin
Thiolated hyaluronan (HS-HA), see section 3.1.2	Synthesized and provided by Dr. Johannes Feierfeil from the company Pharmpur (Königsbrunn, Germany)
N,*N*'-Methylenebis(acrylamide) (MBAA), M_n=154 kDa	Carl Roth®, 101341042
Poly(ethylene glycol)bisacrylate (ACLT-PEG-ACLT), M_n=600 kDa	Creative PEGWorks, ZXM06126
4-arm-polyethylene glycol-vinylsulfon (4-arm-PEG-VS), M_n=10,000 kDa	Creative PEGWorks, MKCK6701
4-arm-polyethylene glycol-acrylate (4-arm-PEG-ACLT), M_n=10,000 kDa	Creative PEGWorks, MKCJ1986
Tris(hydroxymethyl)aminomethane (TRIS)	Sigma Aldrich, T6791
Phosphate buffered saline, (PBS), tablets	Gibco®, 1834896
Teflon sample holder	Manufactured at the precision mechanics workshop of the MPI for Intelligent Systems, Stuttgart
Glass fiber (∅=0.1 mm, l=6-7 mm)	Manufactured at the glass workshop of the MPI for Intelligent Systems, Stuttgart

3.3.2 Immobilization and Formation of HA Hydrogels

This section gives an overview of the immobilization strategy of different hydrogels, used crosslinker and hydrogel compositions that were investigated for their use as hydrogel valves in the new type of glaucoma implant.

Silanization with (3-Glycidyloxypropyl) trimethoxysilane (GPS) or (3-Mercaptopropyl)trimethoxysilane (MPS)

For immobilization of HS-HA the surfaces of large, middle and small glass tubes were either equipped with epoxy-groups by silanization with GPS, or with thiol-groups by silanization with MPS (figure 27).

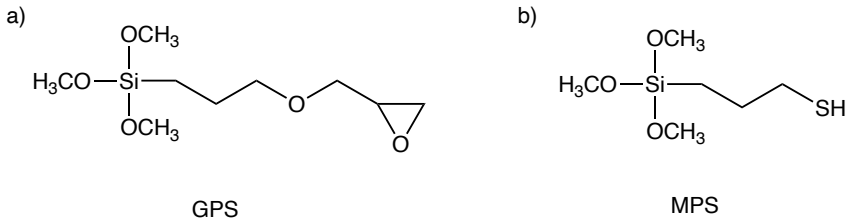

Figure 27: Silanes used for modification of surfaces of glass model tubes. (3-Glycidyloxypropyl)trimethoxysilane (GPS) (a) and (3-Mercaptopropyl)trimethoxysilane (MPS) (b).

Depending on the HA-hydrogel composition, e.g. choice of crosslinker or pH of buffer solution, either one or the other silane was better suited for immobilization. For slow polymerization times of the hydrogels and basic pH (8.5), GPS was used; for rapid gelation times and neutral pH (7.4) of the hydrogel mixture, MPS was used. The glass tubes were activated and cleaned in Extran® for >2 h, rinsed in nanopure H_2O and dried in a N_2 stream. The tubes were immersed in a 2 % (*v*/*v*) solution of GPS or MPS in toluene for 24 h and afterwards sonicated (240 W, 35 kHz)–15 min in toluene, followed by 15 min in EtOH. During the immersion of the small glass tubes in the different solutions (Extran®, silane/toluene) care was taken to ensure that no air bubbles were formed in the inner channel of the tubes.

HA Hydrogel Formation

Hydrogels of different compositions were prepared using HA of different molecular weight (M_n=40 kDa and 100 kDa) and TG (28 %-63 %) (table 2) and mass concentrations of HA (β(HA)=5, 10, 15 and 20 mg/ml) as well as different kinds of crosslinkers (table 3) for hydrogel formation.

The main mechanism for hydrogel formation is based on a Thio-Michael addition reaction. In this case, HS-HA acted as a Michael donor and the different crosslinker as Michael acceptors. For soft hydrogels bi-functional crosslinker were used as Michael acceptors (figure 28). Thereby, the hydrogels were formed by the reaction of bi-functional acrylamides of MBAA or bi-functional acrylates of ACLT-PEG-ACLT with thiol groups of HS-HA. More solid hydrogels were formed using multi-functional crosslinker with a pentaerythritol core structure and four functional groups

linked to this core: 4arm-PEG-VS and 4arm-PEG-ACLT (figure 29). All HS-HA's and crosslinker were stored at -20 °C under argon atmosphere.

Table 2: Thiolated Hyaluronan (HS-HA) used for hydrogel formation. This table summarized all synthesized HS-HA with sample number (according to Pharmpur's numbering system), molecular weigth (M_n), reaction time in [192], thiolation grades (TGs) and the abbreviations used for each HS-HA are listed.

Sample number HS-HA	M_n [g/mol]	Reaction time [min]	TG [%]	Abbreviation
P1625-JoF-015/-027	40	30/60	28	**HA28-1/HA28-2**
P1625-JoF-009		90	49	**HA49**
P1625-JoF-076		30	51	**HA51**
P1625-JoF-084		60	55	**HA55**
P1625-JoF-039		120	57	**HA57**
P1625-JoF-038/-044		90/90	63	**HA63-1/HA63-2**
P1625-JoF-029	100	60	40	**HA40**
P1625-JoF-030/-077		90/30	44	**HA44-1/HA44-2**
P1625-JoF-085		60	61	**HA61**

Table 3: Bi- and multifunctional crosslinker used for hydrogel formation. Name (chemical definition), average molecular weight (M_n), degree of substitution (*DS*) and the abbreviations used for each crosslinker are listed.

	Chemical definition	M_n [g/mol]	*DS* [%]	Abbreviation
Bi-functional crosslinker	*N*,*N*'-Methylenebis(acrylamide)	154.17	100	**MBAA**
	Poly(ethylene glycol)bis(acrylate)	600	100	**ACLT-PEG-ACLT**
Multi-functional crosslinker	4arm-Poly(ethylene glycol)vinylsulfon	10.000	94.5	**4arm-PEG-VS**
	4arm-Poly(ethylene glycol)acrylate	10.000	100	**4arm-PEG-ACLT**

HS-HA and crosslinker were dissolved separately in a solution of 0.4 M tris(hydroxymethyl)aminomethane (TRIS) in a phosphate buffered saline (PBS) solution. In order to control the gelation time of the hydrogels, the pH of the TRIS/PBS buffer solution was adjusted to 8.5 for gels crosslinked with the bi-functional crosslinker and to pH 7.3 for the multi-functional crosslinker. Before use, the buffer solution was purged for 30 min using Argon to avoid air bubbles in the hydrogel.

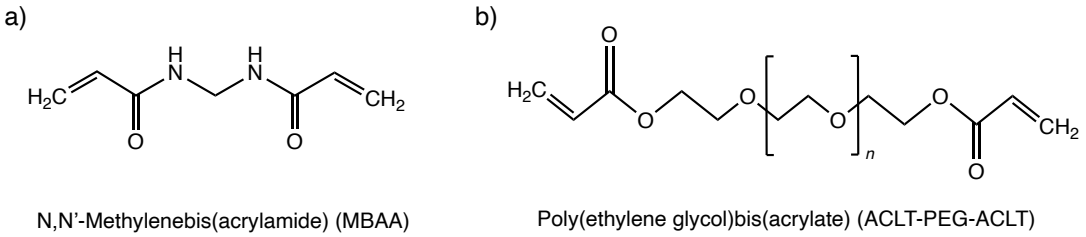

Figure 28: Bi-functional crosslinker used for hydrogel formation. *N,N'*-Methylenebis(acrylamide) (MBAA) (a) and poly(ethylene glycol) (PEG) equipped with two acrylate groups (ACLT) (b).

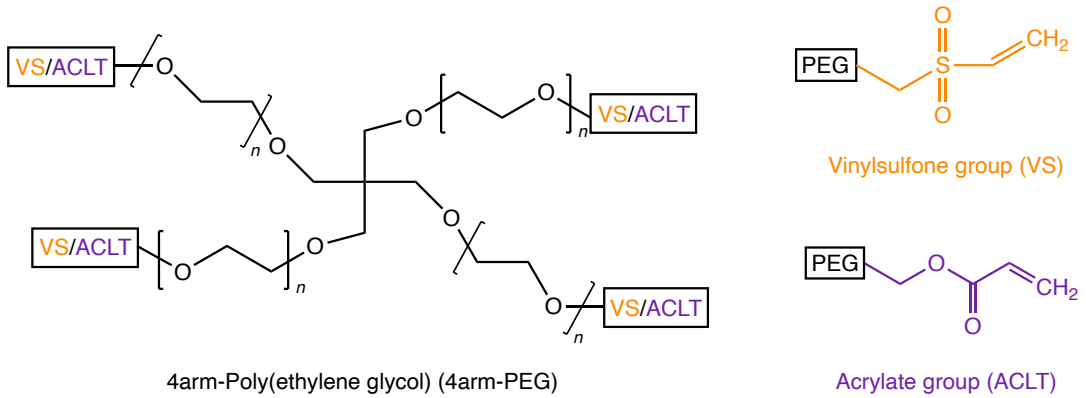

Figure 29: Multi-functional crosslinker used for hydrogel formation. A pentaerythritol core structure, equipped with four vinylsulfon groups (orange) or four acrylate groups (violet).

The desired final mass concentration of HS-HA after mixing was set to β=15 and 20 mg/ml for the hydrogels with the bi-functional crosslinker. For the multi-functional crosslinker the final mass concentrations of HS-HA were set at β=5 and 10 mg/ml, due to the higher stiffness and shorter gelation time of the hydrogels at higher concentrations.

With the TG and the target ratio of reactive groups of V(HA)/V(crosslinker)=1:1, the required volumes of HS-HA and crosslinker were calculated individual for each sample (see appendix, section 6.1.2). The mass concentrations for the crosslinker were listed in table 4.

Table 4: Final concentrations in mg/ml for multi-/ and bi-functional crosslinker used for hydrogel formation, depending on the concentration and the TG of HS-HA. 4arm-PEG-VS (orange), 4arm-PEG-ACLT (violet), MBAA (blue) and ACLT-PEG-ACLT (green).

TG [%]	β(HA) [mg/ml]							
	5		10		15		20	
28	8.61	8.14	17.22	16.27	0.75	2.93	1.0	3.91
40	11.59	11.30	23.91	22.59	1.05	4.07	1.39	5.42
44	13.03	12.31	26.06	24.62	1.14	4.43	1.52	5.91
51	14.86	14.04	29.72	28.09	1.30	5.06	1.73	6.74
55	15.88	15.01	31.76	30.02	1.39	5.40	1.85	7.20
57	16.39	15.48	32.77	30.97	1.43	5.57	1.91	7.43

61	17.38	16.42	34.76	32.85	1.52	5.91	2.03	7.88
63	17.87	16.89	35.74	33.78	1.56	6.08	2.08	8.11

The polymerization times of the different hydrogel compositions were determined in previous studies by Tim Kreuz [178].

After mixing, the gelation of HS-HA/crosslinker solutions started within 5-10 minutes for the bi-functional crosslinker and full gel formation occurred after an incubation in a wet reaction chamber overnight at 37 °C.

For the multi-functional crosslinker gelation started much faster, within 2-3 minutes and full polymerization of the gel occurred within 1-2 hours at room temperature. The final hydrogels were immersed in PBS (0.4 M, pH 7.4) for storage, if not immediately used afterwards.

3.3.3 Model Implant Production

Glass-model implants were manufactured using silanized glass model tubes and different hydrogel compositions as outlined in section 3.3.2.

Preparation of HA Hydrogel-Modified Glass Model Tubes

For the immobilization of HA hydrogels on the inner surface of middle (ID=3, 2 and 1 mm, l=6 mm) or small glass model tubes (ID=0.5 mm, l=10, 8, 6, 5, 4 and 3 mm) (figure 30a), the silanized tubes were connected to each other using short pieces of plastic tubing (1 cm) (figure 30b).

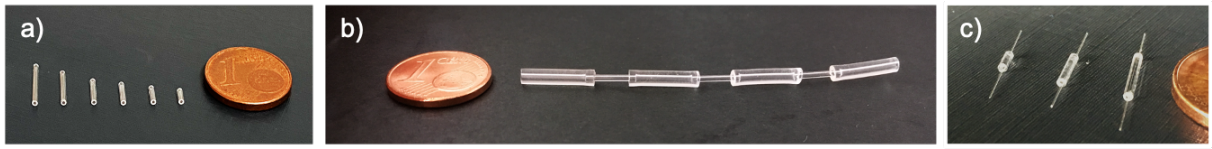

Figure 30: Experimental set-up for immobilization of HA hydrogels on the inner surface small glass tubes silanized with GPS or MPS. Small glass tubes, ID=0.5 mm, length: 10, 8, 6, 5, 4, and 3 mm (a). Set-up for small glass tubes connected with short plastic tubing (b). HA hydrogel- modified glass tubes with glass fiber (c).

The HA/crosslinker-mixture was injected into the glass tubes using a syringe. The setup was placed in a wet chamber (sealed with parafilm) and simultaneous immobilization and crosslinking of the hydrogel occurred after max. 24 h at 37 °C (for bifunctional crosslinker) or room temperature (for multifunctional crosslinker). Afterwards, the plastic tubing was removed and for the pressure measurements an artificial channel was manually introduced into the hydrogels by using a glass fiber with Ø=0.5 mm (figure 30c). The tubes were allowed to swell in PBS (1 M, pH 7.4) for at least 72 h before conducting pressure measurements, otherwise they were stored in PBS (1 M, pH 7.4) until use.

3.4 Characterization of HA Hydrogel-Modified Implants

After preparation, the HA hydrogel-modified glass model tubes were investigated in regard to their swelling behaviour of the immobilized/constrained hydrogels within the glass tubes, as described in previous studies by Thaller [145] and furthermore the degradability of the hydrogels by hyaluronidases was examined following a protocol by Hegger [145].

3.4.1 Materials

Chemicals, reagents, solutions and equipment	**Source**
Small/middle HA hydrogel-modified glass model tubes, ID=1, 2 and 3 mm, l=6 mm (self-made)	See section 3.3
Phosphate buffered saline (PBS), tablets	Gibco®, 1834896
Hyaluronidase IV (from bovine testes)	Sigma Aldrich, SLBL6343V
24-well plates®	Greiner CELLSTAR®, E23093A3

3.4.2 Physical Characterization: Swelling Behaviour of HA Hydrogels

In order to examine the swelling behaviour of constrained HA hydrogels, the masses of glass model tubes were measured before hydrogel modification (m_{tube}), after HA hydrogel polymerization and immobilization ($m_{hydrogel+tube}$), and after swelling in PBS (1M, pH 7.4) for 3 days.

The masses of the hydrogels within the glass tubes ($m_{hydrogel}$) were calculated by:

$$m_{\mathbf{hydrogel}} = m_{\mathbf{hydrogel+tube}} - m_{\mathbf{tube}} \qquad \text{Eq. 1.1}$$

To analyze the swelling ratios of immobilized HA hydrogels, the relative mass gain (m_{rel}) at different time intervals was calculated according to equation 1.2 using 'Excel for Mac 2019' (version 16.78, *Microsoft*).

$$m_{\mathbf{rel}} = \frac{m_{\mathbf{s}}}{m_0} \qquad \text{Eq. 1.2}$$

Thereby, 'm_s' being the absolute mass of the hydrogel in the swollen state, and m_0 being the starting mass of the HA-modified tube, measured directly after hydrogel polymerization. For each hydrogel composition the swelling ratio was calculated from at least three individually prepared HA-hydrogel modified tubes with the standard deviation as error bar. Theoretical dry masses (m_d) were calculated from the combined mass concentrations of HS-HA and crosslinker and the total volumes.

3.4.3 Biological Characterization: Enzymatic Degradation of Constrained HA Hydrogels

To gain information about the durability of HA hydrogels within the glass model tubes, the enzymatic degradation by hyaluronidases was investigated. The model implants were prepared as described previously (see section 3.3.3), and after full polymerization and hydrogel swelling for 3 days the enzyme hyaluronidase IV was added to each sample. The enzyme was used at a concentration of 0.1 U/ml with a volume of 2 ml for each HA hydrogel-modified tube and incubated at room temperature and soft shaking at 100 rpm. The enzyme solution was exchanged every 48 hours. As control solution PBS was used. At different time points the weights of the hydrogel-modified tubes were measured to calculate the rate of degradation: after 1 h, 2 h, 4 h, 6 h, 8 h, 12 h, 24 h, 30 h, 48 h, 72 h, 5 d, 7 d, 14 d and 21 d. The data obtained from the different time points was then fitted to an exponential decay phase using GraphPad Prism 10 for MacOS (version 10.0.2, *GraphPad Software Inc.*) and used to determine the half-life ($t_{1/2}$) of each hydrogel, relating to the time point in which the initial weigth of the hydrogel was halved.

3.5 Pressure Measurements

In order to evaluate the pressure regulation abilities of middle and small HA hydrogel-modified tubes, a pressure measurement setup with different types of measurements was established using the Elveflow® microfluidic device OB1 MK3.

3.5.1 Materials

Chemicals, reagents, solutions and equipment	**Source**
Middle and small HA hydrogel-modified glass model tubes, ID=3, 2, 1 and 0.5 mm, l=10, 8, 6, 5, 4, and 3 mm	Self-made, see section 3.3.3
Phosphate buffered saline (PBS), tablets	Gibco®, 1834896
Elveflow® microfluidic device OB1 MK3 with pressure range from 0 – 2 bar and four pressure/flow sensors ranging from 0-80 µl/min	Elveflow® Plug and Play Microfluidics

3.5.2 Measurement Setup for Middle and Small Model Implants

The whole measurement setup with the Elveflow® microfluidic device OB1 MK3 is summarized in figure 31.

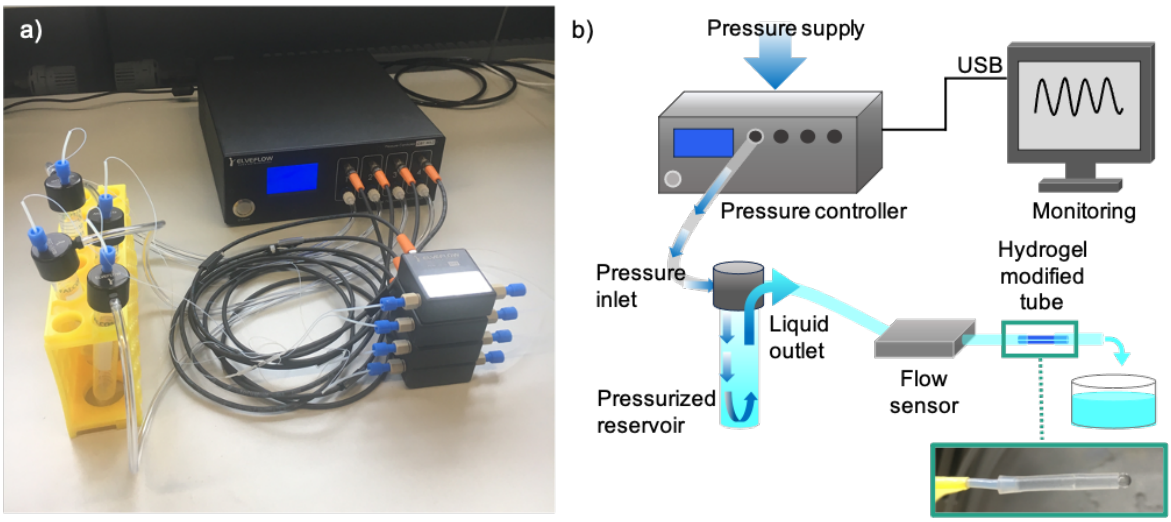

Figure 31: Microfluidic setup for pressure measurements of middle and small HA hydrogel-modified tubes. Experimental setup in the laboratory (a) and schematic drawing of the setup (b).

The device included four switched in parallel pressure/flow sensors for simultaneous measurements. As pressure supply a nitrogen line was connected to the pressure controller, which regulated the pressurized nitrogen gas. The HA-modified glass model tubes were connected behind the flow sensors, using short pieces of plastic tubing. The desired pressure was then applied to a sealed PBS (1 M, pH 7.4) reservoir and pushed the liquid through the flow sensors and finally into

the HA-modified tubes. The applied pressures and flowrates were measured and recorded by the associated Elveflow SDK software. Evaluation of the data was performed using 'Excel for Mac 2019' (version 16.78, *Microsoft*) and GraphPad Prism 10 for MacOS (version 10.0.2, *GraphPad Software Inc.*). For the representation of real conditions different measurement modes were established and conducted, as described in the following.

Pressure Ramp for the Determination of Activation Pressures

After preparation of the HA-modified glass model tubes, each tube had to be 'activated'. That means, the first opening of the artificial channel occurs at a higher pressure value than all following channel openings. This first pressure value was termed as 'activation pressure'. For this, the pressure applied to the HA-modified tubes was gradually increased in a time interval of 300 s, with pressure ramps ranging from 0-100 mbar, 0-200 mbar, 0-300 mbar, 0-500 mbar, 0-1000 mbar and 0-1500 mbar. Depending on the gel composition, different number of pressure ramps were necessary to determine the activation pressure. After the first opening of the channel, which was indicated by liquid flow through the gel and starting/increasing flowrate, the measurement was stopped.

Pressure Regulation Abilities of HA-Modified Tubes at Common Flowrates

After activation, the HA modified glass model tubes were tested for their ability to regulate the pressure at a common flowrate prevalent in the normal human eye (2-3 µl/min). For this, a constant flowrate of 2,5 µl/min was set and the pressure was recorded. The measurement was conducted until a constant pressure was reached and maintained over a certain period of time, which varied between 30 minutes and several hours. To assess the long-term viability of hydrogels some measurements were conducted over 17-24 hours.

Fluid Flow during Pressure Fluctuations

Since it was known that the pressure and flowrate in the normal human eye were no constant but dynamic values, a measurement setup with pressure fluctuations was established. For this, a pressure range like in the normal human eye between 1000 Pa and 3000 Pa was set and applied to the HA modified tubes. The pressure was fluctuated in a pressure sine mode and in different time intervals while the flowrate was recorded. In the first experiments, the time intervals were 100 s, 200 s, 300 s and 500 s. In further experiments the pressure was fluctuated in real-life sine measurements, with IOP changes following a 24-hour sinusoidal curve, peaking during sleep and declining during the day.

3.6 Design and Fabrication of 3D-Printed Patterns

In order to improve the preparation of model implants the CAD (computer added design) software *Inventor* (Autodesk, Mill Valley, USA) was used and different 3D models were designed and exported as stereolithography files (STL). The patterns were printed by Ruben Werbke from the Additive Manufacturing group of the Max Planck Institute for Intelligent Systems (MPI-IS) (Stuttgart, Germany) and by Clara Vazquez-Martel from the Institute for Molecular Systems Engineering and Advanced Materials (IMSEAM) (University of Heidelberg, Germany).
Additive manufacturing was carried out by using a LED light source of 385 nm. The pixel resolution of the 3D printer was 27 µm and the prints were performed at 30 °C with a layer thickness of 100 µm.
As printing material, the clear resin, the carbon resin, and a BPA-based material was tested. Due to size limitations of the 3D printer and for a better handling of the model tubes, the sizes were enlarged to ID=1-3 mm for the tubes and to Ø=0.5 mm for the diameter of the printed fibers.
The designs for 3D-printed patterns focused on different approaches for the preparation of glass model tubes. The different 3D designs were summarized in the following.

3.6.1 Materials

Chemicals, reagents, solutions and equipment	**Source**
Clear resin	Formlabs, FLGPCL04
Carbon resin	Formlabs, PR25
Bisphenol A (BPA)-based ink 'moiin Tech Clear'	Litholabs GmbH
3D-printer at MPI-IS	
3D-printer at IMSEAM	Asgia Max X27 UV DLP

3.6.2 3D-Printed Patterns for Glass Model Implants

The main concept for the first pattern for the preparation of glass model tubes is shown in figure 32. The design relied on a plate equipped with fibers and in-depths (figure 32a), that can serve as tube holder for exact positioning of the glass model tubes (figure 32b), which then were able to be filled with the hydrogel and removed after polymerization occurred. The printing material for this design was clear resin.
A second design, using the material carbon resin, included three plates, shown in figure 33. The first plate serving as bottom closure (figure 33a) for the second plate (figure 33b), equipped with hollow cylindric structures. The third plate (figure 33c) possessing column structures containing each a hole in the middle, with the diameter of the fiber.
The proposed workflow for this second design is exemplary shown in figure 34 for the preparation of one glass model tube: First putting together plate A and plate B (1.), then placing the hydrogel-modified glass tube into the hollow cylinder structure of plate B (2.), then the setup was closed with plate C (3.), containing the small channel for the insertion of the glass fiber (4) and after

channel formation inside the hydrogel, the HA-modified tube can be removed and used for pressure measurements (5.).

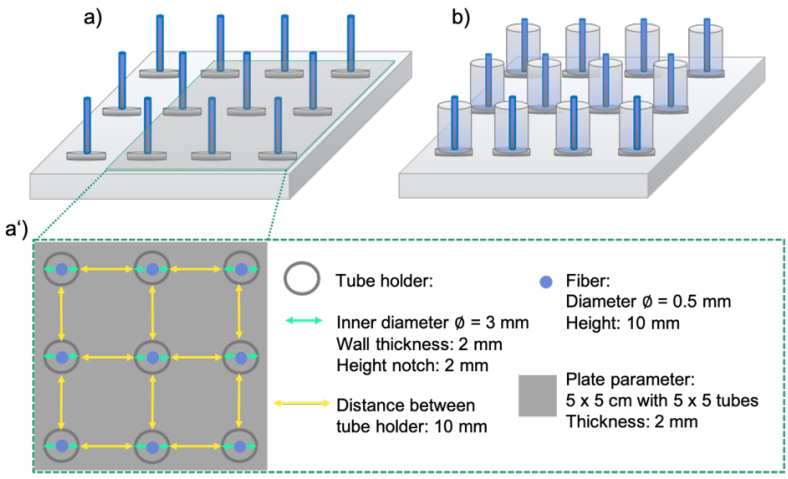

Figure 32: 3D-Design of a pattern for improved glass tube implant production. The concept based on one plate with fibers (a) of ∅=0.5 mm and in-depths for exact positioning of the glass model tubes (b). The parameters of the plate were summarized in (a').

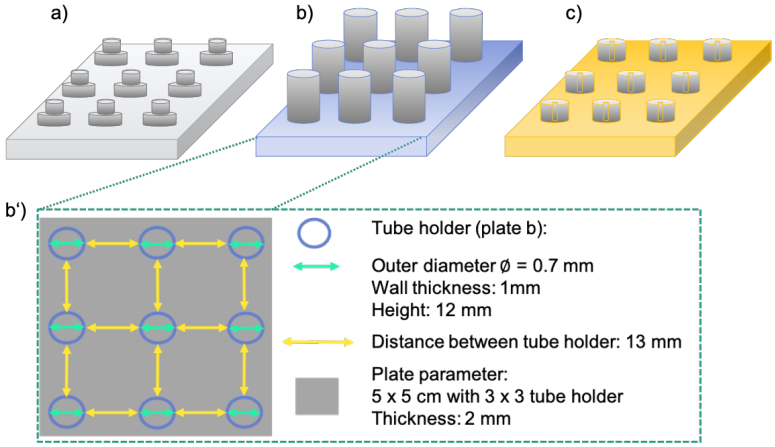

Figure 33: 3D-Design for improved implant production of glass model tubes. This concept based on three plates: one plate serving as bottom closure element (a), a plate with hollow tubes, serving as glass tube holder (b) with parameters summarized in (b'), and a third plate with cylindric structures containing a hole in the middle (c).

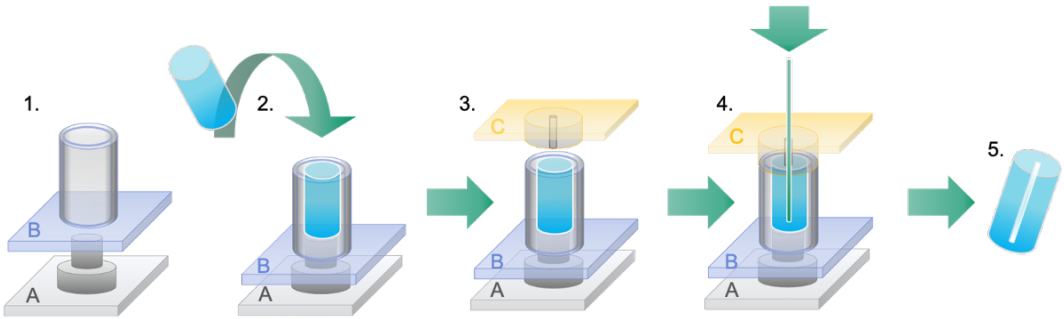

Figure 34: Proposed workflow for the 3D-pattern shown in figure 33. First plate b) is plugged together onto a) (1.), then a hydrogel filled glass tube is inserted into plate b (2.). The setup is closed using plate c (3.) and trough the small hole in c, a glass fiber can be inserted to introduce a channel into the hydrogel (4.). Afterwards the hydrogel filled tube with exact positioned channel is removed (5.).

4 Results and Discussion – Part I

4.1 ^{1}H-NMR Analysis of Synthesized Compounds

The required compounds for the preparation of HA-modified implants were successfully synthesized (figure 35) and analyzed by ^{1}H-NMR.

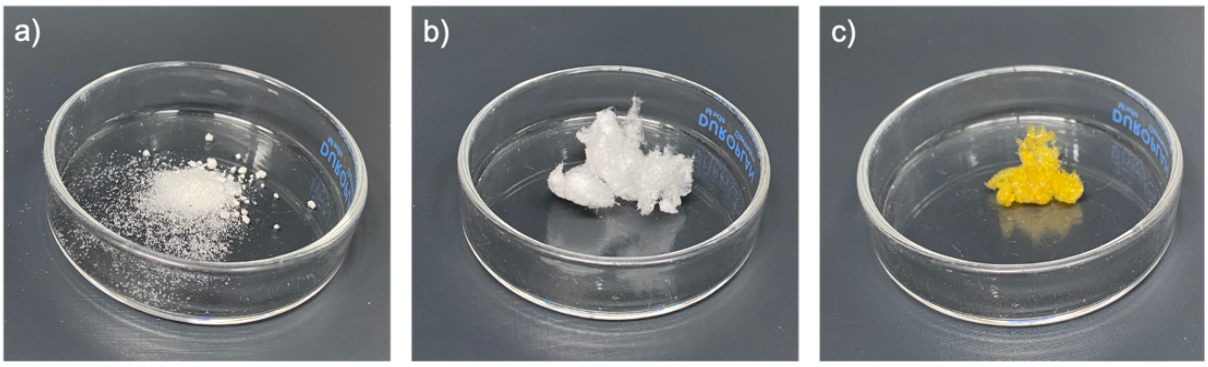

Figure 35: Synthesized compounds in this thesis. DTPH as a crystalline white solid (a), HS-HA with a foam-like appearance (b) and fluorescently labeled HS-HA-FA with a yellow foam-like appearance (c).

4.1.1 ^{1}H-NMR Analysis of 3,3'-Dithiobis(Propanoic Hydrazide) (DTPH)

As outlined in section 3.1.2, first the thiolation reagent DTPH with a crystalline white solid (figure 34a) was synthesized from DTPA according to a protocol developed by Vercruysse [230]. The successful synthesis of DTPH was confirmed using ^{1}H-NMR spectroscopy (400 MHz, D_2O), which verified the chemical structure of the synthesized compound (see appendix, section 6.2.1). The ^{1}H-NMR spectrum displayed two characteristic triplet signals at δ=2.86 ppm and δ=2.55 ppm, corresponding to the -CH_2-CH_2- groups in DTPH. The large peak at δ=4.67 ppm was attributed to the D_2O solvent, while smaller peaks were likely due to impurities or ^{13}C-satellites.
These results aligned with previously reported 1H-NMR spectra for DTPH by Vercruysee [230] (triplets at δ=2.90 ppm and δ=2.58 ppm) and Thaller [145] (triplets at δ=2.96 ppm and δ=2.64 ppm) further confirming the successful synthesis of DTPH.

4.1.2 ^{1}H-NMR Analysis of Thiolated Hyaluronan (HS-HA)

In cooperation with the company Pharmpur (Königsbrunn, Germany), the modification of HA with thiol groups was performed by Dr. Johannes Feierfeil according to Shu et al. [231], with some minor alterations adapted from Thaller [145] (refer to section 3.1.2). By varying different reaction parameters as the size of HA (40 and 100 kDa) or reaction times (30-120 min), HA products with variable amounts of thiol groups were prepared (figure 35b).

General success of HA thiolation was determined via ^{1}H-NMR (400 MHz, D_2O). The spectra was analyzed and compared to literature results [145, 231].
Characteristic resonances proofed the successful synthesis of HS-HA (for NMR-spectra see appendix, section 6.2.2). The spectrum displayed multiple signals between δ=3.9-3.3 ppm, along with a peak at δ=4.462 ppm, corresponding to the pyranose -CH-groups of disaccharide units. A single peak at δ=1.88 ppm was identified as the N-acetyl methyl protons of HA. Resonances specific to the HA-DTPH compound were observed at δ=2.75 ppm and δ=2.60 ppm, indicating the methylene groups (-CH_2-CH_2-) of the thio(propanoic hydrazide) (TPH) chains.

In addition to the general analysis, the NMR method, was considered to determine the degree of substitution with thiol groups (thiolation grade, TG) of the synthesized HS-HA products.
In previous studies the TG was determined by a modified Ellman's assay as described in section 3.2.3, showing in some measurements large deviations and error rates over 10 % [145, 147, 179]. This was also observed for the thiolated samples in this thesis as displayed in table 7 in the appendix (refer to section 6.2.3).
For HA hydrogel formation the exact TGs were necessary and important to calculate the amount crosslinker. If the TG was underestimated and a smaller amount of crosslinker was used, no complete hydrogel polymerization occurred. Conversely, excess crosslinker could leave reactive groups available post-gelation, which could potentially interact with surrounding tissues and cause reactions. This was already observed in previous studies with human corneal endothelial cells (HCEC) in which an excess of the bifunctional crosslinker MBAA led to reduced cell viability [147].
Since in this thesis HA hydrogels were used as the main component of our new type of glaucoma implant, a more accurate and reliable analytical method than the Ellman's assay for the determination of the TG became necessary. For that reason, the NMR spectroscopy was selected for TG determination as summarized in the following.

4.1.3 Thiolation Grade (TG) Determination via ^{1}H-NMR

The determination of the thiolation grade (TG) of HS-HA samples was performed by Dr. Johannes Feierfeil from the company Pharmpur GmbH in Königsbrunn. Therefore, the following explanations were compiled by Johannes Feierfeil and made available for this thesis.
Generally, for NMR spectroscopy the intensity of a signal is known to be directly proportional to the number of H-nuclei causing this signal [235]. If the sample consists of a uniform compound, the quantity ratios of differently bound nuclei can be indicated directly from the intensity ratios by integrating the signal areas in the NMR spectra [235].
For TG determination of HS-HA the following assumptions were made: for a theoretical complete thiolation of HA, the integral of the methyl group (figure 36a, red) was equal to three protons (CH_3) and the two methylene groups (figure 36a, green) were equal to four protons (-CH_2-CH_2-). Dividing the value of the integral at 2.75 ppm (4 protons) and multiplying by 100 resulted in a thiolation grade of 100 %.

However, since the thiolation reaction was stopped at different time intervals, the value of the integral at 2,75 ppm was less than four protons, as exemplary shown in figure 36b for a HS-HA sample with 40 kDa and a reaction time of 30 minutes. The spectra of the sample showed an integral value of 1,33 which resulted in a TG of 33 %.

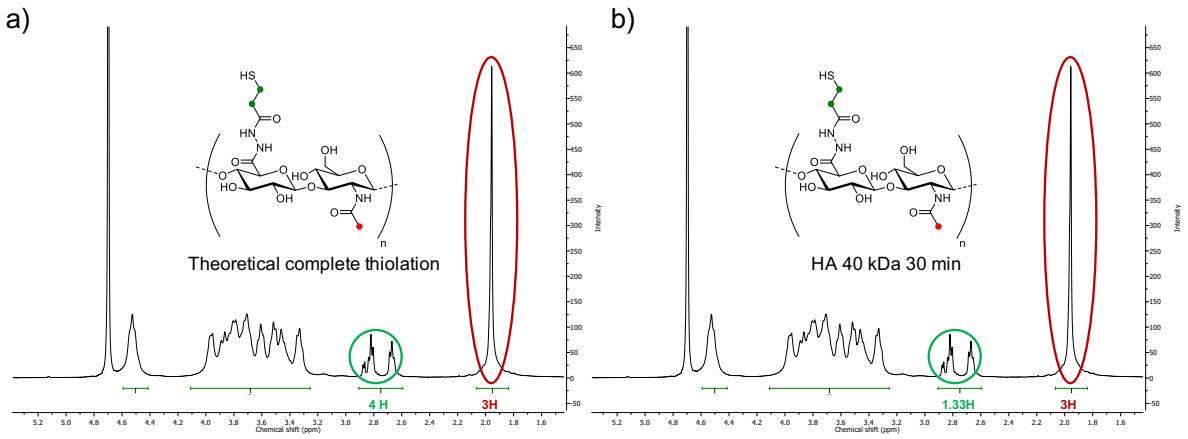

Figure 36: Exemplary ^{1}H-NMR spectra of thiolated hyaluronan for the determination of thiolation grades. Theoretical complete thiolation (a) and partial thiolation of HA sample with 40 kDa and 30 min reaction time (b).

The sources of error in this type of TG determination were mainly related to the accuracy of integration, which was estimated around 1-5 % [236]. Other factors influencing the accuracy of the method were for example variations in temperature during the measurement, the homogeneity of the magnetic field or the concentration of the sample, which altogether accounted approximately 0.5-2 % [236]. However, for NMR the error rates were considered to be smaller (around 5 %) compared to the photometric TG determination by Ellman's, which provided for example a TG value of 83±12 % for sample P1625-JoF-038 (see appendix, section 6.2.3). For that reason, the NMR spectroscopy was the method of choice.

4.2 HA Hydrogels and Preparation of HA-Modified Model Implants

In this section, the preparation and challenges of different HA-hydrogel compositions and small model implants are summarized and discussed.

4.2.1 Polymerization of HA Hydrogels

Various HA hydrogel compositions were prepared, using HA of different molecular weigth (40 kDa and 100 kDa), TG (28-63 %) and mass concentration (β(HA)=5, 10 and 15 mg/ml), as well as different bi- and multifunctional crosslinker: MBAA, ACLT-PEG-ACLT, 4arm-PEG-VS and 4arm-PEG-ACLT.

In continuation of the protocol established by Thaller [145], using MBAA as crosslinker, all samples were initially prepared in a TRIS/PBS buffer solution at pH 8.5 with curing at 37 °C.

With regard to the preparation of glass model implants, it turned out that the gelation of the HA/PEG compositions, especially for the multifunctional and high-molecular PEG-crosslinker (M_n=10.000 kDa), occurred so fast (within seconds to few minutes) that, after mixing of HS-HA and crosslinker, most gels already polymerized in the syringe, before they could be injected into the glass model tubes. Since this rendered the preparation of model implants for pressure measurements, further optimizations were necessary, in order to control the gelation kinetics and extend the gelation time.

In previous studies by Tim Kreuz different attempts were made to slow down the hydrogel formation, as varying the temperature or pH of the buffer solution [178]. It was shown that lowering the temperature did not significantly result in longer gelation times of HA/PEG compositions [178], which was attributed to the strong temperature dependence of the pK_a of TRIS, induced by its high ionization enthalpy [237]. At a temperature of 25 °C the pK_a of the conjugate weak acid of TRIS (TRISH) was approximately 8.08 and increased around 0.03 units per degree Celsius [238]. According to Kreuz, a reduction in temperature from 25 °C to 5 °C resulted in an increase of the pH from 8.5 to 9.09, which counteracted a temperature-induce slowdown of the gelation process [178]. From the results gained by Kreuz, the pH of the buffer solution was adjusted to 7.4 for HA/PEG hydrogels and polymerization occurred at room temperature instead of 37 °C, as for hydrogels with MBAA. With this, the gelation time of HA/PEG compositions extended significantly and enhanced the handling time with the polymerization solutions.

Exemplary macroscopic hydrogels with TG=55 % and β(HA)=15 mg/ml were displayed in figure 36, showing that the PEG-linked hydrogels (figure 37b, c and d) were firmer and more stable in shape in contrast to MBAA crosslinked hydrogels (figure 37a).

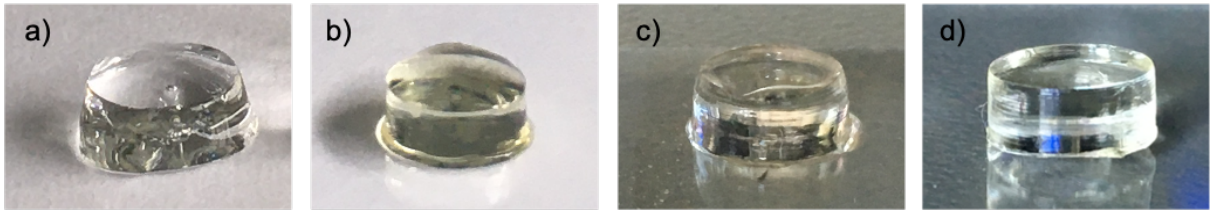

Figure 37: HA hydrogels used in this study crosslinked with different linkers: MBAA (a), ACLT-PEG-ACLT (b), 4arm-PEG-ACLT (c) and 4arm-PEG-VS (d). HA55 (40 kDa, TG=55 %) with β(HA)=15 mg/ml was crosslinked in a buffer solution of 0.4 M TRIS/PBS, pH 8.5 (a) and pH 7.4 (b/c/d).

4.2.2 Immobilization of HA Hydrogels to Glass Surfaces

HA hydrogels were used as main components of our new type of glaucoma implant, therefore it had to be ensured, that the hydrogel was permanently immobilized on the tube interior for a reliable and long-lasting performance as pressure sensitive valve.

The grafting of epoxides to glass surfaces for the immobilization of HA hydrogels was already used in previous studies by Thaller [145] and was adapted in this thesis.
The surface-bound epoxides, which were linked to the glass surfaces via silanization with GPS, enabling Michael addition with the hydroxyl and thiol groups of HS-HA in a nucleophilic ring-opening mechanisms [239]. This immobilization strategy worked well for HA hydrogels crosslinked with MBAA under basic conditions (0.4 M TRIS/PBS, pH 8.5). In this thesis further hydrogel compositions were investigated: HA crosslinked with bi- and multifunctional PEG linker, ACLT-PEG-ACLT, 4arm-PEG-ACLT and 4arm-PEG-VS.

One advantage of epoxides is the versatile reactivity and the reaction of epoxide ring-opening, which could proceed under neutral, basic or acidic conditions, but in acidic and basic solution the epoxide ring opening proceeds much faster, than at neutral pH [240, 241].
Therefore, the initial immobilization strategy from Thaller with the silane GPS [145] was maintained to immobilize the new hydrogel compositions.
However, after adjusting the pH, in order to extend the gelation time (see section 4.2.1), the prepared glass model implants showed failed immobilization (figure 38a) and the gels were pulled out with the glass fiber (figure 38b), that was used to generate the artificial channel.

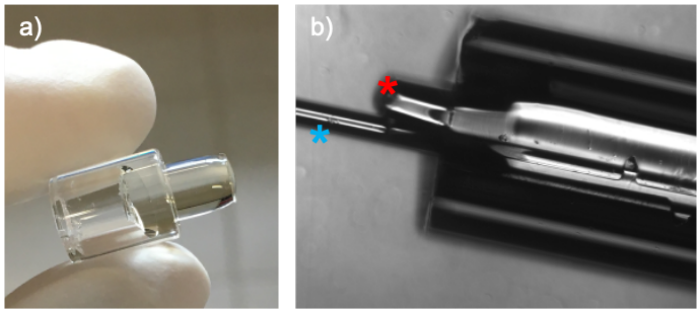

Figure 38: Failed silanization of HA hydrogel on the inner tube surface of a large (a) and small (b) glass model tube. Tubes were silanized with GPS. Hydrogel mixture shown in the pictures: HA55 (40 kDa, TG=55 %) with β(HA)=15 mg/ml and crosslinked with 4armPEG-VS in a buffer solution of 0.4 M TRIS/PBS, pH 7.4. Hydrogel pushed out of large glass tube (a). Hydrogel in small glass tube (red) pulled out with the glass fiber (blue) used for channel generation (b).

In general, the epoxide ring opening reaction was known to follow the same reaction mechanism (S_N2 mechanism) in both, neutral and basic solution, but it is clearly slow downed at neutral pH [241]. Hence, the pH shift from 8.5 to 7.4 could be one reason for failed immobilization of HA/PEG hydrogel compositions.
Another assumption was the overall rapid polymerization time of HA/PEG gels in contrast to HA/MBAA gels, where full polymerization and immobilization occurred within 24 h. Presumably, the epoxide reaction, thus bond breaking and subsequent bond making between the epoxide and functional groups of HA, required more time at neutral pH than it was given by the rapid polymerization of the HA hydrogels crosslinked with multifunctional PEGs.
However, further increase of gelation time would include additional lowering of pH and total polymer concentration. The latter in particular would impact mechanical properties, as the elastic modulus and the swelling behaviour of the hydrogels and strongly effect the valve mechanism of the hydrogel-modified implants [178].
The molecule size of PEG crosslinker could also give an explanation for failed immobilization, since S_N2 mechanisms were known to be highly susceptible to steric hindrance, and the nucleophilic attack on the epoxide group was impeded or prevented due to large atomic groups [241].
In a logical progression from the assumptions made above a new immobilization strategy of HA/PEG hydrogels was required.

New Immobilization Strategy for HA/PEG Hydrogel compositions

For the use of the hydrogel-modified glass model tubes in pressure measurements, a permanent immobilization was a prerequisite, otherwise the hydrogel was forcefully ejected out of the tube. For that reason, another silane containing thiol-groups - MPS - was tested to immobilize the new hydrogel compositions with PEG crosslinker.
The grafting of thiol groups to the surfaces of glass model tubes was also considered by Thaller, but since thiols were not stable under basic conditions and over long time periods, this approach was discarded [145]. As for our new HA/PEG hydrogels the parameters pH and polymerization time were significantly decreased, thiol groups became appropriate candidates for the immobilization of the new hydrogel compositions.

To confirm the success of immobilization of HA under different conditions and with the different silanes GPS and MPS, fluorescently labeled HS-HA (HS-HA-FA) was used. In buffer solution a partial re-oxidation of thiol groups to disulfides resulted in a gel formation, which afterwards was removed carefully by rinsing in water through the glass tube. By this, only the silanized parts of the glass tubes were covered with HS-HA-FA bound to the surface, which were visualized by fluorescence microscopy.
The results (figure 38) displayed a clear difference between non-silanized (control) and silanized samples as well as a difference of fluorescence signals between the silanes GPS and MPS under different conditions (pH 7.4 and pH 8.5). The immobilization worked well with GPS, pH 8.5 and

MPS, pH 7.4, less good with GPS, pH 7.4, and – as expected - no immobilization occurred with MPS, under basic conditions (pH 8.5), similar to the non-silanized control samples.
This indicated, that an immobilization with GPS at pH 7.4 was also possible, although the fluorescence signal was less intensive than at pH 8.5. These outcomes supported the assumption that the molecule size as well as the fast polymerization time of multifunctional PEGs additionally preventing an immobilization of the hydrogels when using GPS.

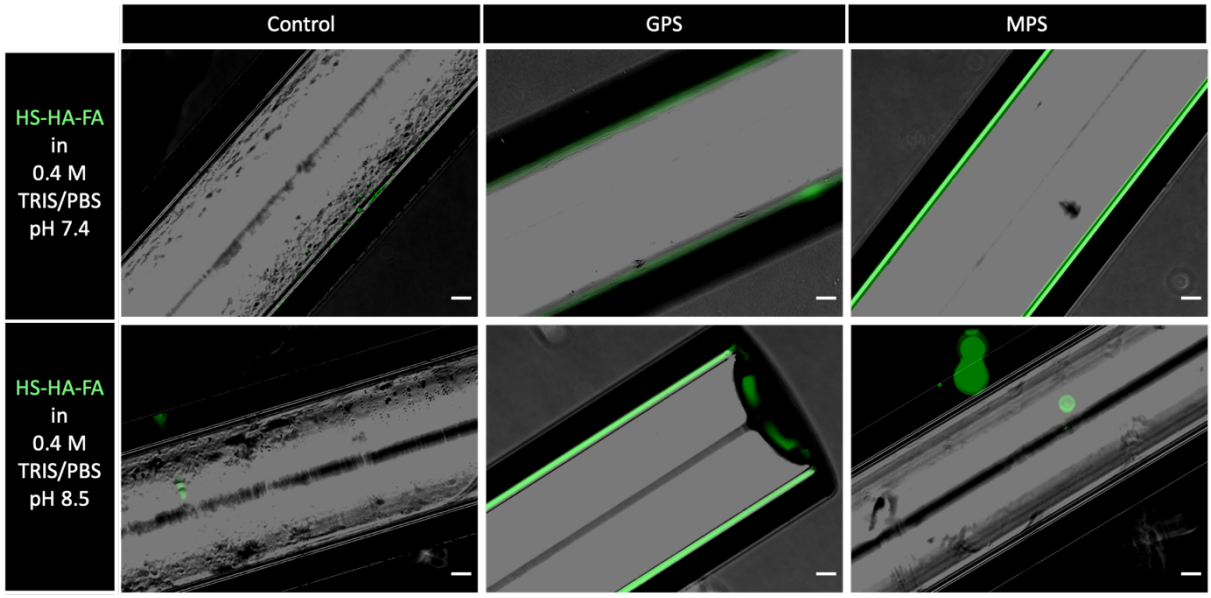

Figure 39: Comparison of silanization of small glass tubes (ID=0.5 mm) with GPS and MPS. HS-HA-FA dissolved in 0.4 M TRIS/PBS pH 7.4 and 8.5 and injected in small glass tubes silanized with GPS or MPS or without silanization (control). Visualization with fluorescence microscopy (λ_{ex}=470 nm, λ_{em}=525 nm). Scale bar respresents a length of 100 µm.

With these findings, the silanization of the small glass model tubes was adapted for the different hydrogel compositions and performed either with GPS or MPS, depending on the gel compositions used. For slow polymerization time of hydrogel compositions such as with the bifunctional linker MBAA the silane GPS was used. Hydrogels crosslinked with the PEG linker ACLT-PEG-ACLT, 4arm-PEG-VS and 4arm-PEG-ACLT, showed a fast polymerization, hence MPS was used for immobilization. It was confirmed, that the findings from the fluorescence coating were transferable to the entire gel compositions, enabling immobilization.

4.2.3 Preparation of Miniaturized Glass Model Tubes

One main goal of the first experimental part in this thesis was the miniaturization of the whole large implant model setup (ID=5 mm, l=10 mm), established by Thaller [145], to a scale of a real future GDD. Thereby, different implant sizes were considered, which were in the size range of MIGS-devices, ranging between 1 mm and 8.5 mm in length, and an inner diameter from 63 µm to 300 µm [68-72, 242] (see section 1.1.5, glaucoma drainage devices). In order to keep all possibilities open, different miniaturized implant dimension were explored, as summarized below. In this thesis, the innovative feature of the new type of glaucoma implant was the inner tube modification using HA hydrogels, acting as a duct to prevent hypotony at lower pressures and as a

valve to drain excess fluid at elevated pressures. Since the valve mechanism of the hydrogel was given by the artificial channel that was introduced using a glass fiber with ∅=0.1 mm, the dimensions of the miniaturized glass model tubes were set at 0.5 mm and 1 mm for the inner diameter (ID) and furthermore different tube lenghts (l=3, 4, 5, 6, 8 and 10 mm) were tested in order to find the best tube dimension.
As outlined before small glass model implants were modified with various hydrogel compositions, using HA of different molecular weigth (40 and 100 kDa), TG (28-63 %), mass concentrations (ß(HA)=5, 10 and 15 mg/ml) and crosslinker (MBAA, ACLT-PEG-ACLT, 4arm-PEG-VS and 4arm-PEG-ACLT.

Error Prone Channel Formation

The method for the insertion of an artificial channel inside the hydrogel of a glass model implant was established by Thaller for large hydrogel modified tubes (ID=5 mm and l=10 mm) [145]. This approach was adapted in this thesis for the miniaturized glass model tubes, but it became clear that this method for channel formation was quite challenging for small model implants and the handling with the very small tubes proved to be difficult, as shown in figure 40.

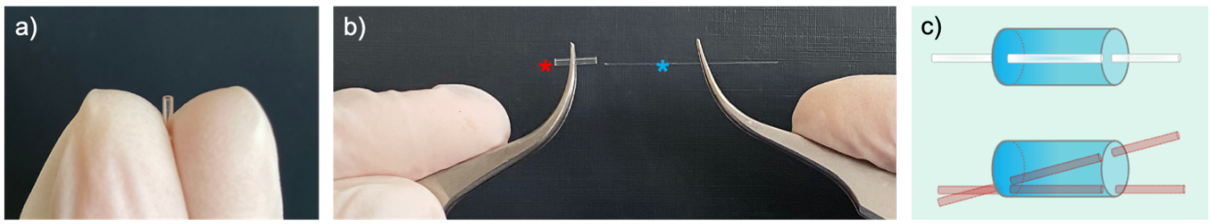

Figure 40: Exemplary handling with small glass model tubes (ID=0.5 mm, l=5 mm) during preparation. Small glass tube between fingers (a) and artificial channel generation into the hydrogel of a small glass tube (red) using a glass fiber (blue) with a diameter of ∅=0.1 mm (b). Centrally positioned glass fiber (c, top) and exemplary incorrectly positioned glass fibers (c, bottom) for channel generation.

Due to the tiny diameter of the glass tubes, the formation of the artificial channel using a glass fiber with ∅=0.1 mm (figure 40b) was error prone. For an accurate function of the HA-modified glass model tube and reproducible results, it was assumed that a centrally positioned channel inside the hydrogel was important (figure 40c, top). In fact, the manual insertion resulted in different and in part incorrect positioning of the glass fiber (figure 40c, bottom), which made the reproducibility of channel formation impossible.
Nevertheless, initially this approach was sufficient to establish further investigations with the small glass model tubes, as the development of a new pressure measurement setup for the miniaturized tubes (see section 4.4). In a later stage it became clearer that further optimizations for the preparation of small model implants were necessary and were therefore explored in more detail to solve the problems outlined here (see section 4.5).

4.3 Properties of HA Hydrogel-Modified Implants

The incorporation of HA hydrogels into small model tubes confer distinct properties to our new type of glaucoma implant, necessitating thorough characterization.

A particularly notable feature of hydrogels is their capacity to absorb water or biological fluids in quantities exceeding their own weight, resulting in significant volumetric expansion [159]. This swelling behavior is a critical parameter in various applications [151] and also crucial for the function of hydrogels as pressure-sensitive valves in the new glaucoma implant, as it directly influences the hydrogels' elasticity.

Another relevant objective in this study was to assess the hydrogels' resistance against enzymatic degradation, since hyaluronidases are known to be present in the ocular outflow structures, particularly within the ECM of trabecular meshwork (TM) cells [13].

4.3.1 Swelling Behaviour of Constrained HA Hydrogels

The mechanisms of hydrogel swelling were already well explored and published for a variety of hydrogel compositions [157, 159, 178, 179, 222, 225, 243], but indeed, for constrained hydrogels only less data existed.

Therefore, in this section the swelling behavior of HA hydrogels immobilized on the tube interior of small glass model tubes was investigated.

For this, the tubes were prepared as outlined in section 3.3 using hydrogels with TG=51 %, different mass concentrations (β(HA)=5, 10 and 15 mg/ml) and PEG linker (ACLT- PEG-ACLT, 4arm-PEG-ACLT and 4arm-PEG-VS).

After full polymerization the HA-modified tubes were incubated in PBS (0.4 M, pH 7.4) for 72 h and the mass swelling ratio was calculated from their starting masses after polymerization (m_0) related to the swollen gels (m_s).

Since in general the swelling behavior was related to the dry (non-hydrated) mass of the gel, the theoretical dry masses (m_d) were additionally calculated from the starting materials. A lyophilization of the hydrogel samples in order to determine the "real dry" masses was not pursued, since ions from PBS would also create crusts, causing errors by additional weight [145].

For macroscopic (non-immobilized) hydrogels with similar hydrogel compositions as investigated in this thesis, Tim Kreuz already compiled extensive data on the swelling behaviour [178], which was used for comparison with the data obtained here for the constrained hydrogels.

For hydrogel compositions with MBAA the swelling behavior was already well explored in previous studies for different TGs and comparing constrained and macroscopic hydrogels [145, 147], therefore a re-examination with MBAA gels was not carried out in this study.

The swelling behavior of macroscopic and constrained HA hydrogels is exemplary shown in figure 41.

In this thesis, the swelling studies of constrained hydrogels were expanded to include further parameters that were also relevant in regard of our new type of glaucoma implant, such as different polymer concentrations, that were used in this thesis, or tube dimensions (ID=1, 2 and 3 mm, l=6 mm). For the gels with HA51 and ACLT-PEG-ACLT the mass concentrations 10 and 15 mg/ml were investigated, for lower concentrations no gel formation occurred in these polymer systems. For the multifunctional PEG linker 4arm-PEG-ACLT and 4arm-PEG-VS concentrations of 5 and 10 mg/ml were used, for higher concentrations the gelation occurred too fast and impeded the preparation of HA-modified tubes.

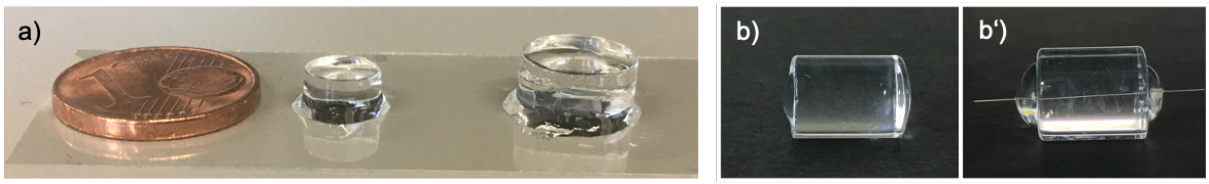

Figure 41: Swelling behaviour of macroscopic (a) and constrained HA hydrogels (b/b'). Macroscopic HA/PEG hydrogel with *β*(HA)=10 mg/ml, TG=51 % and crosslinked with 4arm-PEG-ACLT before (left) and after (right) swelling in PBS for 72 h, pH 7.4 (a). HA/MBAA hydrogel immobilized on the interior of large glass model tube (ID=0.5 mm, l=10 mm), with *β*(HA)=15 mg/ml and TG=58 % before (b) and after (b') swelling in PBS for 24 h. Pictures from b and b' were adapted from previous studies [147].

First, the relative mass gains of the immobilized hydrogels were determined from their starting masses after curing related to the swollen gels. This data is summarized in figure 42.

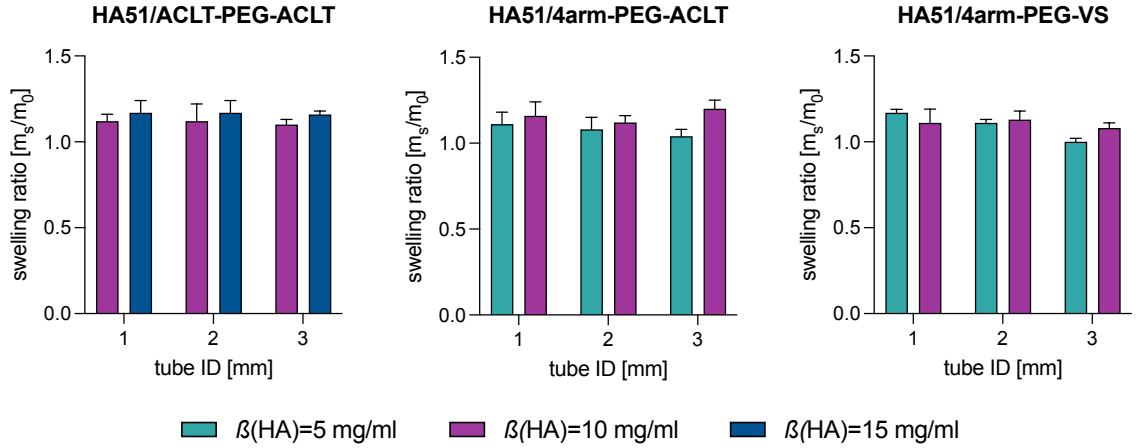

Figure 42: Relative swelling ratios (m_s/m_0) for constrained HA/PEG hydrogels. Various gel compositions with different mass concentrations of HA51 (*β*(HA)=5, 10 and 15 mg/ml) and different kind of PEG linker (ACLT-PEG-ACLT, 4arm-PEG-ACLT and 4arm-PEG-VS) were immobilized on the tube interior of small glass model tubes with different inner diameters (ID=1, 2 and 3 mm). Hydrogels were formed in 0.4 M TRIS/PBS, pH 8.5 and the relative mass gains of the gels after 72 h of swelling in PBS (pH 7.4) were determined in contrast to the pre-swollen state of the gels. Averages were taken from 3-6 individual samples with the standard deviation as error bar.

Overall, comparing the different hydrogel compositions immobilized on the tube interior of middle and small glass model tubes with different inner diameter (ID=1, 2, and 3 mm) no big differences were observed and relative mass swelling ratios (m_s/m_0) were in a similar range between 1.00 and 1.20. Comparing the mass concentrations of HA for each HA/PEG composition a slightly higher swelling value was observed for the higher concentrations.

For HA51/ACLT-PEG-ACLT the swelling ratios ranged between 1.10–1.12 for 10 mg/ml and 1.16–1.17 for 15 mg/ml. For the compositions with 4arm-PEG-ACLT the ratios were 1.04–1.11 for 5 mg/ml and 1.12–1.20 for 10 mg/ml. Swelling ratios of 1.00–1.17 were observed for HA51/4arm-PEG-VS with 5 mg/ml and for 10 mg/ml the values were at 1.07–1.13.

As mentioned before, usually the swelling behaviour was related to the dry mass of the gel, as summarized in figure 43, showing the differences between the hydrogels and different tube IDs much clearer.

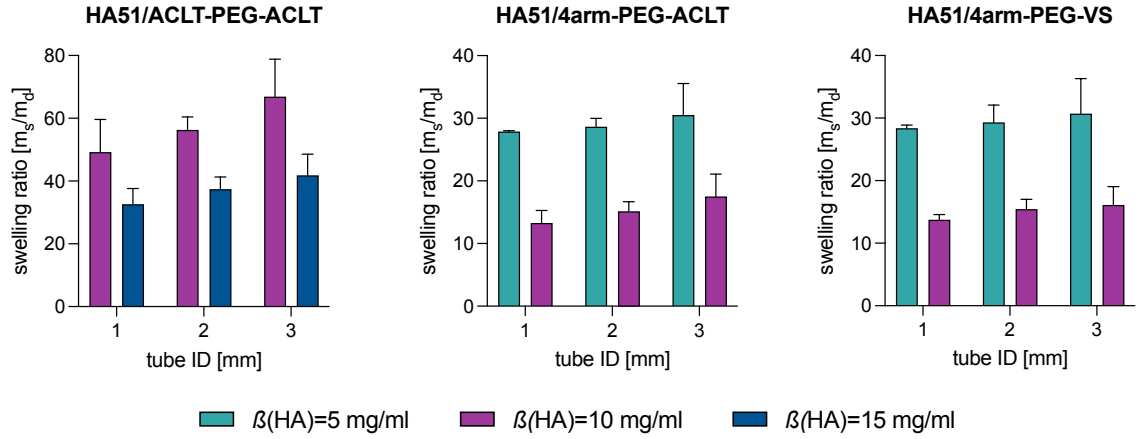

Figure 43: Relative swelling ratios (m_s/m_d) for constrained HA/PEG hydrogels. Various gel compositions with different mass concentrations of HA51 (*ß*(HA)=5, 10 and 15 mg/ml) and different kind of PEG linker (ACLT-PEG-ACLT, 4arm-PEG-ACLT and 4arm-PEG-VS) were immobilized on the tube interior of small glass model tubes with different inner diameters (ID=1, 2 and 3 mm). Hydrogels were formed in 0.4 M TRIS/PBS, pH 8.5 and the relative mass gains of the gels after 72 h of swelling in PBS (pH 7.4) were determined in contrast to the theoretical dry masses calculated from the starting materials. Averages were taken from 3-6 individual samples with the standard deviation as error bar.

Depending on the mass concentration of HA and the ID of the glass tube, swelling ratios ranged from 32.6 to 66.9 for the HA51/ACLT-PEG-ACLT gels, between 15.1 and 30.5 for HA51/4arm-PEG-ACLT and from 13.7 to 30.7 for HA51/4arm-PEG-VS hydrogels.
For all hydrogel compositions a higher HA concentration resulted in significantly lower swelling ratios, compared to the lower mass concertation of the same hydrogel composition. This behaviour was already well explored and explained by the tighter network structure with higher concentration which was correlated to an increase in crosslinking density [178]. The equilibrium swelling ratio was a function of a networks' crosslinking density and thermodynamic interactions between polymer and solvent [178, 244]. Thereby, an increased crosslinking density resulted in a higher retraction force, which influenced the network upon swelling and by this limiting water uptake [178]. This explanation was also the reason for higher swelling ratios of hydrogels with the bifunctional crosslinker ACLT-PEG-PEG in contrast to the multifunctional and high molecular linker 4arm-PEG-ACLT and 4arm-PEG-VS. Another important finding for the design of our new glaucoma drainage device was the increased swelling with higher diameter of the tube, since the dimensions of the future implant were not set. The reduced limitation due to the wider tubes allowed the gels to swell further, explaining the higher ratios at larger diameter.

Differences between Constrained and Unobstructed Hydrogels

Some differences between constrained and unobstructed hydrogels were already known from previous studies by Thaller, using large glass model implants (ID=5 mm, l=10 mm) and HA/MBAA compositions with β(HA)=15 mg/ml and TG=57 % [145].

For example, immobilized hydrogels showed a decreased swelling behaviour during the first two days in contrast to non-immobilized ones due to the physical barrier of the tubes' walls [145].

In a later swelling stage (after 45-50 hours), Thaller showed that the swelling ratios were higher for immobilized hydrogels and this effect was present over the course of the measurement (several weeks) [145].

This behaviour was explained by the covalent immobilization of HA hydrogels into the glass tubes [145]. At first, the reduced amount of water in the hydrogel network of constrained gels resulted in smaller pore sizes [180], which then led to a limited diffusion of TRIS molecules within the immobilized network [145, 180]. Due to the fact that the molecule exchange with the hydrogel and medium was only possible at the tubes' ends, the removal of TRIS molecules was slow downed, which in turn led to a higher mass of immobilized hydrogels in comparison to non-immobilized hydrogels after 50 hours [145]. Further swelling studies with HA/MBAA and large glass model implants, focused on investigations of different TGs, showing that swelling ratios decreased with increasing TGs [147].

For HA/PEG hydrogel compositions, investigated in this thesis, further observations were made, comparing immobilized and non-immobilized hydrogels.

As mentioned before, some data was already available for similar gel compositions (HA49/4arm-PEG-ACLT and HA49/4arm-PEG-VS), for macroscopic hydrogels [178]. This data was compared with the swelling ratios of small glass model tubes in this thesis.

Clearly, the values of macroscopic gels with the multifunctional PEGs obtained from Kreuz were not completely the same as our compositions (TG 49 % and TG 51 %), but they were nevertheless very close to each other and comparable to our hydrogels.

For tube IDs with 3 mm the same observations were made as described by Thaller: after 72 h the swelling ratios were higher for constrained hydrogels compared to macroscopic ones due to reasons described above.

For tube IDs with 2 mm this effect was only present for β(HA)=15 mg/ml, for lower concentrations (β(HA)=10 and 5 mg/ml) the swelling ratios were decreased. As shown in figure 44, for tubes with ID=1 mm the opposite was observed: for all hydrogel compositions the swelling ratios of macroscopic hydrogels were higher than for immobilized ones. For the bifunctional crosslinker ACLT-PEG-ACLT and β(HA)=10 mg/ml the values were at 61.81±3.6 for the macroscopic gels and 49.25±10.4 for the immobilized hydrogels. For a higher mass concentration (β(HA)=15 mg/ml), the differences were lower: 33.58±2.6 was calculated for the macroscopic gels and 32.6±5.0 for the constrained ones. The results for multifunctional crosslinker (4arm-PEG-ACLT and 4arm-PEG-VS) showed that, for lower concentration (β(HA)=5 mg/ml) the swelling values differed less and were in a similar range, whereas at higher polymer concentrations the values

for macroscopic gels were significantly higher. These results clearly showed, that the effects described by Thaller [145] for hydrogels immobilized on the interior of large glass model tubes, played a minor role for small ones. The exact values for all samples presented in figure 42, 43 and 44 are summarized in the appendix (section 6.3.1, table 8).

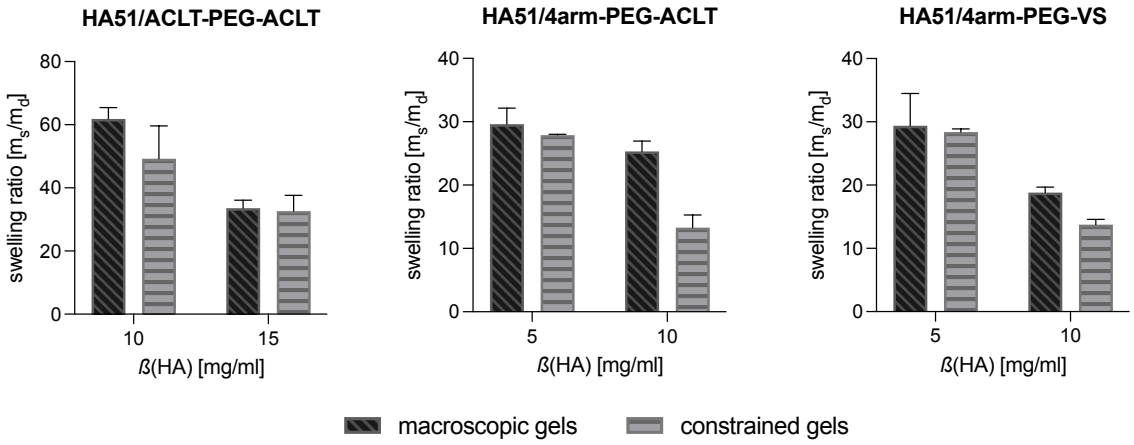

Figure 44: Comparison of relative swelling ratios (m_s/m_d) for macroscopic and constrained HA/PEG hydrogels. Various gel compositions with different mass concentrations of HA51 (β(HA)=5, 10 and 15 mg/ml) and different kind of PEG linker (ACLT-PEG-ACLT, 4arm-PEG-ACLT and 4arm-PEG-VS) were immobilized on the tube interior of small glass model tubes with ID=1 mm. Macroscopic hydrogels with HA51/ACLT-PEG-ACLT were formed in special teflon sample holder. Hydrogels were formed in 0.4 M TRIS/PBS, pH 8.5 and the relative mass gains of the gels after 72 h of swelling in PBS (pH 7.4) were determined in contrast to the theoretical dry masses calculated from the starting materials. The swelling ratios for macroscopic hydrogels with 4arm-PEG-ACLT and 4arm-PEG-VS were obtained from previous studies by Tim Kreuz [178] using HA49. Averages were taken from 3-6 individual samples with the standard deviation as error bar.

Further comparison of our data to other hydrogel compositions, published by Thaller [145], Hegger [179], Shu et al. [159] and Hagel et al. [157] are compiled in table 5.

Table 5: Comparison of swelling ratios of HA hydrogels investigated in this thesis and in literature with corresponding parameters for hydrogel formation. *For desmosine-inspired crosslinker two swelling values were given (charged/uncharged crosslinker). **Average swelling ratios were exemplary taken from the immobilized hydrogels (ID=1 mm). Error= standard deviation.

	M_n (HA) [kDA]	β(HA) [mg/ml]	TG [%]	Crosslinker	Swelling ratio (m_s/m_d)
Thaller [145]	100	15	57	MBAA	43.7±0.4
Hegger [179]	74	2.8	33	$T^+A_2C_4$	42.5±1.4
Shu et al. [159]	120	10	42	PEGDAA	39.41
Hagel et al. [157]	450	28	49	Desmosine inspired	27/30*
Thesis	40	15, 5	51	ACLT-PEG-ACLT 4arm-PEG-ACLT 4arm-PEG-VS	32.6±5.0** 27.88±0.1** 28.37±0.5**

The theoretical values calculated from the starting materials were not completely accurate, however our data was still comparable to the swelling rates gained from the other groups, especially to the results from Hagel et al. with the desmosine inspired crosslinker. Value variations to others were attributed to different parameters used.

4.3.2 Enzymatic Degradation of HA Hydrogels

In the human body hyaluronan is a major component of the ECM in various tissues, including the TM of the ocular outflow structures, making HA a suitable candidate for a novel GDD utilizing a naturally biocompatible material.
The degradability of HA in the ECM was known to be an important attribute, playing a significant role in wound healing processes [226]. Thereby the enzyme hyaluronidase IV was secreted by human cells for ECM remodeling and HA degradation [226].
Regarding the use of HA as hydrogel material in our new type of glaucoma implant, a degradation would be devastating and would completely destroy the main function of the implant: the valve functionality of the hydrogel to drain excess fluid to a normal IOP.
Therefore, it must be ensured that our HA hydrogel, unlike HA in the human body, was not degraded but remained completely and permanently on the inner tube surface, to ensure a reliable and long-term functionality of the implant.

For that reason, the durability of constrained hydrogels within small glass model tubes against enzymatic degradation was explored more closely.
After conducting swelling experiments (see section 4.3.1), the samples with ID=2 mm and l=6 mm were incubated in hyaluronidase IV solutions (0.1 U) over a time period of 21 days, and hydrogel weigth was recorded. For comparison, again macroscopic hydrogels of the same compositions were included. As control, hydrogels and hydrogel-modified tubes were incubated simultaneously in PBS. The enzymatic degradation of HA hydrogels was determined by calculating the half-life ($t_{1/2}$) of each hydrogel, which corresponded to the time frame in which the hydrogel lost half of its initial weigth. For this, an exponential decay of first order was fitted to the weigth measurements conducted for each hydrogel.
For some hydrogel compositions no complete, but a partial degradation was observed over a time period of 21 days. In these cases, a percentage hydrogel reduction was declared.
Three independent experiments were performed for each hydrogel composition; however, only one representative graph for each composition is presented in the following.

Enzymatic Degradation Assay of Macroscopic Hydrogels

Exemplary graphs for macroscopic hydrogels with different mass concentrations of HA (β(HA)=25, 20, 15 and 5 mg/ml) and crosslinked with different bi-and multifunctional linker were compiled in figure 45 and figure 46.
For corresponding negative controls of each hydrogel composition see appendix (section 6.4.1), showing a constant hydrogel weight over the course of three weeks.

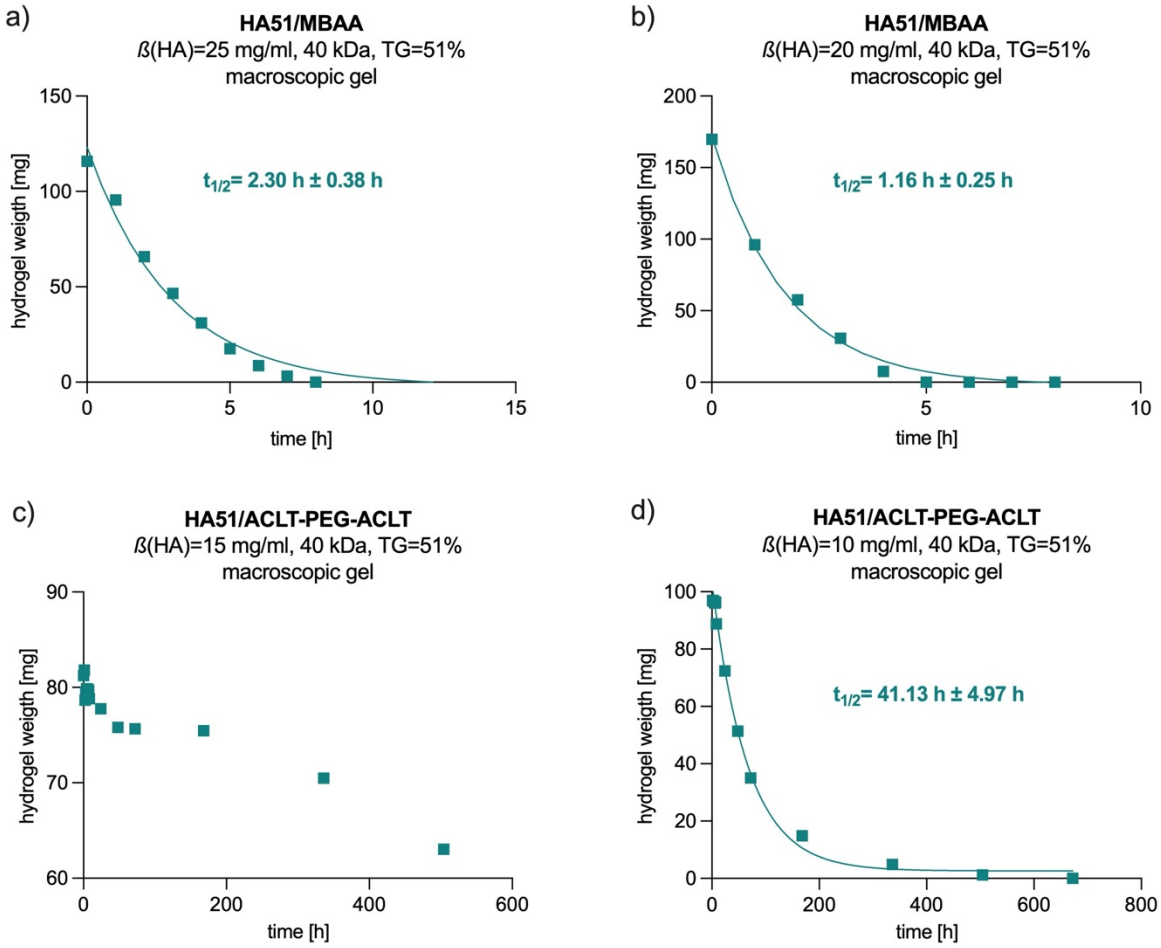

Figure 45: Exemplary graphs for enzymatic degradation of macroscopic HA51 hydrogels crosslinked with bifunctional crosslinker. Hydrogels were formed in 0.4 M TRIS/PBS pH 8.5, using HA51 with different mass concentrations (β(HA)=25, 20 and 15 and 10 mg/ml) and crosslinker: MBAA (a/b) and ACLT-PEG-ACLT (b/c). After swelling, hydrogels were immersed in hyaluronidase IV solutions (0.1 U) at room temperature and hydrogel weigth was determined over three weeks, whereby enzyme solution was exchanged every two days. For the hydrogel compositions with HA51/MBAA (β(HA)=25 and 20 mg/ml) (a/b) and HA51/ACLT-PEG-ACLT (β(HA)=10 mg/ml) a complete degradation occurred (a, b and d). The half-lives ($t_{1/2}$) for these hydrogel compositions were: 2.30±0.38 h (a) and 1.16±0.25 h (b) for the MBAA crosslinked gels; and 41.13±4.97 h (d) for the ACLT-PEG-ACLT gels with β(HA)=10 mg/ml. The half-lifes were determined from three individual prepared hydrogels with the standard deviation as error bar. For the hydrogels with HA51/ACLT-PEG-ACLT and β(HA)=15 mg/ml no complete but a partial degradation was observed with around 20 % of hydrogel loss after three weeks.

For hydrogel compositions with HA51/MBAA a complete degradation was observed with resulted half-lifes from three measurements of $t_{1/2}$= 2.30±0.38 h for β(HA)=25 mg/ml (figure 45a) and $t_{1/2}$= 1.16±0.25 h for β(HA)=20 mg/ml (figure 45b).

For HA51/ACLT-PEG-ACLT a higher stability against enzymatic degradation was observed, shown by an increased half-life of $t_{1/2}$= 41.13±4.97 h for β(HA)=10 mg/ml (figure 45d).

For a higher mass concentration of HA (figure 45c), no complete, but a partial hydrogel degradation was observed with around 20 % of hydrogel loss after three weeks.

These trends were mainly attributed to the crosslinking density of the hydrogel, which was less for lower concentrations and also for smaller crosslinker as MBAA (M_n=154 kDA) in contrast to ACLT-PEG-ACLT (M_n=600 kDa). This corresponded to softer hydrogels with larger mesh sizes, and this led to more enzyme diffusion into the hydrogel and faster degradation.

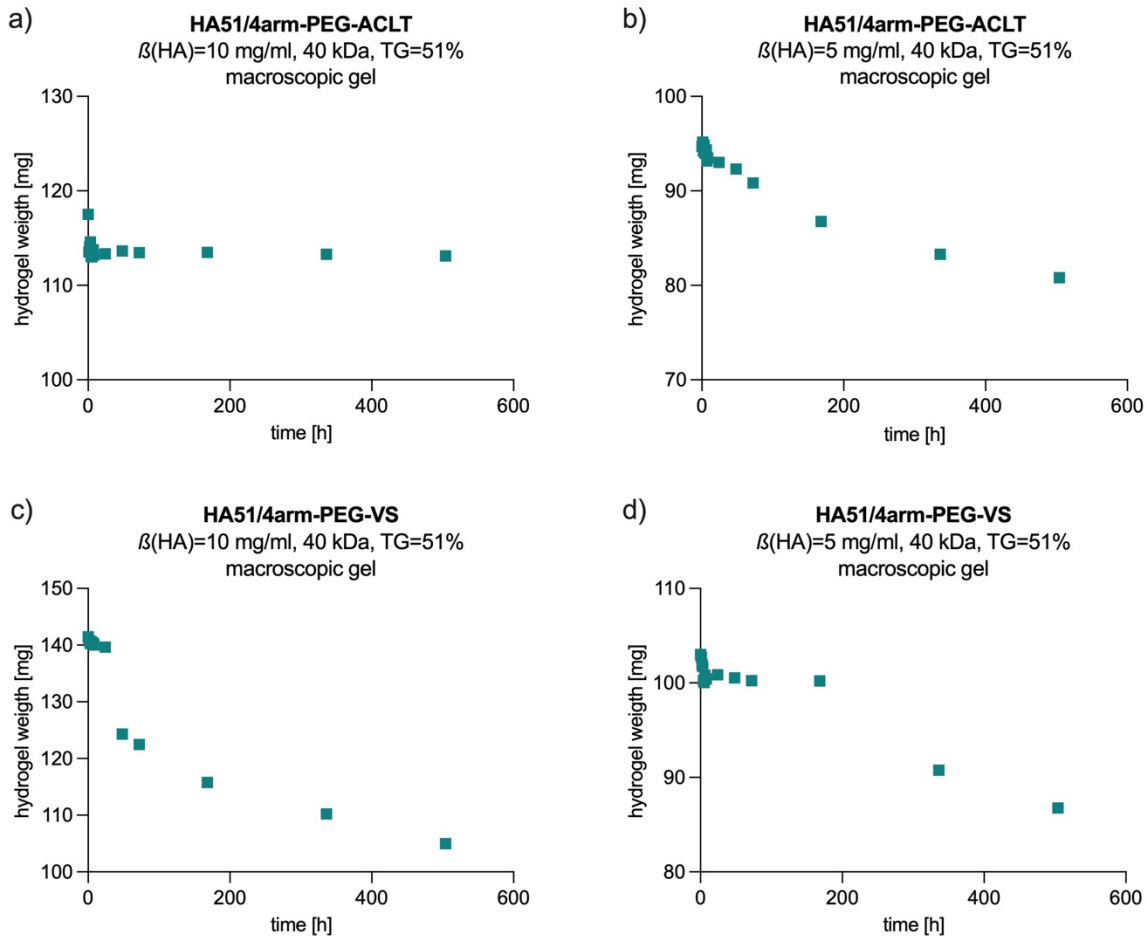

Figure 46: Exemplary graphs for enzymatic degradation of macroscopic HA51 hydrogels crosslinked with multifunctional crosslinker. Hydrogels were formed in 0.4 M TRIS/PBS pH 7.4, using HA51 with different mass concentrations (β(HA)=10 and 5 mg/ml) and crosslinker: 4arm-PEG-ACLT (a/b), 4arm-PEG-VS (b/c). After swelling, hydrogels were immersed in hyaluronidase IV solutions (0.1 U) at room temperature and hydrogel weigth was determined over three weeks, whereby enzyme solution was exchanged every two days. Most hydrogels showed no complete, but only partial degradation over the course of three weeks. For HA51/4arm-PEG-ACLT and β(HA)=10 mg/ml hydrogel weight was constant – no degradation was observed (a). For other compositions the hydrogels lost around 15 % (b), 30 % (c) and 15 % (d) of its initial weigth. The experiments were performed three times for each hydrogel composition.

For multi-functional crosslinked hydrogels, a significantly higher stability was determined, as none of the hydrogels was completely degraded over the course of three weeks.

For HA51/4arm-PEG-ACLT no degradation was observed for β(HA)=10 mg/ml (figure 46a). For a lower concentration (β(HA)=5 mg/ml) the hydrogels lost around 15 % of its initial weigth (figure 46b). Hydrogels crosslinked with 4arm-PEG-VS showed a different behaviour: for β(HA)=10 mg/ml, around 30 % of the hydrogel was degraded (figure 46c), while the hydrogels with lower concentrations (β(HA)=5 mg/ml) showed a higher stability with only 15 % loss of its initial weigth.

The higher stability of 4arm-PEG-ACLT linked gels was attributed to the higher crosslinking density and lower mesh size of the hydrogel compounds, compared to HA/4arm-PEG-VS.

In previous studies by Kreuz, it was shown that the mesh size of HA/4arm-PEG-ACLT was around 80 nm for total polymer concentrations of 15 mg/ml with decreasing in size with higher concentrations (30 nm for 65 mg/ml) [178].

For hydrogels with HA/4arm-PEG-VS the mesh size values were at 110 nm for 15 mg/ml total polymer concentration and ending at 30 nm for 70 mg/ml [178].
It was assumed, that the mesh size influenced the diffusion of hyaluronidase enzymes into the hydrogels. The approximate molecular weight of a hyaluronidase molecule is around 60 kDa and the volume can be estimated around 5 nm, using the relationship between the physical dimensions of a molecule on its mass [245].
In conclusion, the tighter network of 4arm-PEG-ACLT gels reduced enzyme accessibility and were hence more stable against enzymatic degradation than 4arm-PEG-VS.
However, for the degradation of 10 and 5 mg/ml 4arm-PEG-VS hydrogels our observations clashed with the mesh size calculations by Kreuz, since the higher concentration was more degradable than the lower concentration, despite smaller mesh size at higher concentrations.

The differences between hydrogels of HA51/4arm-PEG-ACLT and HA51/4arm-PEG-VS were also evident in the morphology of the gels post-immersion in hyaluronidase IV solution for three weeks (figure 47). For the ACLT-terminated linker, both hydrogels, the control (PBS) and treated one (hyaluronidase IV), looked quite similar with smooth surface (figure 47a). In contrast, the VS-linked gels displayed a fragile and crumbly surface after the same treatment period (figure 47b).

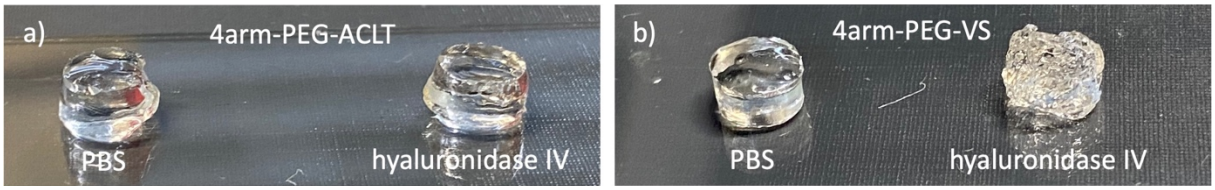

Figure 47: Comparison of macroscopic hydrogels with multifunctional crosslinker (4arm-PEG-ACLT and 4arm-PEG-VS) after immersion in PBS (control) and hyaluronidase IV solution for three weeks. Hydrogels were formed in 0.4 M TRIS/PBS pH 7.4, using HA51 with β(HA)=10 mg/ml and crosslinker. After swelling, hydrogels were immersed in PBS or hyaluronidase IV solutions (0.1 U) at room temperature, whereby enzyme solution was exchanged every two days. Hydrogels with 4arm-PEG-ACLT showed similar shapes as controls with smooth surfaces (a), while for 4arm-PEG-VS a fragile and crumbly surface was observed after three weeks in hyaluronidase IV solution (b, right).

Enzymatic Degradation Assay of Constrained Hydrogels

As already observed in swelling studies of immobilized and non-immobilized HA hydrogels, differences were also expected in regard of their sustainability against enzymatic degradation. Exemplary graphs for each hydrogel composition are compiled in figure 48. Corresponding control graphs were shown in the appendix (see section 6.4.1)
The results clearly showed, that the hydrogel weigth was constant over the course of three weeks and no degradation was observed. One explanation for the higher stability of immobilized hydrogels was, the reduced amount of water in the hydrogel network resulted in smaller pore sizes [180], which in turn reduced the enzyme diffusion into the hydrogel network. Furthermore, due to the physical barrier of the tube, the enzymes could only target the hydrogels at the tubes' ends, which made it also difficult to penetrate the hydrogel.
No data was available for hydrogel-modified tubes with HA/MBAA, as the model tubes used in these experiments had been previously utilized for swelling experiments (see section 4.3.1), which

were not repeated for MBAA. However, from the previous results with macroscopic HA/MBAA gels and the short half-lifes of these hydrogels, it might be expected that there could possibly also be a degradation of constrained HA/MBAA hydrogels.

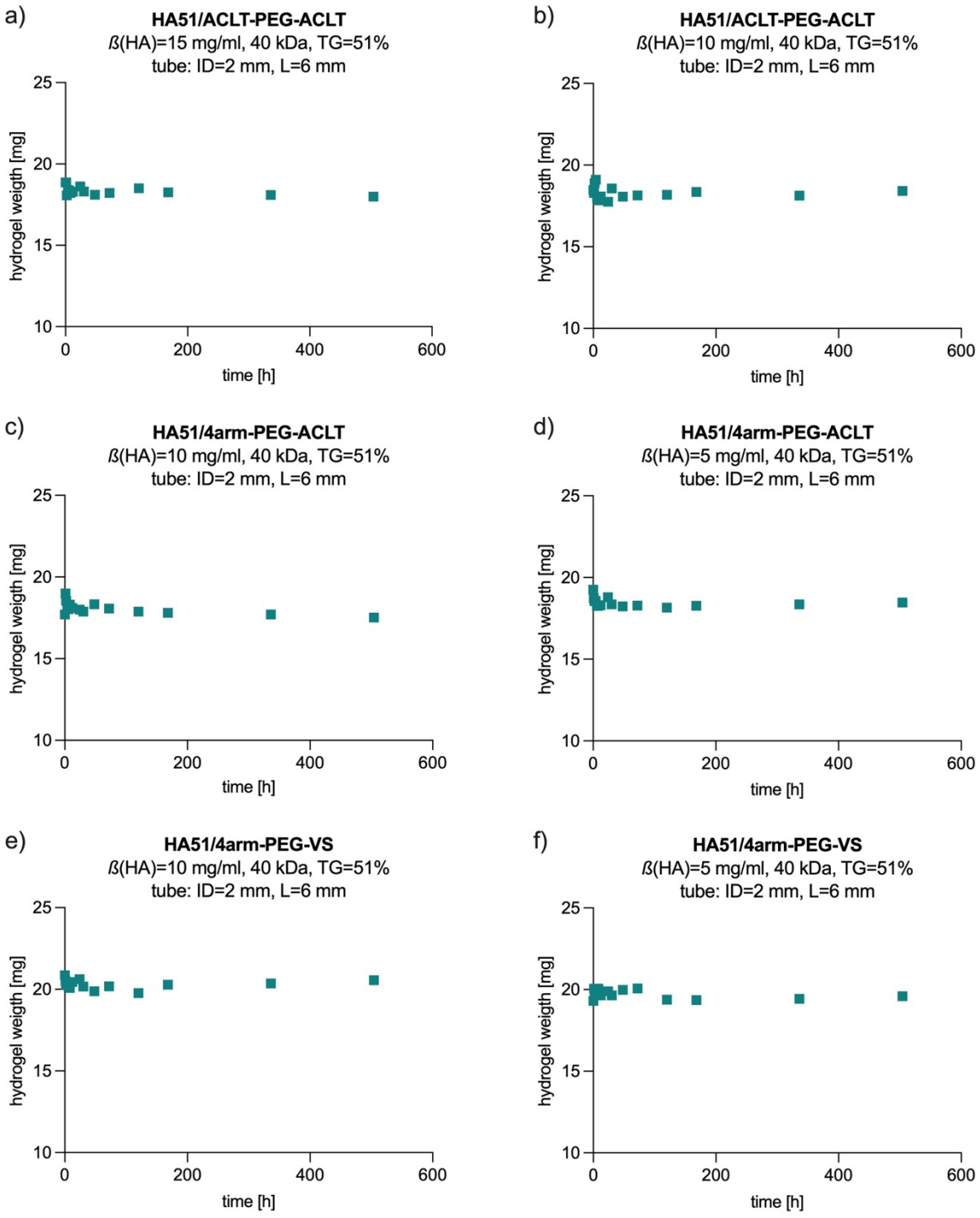

Figure 48: Exemplary graphs of enzymatic degradation assays using small HA modified tubes (ID=2 mm, l=6 mm) with different hydrogel compositions immobilized on tube interior (a-f). Hydrogels were formed using HA51 with different mass concentrations (β(HA)= 5, 10 and 15 mg/ml) and different crosslinker: ACLT-PEG-ACLT (a/b), 4arm-PEG-ACLT (b/c) and 4arm-PEG-VS (e/f). After hydrogel swelling, tubes were immersed in hyaluronidase IV solutions at a concentration of 0.1 U and at room temperature and hydrogel weigth was determined over three weeks, whereby enzyme solution was exchanged every two days. None of the hydrogels were degraded by hyaluronidase IV over the course of three weeks.

4.4 Pressure Measurements of HA Hydrogels

Given by the nature of liquid flow through a tiny tube a certain pressure is needed to break the surface tension of the fluid so that the fluid can flow through the tube. Accordingly, when a tube is filled with a hydrogel higher pressure is required, creating a channel through the hydrogel due to the liquid pressure. The elastic force of the hydrogel acting as counterforce while the liquid pressure pushing the gel against the wall.
Previous studies by Thaller showed that the channel formation was not a straight-line passage, rather the gel was torn in a randomized manner [145]. Thaller demonstrated that a uniform channel formation inside the hydrogel was possible, when using a glass fiber [145]. This worked well for large hydrogel filled tubes, but in this thesis miniaturized tubes were used. As already mentioned before, the channel formation in small hydrogel modified tubes was challenging and error prone (see section 4.2.3) and this provided several issues for the following pressure measurements.

Nevertheless, a pressure measurement setup was established using the microfluidic device Elveflow OB1 MK3 and different measurement modes were implemented to investigate the pressure regulation abilities of small HA-modified glass model tubes with different hydrogel compositions. The results in the following sections were compared to a famous and widely used current glaucoma implant, owning a mechanical valve functionality: the Ahmed glaucoma valve (AGV).

4.4.1 Activation Pressures of Small HA-Modified Tubes

Current GDDs with a valve functionality, as the Ahmed glaucoma valve (AGV) were known to be primed before use, which was a routine process to open the valve, as the mechanical leaflets of the AGV [246-249]. This priming process was always performed just prior to implantation of the device by the surgeon by manual injection of a balanced saline solution (BSS) through the AGV until fluid flow was visible at the valve outlet [249]. The priming required a hard push with a very high pressure to overcome the initial pressure resistance of the valve, and once opened, the resistance suddenly dropped to a lower pressure range [246].

With regard to our hydrogel-modified glass model implant, also owning a valve functionality, it came out that they also had to be primed or 'activated'. As outlined above, the hydrogel inside was acting as counterforce to the liquid pressure applied to the hydrogel. Depending on the hydrogel composition, more or less pressure was needed to overcome this counterforce for channel opening. In previous studies large hydrogel filled tubes (ID=5 mm and l=10 mm) were investigated and it was shown, that for all samples the first channel opening occurred at a higher pressure than all following openings, therefore this pressure was termed as 'activation pressure', the following openings were termed 'opening pressure' [145, 147, 246]. For all measurements PBS was used instead of BSS, since previous studies showed no differences in the measurements [145].

An exemplary typical course of the measurement of a large HA-modified tube, measured in previous studies with a hydrostatic pressure setup [147], is shown in figure 49a. The pressure is illustrated by the dark grey curve, the blue curve represents the fluid flow. Once opened at around 1800 Pa, the high initial pressure decreased while the fluid was drained, ending at an equilibrium pressure around 1000 Pa, also called the 'closing pressure', since no liquid flow occurred at this pressure.

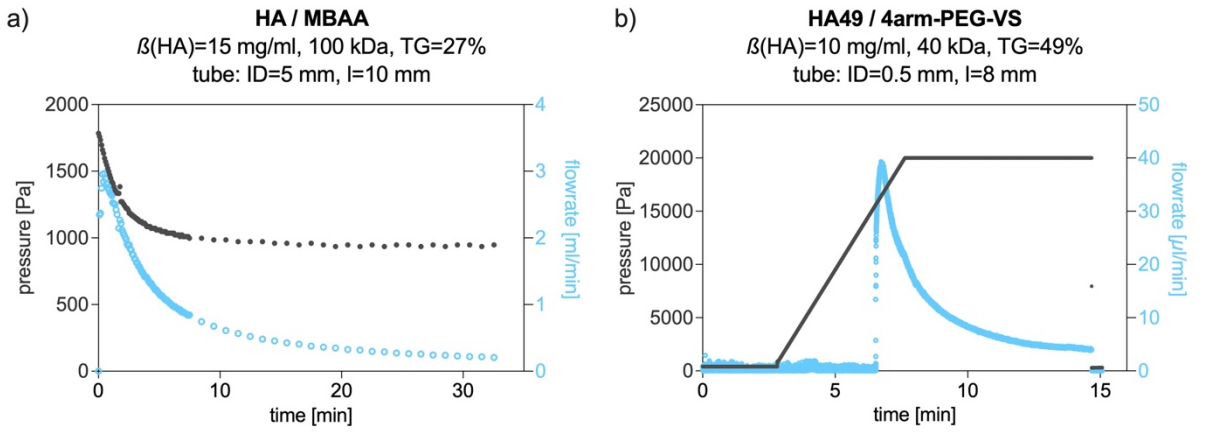

Figure 49: Exemplary pressure measurements of a large (a) and small (b) glass model tube for the determination of activation pressure. Measurement of large HA hydrogel modified glass model tube (ID=5 mm, l=10 mm) with β(HA)=15 mg/ml, 100 kDa, TG=27 % and MBAA as crosslinker was taken from previous studys [147]: the channel opened at ~1800 Pa and the liquid was drained to an equilibrium pressure of ~1000 Pa (a). Small HA-modified glass tube (ID=0.5 mm, l=8 mm) with HA49 (β(HA)=10 mg/ml, 40 kDa, TG=49 %) and crosslinker 4arm-PEG-VS was measured using the microfluidic device from Elveflow with the pressure ramp mode: pressure was increased gradually in a time interval of 5 min and the flowrate was recorded. The channel opened at ~15,000 Pa with a fluid flow of 40 µl/min, reaching an equilibrium flow of ~5 µl/min after ~8 min after channel opening (b). Pressure was illustrated by the dark grey curve; the blue curve represented the fluid flow.

To determine the activation pressure of small HA modified glass model tubes of different length (ID=0.5 mm and l=10, 8, 6, 5, 4 and 3 mm) and with different hydrogel compositions, a microfluidic setup was used and a measurement profile with pressure ramps of different ranges was performed. Thereby, the pressure was gradually increased to a certain value and in a defined time interval (within 300 s) and the flowrate of outflowing fluid was measured and used to determine the activation pressure. Differently to the AGV, where a short and hard push was used to open the valves [246], the ramp application ensured that the pressure on the hydrogel was increased slowly to prevent destruction of the gel.

An exemplary ramp measurement for a small hydrogel filled tube with ID= 0.5 mm and l=8 mm is shown in figure 49b for a hydrogel composition with HA49 crosslinked with 4arm-PEG-VS.
The beginning of fluid flow after 6 minutes marked the channel opening around 15,000 Pa and showed a comparable course as displayed for the large HA hydrogel filled tube. After 13 minutes of measurement, the flowrate reached an equilibrium state around 5 µl/min. The measurement, was stopped after 15 minutes and no fluid flow was detected anymore, showing that the channel worked correctly and only opened when pressure was applied.

Error-Prone Activation Pressure Determination

For most measurements of miniaturized glass model tubes, a determination of the activation pressure was not that clear and, in most cases, not possible. This was mainly caused by the challenging preparation of the small hydrogel filled tubes (see section 4.2.3) or insufficient immobilization of the hydrogel on the inner tube surface (see section 4.2.2).
Some exemplary results for the determination of the activation pressure were summarized in figure 50 for a hydrogel composition with HA44-1 (β(HA)=15 mg/ml) crosslinked with MBAA and small tubes of different lengths (ID=0.5 mm and l=10, 8, 6, 5, 4 and 3 mm), showing some of the problems encountered during the priming measurements.

For a tube with a length of 10 mm (figure 50a) no activation pressure could be determined, since the hydrogel was forcefully ejected out of the tube as shown by the highest fluid flow of 120 µl/min (blue curve) after 45 min, although the pressure was removed.
The measurement of a tube with l=8 mm yielded an activation pressure of ~50,000 Pa (figure 50b), the tube with l=6 mm resulted in ~43,000 Pa (figure 50c) and for the tube with l=5 mm an activation pressure of ~69,000 Pa was determined (figure 50d).
For the tube with l=4 mm an activation pressure of ~10,800 Pa was determined, and for l=3 mm the value was at ~19,000 Pa (figure 50e and 50f).
Indeed, the determination of the activation pressure for the tube with l=3 mm was not that clear, since a first opening of the channel proceeded slowly with the first ramp and complete channel opening was observed after 15 min with a second pressure ramp. Therefore, this second opening was selected as 'activation pressure', although, to be precise, there was already an opening before.
Overall, it was shown, that for most HA44-1/MBAA-modified tubes, several pressure ramps were needed until an opening of the channel, means fluid flow, was detected.

Further difficulties occurred during the measurements and for the determination of activation pressures are exemplary shown in figure 51 for the hydrogel compositions with the multifunctional crosslinker 4arm-PEG-VS and 4arm-PEG-ACLT.
Some samples showed no rapid opening of the channel, but a slow opening, as shown for hydrogel-filled tubes with HA28-1/4arm-PEG-VS or HA40/4arm-PEG-VS (figure 51a and 51b). The measured flowrates followed the applied pressure in the same way as it was increased and hence, in these cases, determination of activation pressure was impossible. Nevertheless, since the valve functionality was not affected, these tubes were still useable for further measurements.
Comparison of the tube samples with the compositions HA49/4arm-PEG-ACLT and HA63-1/4arm-PEG-ACLT (figure 51c and 51d) showed the same activation pressure of ~2600 Pa, despite different hydrogel compositions (TG=49 % vs. TG=63 %) and tube lengths (l=4 mm and l=3 mm).

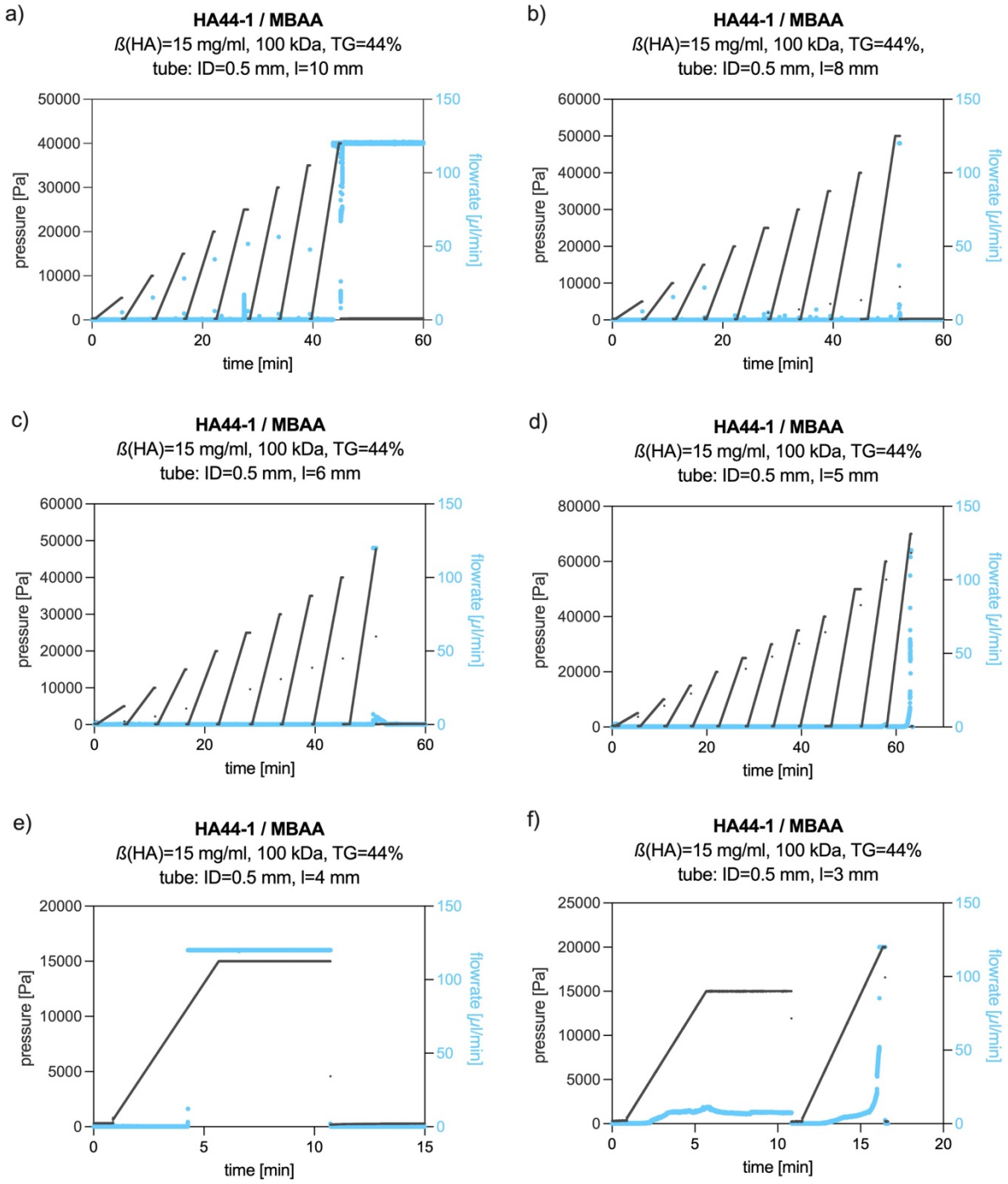

Figure 50: Overview of exemplary pressure ramp measurements of small glass model tubes of different lengths (ID=0.5 mm and l=10, 8, 6, 5, 4 and 3 mm) and with same hydrogel compositions of HA44-1/MBAA (*β*(HA)=15 mg/ml, 100 kDa, TG=44 %) for the determination of activation pressures (a-f). Hydrogel forcefully ejected after ~45 min leading to defect tube (a). Channel opening after ~50 min at ~50,000 Pa for tube with l=8 mm (b). Activation pressures for tube with l=6 mm at ~43,000 Pa (c) and for tube with l=5 mm at ~69,000 Pa (d). Tube with l=4 mm opened at ~10,800 Pa (e); Minor channel opening observed for tube with l=3 mm with first ramp, complete opening with second ramp at 19,000 Pa (f). Small HA-modified glass tubes were measured using the microfluidic device from Elveflow and pressure (dark grey), ranging from 0 to 80,000 Pa, was increased gradually within 5 min and the flowrates (blue) were recorded.

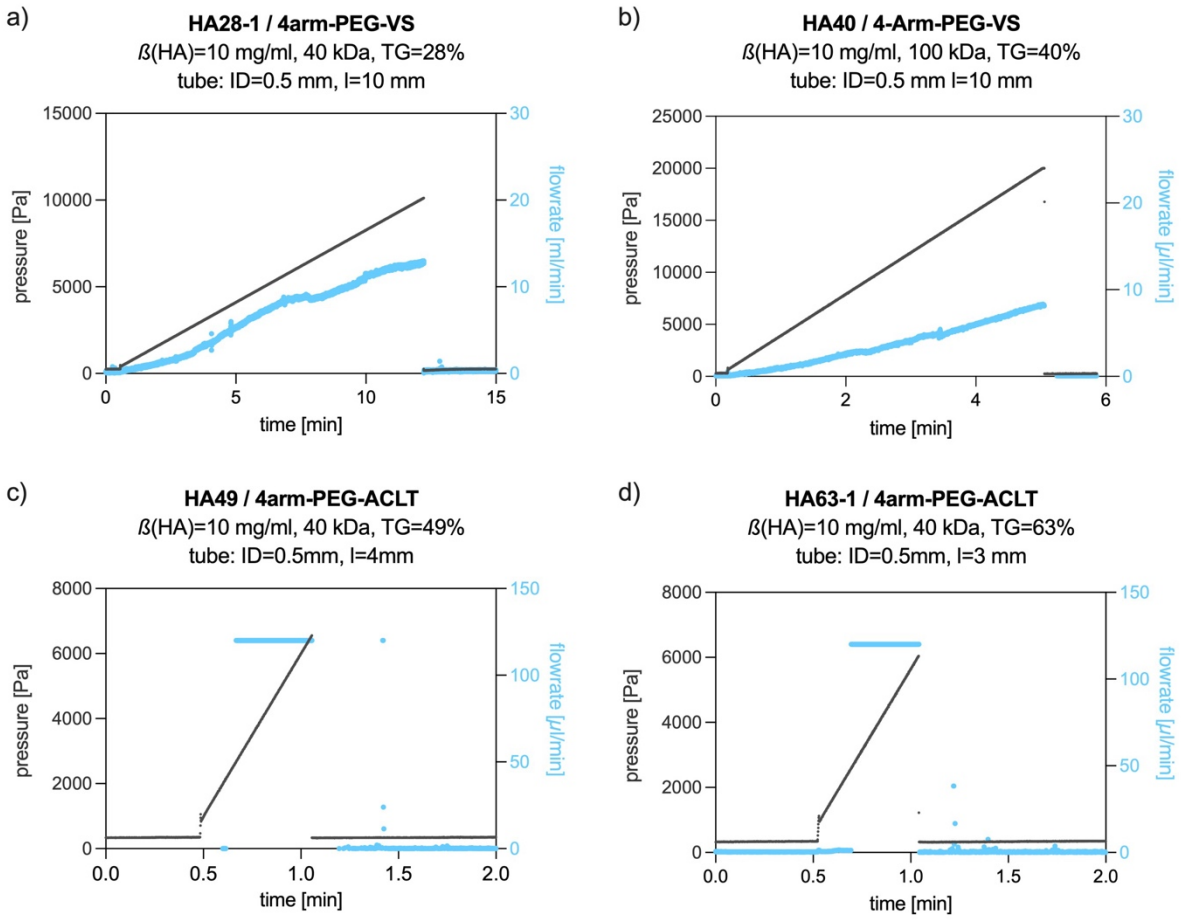

Figure 51: Overview of pressure ramp measurements of small glass model tubes with HA hydrogels crosslinked with multifunctional crosslinker 4arm-PEG-VS (a/b) and 4arm-PEG-ACLT (c/d) for determination of activation pressures. Flowrates followed the applied pressure as it was increased for small tubes (ID=0.5 mm, l=10 mm) with HA28-1/4arm-PEG-VS (*β*(HA)=10 mg/ml, 40 kDA, TG=28 %) (a) and HA40/4arm-PEG-VS (*β*(HA)=10 mg/ml, 100 kDA, TG=40 %) (b). Small glass tubes with HA49/4arm-PEG-VS (*β*(HA)=10 mg/ml, 40 kDA, TG=49 %, l=3 mm) (c) and HA63-1/4arm-PEG-VS (*β*(HA)=10 mg/ml, 40 kDA, TG=63 %, l=4 mm) (d) showed the same activation pressure of 2600 Pa despite different hydrogel compositions. Small HA-modified glass tubes were measured using the microfluidic device from Elveflow and pressure (dark grey) was increased gradually in a certain time interval and the flowrates (blue) were recorded.

A summary of evaluable ramp measurements is compiled in table 6 containing all determined activation pressures of different hydrogel compositions and tube dimensions.

Altogether, the overview showed that the activation pressures for multifunctional-crosslinked hydrogels with 4armPEG-ACLT and HA concentration of 10 mg/ml were higher than observed for the bifunctional crosslinker MBAA and HA concentration of 15 mg/ml.

The tubes with hydrogels of TG=28 % and MBAA as crosslinker displayed the poor reproducibility of the measurement, since the values for the activation pressures deviated very strongly for four independent measurements (3600–47,000 Pa), although the tubes possessed the same length (l=10 mm) and same hydrogel composition.

Table 6: Overview of determined ‚activation pressures' in Pa of small hydrogel-filled tubes (ID=0.5 mm, l=10, 8, 6, 5, 4 and 3 mm) with different gel compositions. HS-HA of different thiolation grade (TG), crosslinked with MBAA, 4arm-PEG-VS or 4arm-PEG-ACLT and with different HA concentrations of β(HA)=5 mg/ml, β(HA)=10 mg/ml and β(HA)=15 mg/ml.

TG [%]	MBAA	4arm-PEG-VS	4arm-PEG-ACLT
28	~ 3600 Pa (l=10 mm) ~ 17,000 Pa (l=10 mm) ~ 30,000 Pa (l=10 mm) ~ 47,000 Pa (l=10 mm)	~ 3300 Pa (l=10 mm) ~ 8000 Pa (l=8 mm)	~ 48,000 Pa (l=4 mm) ~ 86,000 Pa (l=3 mm) ~ 52,000 Pa (l=3 mm)
40	-	~ 24,000 Pa (l=10 mm)	-
44	~ 50,000 Pa (l=8 mm) ~ 43,000 Pa (l=6 mm) ~ 69,000 Pa (l=5 mm) ~ 10,800 Pa (l=4 mm) ~ 19,000 Pa (l=3 mm) ~ 20,000 Pa (l=10 mm)	-	-
49	-	-	~ 100,000 Pa (l=5 mm) ~ 79,000 Pa (l=4 mm) ~ 2600 Pa (l=4 mm)
51	~ 44,000 Pa (l=10 mm) ~ 8800 Pa (l=10 mm)	-	-
57	-	-	~ 20,000 Pa (l=4 mm)
63	-	~ 2600 Pa (l=10 mm)	~ 133,000 Pa (l=4 mm) ~ 48,000 Pa (l=3 mm) ~ 2600 Pa (l=3 mm)

Priming of HA Hydrogel-Modified Tubes versus Ahmed Glaucoma Valve (AGV)

Comparing the priming pressures of AGV with our implant, it was observed that our values for the hydrogel valves were much more below these. For example, Cheng et al. published some data with priming pressures ranging between 2844-3154 mmHg (~380,000–420,000 Pa) [246]. In other studies, the priming values for AGV ranged between 835-1625 mmHg (~111,000–216,000 Pa) [249]. In this thesis the highest priming/activation pressure was measured at 133,000 Pa for the hydrogel with TG=63 % and 4arm-PEG-ACLT (see table 6).

In conclusion, the priming pressures for AGV (835–3154 mmHg) exhibited considerable variability, and the fact that priming was performed manually by the surgeon indicated that the values were also operator-dependent. This suggested, that in clinical practice, the exact value or reproducibility of priming was less important. Instead, the focus was primarily on the activation/priming of the implant itself, rather than on achieving specific pressure values.

As previously discussed, the activation values for our HA hydrogel-modified implants also demonstrated significant variability, which was mainly attributed to the error prone channel formation inside the hydrogel (see section 4.2.3).

Another explanation was a too fast application of too intense pressure that was exerted on the hydrogel, causing the channel to rupture and damaging the valve function which resulted in different activation pressure values or damaged model implants.
For the Ahmed valve the excessive force during priming higher than the priming pressure, was termed 'overpriming' [246], leading potentially to a damage of the valve functionality. Whereby, in studies by Cheng et al. no damage was reported for pressure levels >3 times higher the priming pressure, for the mechanical valve of a AGV [246]. Nevertheless, overpriming was recommended to avoid [250, 251].
In regard of a hydrogel as valve, the matter was clearly different, since our valve was much softer and more fragile and furthermore no literature data was available on the maximum pressure resistance of hydrogels and their use as pressure sensitive valves. Our results showed that much more examinations were necessary and moreover an optimization of model implant preparation and priming measurements was required.
However, some functioning tubes could be selected and used for further experiments, in order to establish pressure measurements more similar to the real situation in the human eye. These measurements were summarized in the following.

4.4.2 Equilibrium Pressures at Conventional Flowrates

In the healthy human eye, there is a constant inflow and outflow of aqueous humor, whereby aqueous humor production occurs at a rate of 2 to 3 µl/min [252, 253]. Insofar, an intraocular device should be able to create steady-state pressures at this rate, which are known to be present in the healthy human eye, ranging from 10 mmHg to 21 mmHg (~1300 Pa to ~2800 Pa).
In order to investigate the pressure regulation abilities of HA hydrogel modified glass model tubes at conventional flowrates, a flowrate of 2.5 µl/min was set and the pressure was measured until an equilibrium state was reached and maintained over a certain period of time. Thereby, the equilibrium pressure value was determined by calculating the average value over the duration of the measurement with the standard deviation, once the desired flowrate of 2.5 µl/min was reached.

In the following, the flowrate and equilibrium pressure measurements of small glass model tubes of different lengths (ID=0.5 mm and l=6, 5, 4 and 3 mm) with a hydrogel composition of HA44-1/MBAA were summarized (figure 51, figure 52 and figure 53), that were previously 'activated' in figure 49 (section 4.4.1). In order to investigate the reproducibility of each tube, the measurement was repeated three times at different days after preparation: m_1=1 d, m_2=2 d, m_3=14 d (figure 52 and figure 53). Additionally a fourth measurement of the tubes (m_4) was conducted as a long-term experiment over 22 hours (figure 54). After each measurement, the tubes were disconnected from the setup and stored in PBS, pH 7.4 until the next measurement. No additional activation was required prior to the measurements, as all tubes only needed a single activation at the initial stage.
For all samples and measurements, the data showed, by starting the measurement, the pressure increased until the set flowrate of 2.5 µl/min was reached. This first phase after activation was

termed 'transient phase' of the hydrogel and was also observed for AGV implants [249]. Whereby, for AGV the transient phases ranged between 3.05 to 12.56 h, with high pressure fluctuations within this phase [249], for our implants these phases were only a few minutes (5-10 min) and without high variations in pressure or flowrate.

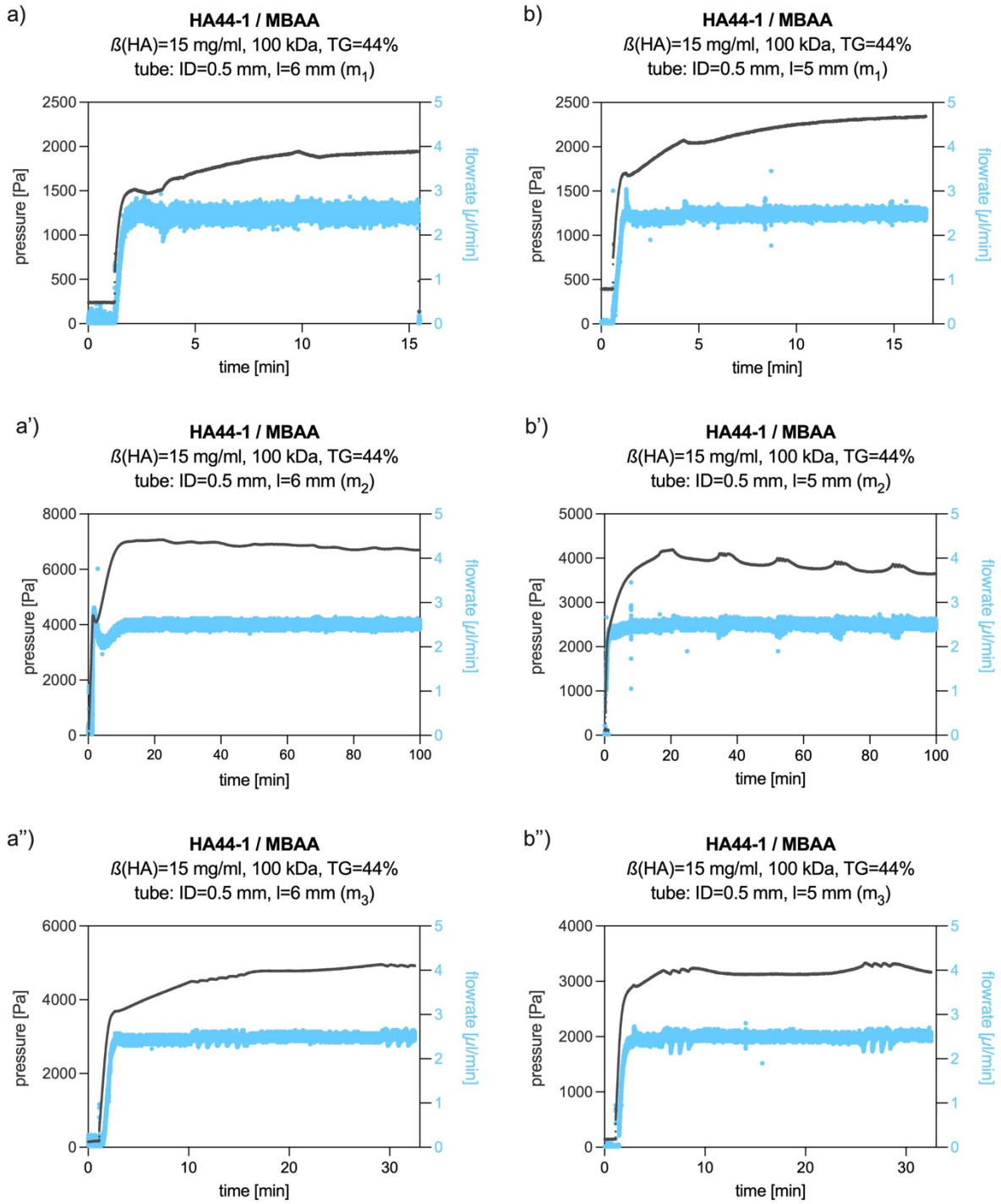

Figure 52: Equilibrium pressure measurements of small HA hydrogel modified tubes (ID=0.5 mm, l=6 and 5 mm) with HA44-1 and MBAA (*β*(HA)=15 mg/ml, 100 kDa, TG=44 %) at a set flowrate of 2.5 µl/min and with multiple repeats at different days (m_1= 1 d, m_2=2 d and m_3=14 d). The tube with l=6 mm resulted in steady-state pressures of m_1=1806±149 Pa (a), m_2=6760±479 Pa (a') and m_3=4601±345 Pa (a"). The tube with l=5 mm showing equilibrium pressures of m_1=2157± 178 Pa (a), m_2=3839±155 Pa (a') and m_3=3172±80 Pa (a"). Pressure increased until the set flowrate of 2.5 µl/min was reached and remained constant over the measurement or adapted to maintain the flowrate. In the graphs, the pressure was illustrated by the dark grey curve, the blue curve represented the flowrate.

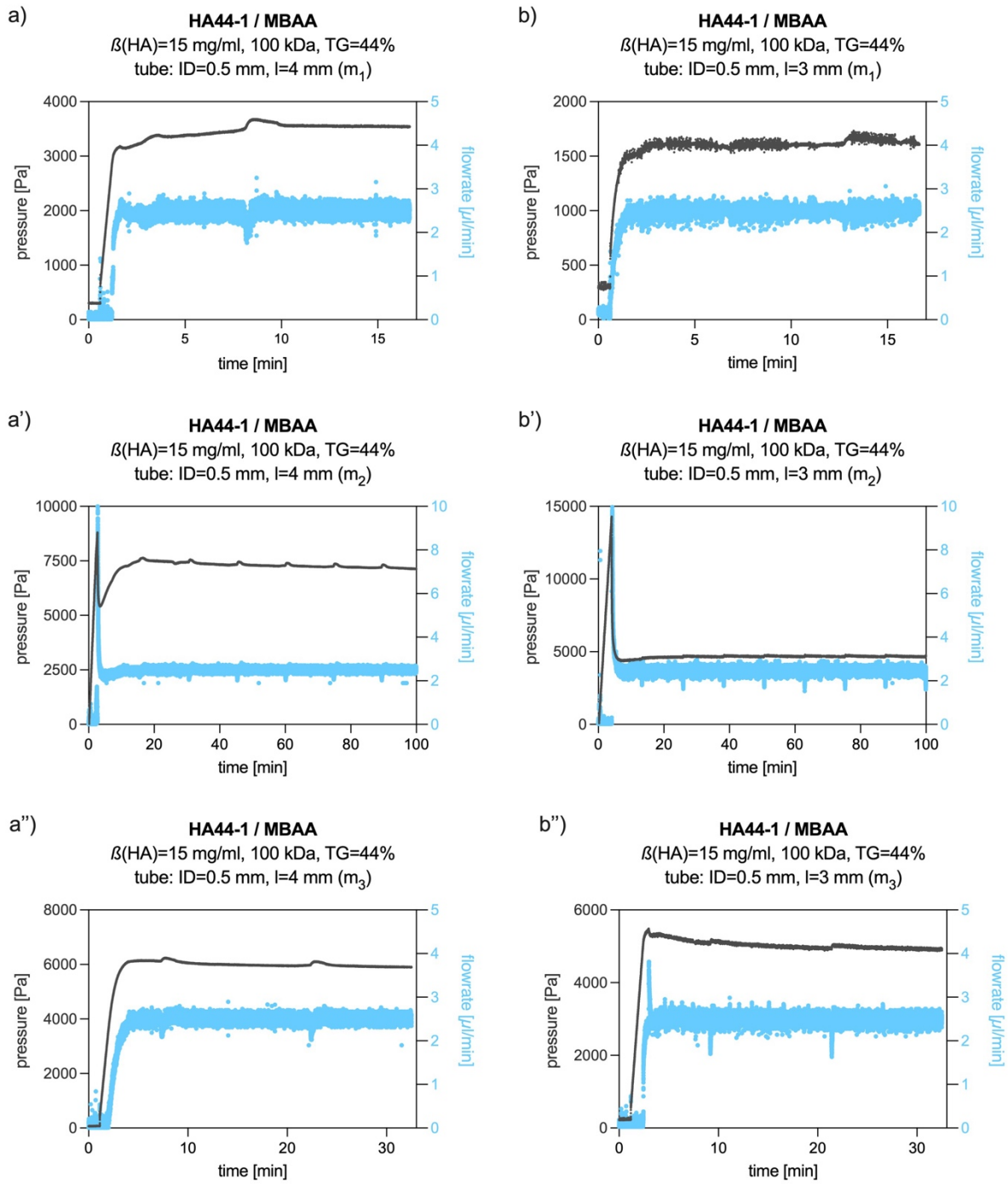

Figure 53: Equilibrium pressure measurements of small HA hydrogel modified tubes (ID=0.5 mm, l=4 and 3 mm) with HA44-1 and MBAA (*β*(HA)=15 mg/ml, 100 kDa, TG=44 %) at a set flowrate of 2.5 µl/min and with multiple repeats at different days (m_1= 1 d, m_2=2 d and m_3=14 d). Equilibrium pressures of tube with l=4 mm: m_1 =3477±125 Pa (a), m_2=7288±121 Pa (a') and m_3=6006±82 Pa (a"); For tube with l=3 mm the following steady-state pressures were determined: m_1=1610±34 Pa (a), m_2=4655±68 Pa (a') and m_3=5033±109 Pa (a"). Pressure increased until set flowrate of 2.5 µl/min was reached and remained constant over the measurement or adapted to maintain the flowrate. In the graphs, the pressure was illustrated by the dark grey curve, the blue curve represented the flowrate.

In the subsequent phase the pressure became quite constant over the measurement or adapted to maintain the value of 2.5 µl/min. This second phase was termed equilibrium phase or stable phase. The results of the long-term measurements showed, even over a longer time period, the steady-state pressures remained quite constant. In regard of the measured flowrates, it was

observed that the fluctuations increased with decreasing tube sizes, but overall, the fluctuations were still in the conventional range of a healthy human eye between 2 to 3 µl/min.

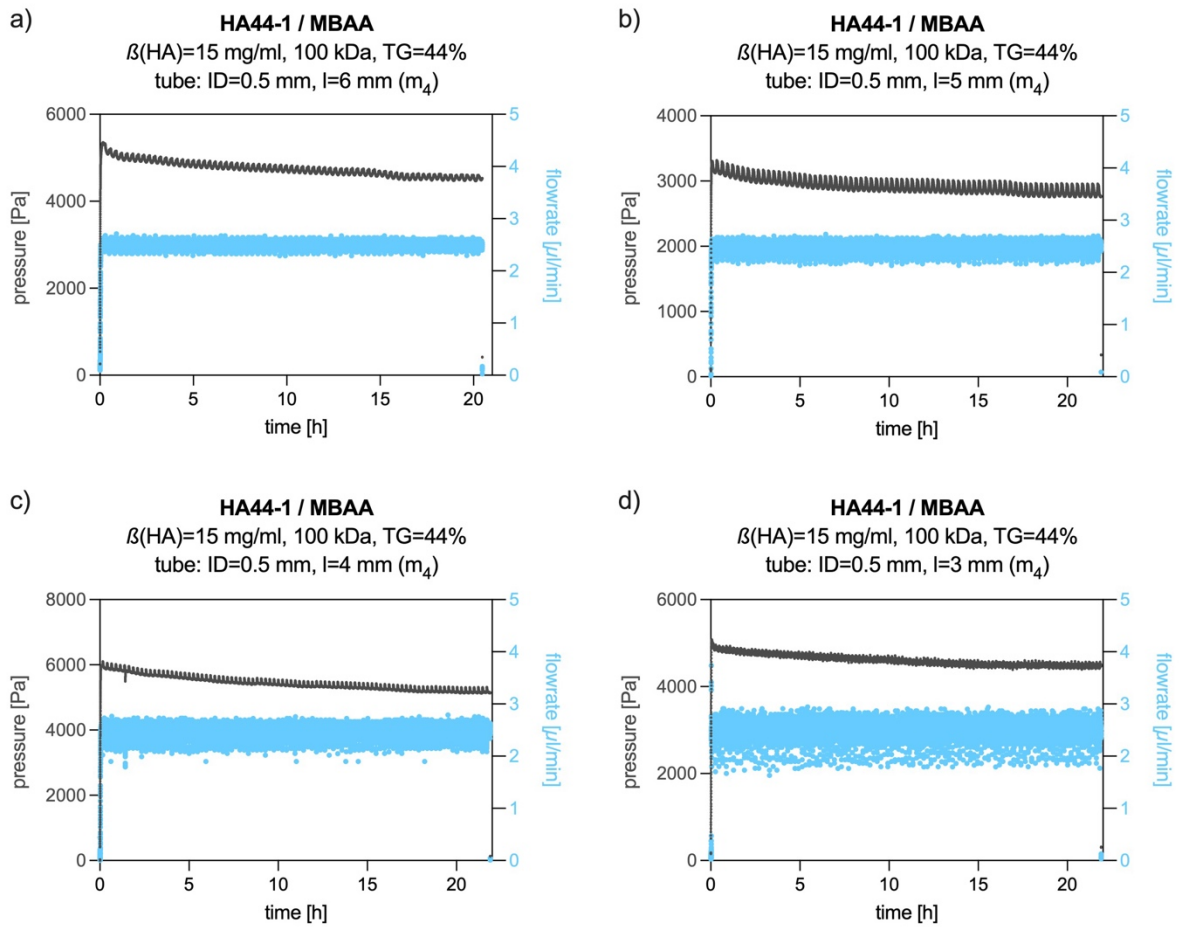

Figure 54: Long-term measurements for the determination of equilibrium pressures of small HA hydrogel modified tubes (ID=0.5 mm, l=6, 5, 4 and 3 mm) with HA44-1 and MBAA (*β*(HA)=15 mg/ml, 100 kDa, TG=44 %) at a set flowrate of 2.5 µl/min measured 14 days after preparation (m_4). The following steady-state pressures were determined: m_4=4746± 172 Pa for the tube with l=6 mm (a), m_4=2926±110 Pa for the tube with l=5 mm (b), m_4=5429±213 Pa for the tube with l=4 mm (c) and m_4=4606±122 Pa for the tube with l=3 mm. Tubes were measured over 22 h and average pressure values were determined with the standard deviation as error bar. In the graphs the pressure was illustrated by the dark grey curve; the blue curve represented the flowrate.

For a better overview, all determined steady state pressures shown in figure 52, 53 and 54 were summarized in figure 55. The data showed, for all tubes the first measurement (m_1) resulted in a lower equilibrium pressure compared to the following measurements (m_2, m_3 and m_4).

For the first measurements (m_1) one day after preparation of the model tubes most pressure values were in a similar range of the healthy human eye: 1806 ±149 Pa for the tube with l=6 mm, 2157±178 Pa for the tube with l=5 mm and 1610±34 Pa for the tube with l=3 mm. Only for the tube with l=4 mm the pressure was higher - compared to the other tubes - at 3477±125 Pa.

For the second measurement (m_2) at day two the equilibrium pressure of each tube was much higher and above the normal pressure, ranging from ~3800 to ~7300 Pa. The significantly higher steady-state pressures were attributed to insufficient hydrogel swelling at the first measurement after 24 hours compared to the second measurement at day three. Further swelling caused an

expansion of volume of the hydrogel network and a higher pressure resistance, which led to higher equilibrium pressures.

Measurements of the small glass model tubes after 14 days (m_3 and m_4) showed a decrease of determined steady-state pressures for the tubes with l=6, 5 and 4 mm; for the tube with l=3 mm the values for m_3 and m_4 were in a quite similar range to the measurement m_2.

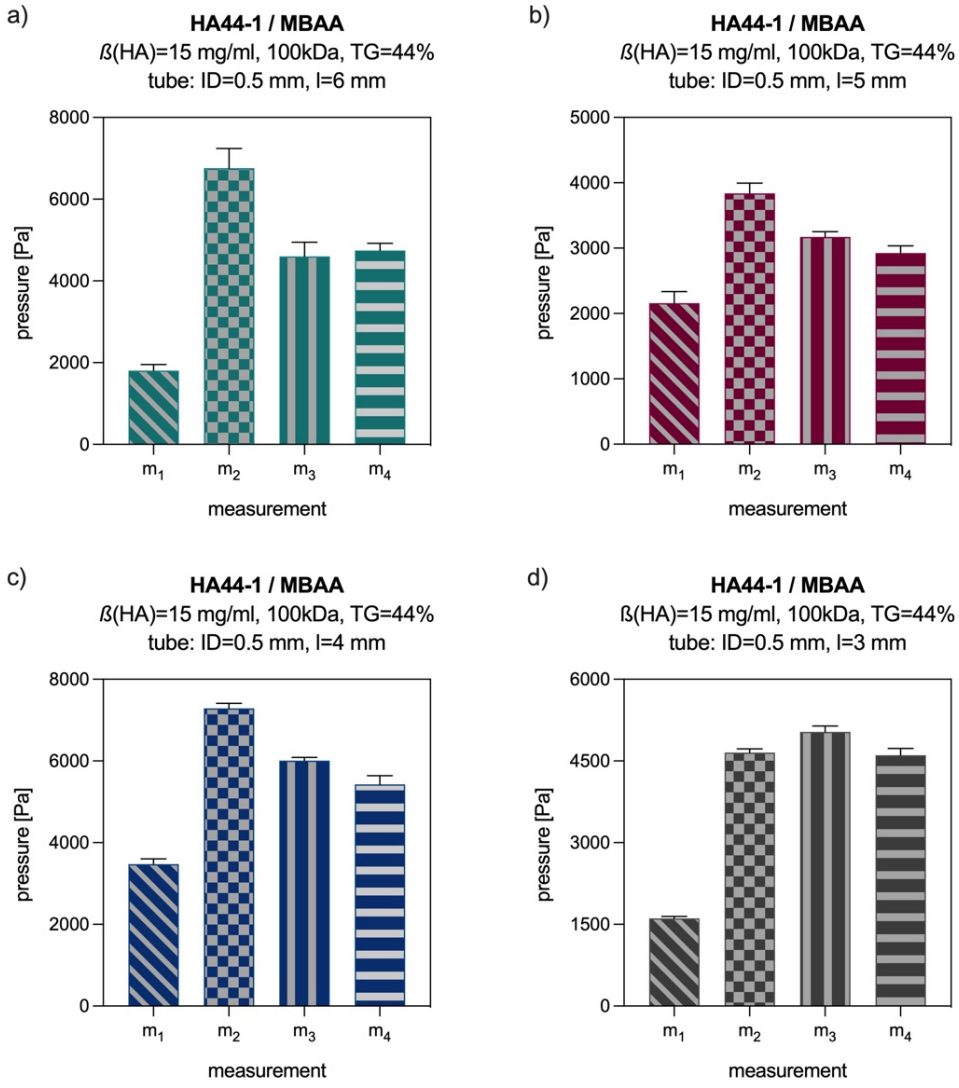

Figure 55: Overview of determined equilibrium pressures from repeated measurements (m_1, m_2, m_3 and m_4) of small HA hydrogel modified tubes (ID=0.5 mm, l=6, 5, 4 and 3 mm) with HA44-1 and MBAA (*β*(HA)=15 mg/ml, 100 kDa, TG=44 %) at a set flowrate of 2.5 µl/min. Same tubes were measured four times at different days (m_1, m_2, m_3, m_4). Average equilibrium pressure values were determined with the standard deviation as error bar. Corresponding measurements are shown in figure 51, 52 and 53.

For all tubes, both measurements after 14 days showed similar equilibrium pressures at a flowrate of 2.5 µl/min: 4601±345 Pa (m_3) and 4746±172 Pa (m_4) for the tube with l=6 mm, 3172±80 Pa (m_3) and 2926±110 Pa (m_4) for the tube with l=5 mm, 6006±82 Pa (m_3) and 5429±213 Pa (m_4) for the tube with l=4 mm and 5033±109 Pa (m_3) and 4606±122 Pa (m_4) for the tube with l=3 mm.

Clearly, the determined average values the equilibrium pressures were above the normal IOP, but the measurements showed a reliable pressure resistance ability with only minor standard deviations.

Additional equilibrium pressure measurements with other hydrogel compositions using the multifunctional PEG crosslinker 4arm-PEG-VS were compiled in the appendix (see section 6.5.1). For all HA/PEG modified tubes, the measurements followed a similar pattern to those presented in this section: the pressure increased until the target flowrate of 2.5 µl/min was reached and subsequently maintained or adjusted during the measurement. However, the steady-state pressure values for HA/PEG compositions also exceeded normal IOP levels.

Flow Characteristics and Valve Mechanism of HA Hydrogel-Modified Tubes versus Ahmed Glaucoma Valve (AGV)

Previous studies by Bochmann et al. showed very high pressure variation and failure rate of currently valved implants as the AGV [254]. After priming, they performed measurements determining opening, closing and re-opening pressures of AGV prior to implantation [254]. The examination of 30 implants revealed opening pressures of 5-30 mmHg (~666–4000 Pa), closing pressures of 3-18 mmHg (~400–2400 Pa) and re-opening pressures of 4-20 mmHg (~533-2666 Pa) [254]. When considering that the normal IOP was a value between 10-21 mmHg, some of these devices were in the area of hypotony (values <5 mmHg). This was also evident after implantation of these 30 devices, since 10 patients received early postoperative hypotony with values between 1-6 mmHg (~133–800 Pa) and with complications as choroidal effusion or shallow anterior chamber which required further management [254].
Further studies with AGV reported the same high variations in opening [248] and closing pressures [248, 255, 256]. Flowrate determinations were not included in these studies [248, 254-256], it was only observed when or at what pressure a liquid flow was visible (opening pressure) and when it stopped again (closing pressure).

Different to the studies mentioned above, Choudhari et al. included a constant flowrate measurement to test the AGV [249] similar to our setup. After priming, they infused a saline solution into the AGV with a rate of 3 µl/min over 24 h and the pressure was determined [249].
Thereby, the results of the steady phase revealed a big difference to our hydrogel-modified GDD. For our implant we recorded a constant flowrate of aqueous and also a constant pressure during the course of the measurements, without fluctuations. Similar to the natural ocular outflow system the fluid was continuously drained with a rate of 2-3 µl/min.
In contrast, the valve mechanism of AGV implicated a permanent opening and closing of the valve when the pressure exceeded a certain threshold or when the pressure dropped below a critical level [249]. The opening pressures for AGV ranged between 10 to 17 mmHg and closing pressures were between 4 to 9 mmHg, with a duration of opening/closing cycles of 51.05-76.67 min [249]. Pressure fluctuations in the steady phase were reported between 3 to 9 mmHg for AGV.
In summation, the AGVs effectively and rapidly reduced elevated IOP; however, the permanent opening and closing mechanism of the valves also resulted in sustained pressure fluctuations of up to 9 mmHg. Such high and repeated IOP fluctuations were known risk factors for glaucoma progression, since they increased the risk of biomechanical stress and optic nerve damage [257-

260]. In the following section our hydrogel-modified implants were investigated for their ability to regulate the flowrate under pressure fluctuations.

4.4.3 Fluid Flow during Pressure Fluctuations

Influenced by different factors, as the circadian variation of aqueous humor production or the position of the person, the IOP is known to vary between 2-6 mmHg (~266 to ~800 Pa) in one eye over the day [22, 24] (see section 1.1.2). These pressure fluctuations also had to be taken into account, when testing a new intraocular implant for glaucoma treatment.
Exemplary sine pressure measurements with HA44-1/MBAA are summarized in figure 56.

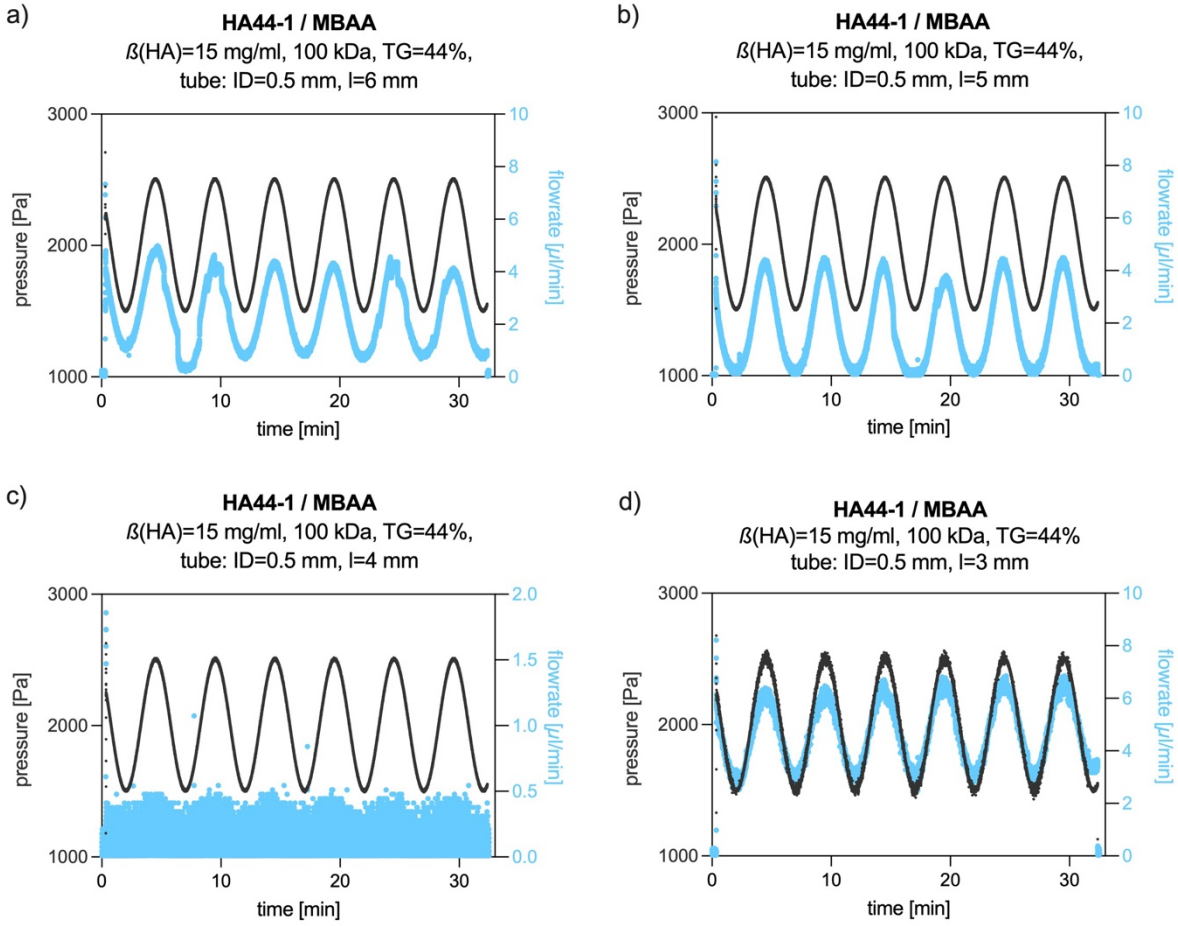

Figure 56: Measurements of fluid flow during pressure fluctuations (a-d). Small hydrogel modified tubes with ID=0.5 mm and different lengths (l=6, 5, 4 and 3 mm) with HA44-1 and MBAA (*β*(HA=)15 mg/ml, 100 kDa, TG=44 %) were measured in a pressure sine mode, whereby pressure was fluctuated in a pressure range of 1500 to 2500 Pa in a time interval of 300 s. Fluid flow for tube with l=6 mm was between 0.5–5 µl/min (a), for tube with l=5 mm fluid flow was 0–4 µl/min (b) and for tube with l=3 mm flowrate was ~3–8 µl/min (d). Almost no fluid flow was detected for the tube with l=4 mm (c). Dark grey curve in the figure displayed the applied pressure, the blue curve showing the measured flowrate.

In this example small HA-modified tubes (ID=0.5 mm and l=6, 5, 4 and 3 mm) with a hydrogel composition of HA44-1/MBAA were shown, that were previously activated in figure 50 (section 4.4.1) and used for the determination of equilibrium pressure at a conventional flowrate in section 4.4.2.

For the measurement a pressure range of the normal human eye (between 1500 to 2500 Pa) was chosen and applied to the HA modified tube in a sine mode, and flowrates were recorded during the course of the measurements.
The data showed that the flowrates followed the applied pressure in the same way as it was increased and decreased. For the tube with l=6 the flowrate was ~0.5–5 µl/min (figure 55a), for l=5 mm the flowrate was quite similar around ~0–4 µl/min (figure 55b) and for the tube with l=3 mm the flowrate was ~3–8 µl/min (figure 55d). For the tube with l=4 mm almost no fluid flow was detected and was around 0.5 µl/min (figure 55c).

In figure 57 further sine measurements with HA28/MBAA were compiled, showing that the tubes were also able to adapt to different time intervals of pressure sine application:

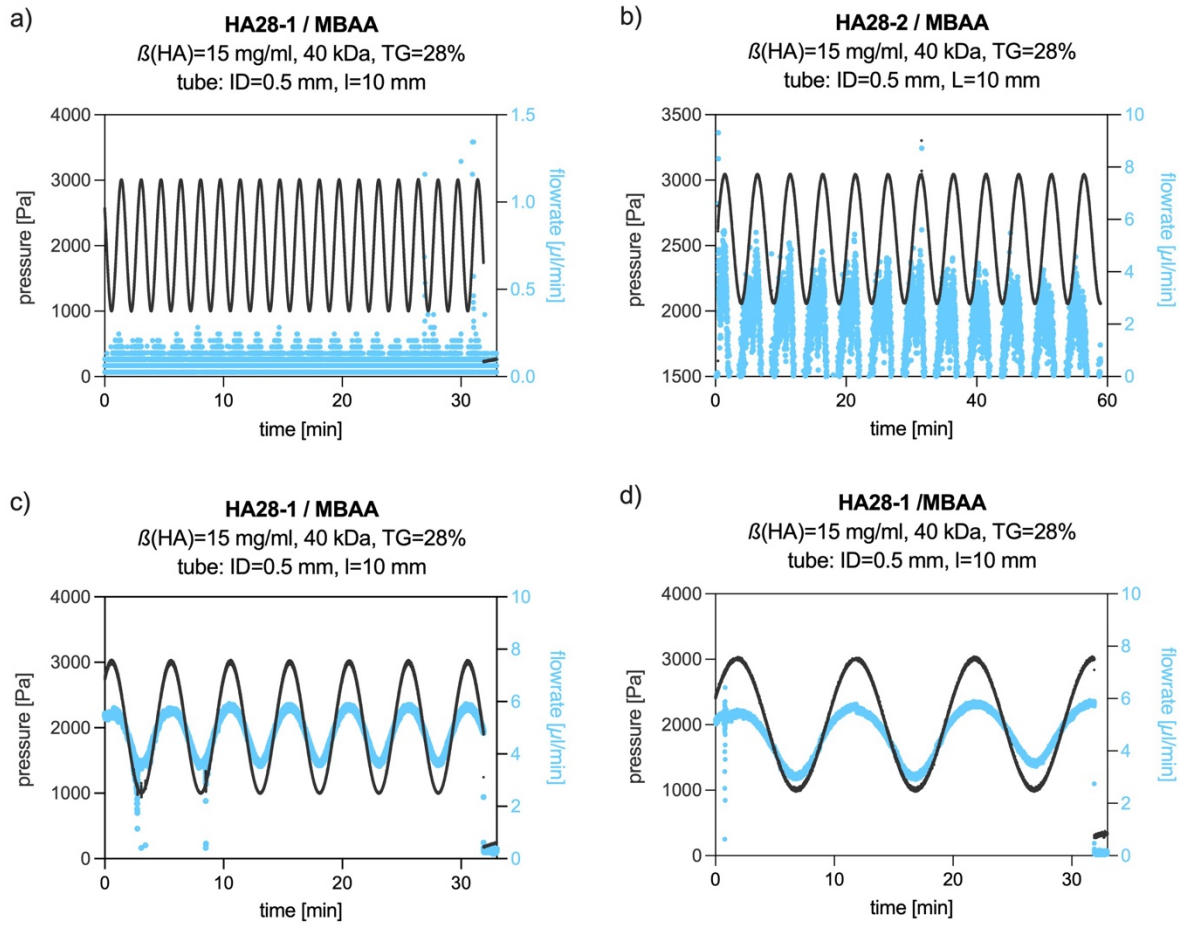

Figure 57: Measurements of fluid flow during pressure fluctuations in different time intervals (a-d). Small hydrogel modified tubes with ID=0.5 mm and l=10 mm with HA44-1/MBAA (*β*(HA=)15 mg/ml, 100 kDa, TG=44 %) were measured in a pressure sine mode, whereby pressure was fluctuated in a pressure range of 1000 to 3000 Pa in a time interval of 100 s (a), 200 s (b), 300 s (c) and 500 s (d). For each tube, fluid flow adapted to the applied pressure and increased with longer time interval: for 100 s the flowrate was 0-0.2 µl/min, for 200 s the rate was 0-4 µl/min, and for 300 s and 500 s the flowrate was between 3-6 µl/min. Dark grey curve in the figure displayed the applied pressure, the blue curve showing the measured flowrate.

Long-term sine measurements demonstrated, that the hydrogel-modified tubes were also capable of functioning effectively over extended time periods (see appendix, section 6.5.2). Further

examples with other hydrogel compositions (HA/4arm-PEG-VS) are also presented in the appendix (section 6.5.2).

Our results showed, that the flowrate was proportional to the applied pressure, and our HA hydrogel-modified tubes successfully adapted to varying pressures and time intervals, and most measured flowrates ranged in the same area as normal flowrates in the human eye.

However, it was important to note that pressure fluctuations in the normal human eye do normally not occur as rapidly as those depicted here or in the appendix. Nevertheless, in exceptional situations, such as during a bungee jump, these properties of the model implants are especially crucial for withstanding rapid pressure increases.

In the next, the measurement parameters were adjusted to a more realistic day life mode, as presented in the following.

Real-life Pressure Sine Measurements of HA Hydrogel-Modified Tubes

Previous studies of IOP measurements showed, that pressure fluctuations in the human eye over a 24-hour period followed a sinusoidal curve [24], as schematically illustrated in figure 58:

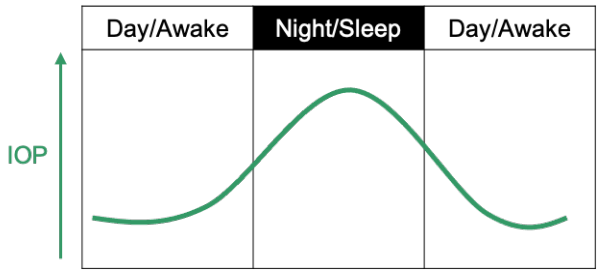

Figure 58: Schematic drawing of a 24-hour pattern of IOP. The picture was adapted from Liu et al. [24] and simplified.

The IOP measurements of different persons in different positions revealed a significant 24-hour rhythm: the peak IOP occured during the night/sleep period, when the person was supine; in the day/awake period the IOP declined due to the upright positions of the person [24]. In addition to body position, circadian variations in aqueous humor production were also known to influence the IOP, with production being twice as high during the day as at night. One would have expected, that the slowdown of aqueous humor production would theoretically decrease the IOP but in reality this reduction was insufficient to counterbalance the IOP elevation caused by the supine position during the night/sleep period. [22]

To test the small glass model implants from the previous sections (ID=0.5 mm and l=6, 5, 4 and 3 mm with HA44-1/MBAA), the measurement was adapted to this real-life 24-hour rhythm (figure 59). The pressure sine was fluctuated in pressure ranges of 1500–2500 Pa (figure 59a and 59b), 2500–3500 Pa (figure 58c) and 1000–2000 Pa (figure 59d) in a time interval of 24 hours and the flowrates were recorded.

The measurements again showed, the HA modified tubes adapted to the applied pressure in the same way as it was increased and decreased. The measured flowrates were for most tubes in a

higher range than the normal aqueous humor flowrate: for the tube with l=6 mm the flowrate was between 0-8 µl/min (figure 59a), for the tube with l=5 mm the flowrate was 0-5 µl/min (figure 59b) and for l=3 mm the values ranging from 1-7.5 µl/min (figure 59d). Only for the tube with l=4 mm the flowrate was lower at 0-1.5 µl/min (figure 59c), and here the pressure range was higher compared to the other tubes. Nevertheless, the values were in a similar size range, and increases were only marginal.

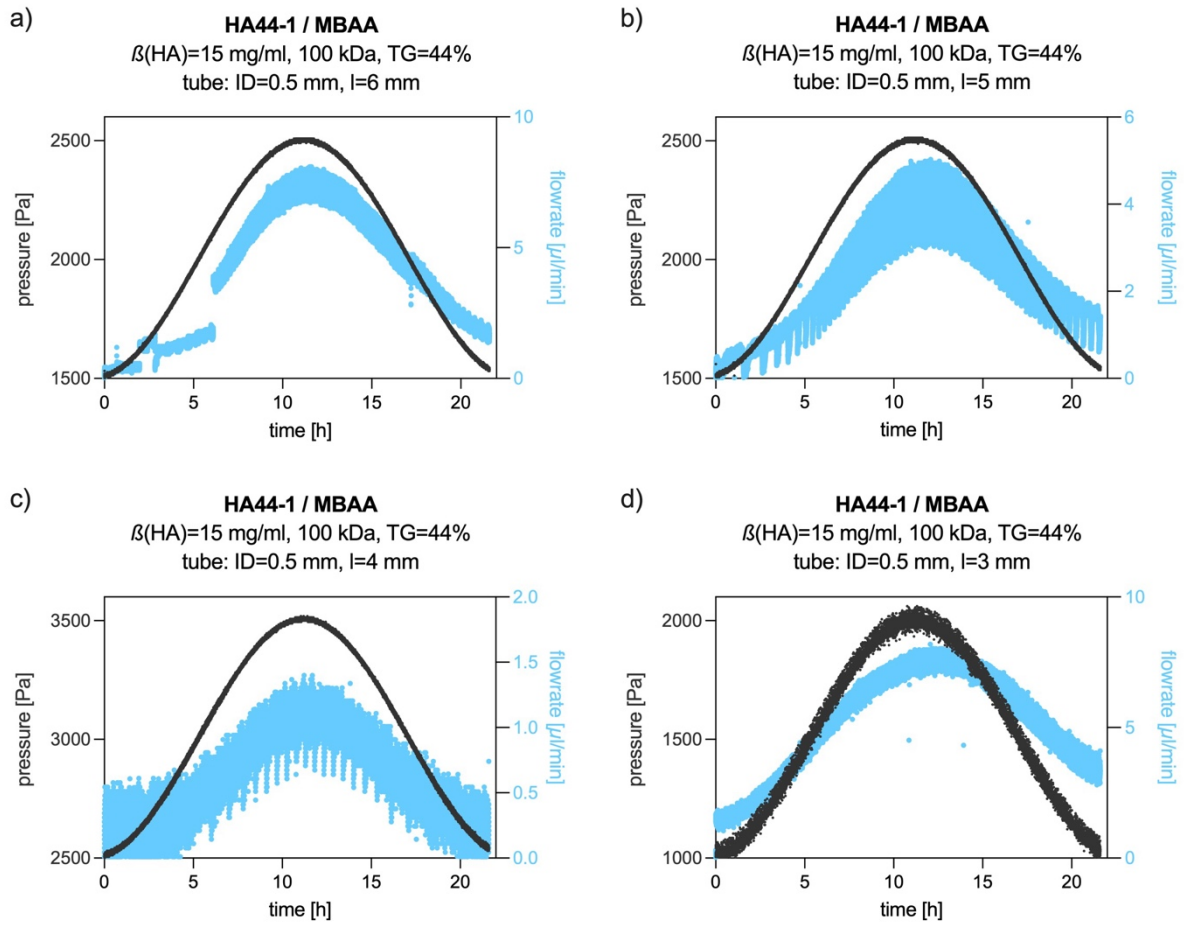

Figure 59: Long-term real-life measurements of fluid flow during pressure fluctuation of small hydrogel modified tubes of ID=0.5 mm and different lengths (l=6, 5, 4 and 3 mm) with HA44-1/MBAA (*β*(HA=)15 mg/ml, 100 kDa, TG=44 %). Tubes were measured in a pressure sine mode, whereby pressure was fluctuated in pressure ranges of 1500 to 2500 Pa (a, b), 2500 to 3500 Pa (c) and 1000 to 2000 Pa. Measured flowrate was at ~0–8 µl/min for the tube with l=6 mm (a), at ~0–5 µl/min for l= 5 mm (b), for the tube with l=4 mm, the flowrate was ~0–1.5 µl/min (c) and for l=3 mm the flowrate was ~0–10 µl/min (d). Dark grey curve in the figure displayed the applied pressure, the blue curve showing the measured flowrate.

4.5 3D-Printed Patterns for Improved Reproducibility

To enhance the reproducibility of glass model implant preparation, different 3D-models were designed using the software AutoCAD.

4.5.1 Design of 3D-Printed Patterns for Glass Model Tubes

In order to improve the channel formation during the preparation of glass model implants two different approaches were designed and investigated for glass model tubes with ID=3 mm and l=6 mm. The first idea based on a plate equipped with fibers and in-depths around these fibers for the exact positioning of the glass tubes (figure 60). Then the silanized glass tubes were filled with the hydrogel-crosslinker mixture and let polymerized in this setup. First experiments with this pattern were conducted and some difficulties became obvious. Although the glass tubes fitted well in the in-depths of the 3D model, the hydrogel filling leaked and the glass tube had to be sealed additionally at the bottom with two-component dental glue before filling, as shown in figure 60b. Another issue was the thickness of the fiber for pre-channeling, which was set at 0.5 mm due to the minimum size resolution of the 3D printer. By this, the channel that was created inside the hydrogel was too large to be closed by swelling and as a result the valve mechanism failed. A further problem was given by the manual removal of the glass model tubes from the pattern, so that small wiggles teared the gel additionally and, in the end, leading to differences of the hydrogel modified tubes. Insofar, another concept was necessary to improve the preparation and minimize the error due to manual insertion of the glass fiber into the hydrogel modified tube.

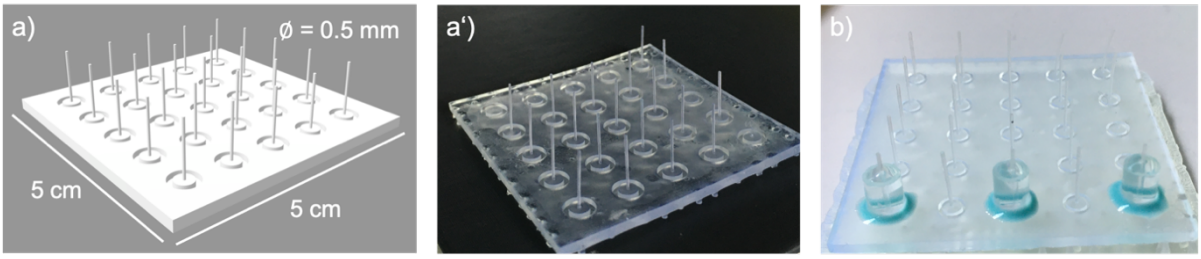

Figure 60: 3D-printed design and pattern for improved production of glass model tubes. AutoCAD design of fiber plate with in depths for exact positioning of the tubes (a) and resulted 3D print of the design (a'). Glass model tubes placed on pattern and filled with HA hydrogel and additionally fixed with two component dental glue (b). Material used for the print: ClearResin from formlabs.

A second 3D design for glass model tubes based on three plates, shown in figure 61. Plate a was designed as bottom closure for plate b, which contained hollow columns serving as tube holder for the glass model tubes. The setup was complemented by another plate c, designed with cylindric structures with a hole in the middle of it for the glass fiber, and placed on the top of plate b. The design of alle three plates stacked on top of each other was illustrated in figure 61d and the respective 3D printed plates in figure 61d' and d". However, the main problem was that the holes in plate c were not formed, due to the resolution limits of the 3D-printer and the CarbonResin material used. The parts were also difficult to put together, so again a new design was required.

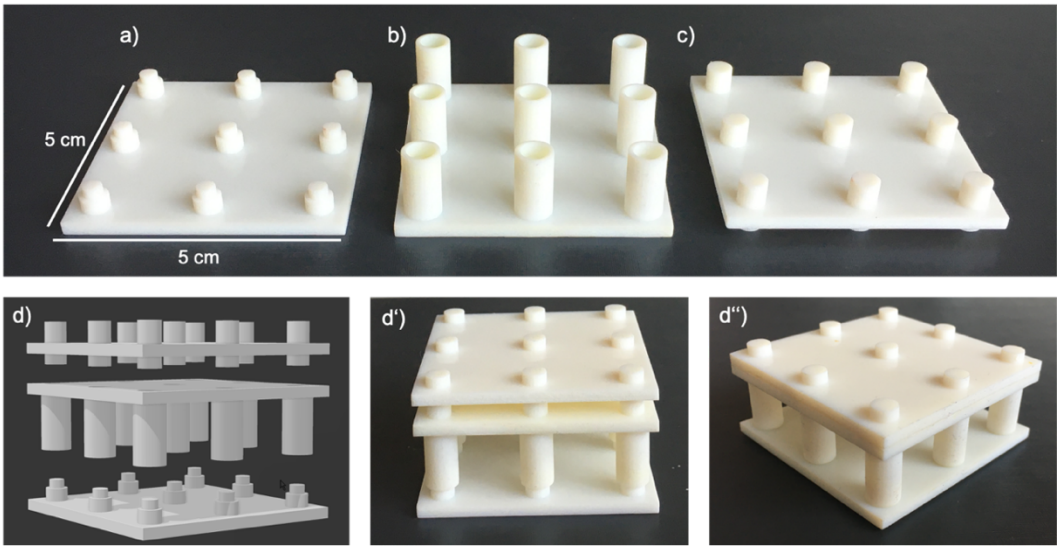

Figure 61: 3D-prints designed for reproducible glass model tube preparation. The concept based on three plates: Plate a) serving as bottom closure for plate b) which contained hollow columns as holder for the glass model tubes. Plate c) was designed with cylindric structures, containing a hole in the middle of it for exact insertion of the glass fiber for channel generation. AutoCAD designs of all three plates stacked on top of each other (d) and resulting 3D-prints put together (d' and d"). Material used for the prints: CarbonResin from formlabs.

As a last approach a simplified version of the 3-plate-pattern in figure 61 was designed and printed, using a 3D-printer with a higher resolution limit of 27 µm and a bisphenol-A (BPA)-based material. The pattern consisted of two plates that could be stuck together by the columns in plate A and the corresponding holes in plate B. In the middle of plate A the HA hydrogel-modified tube was placed and held in position by the two plates while the artificial channel was created (figure 62).
This last design worked quite well for the creation of artificial central channels in small glass model tubes with ID=2 and 3 mm and l=6 mm. Another advantage of this two-plate design was, that it could be used for different tube lengths, as the plates were pushed into each other until the tube was fixed. The prepared hydrogel-modified tubes were used for further pressure measurements to evaluate the reproducibility of pressure regulation, as summarized in the following.

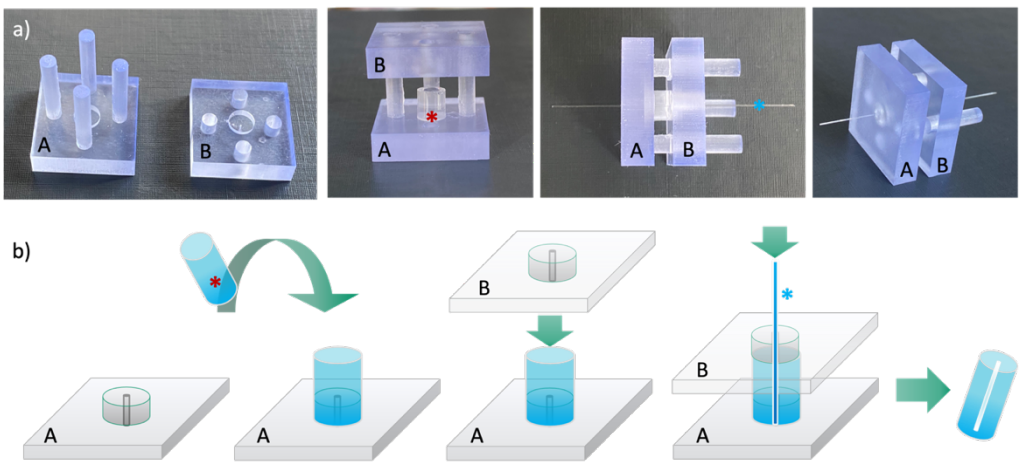

Figure 62: Printed 3D-pattern for artificial channel generation in hydrogel-modified glass model tubes. The concept was a simplified version of the design shown in figure 61, based on two plates that can be stuck together. Furthermore, each plate contains a small hole with 0.1 mm for the glass fiber. In the middle, the hydrogel-modified glass model tube (*) (ID=3 mm, l=6 mm) can be placed and held in position by the two plates. In a last step, the artificial channel can be introduced with the glass fiber (*) and the glass tube can be removed for pressure measurements.

4.6 Pressure Measurements with Improved Setup

In this section further pressure measurements were conducted on hydrogel compositions of HA51 crosslinked with ACLT-PEG-ACLT, 4arm-PEG-ACLT and 4arm-PEG-VS, using an enhanced measurement mode and an optimized implant preparation setup, which incorporates a 3D-printed pattern developed in section 4.5.1.

The HA-modified tubes (ID=1, 2 and 3 mm and l=6 mm) were prepared according to previously outlined protocols (refer to section 3.3). For tubes with ID=1 mm an artificial channel was generated manually as per the standard procedure (see section 3.3.3); in contrast, tubes with ID=2 and 3 mm utilized the 3D-printed pattern described in section 4.5.1 (figure 62).

Alongside optimizing the implant preparation process, the measurement setup for small hydrogel-modified tubes was also refined.

Unlike previous pressure measurements detailed in section 4.4.1, no activation pressure was assessed through the ramp mode on this occasion. Instead, the first measurement employed an equilibrium pressure measurement as shown in section 4.4.2, in which a constant flowrate of 2.5 µl/min was set and the measurement was conducted until a steady-state pressure was reached and maintained over a specific time period.

These methodological changes were introduced for two main reasons. First, in earlier experiments (see section 4.4.1) a large number of model tubes sustained damaged during the activation pressure measurements, likely due to hydrogel disruption caused by excessive force during ramp application. Second, prior equilibrium pressure measurements (refer to section 4.4.2) indicated that the measured pressure also followed a ramp until the channel opened and the desired flowrate of 2.5 µl/min was reached. Accordingly, an activation pressure was also expected with the equilibrium measurement, if this was carried out as the first measurement.

4.6.1 Flow Characteristics of Pressure Measurements at Conventional Flowrates

Exemplary pressure measurement results for different hydrogel compositions and tube dimensions were compiled in figure 63. For tubes with ID=3 mm no data was available since these measurements showed large fluctuations in pressure, therefore this tube dimension was discarded. As expected, the graphs showed a similar course of the pressure as observed in section 4.4.1for the activation of small glass model tubes measured with the ramp-mode. By starting the measurement the pressure increased until the pressure resistance of the hydrogel valve was overcome (activation pressure), and suddenly the resistance dropped to a lower pressure range and remained constant over the course of the measurement (equilibrium pressure).

However, the results also showed that for some samples the activation values exhibited again considerable variability as before (see section 4.4.1) and some equilibrium pressures were also in a higher pressure range than the normal IOP.

Nevertheless, with the optimizations outlined before the number of deficient model implants significantly decreased, but not all tubes performed as shown in figure 63. Differences in

performance were summarized separated for bi- and multifunctional crosslinked hydrogels in the following.

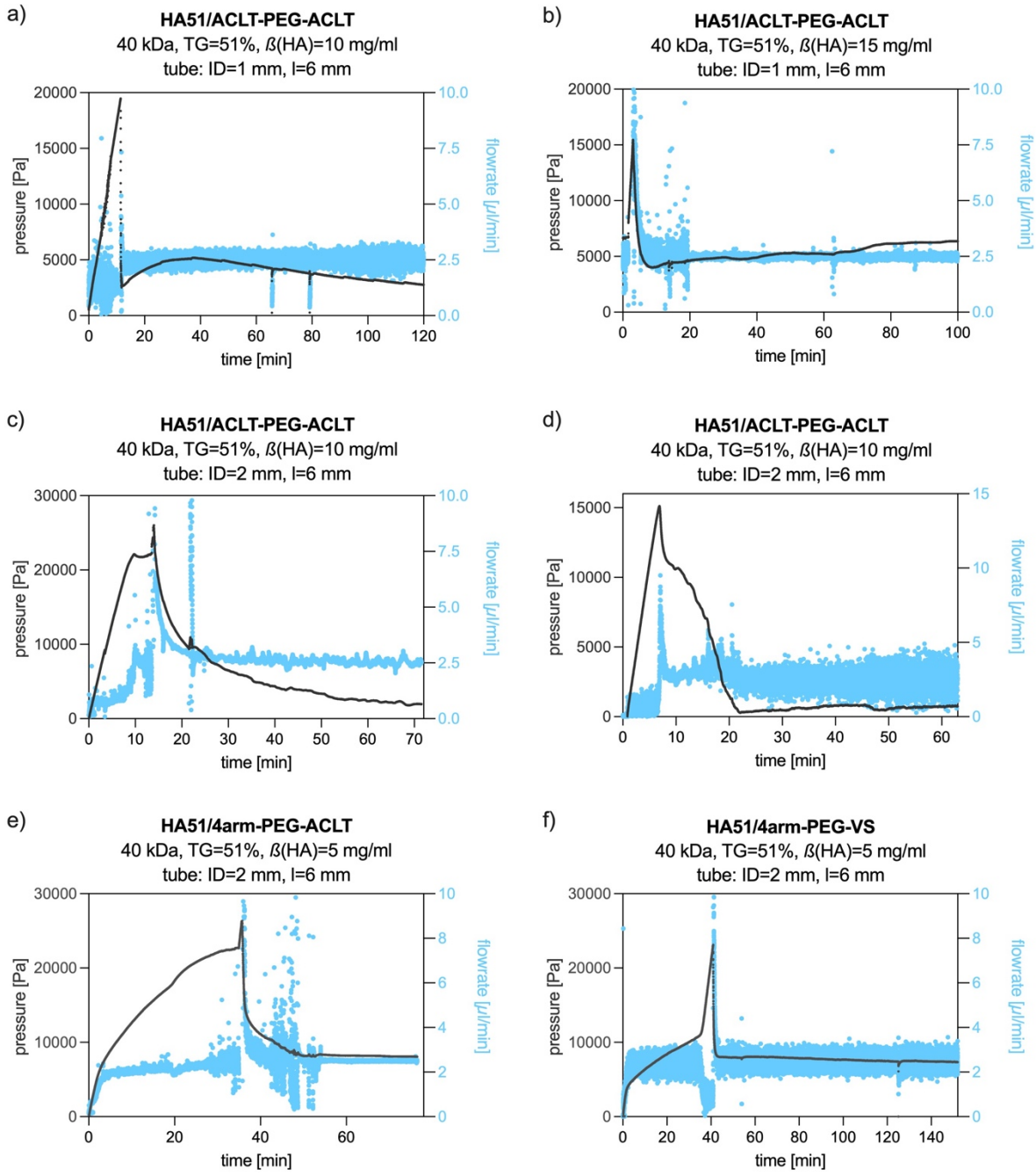

Figure 63: Exemplary pressure measurements of small glass model tubes with improved setup at a conventional flowrate of 2.5 µL/min. Small HA-modified glass model tubes (ID=1 and 2 mm, l=6 mm) were prepared with different hydrogel compositions as specified above and measured with the constant flowrate mode. For each measurement the results showed a gradual increase of pressure (activation pressure) which dropped to a lower pressure (equilibrium pressure) over the course of the measurement. For small glass model tubes with ID=1 mm the artificial channel was created manually, for the larger tubes with ID=2 mm the 3D-printed pattern from section 4.5.1 was used to generate an artificial channel. For hydrogels crosslinked with ACLT-PEG-ACLT and tubes with ID=1 mm the following pressure values were determined: activation pressure of 19468 Pa and equilibrium pressure of 3463±512 Pa for β(HA)=10 mg/ml (a) and activation pressure of 15466 Pa and equilibrium pressure of 6149±201 Pa for β(HA)=15 mg/ml (b). For tube ID=2 mm and β(HA)=10 mg/ml the values were at 25719 Pa (c) and 15472 Pa (d) for the activation and 2413±359 Pa (c) and 637±167 Pa (d) was determined for the equilibrium pressure. For multifunctional crosslinked hydrogels the values were at: 26330 Pa (activation) and 8186±73 Pa (equilibrium) for 4arm-PEG-ACLT (e); for 4arm-PEG-VS the values were at 23121 Pa (activation) and 7644±231 Pa (equilibrium) (f). Dark grey curve in the figure displayed the applied pressure, the blue curve showing the measured flowrate.

Pressure Regulation of Bifunctional-Crosslinked HA Hydrogels

For small HA hydrogel-modified tubes crosslinked with the bifunctional linker ACLT-PEG-ACLT different 'groups' of samples were identified. The first group performed as already outlined in figure 63, other samples in turn showed a different behaviour, as summarized in figure 64. The course of the measurement was similar as already shown for measurements with the constant flowrate mode in section 4.4.2: the pressure increased until the set flowrate of 2.5 µL/min was reached and afterwards remained quite constant or adapted to maintain the desired flowrate.

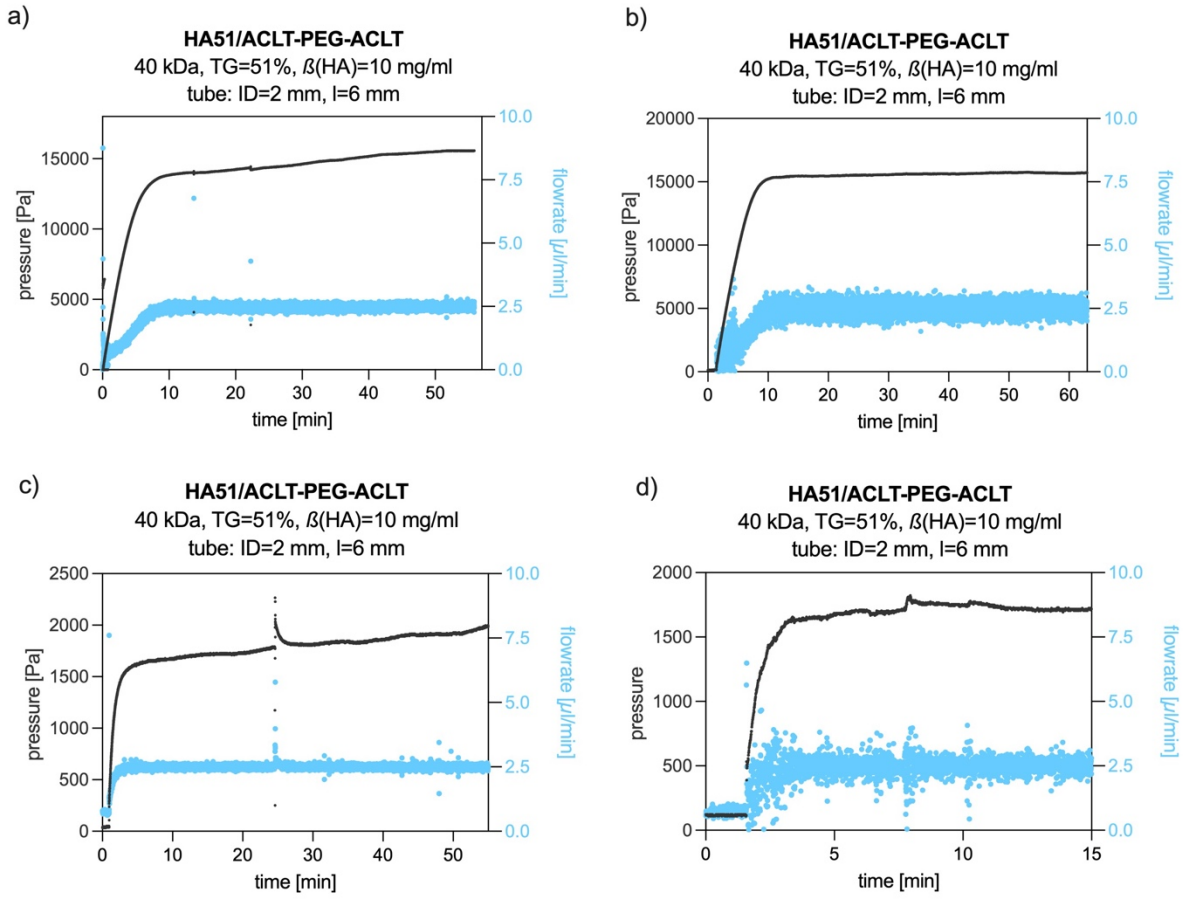

Figure 64: Exemplary pressure measurements of small glass model tubes (ID=2 mm and l=6 mm) modified with HA51/ACLT-PEG-ACLT (*β*(HA)=10 mg/ml) and measured with improved setup at a conventional flowrate of 2.5 µL/min. For each measurement the results showed a gradual increase of pressure until the desired flowrate of 2.5 µL/min was reached and remained constant over the course of the measurement. The values for the equilibrium pressures were classified in two different groups: One group of tubes showed a constant pressure value in the range of the activation pressure (a and b); the second group showed a steady-state pressure in the range of equilibrium pressure (c and d). The values for each measurement were: 14781±583 Pa (a), 15595±113 Pa (b), 1809±97 Pa (c), 1714±36 Pa (d). The tubes were measured with the constant flowrate mode using the microfluidic device from Elveflow. Dark grey curve in the figure displayed the applied pressure, the blue curve showing the measured flowrate.

Differences were observed in regard of different pressure value ranges, so that the samples were classified into two groups. One group of tubes performed in a pressure range similar to the activation pressure (figure 64a and 64b), the other group performed in lower pressure ranges, more similar to equilibrium pressure or normal IOP (figure 64c and 64d). Further results for ACLT-PEG-ACLT linked gels are compiled in the appendix (see section 2.4.3).

In the first case, it was assumed that the pressure was not yet sufficient to overcome the corresponding resistance, since pressures of up to 26,000 Pa were reached in other measurements, as shown in figure 63c for the same hydrogel composition. Therefore, a higher set flowrate of 3 or 4 µL/min could have eventually led to 'activation'. Another explanation was that the measurements were performed to short and the pressure peak would have been present in a later stage, as observed for 4arm-PEG-VS (figure 63f), where the pressure increased lately after 40 minutes in contrast to other measurements.
The second type of samples performed in a lower pressure range similar to normal IOP without 'activation' (figure 64c and 64d). This behaviour was observed before in previous studies for large hydrogel-filled tubes, which partly also performed without activation [147].

However, for each measurement again an equilibrium pressure value with the standard deviation as error was determined according to section 4.4.2 and the data was summarized in figure 65, separating the two groups of samples in 'activation' and 'equilibrium' pressure:

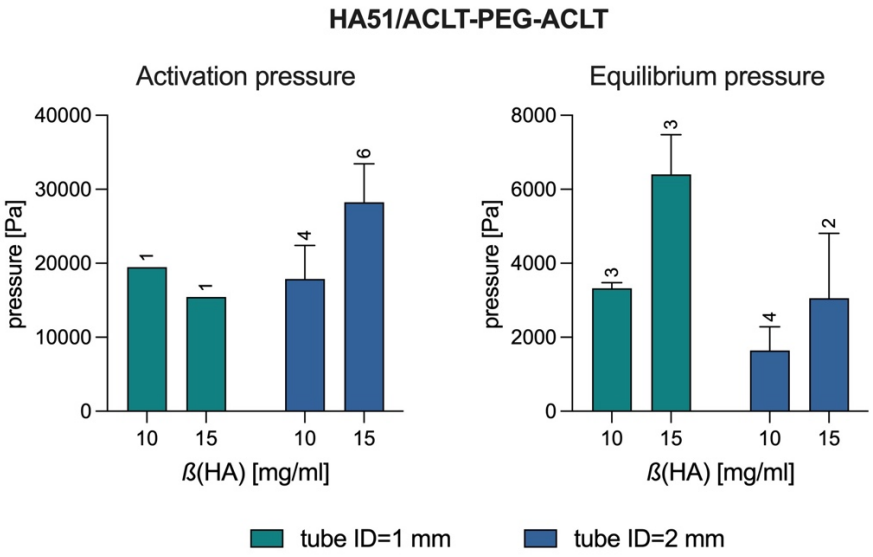

Figure 65: Overview of determined activation and equilibrium pressures from repeated measurements of small HA hydrogel modified tubes (ID=2 mm, l=6 mm) with HA51/ACLT-PEG-ACLT (*β*(HA)=10 and 15 mg/ml, 40 kDa, TG=51 %) at a set flowrate of 2.5 µl/min. Average equilibrium pressure values were determined with the standard deviation as error bar and above columns/error bars the sample size was specified. Corresponding measurements are shown in figure 63, 64, 45 and 46.

As expected, the results showed higher pressure values for higher mass concentrations of HA, explained by the increased crosslinking density which resulted in a higher retraction force of the gel and higher pressure resistance.
Furthermore, tubes with ID=1 mm resulted in a higher pressure resistance compared to tubes with ID=2 mm. Only for the 'activation pressure', the values for ID=1 mm were lower than for 2 mm, but this was attributed to the small sample size (n=1), which is of course not representative data, but was included for the sake of completeness as these values were shown in figure 63a and 63b. Clearly, here more measurements were necessary.

All other measurements showed a reliable pressure resistance ability with only minor standard deviations. The activation pressure values for all samples were similar to the results in section 4.4.1. Regarding the equilibrium pressure values, the results for ID=2 mm were in a similar range as the normal IOP, especially for β(HA)=10 mg/ml with 1643±640 Pa (n=4). However, these tube dimensions were clearly much too large for a potential GDD, which should be in range of 0.5-1 mm for inner diameter. Unfortunately, for tubes with ID=1 mm the equilibrium values were in a higher pressure range than normal IOP, necessitating further optimization in hydrogel composition.

Pressure Regulation of Multifunctional-Crosslinked HA Hydrogels

Multifunctional-crosslinked HA hydrogels showed much higher pressure resistance at a constant conventional flowrate, attributed to the higher crosslinking density of the polymer systems. The pressure values were all together similar to values obtained from activation pressure measurements in section 4.4.1. The graphs from the measurements were compiled in the appendix (see section 6.5.3), average pressure values were again summarized in a bar chart (figure 66), showing that multifunctional-crosslinked hydrogels were not suitable for their use a pressure-sensitive valves in a new type of GDD.

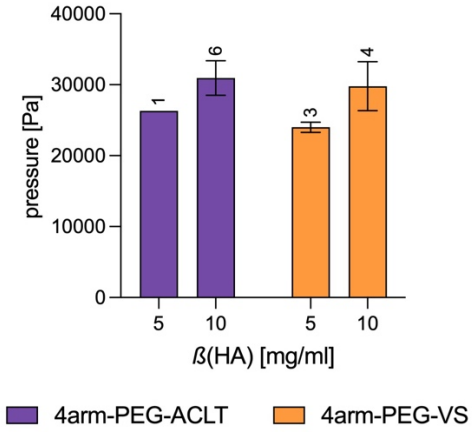

Figure 66: Overview of determined activation pressures from repeated measurements of small HA hydrogel modified tubes (ID=2 mm, l=6 mm) with HA51/4arm-PEG-ACLT and HA51/4arm-PEG-VS (β(HA)=10 and 15 mg/ml, 40 kDa, TG=51 %) at a set flowrate of 2.5 µl/min. Average equilibrium pressure values were determined with the standard deviation as error bar and above columns/error bars the sample size was specified. Corresponding measurements are shown in figure 48 and 49.

5 Summary and Outlook – Part I

5.1 Design of a Hyaluronan-based Glaucoma Drainage Device (GDD)

In the first part of this thesis a new type of glaucoma implant was developed and investigated, outgoing from previous studies of Michael Thaller. The main concept of this new GDD relies on a small titanium tube, modified on its interior with a hyaluronan hydrogel that tackles the main problems of current implants for controlling IOP. The primary function of the HA hydrogel is to act as a pressure-sensitive valve, draining excess fluid to reduce elevated IOP and closing at lower pressure to prevent hypotony, a common complication of current GDDs. Additionally, this hydrogel should possess cell repellant properties to prevent clogging due to cell growth.
Overall, the experimental parts and methods for implant development and exploration of its functionality are broad. They are ranging from chemical synthesis of starting compounds for implant creation, the assessment of different implant characteristic as hydrogel swelling and durability against enzymatic degradation and the development of miniaturized model implants and a new measurement setup to test the pressure regulation abilities under realistic conditions.
Clearly, much more research has to be conducted to complete the picture before a commercial product can be realized. Nevertheless, the results and findings in this work are promising and fundamental steps towards a new type of GDD, fulfilling the desired properties.

5.1.1 Synthesis and Analysis of Starting Materials

At first, all starting materials for the production of HA hydrogels for implant modification were successfully synthesized (refer to section 4.1), confirmed by the analysis of the compounds by NMR spectroscopy.
The corporation with the company Pharmpur (Königsbrunn, Germany), who adopted the synthesis of the compounds according to our methods, approved that they were all well-suited for industrial scale production. All methods are reproducible, the reactions are scalable and the chemical substances are cost-effective and minimal hazardous. Additionally, by modulating the reaction times, it is feasible to adjust thiolation levels, enabling the production of hydrogels with varying crosslinking densities and properties.
Another approach in this section was the determination of the TG of thiol-modified HA, using a more accurate and reliable analytical method than the photometric Ellman's assay, which in previous studies showed large deviations and error rates over 10 % [145, 147, 179].
In corporation with Pharmpur, the NMR spectroscopy was selected, due to its direct proportionality between signal areas and the number for H nuclei causing this signal, allowing for quantitative analysis by integrating signal areas in the NMR spectra (section 4.1.3).

In summation, the application of NMR spectroscopy provided a reliable and precise method for evaluating TGs in HS-HA products.
Moving forward, further optimization of sample preparation and measurement conditions could reduce potential errors, increasing the robustness of this method for large-scale analyses.

5.1.2 Preparation of HA-Modified Glass Model Implants

For the preparation of glass model implants a variety of different hydrogel compositions were explored to enhance the implant's performance by using HA of varying molecular weights (40 and 100 kDa), varying degrees of thiolation (28–63 %), and different mass concentrations (β(HA)=5, 10 and 15 mg/mL). Furthermore, various bi- and multifunctional crosslinkers were employed, including MBAA, ACLT-PEG-ACLT, 4arm-PEG-ACLT, and 4arm-PEG-VS.
For hydrogel compositions crosslinked with multifunctional PEGs and for high HA concentration (β(HA)=15 mg/ml) optimizations were necessary, since rapid gelation times rendered the preparation of small glass model implants (see section 4.2.1). The gelation kinetics were controlled and significantly slowed by reducing the buffer solution's pH from 8.5 to 7.4 and curing at room temperature instead of 37 °C.
Difficulties associated with the immobilization of HA/PEG hydrogel compositions on the inner surfaces of glass model tubes showed, that a new immobilization approach became necessary to address these challenges. Experiments using the silane MPS demonstrated its feasibility to immobilize HA/PEG hydrogels similarly to GPS and HA/MBAA hydrogels, but utilizing thiol groups rather than epoxide groups (see section 4.2.2).
As a last objective in this section, the large scale model setup developed by Thaller [145] was successfully miniaturized to a size comparable to a real GDD with inner diameters of 0.5–1 mm and lengths of 3–6 mm (refer to section 4.2.3).
However, it was outlined that Thallers concept for model implant preparation, specifically the channel formation using glass fibers, proved inadequate due to the very small diameters of the miniaturized model implants, which led to functional inconsistencies in the valve. Further refinement of the implant preparation process was necessary and was pursued in a later stage of this first experimental part as summarized in the following in section 5.3.

5.1.3 Characteristics of HA Hydrogel-Modified Implants

The integration of HA hydrogels into small model tubes imparts unique properties to the novel GDD, necessitating comprehensive characterization.
Therefore, two characterization methods were applied to assess HA hydrogel compositions, specifically targeting HA-modified tubes that mimic glaucoma implants.
For this HA hydrogels with HA51 crosslinked with ACLT-PEG-ACLT, 4arm-PEG-ACLT and 4arm-PEG-VS were investigated in different mass concentrations (β(HA)=5, 10 and 15 mg/ml) and for different tube dimensions (ID=1, 2 and 3 mm and l=6 mm).

In a first approach, basic swelling experiments were conducted comparing non-immobilized (macroscopic, free-swelling) and immobilized (constrained) HA hydrogels (section 4.3.1). From few previous studies it was already known and expected that, the swelling behaviour of immobilized and non-immobilized hydrogels is different [145, 147].
In regard for the use of hydrogels as pressure sensitive valves in the new type of glaucoma implant, the swelling behaviour is an important attribute and requires a precise characterization.
For this, the swelling studies of constrained hydrogels were expanded to include further parameters that were also relevant in regard of our new type of glaucoma implant, such as different polymer concentrations, that were used in this thesis, or tube dimensions that were in the range of a real GDD (ID=1, 2 and 3 mm, l=6 mm).
In summation, not only the TG [145, 147, 179], crosslinker [179], crosslinking densities and the surrounding medium [179] influenced the hydrogel swelling, but also the diameter of the tube made a difference which was an important finding for the design of our new glaucoma implant.
It was shown that smaller tube diameter (<2 mm), led to decreased swelling ratios as a result of the tubes' walls barrier. Thermodynamical effects (e.g. diffusion of TRIS molecules or smaller pore sizes of constrained gels), which played a role for large glass tubes can be neglected for smaller ones. However, an in-depth swelling examination will be necessary when the exact dimensions of the GDD were set and also the final gel composition was found.
A further objective was to explore the enzymatic degradation of various hydrogel compositions used in our new type of glaucoma implant (see section 4.3.2). The primary function of these hydrogels is to maintain valve functionality, draining excess fluid and thereby regulating IOP. Ensuring that the HA hydrogels remain stable and resist degradation is critical for long-term effectiveness of the implant.
To assess durability, immobilized hydrogels were subjected to hyaluronidase IV solutions over a period of 21 days.; comparisons were made with macroscopic hydrogels with equal compositions. For macroscopic hydrogels significant differences were found in degradation rates, depending on the hydrogel composition and crosslinking density. Hydrogels with HA/MBAA showed rapid degradation with short half-lifes, while HA/ACLT-PEG-ACLT displayed much higher stability.
Multifunctional crosslinked hydrogels with HA/4arm-PEG-ACLT were particularly resistant to degradation, with no complete degradation observed over three weeks. In contrast, HA/4arm-PEG-VS hydrogels exhibited higher degradation, with stability varying according to the HA concentration.
The results indicated that crosslinking density and mesh sized played a crucial role in the stability of hydrogels. Smaller mesh sizes in HA/4arm-PEG-ACLT gels (approx. 80 nm at 15 mg/ml) likely hindered the diffusion of hyaluronidase enzymes (molecule size: Ø=~5 nm) more, compared to HA/4arm-PEG-VS gels (around 110 nm at 15 mg/ml). This resulted in higher resistance to enzyme degradation.
For constrained HA hydrogels immobilized within small model tubes, no degradation was observed over the study period. This increased stability was attributed to reduced enzyme penetration due to smaller pore sizes and the physical barrier provided by the tube.

In conclusion, these results highlighted the importance of hydrogel compositions and type of crosslinking in determining the durability of HA-based hydrogels for use in glaucoma implants. 4arm-PEG-ACLT linked hydrogels and immobilized hydrogels showed the highest resistance to enzymatic degradation, making them promising candidates for long-term implant functionality. Nevertheless, further studies will be necessary, to test the hydrogels over longer periods and under physiological conditions to validate their sustainability for clinical use.

5.1.4 Outlook and Perspectives for Future experiments

For future experiments, further hydrogel characteristics could be interesting, such as mechanical characterizations of the hydrogel. For the evaluation of mechanical properties of hydrogels, the most common categories of techniques are axial testing, frequency-based measurements and non-contact techniques [261-263]. However, since our hydrogels are immobilized within small tubes a uniaxial compression would most closely represent our system. This technique was already well established and documented in previous studies by Tim Kreuz [178]. When the final hydrogel compositions of our new GDD will be set this approach can be used to characterize mechanical properties as the elastic modulus of the hydrogel, which then can be used to predict for example the pressure resistance of the hydrogel and be correlated with equilibrium pressure.
Future experiments should also include cell studies with final GDDs, to assess the biocompatibility of the implant and furthermore cell repellant properties of the interior hydrogel composition.
One main problem of many current glaucoma implants is the progressive corneal endothelial cell loss after implantation, as happening for the Baerveldt implant [264, 265], the EX-PRESS shunt [266] or the AGV [267-269], and also observed after trabeculectomy surgeries [268, 270, 271]. For biocompatibility studies with our implant, two different types of human corneal endothelia cells (HCEC) were already propagated in previous studies, originated from the center (H9C1) and the peripherie (B4G12) of the human cornea [147] (figure 67).

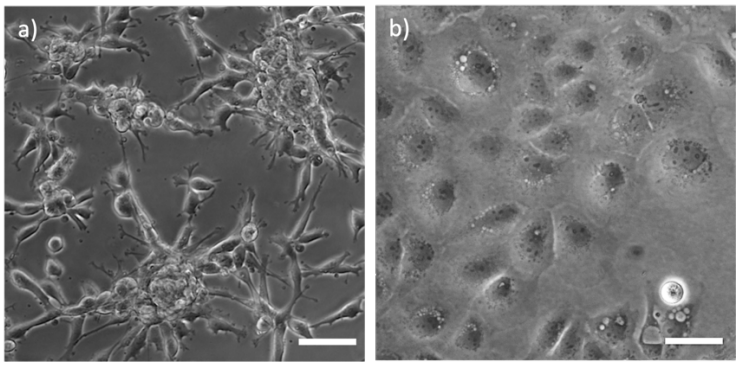

Figure 67: Cell morphology of human corneal endothelia cells (HCEC) derived from the periphery (a) and center (b) of the human cornea. Two different corneal cell lines were cultured for 14 days under serum-free conditions on laminin/chondroitin-6-sulfate coated wells, and differed markedly in their morphology. Cells of the clonal cell line HCEC-H9C1 are periphery-derived, building round and elongated cells and growing in a network- and aggregated sphere-like formation; they showed only weak adherence to their substrate and the mean generation time was t_D=43.8±3.8 h (a). B4G12 reflect model lines for central HCEC; the grew very adherent in a monolayer formation and mean generation time was t_D=62.8±10.7 h (b). Scale bar represents a length of 50 µm.

Moreover, two different cell assays were established, to investigate cell viability and cell proliferation on/in hydrogel-modified tubes [147]. First cell experiments were conducted using HA/MBAA hydrogel-modified tubes with different TGs, showing overall good biocompatibility and no cell proliferation inside the tubes over 14 days [147]. However, in some cases it was observed that excess MBAA led to decreased cell viability around the tube, which could be improved by extensive washing of the implant in PBS after polymerization.

Furthermore, in this work a new and improved setup for cell experiments was developed as shown in figure 68. Previous studies often struggled to clearly determine whether cells were growing on or within the hydrogel tube [147]. To address this issue, the experimental design was improved by a two-chamber setup. The main idea was, that one chamber was filled with cells, while the second one contained no cells. The hydrogel-modified tube was placed between these two chambers. With this it was ensured, that only one of the tubes' edges came into direct contact with the cells, with the outer surface exposed externally. This setup allowed for clearer observation of cell proliferation within the hydrogel-modified tube. Additionally, since HCECs are also capable of cell migration [272] [273], the presence of cells in the second chamber could also be analyze to determine whether migration through the implant occurred.

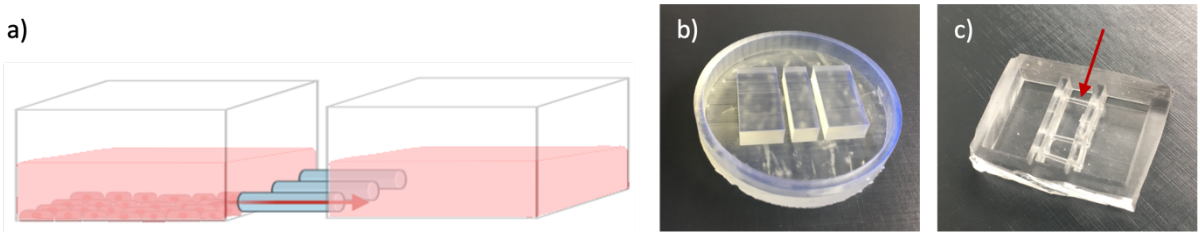

Figure 68: Experimental setup for cell experiments with HA hydrogel-modified tube placed between two wells/chambers with cells (a) and 3D-printed pattern of the setup (b) with corresponding PDMS mold of the pattern (c). The negative master structure of the two-chamber setup was designed with AutoCAD and printed with ClearResin from formlabs. PDMS was poured on the master structure, let polymerized and afterwards cut out and peeled off. In-between the chambers small holes were punched in using a biopsy puncher (Ø=0.5 mm) for insertion of the small hydrogel-filled tubes (red arrow in c). The drawing in a) was created with BioRender.com.

First experiments with the two-chamber setup over 14 days were quite promising and showed no cell proliferation or migration inside the model tubes [147]. Nonetheless, much more research and experiments are necessary to evaluate long-term stability of the implant and to ensure that no clogging of the implant occurs.

The hydrogel should possess cell repellant properties and this can be tuned with an appropriate hydrogel composition (e.g. crosslinker), as shown in previous studies by Hegger [179]. For example, the cell behaviour and adhesion of HDLEC, MCF7 and NHDF lines increased with higher TG of HA, stiffness of the gel, and different network charges, which was influenced by different crosslinkers [179].

One option for cell repellence could be HS-HA-PEGDA hydrogels, showing poor cell attachment in *in vitro* studies [274, 275]. PEGDA with low molecular weigth (M_n= 250 kDa) could be an appropriate candidate for our purpose, but this has to be proven in future experiments.

Another important focus should be the biocompatibility of the implant, including an appropriate surface of the tube, that enables cells adhesion to avoid inflammations of surrounding tissue.
One possible approach would be a structuring of the implants' outer surface, as shown in previous studies by Choritz et al. [276]. They explored adhesive properties of human tenon fibroblasts on different GDDs, as the AGV, Baerveldt or Molteno implant and it was shown that cell adhesion was most prevalent on surfaces of AGV, due to the higher roughness of its surface [276].
Another approach for the promotion of cell adhesion on the implants' outer surface is the functionalization with cell adhesive proteins (e.g. fibronectin or laminin) or peptides. The tripeptide RGD, which is present in different proteins of the ECM (such as collagen or laminin), can influence cell behaviour, adhesion and survival of cells [277]. RGD can for example be linked to HA, as shown by Karel et al., building RGD-HA [278]. Hydrogels of RGD-HA promote cell attachment of e.g. fibroblasts and can be used to coat the implants outer surface in order to enhance a good incorporation of the implant [275, 278].
Further conceivable options are HS-HA-PEGDA-RGD hydrogels, which also enhance cell adhesion, spreading and proliferation of fibroblast (CF-31 and NIH-3T3) in a concentration dependent-manner of RGD [275].
However, cell behaviour is highly dependent on the hydrogel composition, meaning that cell experiments become truly relevant only once the final hydrogel formulation – optimized for the valve functionality – is established. The primary focus should remain on achieving an effective valve mechanism, and any cell repellant properties, though important and beneficial, serve as complementary features. Consequently, until the hydrogel composition necessary for optimal pressure regulation is finalized, cellular studies will provide limited insight into the implant's long-term performance.

5.2 Pressure Regulation Abilities of HA Hydrogel-Modified Implants

In order to test the pressure regulation abilities of miniaturized hydrogel-modified tubes a new measurement setup was established with the microfluidic device OB1 MK3. Different measurement modes were established, using mainly small glass model tubes with hydrogels crosslinked with the small bifunctional crosslinker MBAA (M_n= 154 kDa).

5.2.1 Activation Pressure Determination

Initially, it was demonstrated that each hydrogel-modified implant required 'activation' after preparation, similar to the implant priming process of current GDDs, as the AGV, in order to overcome the initial pressure resistance of the valve [247-249, 279]. AGVs typically required manual priming with a high initial pressure [249]. For our hydrogel-modified implants a microfluidic setup with the ramp-mode was used, where pressure was gradually and slowly increased over a specific time interval to avoid damaging of the hydrogel valve, with the flowrate of outflowing fluid indicating the channel opening and activation pressure (See section 4.4.1).

The results revealed that determining precise pressures values was challenging and, in most cases, not feasible, as many samples exhibited varying behaviors in the way the channel opened. Consequently, activation pressure values differed significantly in most cases, even for the same gel compositions and tube dimensions.

These variations were primarily attributed to the challenging preparation of the small glass model implants, particularly the manually created artificial channels.

However, it was noted, that priming pressures for AGV also exhibited considerable variability [249, 279] and in clinical practice, the exact value or reproducibility of priming was less critical. Instead, the primary focus was on the activation/priming of the implant itself, rather than on achieving specific pressure values. Literature results also showed that the priming values for AGV were much higher than those observed for our HA hydrogel-modified implants, indicating a fundamental difference in behaviour.

Variability in activation values of hydrogel valves were influenced by the composition and structure of the hydrogel, along with external factors such as speed and intensity of pressure application. The hydrogel valves were softer and more fragile compared to mechanical valves, making them susceptible to damage from overpriming.

Future studies should focus on optimizing the preparation of hydrogel models and refining the priming process to ensure accurate, reproducible results. However, functioning hydrogel-modified tubes were identified for further testing.

5.2.2 Pressure Regulation at Conventional Flowrates

Next up, the pressure regulation during conventional flowrates was investigated, similar to the real flow of aqueous humor (See section 4.4.2). Flow characteristics of hydrogel-modified tubes were

compared with AGV. In a healthy human eye, the production and outflow of aqueous occurred at a rate of 2-3 µl/min, with IOP ranging from 1300-2800 Pa (10-21 mmHg) [252, 253].
It was shown, that at a set flowrate of 2.5 µl/min our hydrogel modified implants were able to create a steady-state pressure and even over longer periods, the tubes demonstrated consistent pressure regulation with minor fluctuations, although the pressures exceeded normal IOP values. Comparatively, AGVs, while effective in IOP reduction, showed much higher pressure variations, with rapid opening and closing cycles of the mechanical valve [248, 249, 254-256]. This contributed to significant fluctuations, which could pose risks for glaucoma patients as contributing to glaucoma progression. Our results suggested a reliable pressure resistance, albeit with the need for further optimizations to match physiological IOP levels.

5.2.3 Pressure Regulation During Pressure Fluctuations

As a last objective in this section, sine pressure measurements were conducted to simulate normal eye pressure fluctuations (See section 4.4.3), which were known to range between 2-6 mmHg (=266-800 Pa) in one eye over the day.
In a first approach the pressure was fluctuated in different time intervals, and fluid flow was measured. The results showed that the flowrates correlated to the applied pressure fluctuations, with flowrates ranging from 0-8 µl/min. Additional long-term sine measurements confirmed the hydrogel tubes' ability to adapt to varying pressures over time.
In a next step, real-life sine measurements were investigated, where IOP changes followed a 24-hour sinusoidal rhythm, peaking during sleep and declining during the day. The hydrogel-modified tubes effectively responded to these pressure fluctuations, maintaining continuous flow in correlation with the applied pressures.
In contrast, AGVs do not exhibit a constant natural flow of aqueous, instead their mechanical valve mechanism alternates between opening and closing when the IOP exceeds a certain threshold or drops below a critical level [249]. The opening pressures for AGV ranged between 10 to 17 mmHg and closing pressures were between 4 to 9 mmHg, with opening/closing cycles of 51.05-76.67 min [249]. Reported pressure fluctuations in the steady phase ranged from 3 to 9 mmHg.
In summation, while AGVs effectively and rapidly reduce elevated IOP; our findings suggest that hydrogel-based implants have the potential to mimic natural eye drainage more closely as AGVs. Although flowrates were slightly higher than normal, the results indicated that the hydrogel implants could give a viable option for regulation IOP in glaucoma patients.
Further refinement may be required to reduce flowrates closer to physiological levels, but the tubes demonstrated promising adaptability and stability under varying pressure conditions.

5.2.4 Outlook and Perspectives for Future experiments

Outgoing from our pressure measurement studies, the best results in pressure regulation were obtained for HA hydrogels with small bifunctional crosslinker as MBAA or ACLT-PEG-ACLT, although some values exceeded normal levels. However, unfortunately these hydrogel compositions showed a decreased stability against enzymatic degradation in contrast to e.g. 4arm-PEG-ACLT, but these in turn showed a pressure resistance above normal IOP. To reduce a hydrogels' pressure resistance different attempts can be made, including for example lowering mass concentrations of HA or decreasing TG. Furthermore, the diameter of the artificial channel can be tuned to an e.g. conical shape or a step-wise increase from 0.1 mm to e.g. 0.12 mm, 0.15 mm, and so on, until the desired value of pressure or flowrate is reached.

The optimization of hydrogel-modified tubes or the exploration of a new hydrogel composition should be in focus of future research. The difficulty of finding an appropriate hydrogel for our purpose is related to the unique combination of cell repellant properties, the stability of the hydrogel against enzymatic degradation, and additionally the adjustment of the valve functionality to match physiological IOP levels.

A new and promising hydrogel composition could be HS-HA-PEGDA hydrogels, mentioned before in section 5.1.4 due to its known cell repellant characteristics [274, 275]. The pressure regulation abilities of these hydrogels could be tested in future experiments.

Nonetheless, the main problem of our model implants was less attributed to its gel compositions, than to the implant preparation process, especially the formation of a centrally positioned channel inside the hydrogel, which was found to be error prone due to the tiny diameters of the tubes. Therefore, in the last chapter of this first experimental part different attempts were made to improve the preparation process as summarized in the following

5.3 Improvement of Implant Preparation and Measurement Setup

In order to enhance the reproducibility of model implants, the main focus in this last section was on improving the model implant preparation and the measurement mode, as summarized in the following.

5.3.1 3D-Printed Patterns for Improved Implant Preparation

The artificial channel inside the hydrogel is the basis for the valve functionality of HA hydrogel-modified model implants. Therefore, different 3D-models were designed using the software AutoCAD to improve the formation of a centrally positioned channel inside the hydrogel of small model tubes.

For this, different designs were explored. The first 3D-model involved a fiber-equipped plate to hold the glass tubes, but encountered issues such as hydrogel leakage. The second design featured a three-plate system to better position the tubes, but the printing resolution was insufficient to achieve the required precision. A simplified two-plate version with improved printing resolution was ultimately successful in creating consistent artificial channels in hydrogel-modified tubes with ID=3 and 2 mm and a length of 6 mm.

The iterative development of 3D-printed model implants highlighted the importance of design precision and material compatibility. While initial designs faced challenges with alignment and material properties, subsequent modifications led to successful prototypes. This demonstrated that careful consideration of material choice, printing resolution, and surface functionalization is critical in the fabrication of reproducible implant models. This research laid the groundwork for future development of more reliable and scalable glaucoma implants, with potential for further optimization in both design and material selection.

5.3.2 Pressure Measurements with Optimized Setup

Further pressure measurements were conducted using HA hydrogel modified tubes (ID=2 mm, l=6 mm), with various hydrogel compositions, which were prepared utilizing 3D-printed patterns to optimize the introduction of an artificial channel. Furthermore, the measurement setup was refined, as the ramp mode for activation pressure determination was not performed this time, instead the constant flowrate mode was used and tested additionally for glass model tubes with ID=1 mm.

With these improvements, the number of deficient model implants significantly decreased. However, the course of the measurements was in part different for the same hydrogel compositions as shown for HA hydrogel compositions with the bifunctional crosslinker ACLT-PEG-ACLT.

Some model tubes displayed a similar course as observed for ramp measurements, with an increase of pressure until the pressure resistance was overcome (activation pressure) and suddenly the resistance dropped to a lower range and remained constant (equilibrium pressure).

Other samples achieved equilibrium pressures without reaching the activation threshold, but showing a steady-state pressure in a high-pressure range similar to activation pressure (15.000-35.000 Pa). Other samples in turn displayed equilibrium pressures in the area of normal to elevated IOP (2000-4000 Pa), also without 'activation'. Both 'groups' of samples showed a reliable pressure resistance with minor standard deviation, but overall, most tubes were above the normal IOP especially for ID=1 mm.

As already expected, for multifunctional-crosslinked hydrogels (4arm-PEG-ACLT and 4arm-PEG-VS) the pressure resistance was much higher due to the higher crosslinking density and stiffness of the gels. Although the measurements showed a reliable pressure resistance with only minor standard deviations, average pressure values range between ~25.000–35.000 Pa, and were therefore found to be unsuitable for our GDDs.

The study concludes that bifunctional-crosslinked HA hydrogels offer promising potential for use in biomedical implants requiring moderate pressure regulation. However, further optimization is needed to consistently achieve target pressure ranges, particularly at smaller tube diameters. Future work should focus on refining hydrogel compositions with smaller bifunctional linker and crosslinking densities to balance mechanical strength with responsive pressure modulation.

5.3.3 Outlook and Perspectives for Future Experiments

With the findings obtained from these additional pressure measurements it became clear, that a new hydrogel composition would be necessary to match physiological IOP, combined with cell repellence and stability against enzymatic degradation.

However, when the final gel composition is found and tube dimension is set, another approach for a more realistic pressure measurement would become necessary. For this, an eye model setup was established in corporation with the company Pharmpur. The setup is composing of a silicon eye, built up like a real human eye with an AC and PC, and a sample holder which can be connected to the silicon eye and the microfluidic device to fill the eye with "aqueous humor" (figure 69).

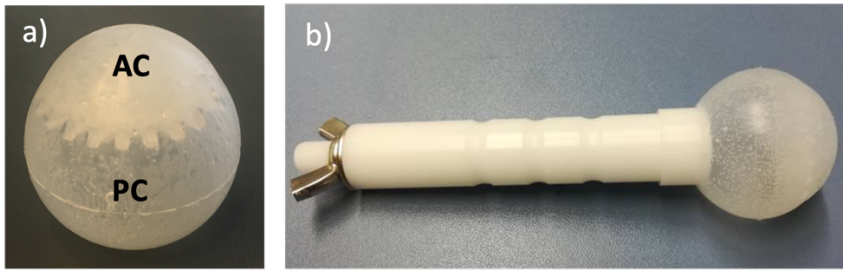

Figure 69: Eye model setup for pressure measurements. Silicon eye designed with anterior chamber (AC) and posterior chamber (PC) (a); Silicon eye connected to a sample holder for pressure measurements with microfluidic setup (b).

A first pressure measurement with this eye model was performed, after 'activation' of the model tube using the constant flowrate mode as shown in figure 70a. The course of the measurement showed an increase in pressure up to 24,000 Pa, and a subsequent drop to an equilibrium pressure around 4000 Pa.

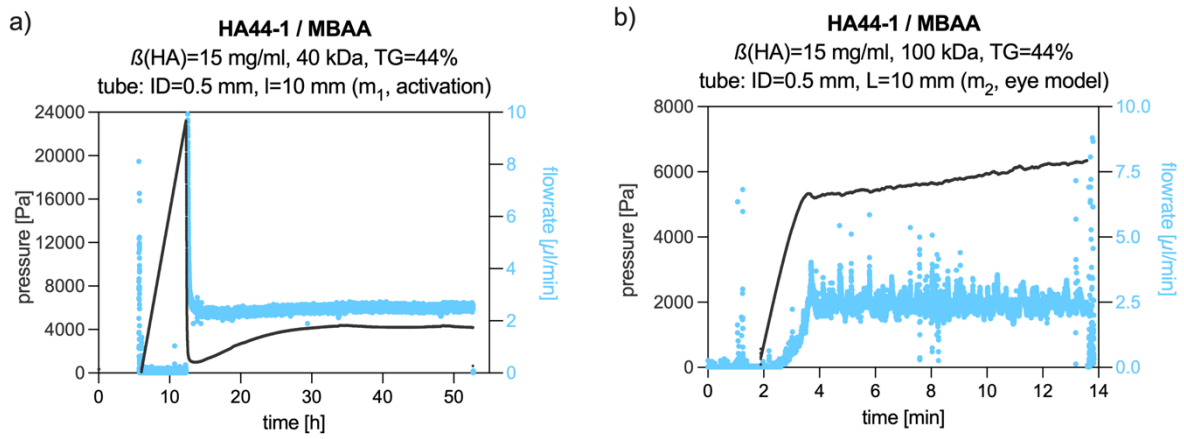

Figure 70: Activation (a) and eye model measurement (b) of a small HA44-1/MBAA-modified glass tube (ID=0.5 mm and l=10 mm) with *β*(HA)=15 mg/ml. After preparation the small glass model tube was activated using the constant flowrate mode; the course of the measurement showed an increase in pressure up to 24000 Pa, and a subsequent drop to an equilibrium pressure around 4000 Pa (a). Afterwards the tube was inserted in the anterior chamber (AC) of the silicon eye, that was filled with PBS, and a constant flowrate of 2.5 µl/min was applied to mimic natural eye drainage. The measurement showed an increased pressure in contrast to the measurement with the eye model and furthermore an expansion of the silicon eye (b). Dark grey curve in the figures displayed the applied pressure, the blue curve showing the measured flowrate.

After activation the tube was inserted in the AC, whereby the silicon eye was filled up with PBS before, and after implantation a physiological flowrate of 2.5 µl/min was applied to mimic natural eye drainage. This first measurement showed (figure 70b), that in principle this approach works, but leads also to an expansion of the silicon eye, shown by increasing pressure over the course of. Furthermore, flowrate fluctuations were also higher than before. For future experiment with this setup, further improvements are necessary, as the implementation of an eye socket, that counteracts the expansion of the silicon eye, similar to the normal human eye.

6 Appendix – Part I

6.1 Calculations

6.1.1 Calculations for TG Determination by Ellman's Assay

The TG was defined as the molar ratio of SH-groups linked to the HA and was calculated according to previous studies by Dr. Patricia Hegger as described in the following [179].
The absorption of the standard dilution was plotted against the cystamine concentrations (= concentrations of -SH groups) and the equation of this linear fit was determined:

$$A_{420} = (\mathrm{a} * c_{\mathrm{SH}}) + \mathrm{b} \qquad \text{Eq. 1.3}$$

With 'a' being the slope of the linear fit and 'b' being the y-intercept. From this the thiol concentrations of the samples (c_{SH}) were calculated using the molecular mass of the thiol linker, M_{SH} = 103.2 g/mol and the measured absorbance of the HA sample at 420 nm:

$$c_{\mathrm{SH}} = \frac{A_{420} - \mathrm{b}}{\mathrm{a}} * M_{\mathrm{SH}} \qquad \text{Eq. 1.4}$$

The mass of thiols in the samples (m_{SH}) were calculated using c_{SH} and the volume of the solution (V_{sample}):

$$m_{\mathrm{SH}} = c_{\mathrm{SH}} * V_{\mathrm{sample}} \qquad \text{Eq. 1.5}$$

From the initial weigth of HS-HA ($m_{\mathrm{HS\text{-}HA}}$) the thiol mass was subtracted, yielding the pure mass of HA (m_{HA}):

$$m_{\mathrm{HA}} = m_{\mathrm{HS-HA}} - m_{\mathrm{SH}} \qquad \text{Eq. 1.6}$$

The HA concentration c_{HA} of the sample was determined after the formula:

$$c_{\mathrm{HA}} = \frac{\left(\frac{m_{\mathrm{HA}}}{\bar{M}_{\mathrm{HA}}}\right)}{V_{\mathrm{sample}}} \qquad \text{Eq. 1.7}$$

For the molecular weigth of one HA repeating unit ($\bar{M}_{\mathrm{HA}}$) an average value of 401.3 g/mol was assumed. In the last step the TG was calculated as the ratio of thiol and HA concentration:

$$\text{degree of thiolation (TG)} = \frac{c_{\mathrm{SH}}}{c_{\mathrm{HA}}} * 100 \qquad \text{Eq. 1.8}$$

6.1.2 Calculations for HA Hydrogel Formation

The following calculations for the amount of crosslinker and HS-HA for hydrogel formation were adapted from Tim Kreuz and described for a stochiometric/volumetric mixing ratio between crosslinker and HA of 1:1 [178]. The molecular mass of the HS-HA ($M_{\text{HS-HA}}$) is calculated by

$$M_{\mathrm{HS-HA}} = \bar{M}_{\mathrm{HA}} * M_{\mathrm{SH}} * \mathrm{TG} \qquad \text{Eq. 1.9}$$

With $\bar{M}_{\mathrm{HA}}$=401.3 g/mol, being the average molecular weigth of a monomer unit of HA and M_{SH}=103.2 g/mol, the molecular weigth of a thiol side group, multiplied with the thiolation grade (TG) of the HA. For a mixing ration of 1:1, the required mass concentration of the HA mixing/stock solution ($\gamma_{\text{stock, HS-HA}}$) is given by doubling the desired final mass concentration of HS-HA ($\gamma_{\text{end, HS-HA}}$):

$$\gamma_{\mathrm{stock,\ HS-HA}} = 2 * \gamma_{\mathrm{end,\ HS-HA}} \qquad \text{Eq. 1.10}$$

The amount of buffer solution needed (V_{stock}) for this concentration, is calculated by the mass of HS-HA ($m_{\text{HS-HA}}$)

$$V_{\mathrm{stock}} = \frac{m_{\mathrm{HS-HA}}}{\gamma_{\mathrm{stock}}} \qquad \text{Eq. 1.11}$$

and considering a volume expansion upon dissolution (assumption: 1 ml per g of polymer), a final volume of buffer solution to be added (V_{final}) is

$$V_{\mathrm{final}} = V_{\mathrm{stock}} - 1\frac{\mathrm{ml}}{\mathrm{g}} * m_{\mathrm{HS-HA}} \qquad \text{Eq. 1.12}$$

To fully crosslink the HA solution, the required mass of PEG-crosslinker, m_{PEG}, was calculated as

$$m_{\mathrm{PEG}} = n_{\mathrm{PEG}} * \bar{M}_{\mathrm{PEG}} \qquad \text{Eq. 1.13}$$

With n_{PEG} being the amount of substance of the PEG crosslinker and $\bar{M}_{\mathrm{PEG}}$ being the average molecular weigth of the crosslinker. From this, the amount of substance was calculated as:

$$n_{\mathrm{PEG}} = \frac{[n_{\mathrm{HA}} * \mathrm{TG}]/\text{number of functional groups}}{DS_{\mathrm{PEG}}} \qquad \text{Eq. 1.14}$$

With DS_{PEG} being the degree of substitution of the PEG linker, and n_{HA} being the amount of substance of a monomeric unit of HA, which is finally calculated by

$$n_{\mathrm{HA}} = \frac{m_{\mathrm{HA}}}{M_{\mathrm{HS-HA}}} \qquad \text{Eq. 1.15}$$

6.2 ^{1}H-NMR Analysis of Synthesized Compounds

6.2.1 ^{1}H-NMR Spectra of DTPH

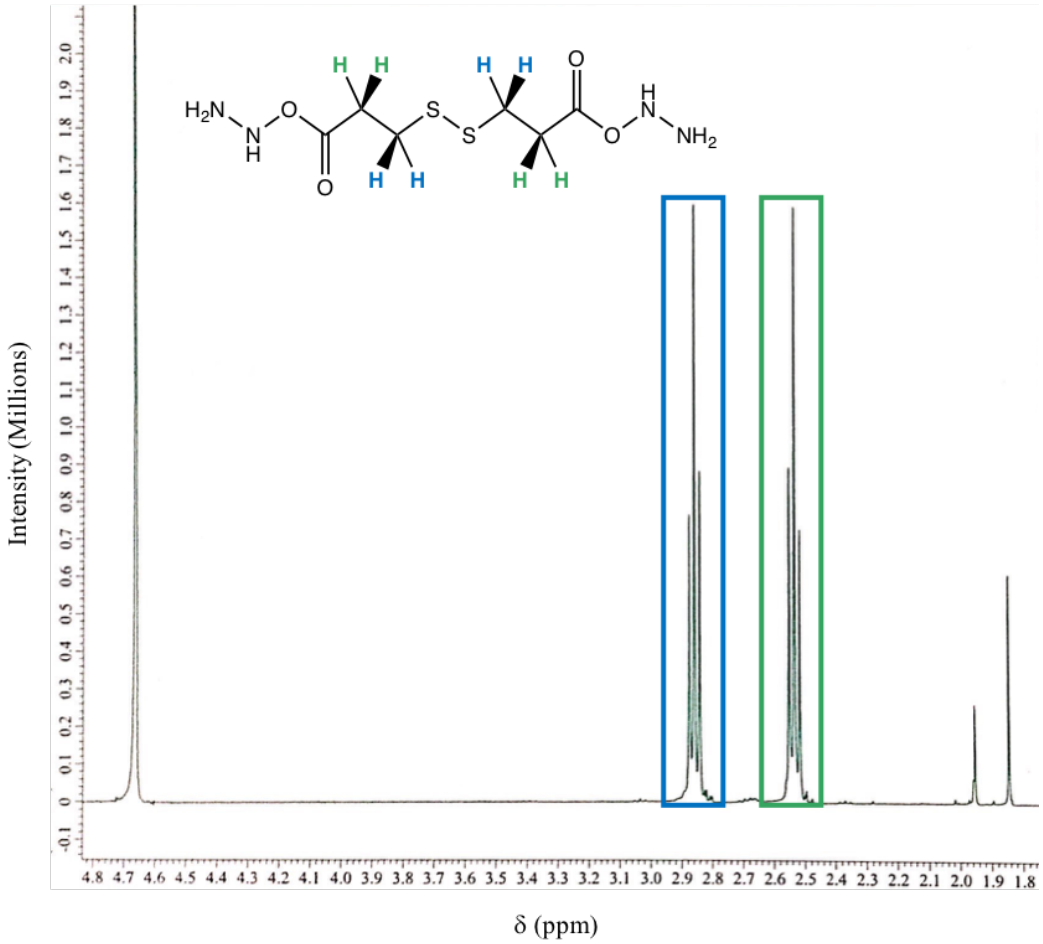

Figure 71: ^{1}H-NMR spectra (400 MHz, D_2O) and chemical structure of DTPH. The triplets at δ=2.859 ppm (blue) and at δ=2.551 ppm (green) belonged to the -CH_2-CH_2- functions of DTPH and showed a typical roof effect of coupling cores. The signal at δ=4.67 ppm belonged to the solvent D_2O and the smaller peaks were attributed to either impurities or ^{13}C-satelites. DTPH was already synthesized in previous studies and partly used in this thesis for HA modification. For that reason, a new NMR-measurement the spectra was adapted from these previous studies [147]. New synthesized DTPH showed a similar spectrum, however, an identical presentation of the results has been omitted here.

6.2.2 ^{1}H-NMR Spectra of HS-HA

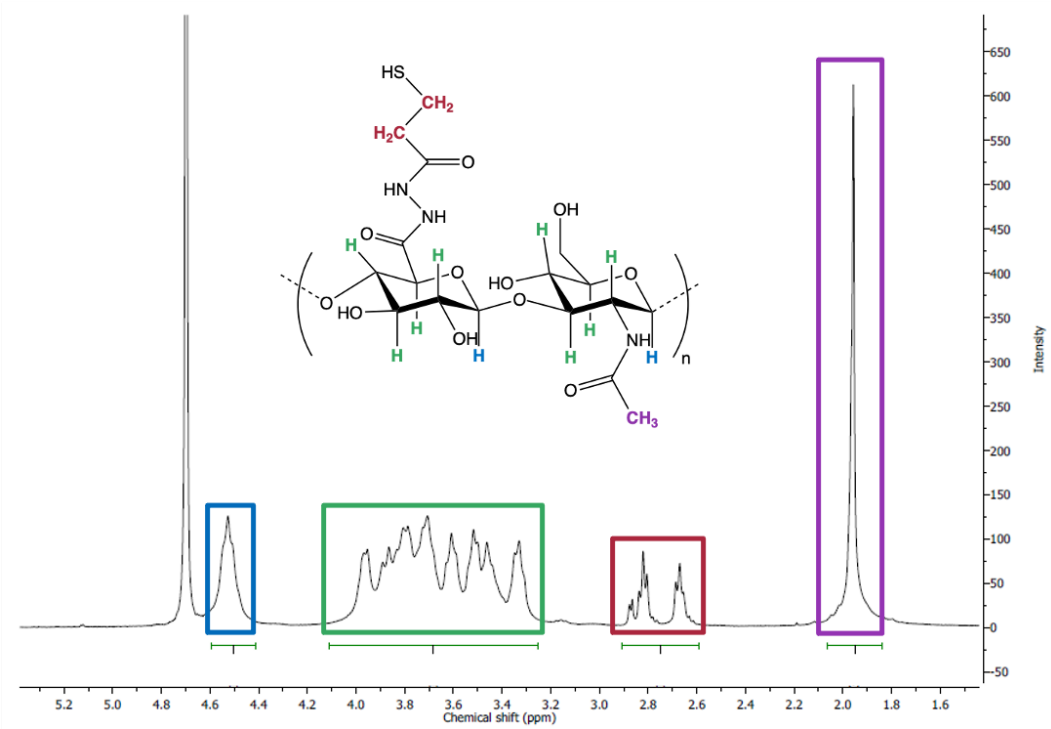

Figure 72: ^{1}H-NMR spectra (400 MHz, D_2O) and chemical structure of HS-HA. The Signals were attributed to the respective H-atoms according to Shu et al. [231]and Thaller [145]. The singlet at δ=1.88 ppm belonged to the N-acetyl methyl protons of HA (violet) and the multiple signals at δ=3.9–3.3 ppm (green) and the signal at δ=4.5 ppm (blue) originated from the pyranose -CH- groups of the disaccharide units. Resonances specific for HA-DTPH appeared at δ=2.75 ppm and δ=2.6 ppm, corresponding to the two side chain methylenes (-CH2-CH2-, red) of the thio(propanoic hydrazide) (TPH) chains. The spectra was recorded and analyzed by Dr. Johannes Feierfeil and provided for this thesis.

6.2.3 Thiolation Grade (TG) Determination

Table 7: Comparison of thiolation grades (TGs) obtained by ^{1}H-NMR (analyzed by Johannes Feierfeil) and Ellman's assay (determined by Elke Völkle). The average TG values obtained by Ellman's assay were determined from at least three individual measurements of each HS-HA sample with the standard deviation as error.

Sample number	TG [%] determined by	
	^{1}H-NMR	Ellman's assay
P1625-JoF-009	49	55 ± 6
P1625-JoF-015	28	26 ± 4
P1625-JoF-027	28	24 ± 1
P1625-JoF-029	40	39 ± 3
P1625-JoF-030	44	48 ± 5
P1625-JoF-038	63	82 ± 12
P1625-JoF-039	57	59 ± 3

6.3 Additional Information for Swelling Ratios

6.3.1 Exact Values of Mass Swelling Ratios of Macroscopic and Constrained HA Hydrogels

Table 8: Exact values of relative mass swelling ratios (m_s/m_d) of HA51 with different crosslinker (ACLT-PEG-ACLT, 4arm-PEG-ACLT, 4arm-PEG-VS) comparing macroscopic (non-immobilized) and constrained (immobilized) hydrogels presented in figure 42, 43 and 44. Swelling ratios were determined with different mass concentrations of HA (β(HA)=5 mg/ml, β(HA)=10 mg/ml and β(HA)=15 mg/ml) and different tube dimensions of immobilized hydrogels (l=6 mm and ID= 1, 2 and 3 mm). All values were determined from at least three individual prepared samples and swollen in PBS (pH 7.4) for 72 h, with the standard deviations as error bar. The swelling ratios for macroscopic hydrogels with 4arm-PEG-ACLT and 4arm-PEG-VS were obtained from previous studies by Tim Kreuz [178] using HA49.

Crosslinker	Relative swelling ratio (m_s/m_d) of macroscopic hydrogels	Relative swelling ratio (m_s/m_d) of immobilized hydrogels	Relative swelling ratio (m_s/m_0) of immobilized hydrogels
ACLT-PEG-ACLT	61.81 ± 3.6 33.58 ± 2.6	49.25 ± 10.4 (ID=1 mm) 56.31 ± 4.1 (ID=2 mm) 66.90 ± 11.9 (ID=3 mm) 32.6 ± 5.0 (ID=1 mm) 37.42 ± 3.9 (ID=2 mm) 41.85 ± 6.7 (ID=3 mm)	1.12 ± 0.04 (ID=1 mm) 1.12 ± 0.1 (ID=2 mm) 1.10 ± 0.03 (ID=3 mm) 1.17 ± 0.07 (ID=1 mm) 1.17 ± 0.07 (ID=2 mm) 1.16 ± 0.02 (ID=3 mm)
4arm-PEG-ACLT	29.60 ± 2.6 [178] 13.28 ± 2.0 [178]	27.88 ± 0.1 (ID=1 mm) 28.64 ± 1.3 (ID=2 mm) 30.5 ± 5.0 (ID=3 mm) 13.28 ± 2.0 (ID=1 mm) 15.14 ± 1.5 (ID=2 mm) 17.50 ± 3.6 (ID=3 mm)	1.11 ± 0.07 (ID=1 mm) 1.08 ± 0.07 (ID=2 mm) 1.04 ± 0.04 (ID=3 mm) 1.16 ± 0.08 (ID=1 mm) 1.12 ± 0.04 (ID=2 mm) 1.20 ± 0.05 (ID=3 mm)
4arm-PEG-VS	29.38 ± 5.1 [178] 18.83 ± 0.8 [178]	28.37 ± 0.5 (ID=1 mm) 29.30 ± 2.8 (ID=2 mm) 30.7 ± 5.6 (ID=3 mm) 13.74 ± 0.8 (ID=1 mm) 15.54 ± 1.6 (ID=2 mm) 16.12 ± 2.9 (ID=3 mm)	1.17 ± 0.02 (ID=1 mm) 1.11 ± 0.02 (ID=2 mm) 1.00 ± 0.02 (ID=3 mm) 1.11 ± 0.08 (ID =1 mm) 1.13 ± 0.05 (ID=2 mm) 1.08 ± 0.03 (ID=3 mm)

6.4 Enzymatic Degradation of HA Hydrogels

6.4.1 Exemplary Controls of Macroscopic and Constrained HA Hydrogels in PBS Solution

Controls for Macroscopic Bifunctional-Crosslinked HA Hydrogels

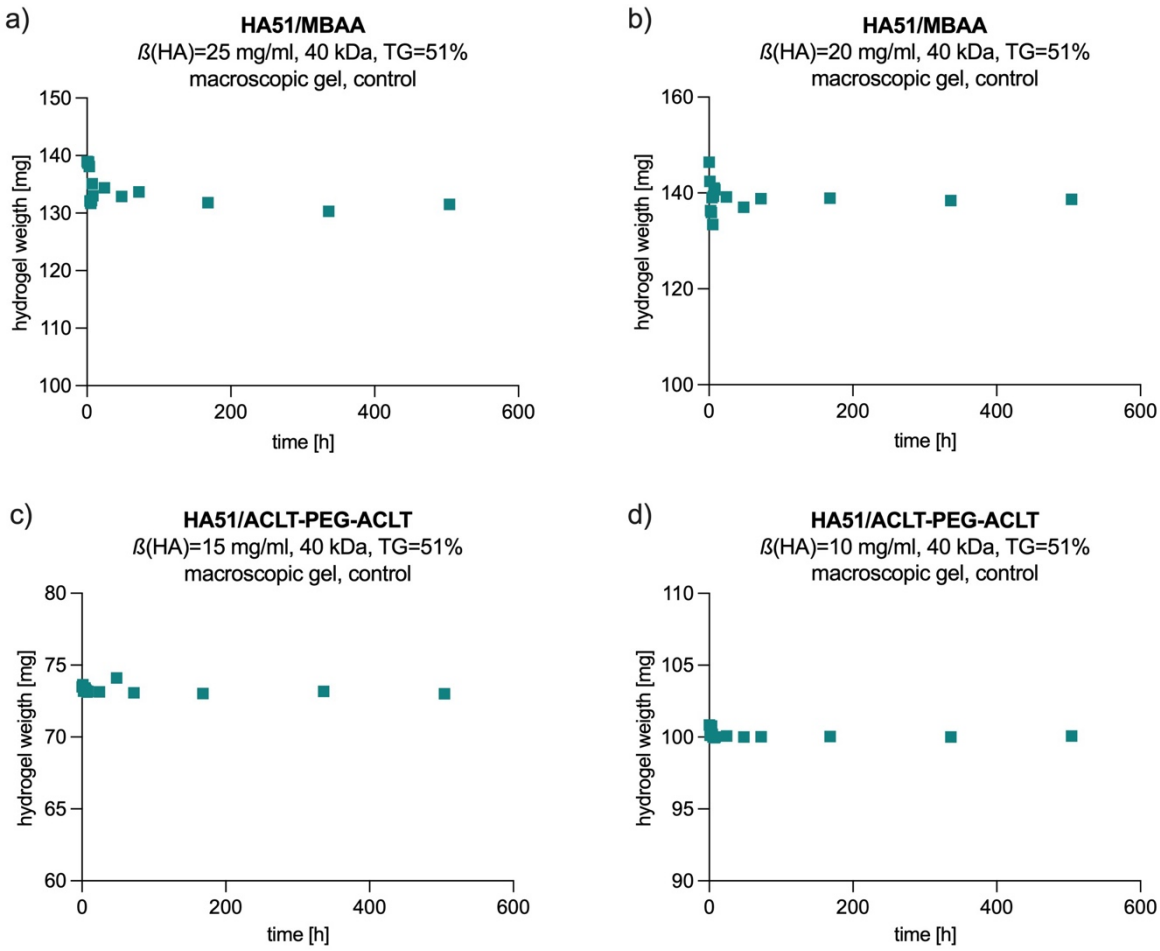

Figure 73: Exemplary graphs for controls of macroscopic HA hydrogels with bifunctional crosslinker (a-d). Hydrogels were formed using HA51 with different mass concentrations (β(HA)=25, 20, 15 and 10 mg/ml) and bifunctional crosslinker: MBAA (a/b), ACLT-PEG-ACLT (b/c). After hydrogel swelling, tubes were incubated in PBS (pH 7.4) at room temperature and hydrogel weigth was determined over three weeks. As expected, the weigth of the hydrogels were constant over the course of three weeks.

Controls for Macroscopic Multifunctional-Crosslinked HA Hydrogels

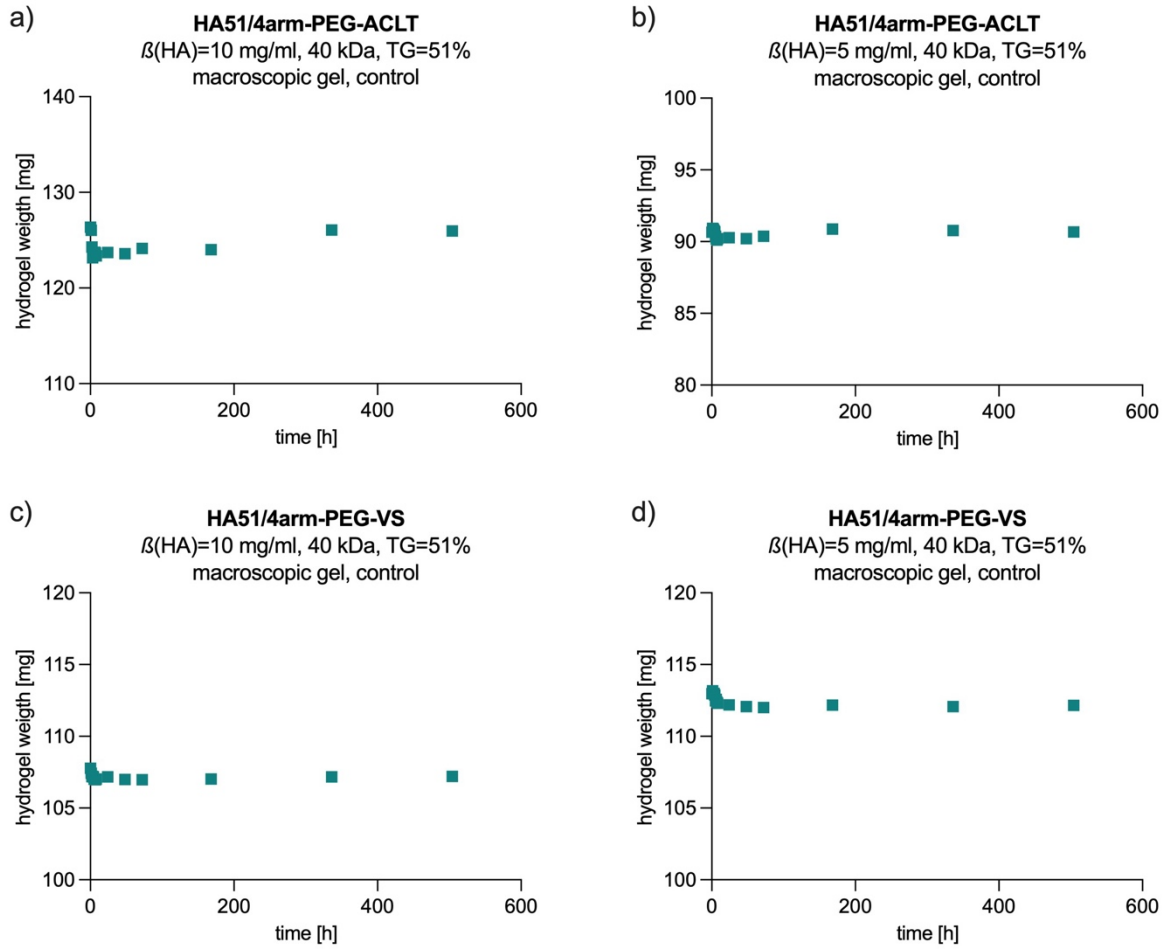

Figure 74: Exemplary graphs for controls of macroscopic HA hydrogels with multifunctional crosslinker (a-d). Hydrogels were formed using HA51 with different mass concentrations (β(HA)=10 and 5 mg/ml) and multifunctional crosslinker: 4arm-PEG-ACLT (a/b), 4arm-PEG-VS (b/c). After hydrogel swelling, tubes were incubated in PBS (pH 7.4) at room temperature and hydrogel weigth was determined over three weeks. As expected, the weigth of the hydrogels were constant over the course of three weeks.

Controls for Constrained HA Hydrogels of Different Compositions

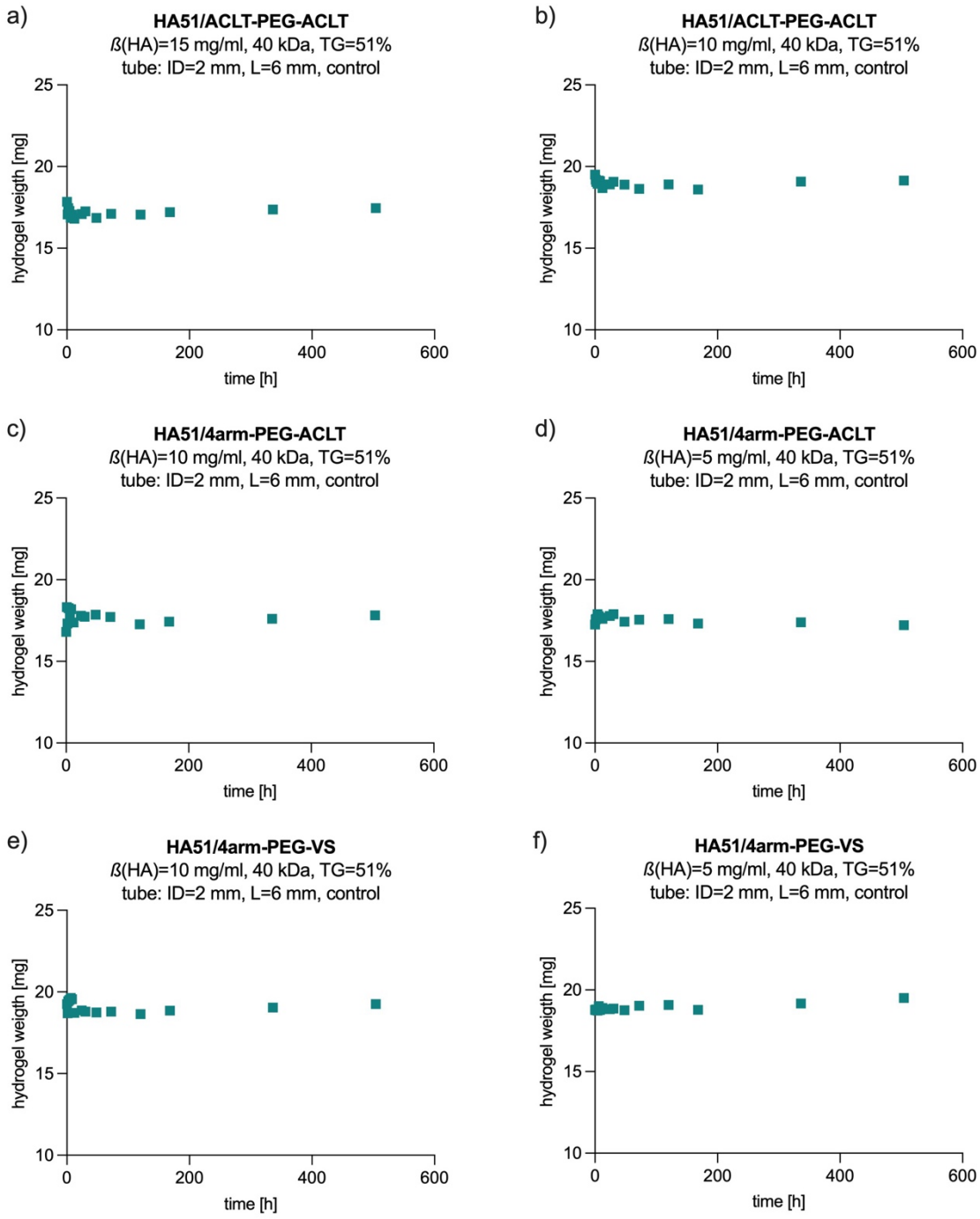

Figure 75: Exemplary graphs for controls of small HA modified tubes (ID=2 mm, l=6 mm) with different hydrogel compositions immobilized on tube interior (a-f). Hydrogels were formed using HA51 with different mass concentrations (β(HA)= 5, 10 and 15 mg/ml) and different crosslinker: ACLT-PEG-ACLT (a/b), 4arm-PEG-ACLT (b/c) and 4arm-PEG-VS (e/f). After hydrogel swelling, tubes were incubated in PBS (pH 7.4) at room temperature and hydrogel weigth was determined over three weeks. As expected, the weigth of the hydrogels were constant over the course of three weeks.

6.5 Pressure Measurements of HA Hydrogel-Modified Model Tubes

6.5.1 Physiological Flowrate Measurements of HA/PEG Hydrogels

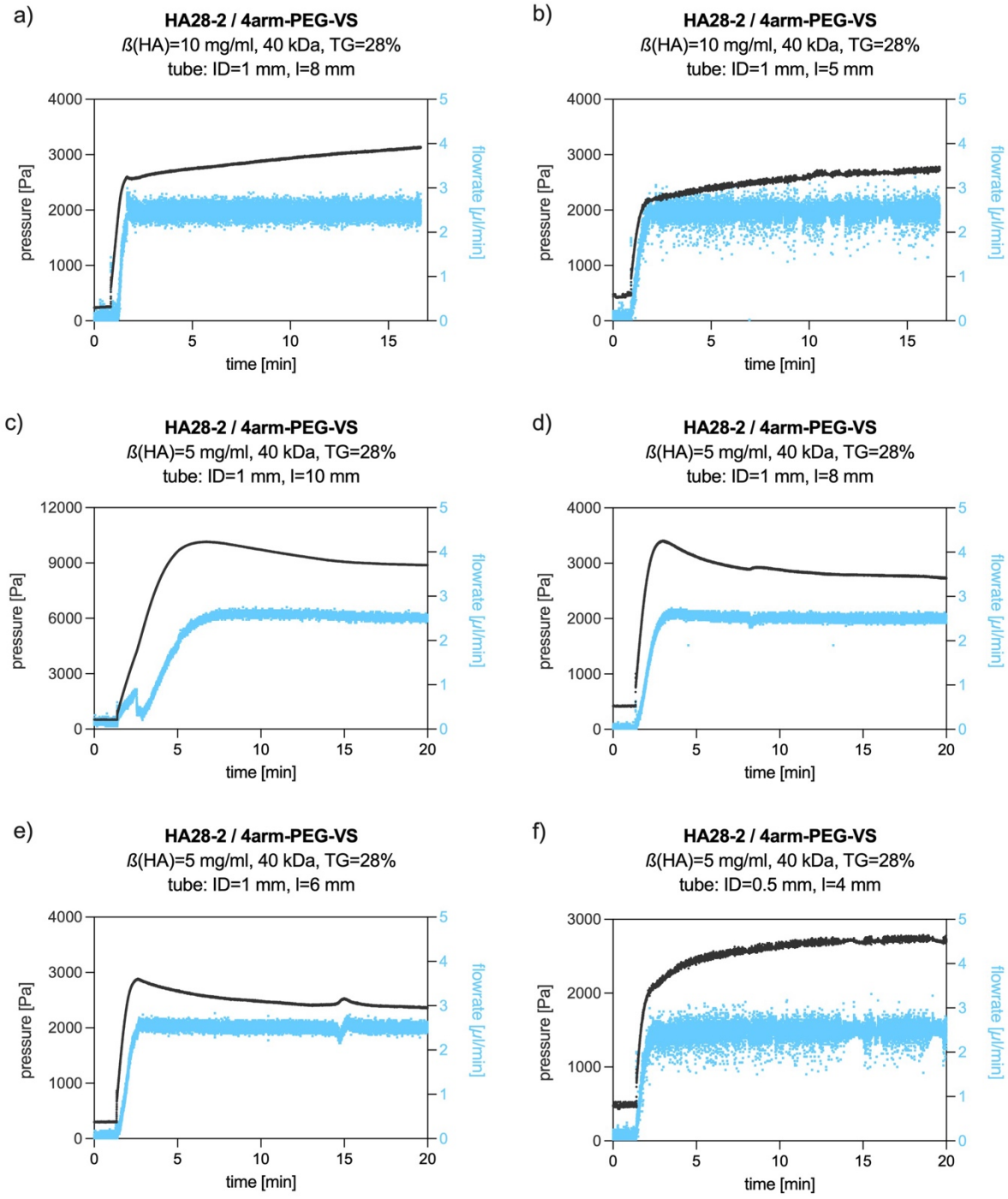

Figure 76: Equilibrium pressure measurements of small HA hydrogel modified tubes (ID=1 mm, l=10, 8, 6, 5 and 4 mm) with HA28-2/4arm-PEG-VS, (*β*(HA)=15 mg/ml, 100 kDa, TG=44 %) at a set flowrate of 2.5 µl/min. For all tubes pressure increased until the set flowrate of 2.5 µl/min was reached and remained constant over the measurement or adapted to maintain the flowrate. In the graphs, the pressure was illustrated by the dark grey curve, the blue curve represented the flowrate.

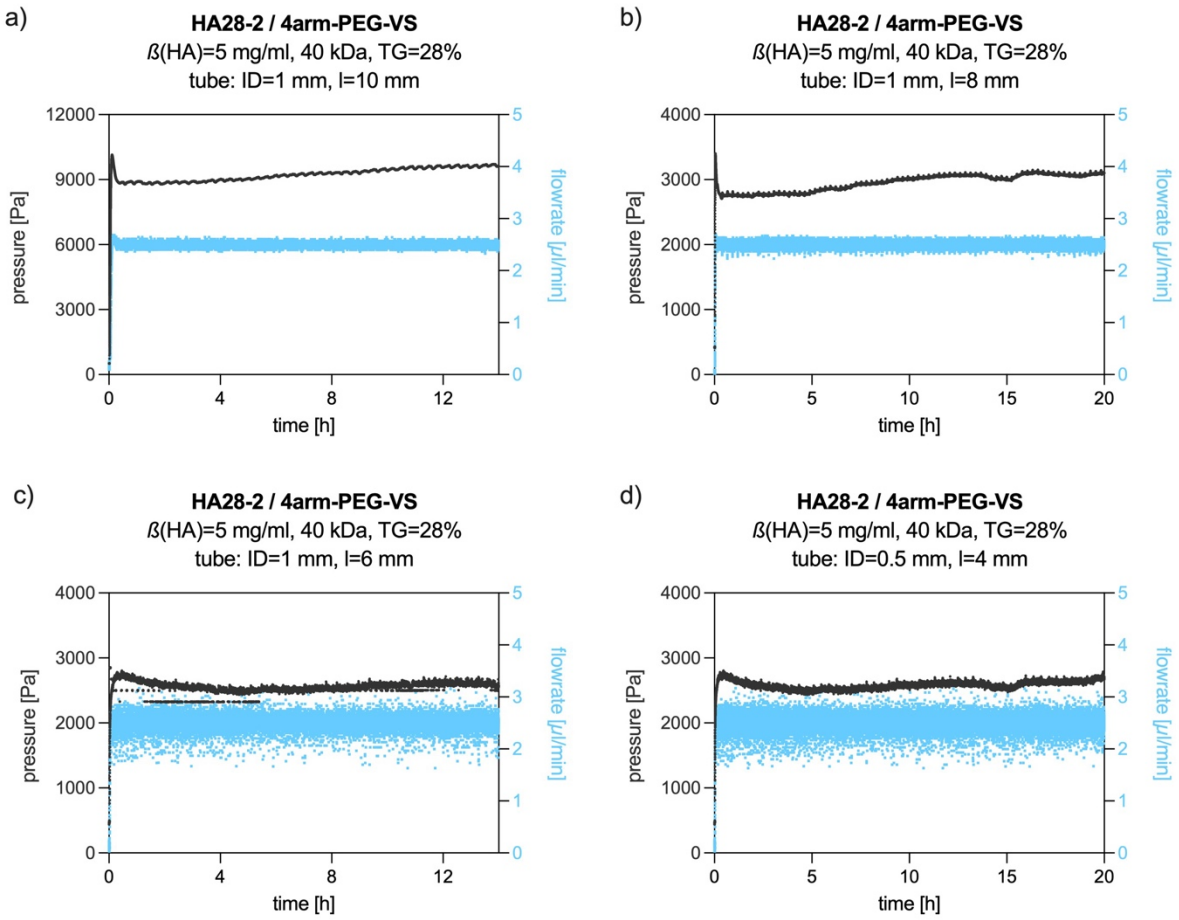

Figure 77: Long-term measurements for the determination of equilibrium pressures of small HA hydrogel modified tubes (ID=1 mm, l=10, 8, 6 and 4 mm) with HA44-1/4arm-PEG-VS (*ß*(HA)=5 mg/ml, 40 kDa, TG=28 %) at a set flowrate of 2.5 µl/min. Tubes were measured over 15 h (a/c) and 20 h (b/d) and showed constant pressure regulation abilities over the course of the measurement. In the graphs the pressure was illustrated by the dark grey curve; the blue curve represented the flowrate.

6.5.2 Pressure Fluctuations Measurements

Long-Term Measurements of HA/MBAA Hydrogel-Modified Tubes

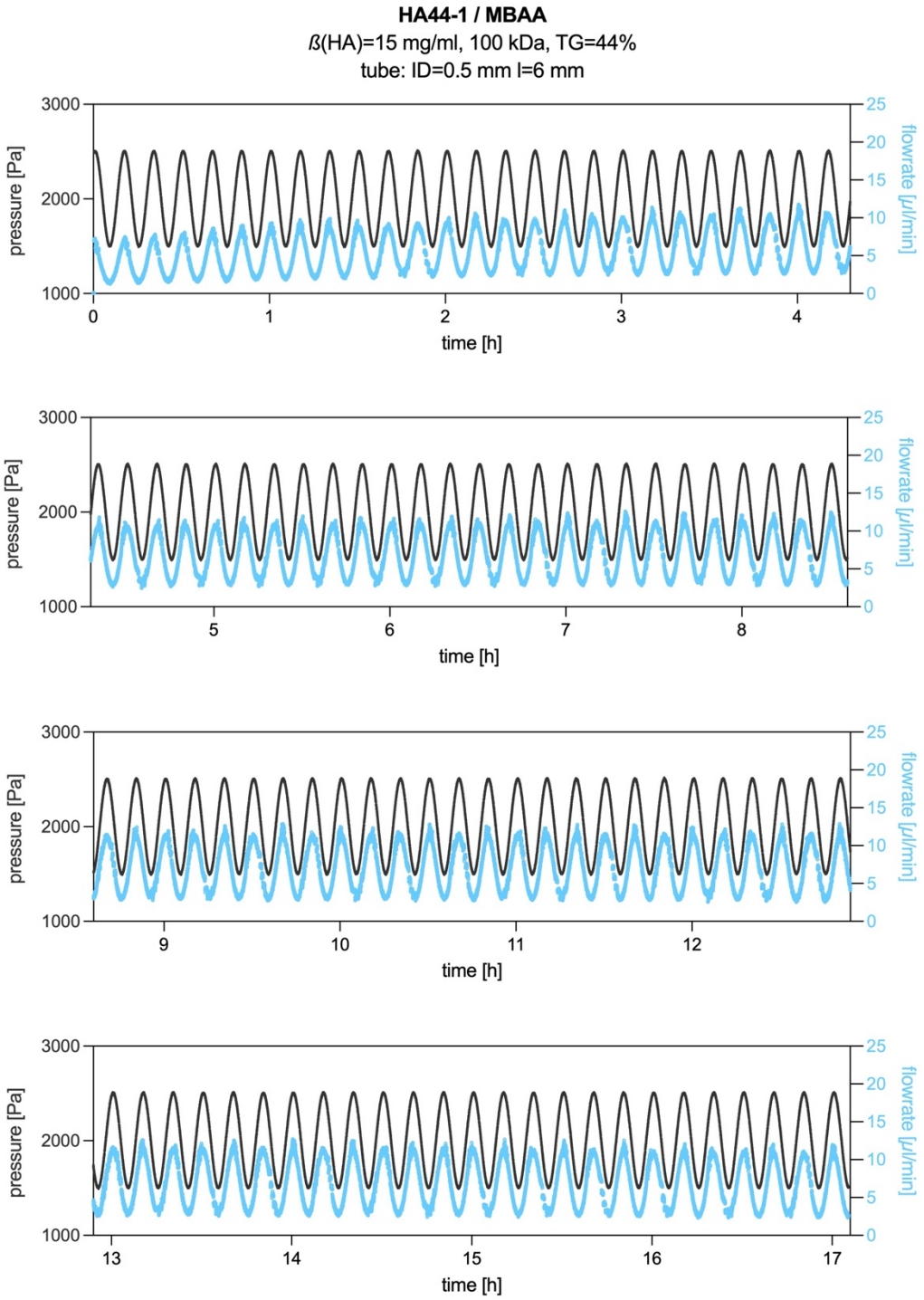

Figure 78: Long-term measurement of fluid flow during pressure fluctuation. Small hydrogel modified tube of ID=0.5 mm and l=6 mm with HA44-1 and MBAA (β(HA)=15 mg/ml, 100 kDa, TG=44 %) was measured in a pressure sine mode, whereby pressure was fluctuated in a pressure range of 1500 to 2500 Pa over a period of ~17 h. Measured flowrate ranged between 1 and 12 µl/min. Dark grey curve in the figure displayed the applied pressure, the blue curve showing the measured flowrate.

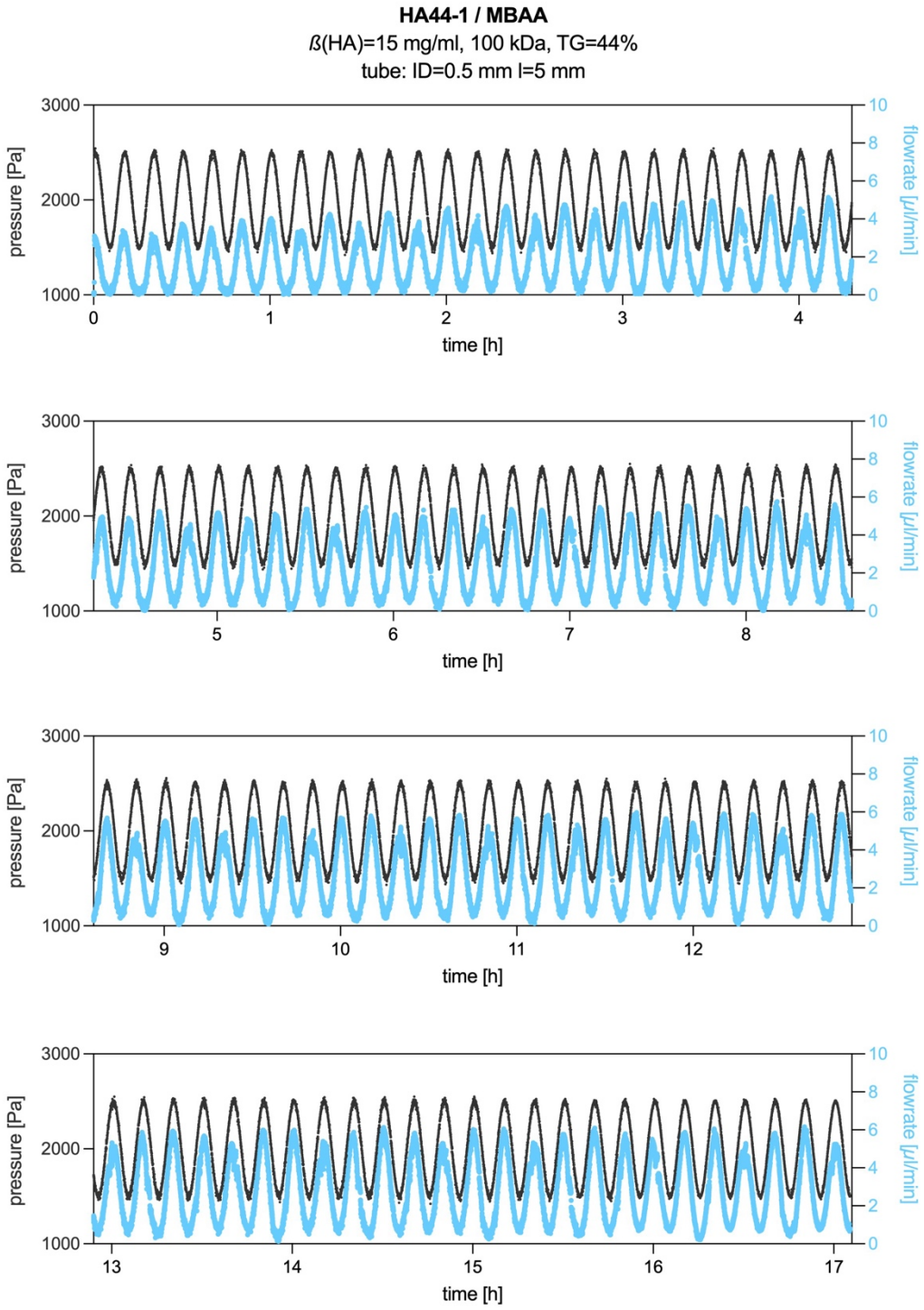

Figure 79: Long-term measurement of fluid flow during pressure fluctuation. Small hydrogel modified tube of ID=0.5 mm and l=5 mm with HA44-1 and MBAA (β(HA=)15 mg/ml, 100 kDa, TG=44 %) was measured in a pressure sine mode, whereby pressure was fluctuated in a pressure range of 1500 to 2500 Pa over a period of ~17 h. Measured Flowrate ranged between 0 and 6 µl/min over the course of the measurement. Dark grey curve in the figure displayed the applied pressure, the blue curve showing the measured flowrate.

Measurements of HA/4arm-PEG-VS Hydrogel-Modified Tubes

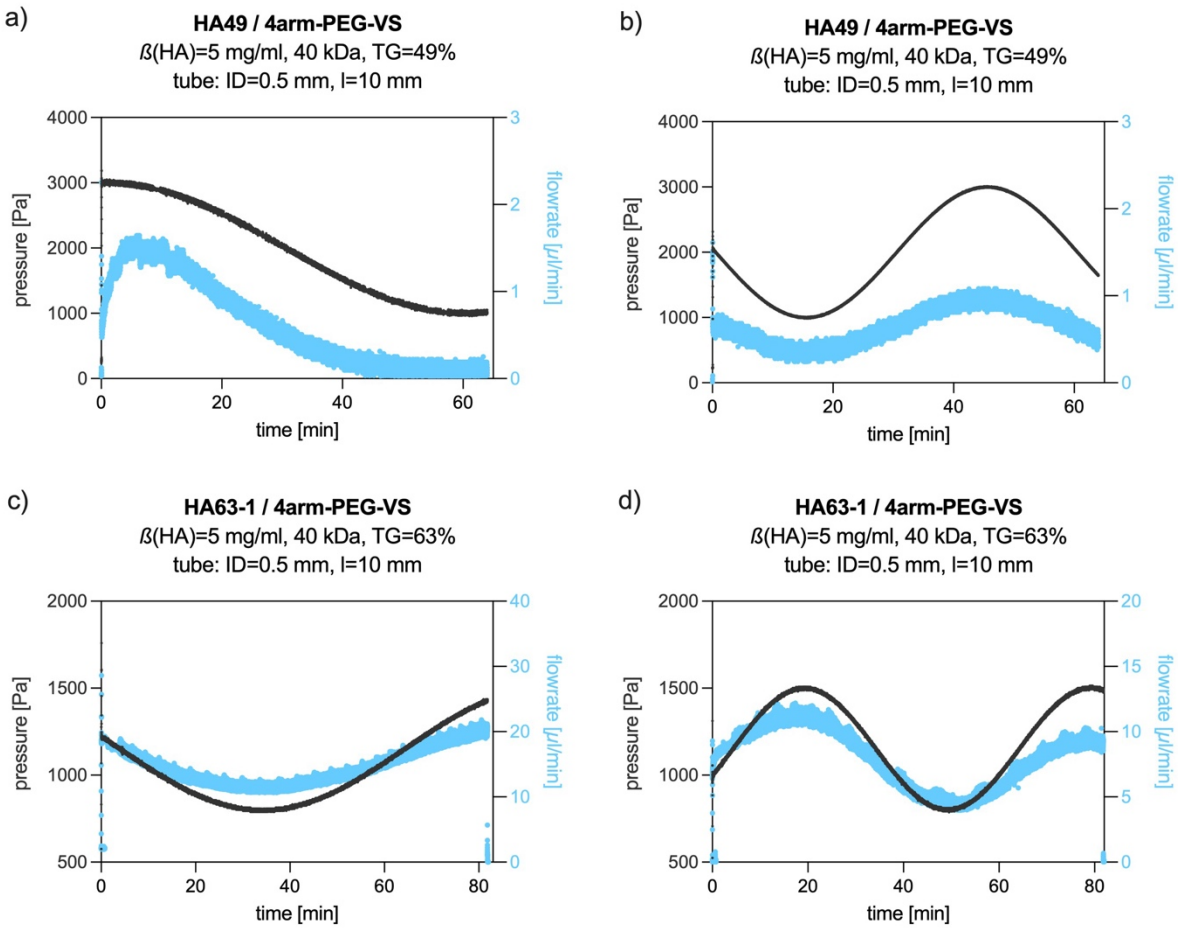

Figure 80: Measurements of fluid flow during pressure fluctuations in different time intervals (a-d). Small hydrogel modified tubes with ID=0.5 mm and l=10 mm with HA49/4arm-PEG-VS and HA63-1/4arm-PEG-VS (β(HA=)5 mg/ml, 40 kDa, TG=44 % and TG=63 %) were measured in a pressure sine mode, whereby pressure was fluctuated in a pressure range of 800 to 3000 Pa in a time interval of 7200 s (a), 3600 s (b), 7200 s (c) and 3600 s (d). For each tube, fluid flow adapted to the applied pressure., the flowrates ranged between 0-1 µl/min (a/b), 10-20 µl/min (c) and 5-10 µl/min (d). Dark grey curve in the figure displayed the applied pressure, the blue curve showing the measured flowrate.

6.5.3 Pressure Measurements with Improved Setup

Pressure Regulation of HA51/ACLT-PEG-ACLT Hydrogel-Modified Tubes

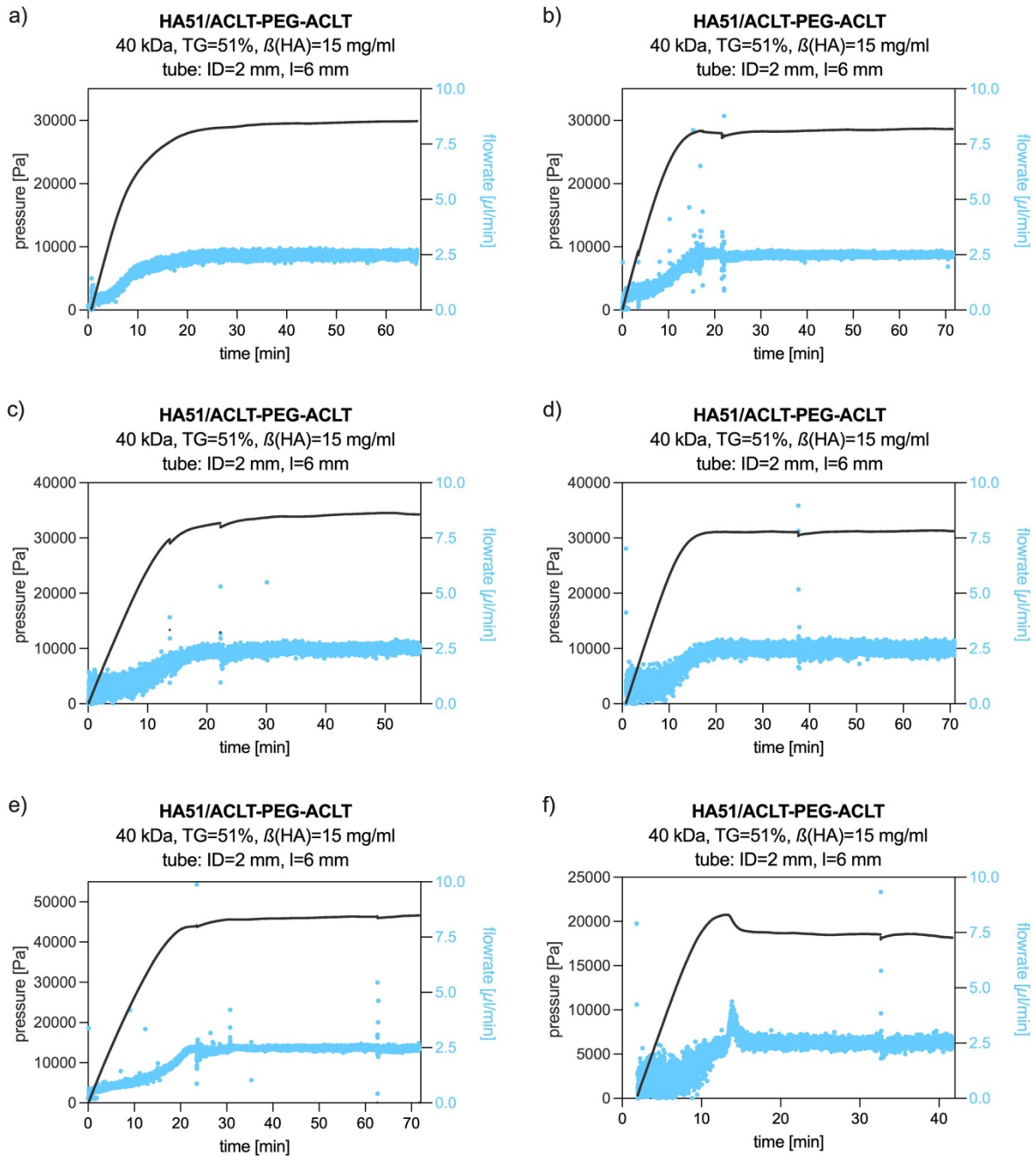

Figure 81: Exemplary pressure measurements of small glass model tubes (ID=2 mm and l=6 mm) modified with HA51/ACLT-PEG-ACLT (*β*(HA)=15 mg/ml) and measured with improved setup at a conventional flowrate of 2.5 µL/min. For each measurement the results showed a gradual increase of pressure until the desired flowrate of 2.5 µL/min was reached and remained constant over the course of the measurement. The values for the equilibrium pressures were in the range of activation pressure: 29398±449 Pa (a), 28391±380 Pa (b), 31135±366 Pa (c), 33841±686 Pa (d), 45761±986 Pa (e), 18558±305 Pa (f). Dark grey curve in the figure displayed the applied pressure, the blue curve showing the measured flowrate.

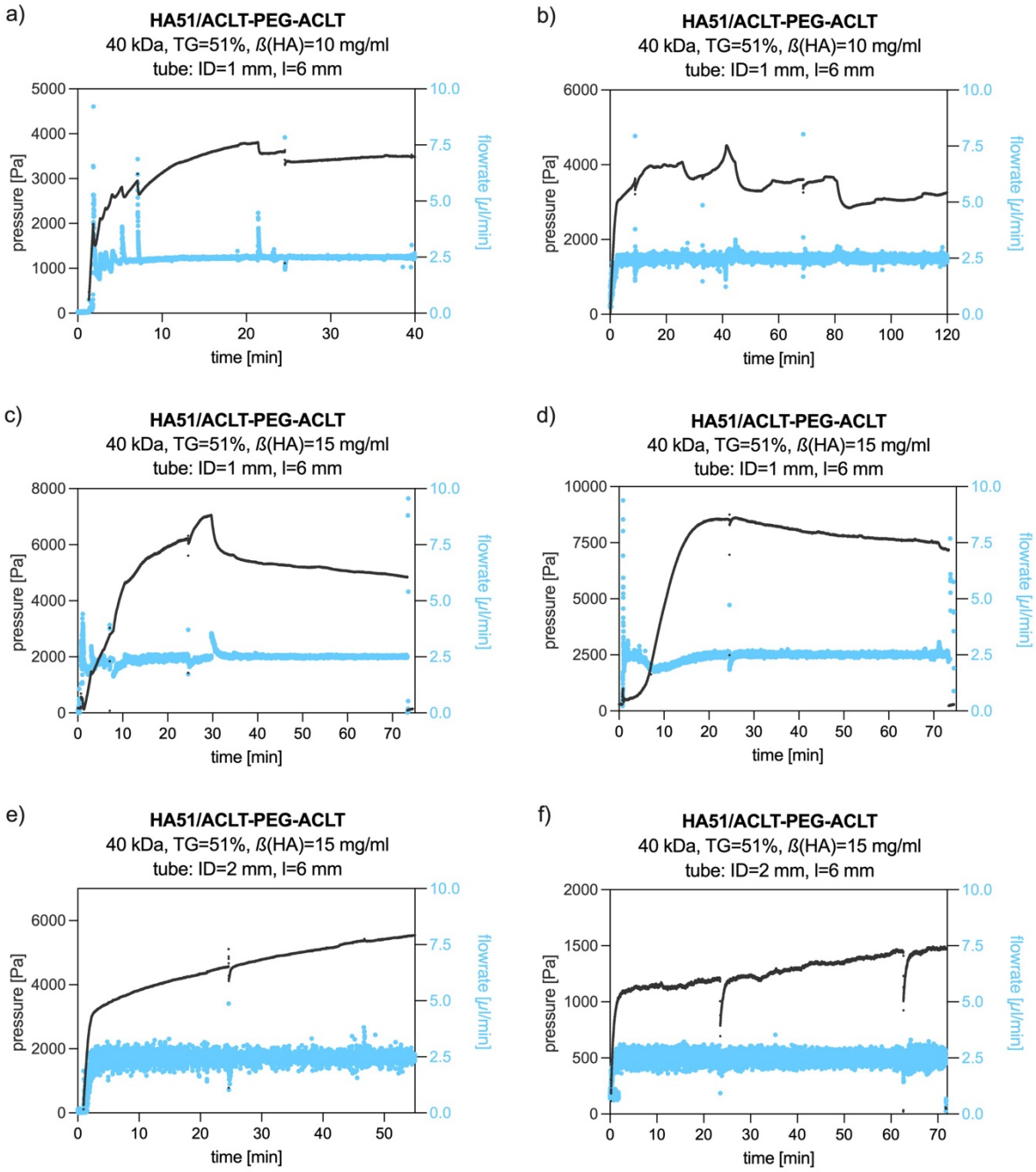

Figure 82: Exemplary pressure measurements of small glass model tubes (ID=1 and 2 mm and l=6 mm) modified with HA51/ACLT-PEG-ACLT (*β*(HA)=10 and 15 mg/ml) and measured with improved setup at a conventional flowrate of 2.5 µL/min. For each measurement the results showed a gradual increase of pressure until the desired flowrate of 2.5 µL/min was reached and remained constant over the course of the measurement. The values for the equilibrium pressures were in the range of normal IOP: 3394±354 Pa (a), 3112±442 Pa (b), 6149±201 Pa (c), 7829±277 Pa (d), 4812 Pa ± 498 Pa (e), 1295 Pa ± 118 Pa (f). Dark grey curve in the figure displayed the applied pressure, the blue curve showing the measured flowrate.

Pressure Regulation of HA51/4arm-PEG-ACLT Hydrogel-Modified Tubes

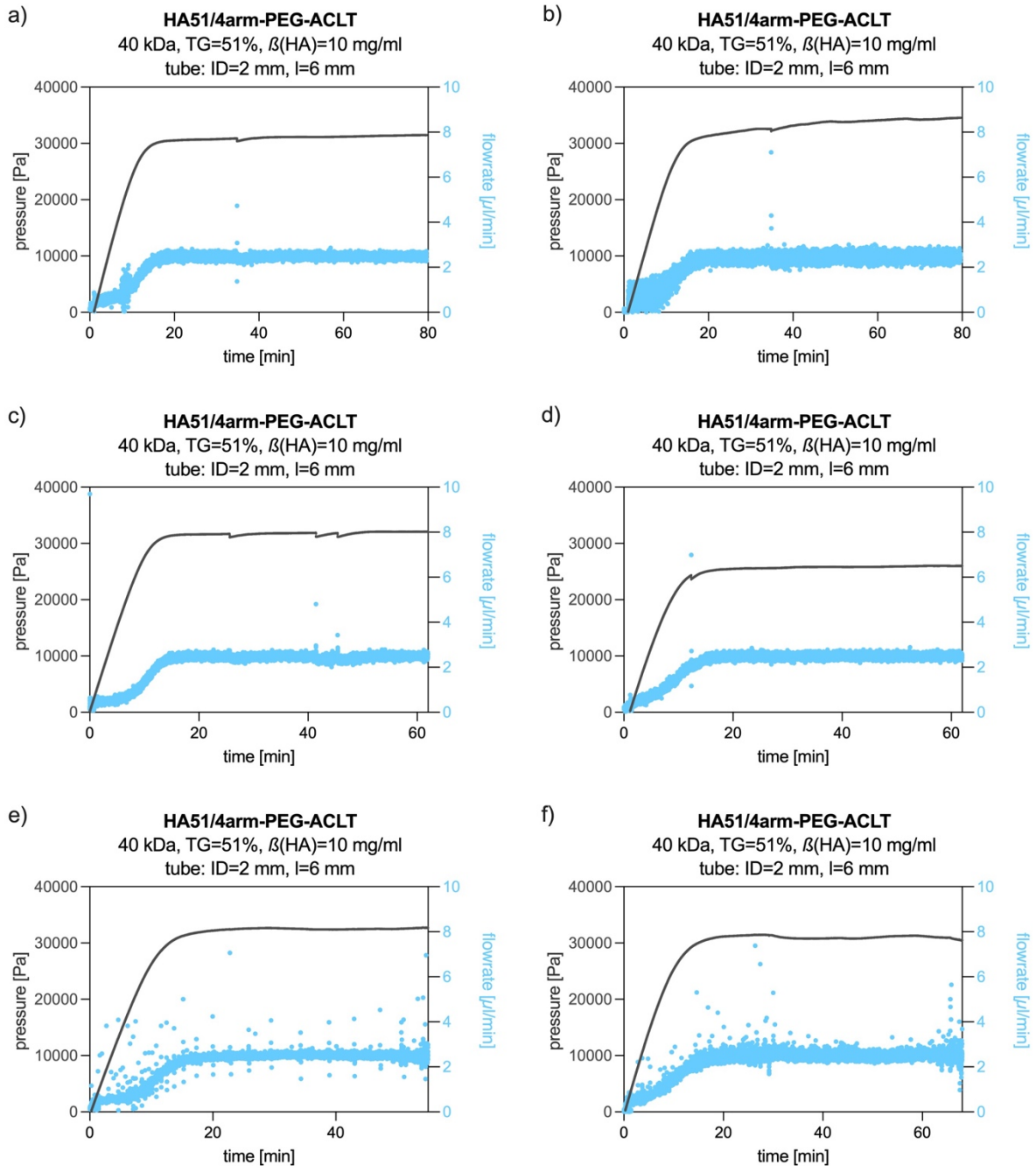

Figure 83: Exemplary pressure measurements of small glass model tubes (ID=2 mm and l=6 mm) modified with HA51/4arm-PEG-ACLT (*β*(HA)=10 mg/ml) and measured with improved setup at a conventional flowrate of 2.5 µL/min. For each measurement the results showed a gradual increase of pressure until the desired flowrate of 2.5 µL/min was reached and remained constant over the course of the measurement. The values for the equilibrium pressures were in the range of activation pressure values: 31,061±397 Pa (a), 33,440±963 Pa (b), 31,764±403 Pa (c), 25,811±146 Pa (d), 32,509±102 Pa (e), 31,059±308 Pa (f). Dark grey curve in the figure displayed the applied pressure, the blue curve showing the measured flowrate.

Pressure Regulation of HA51/4arm-PEG-VS Hydrogel-Modified Tubes

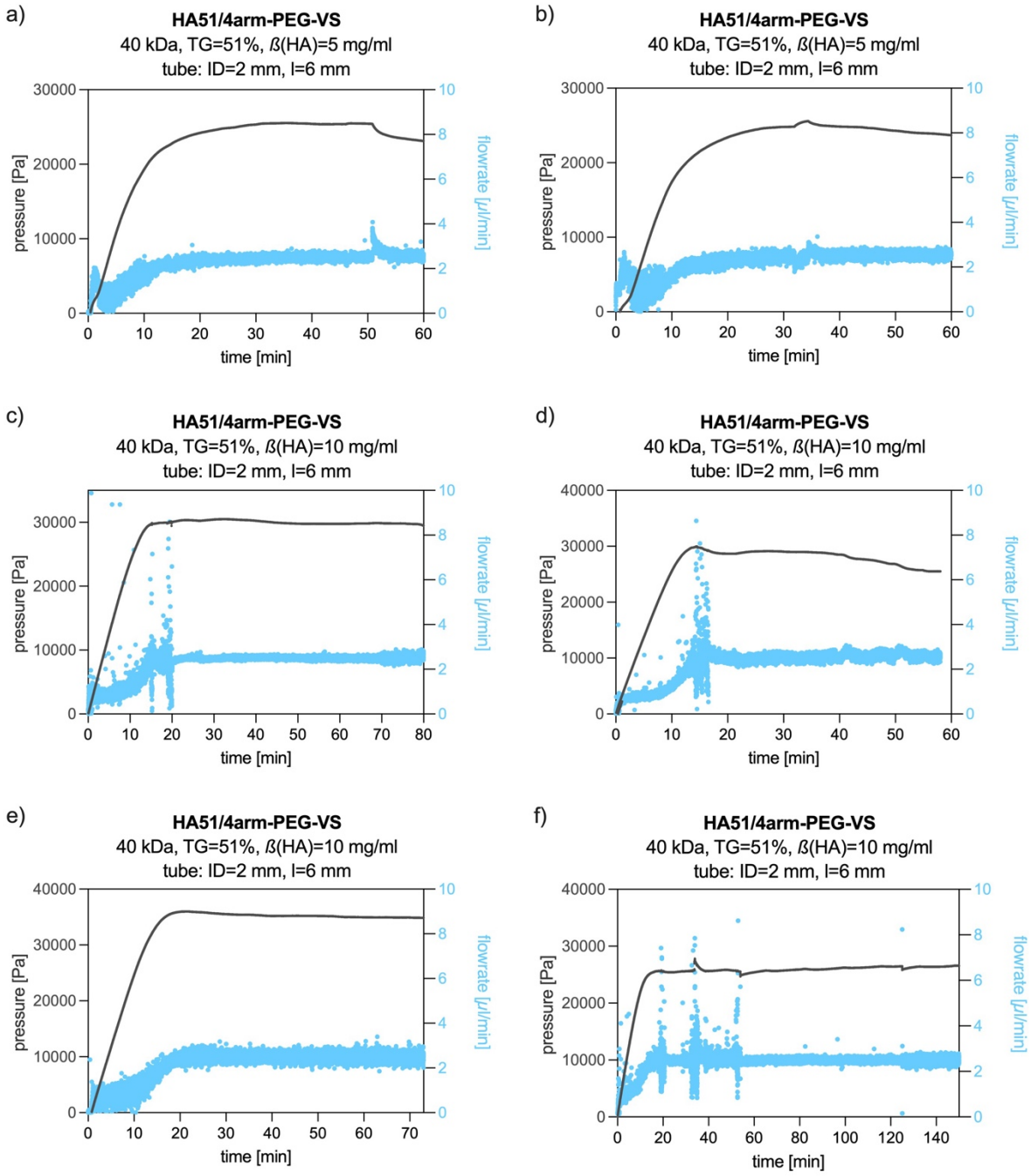

Figure 84: Exemplary pressure measurements of small glass model tubes (ID=2 mm and l=6 mm) modified with HA51/4arm-PEG-ACLT (*β*(HA)=5 and 10 mg/ml) and measured with improved setup at a conventional flowrate of 2.5 µL/min. For each measurement the results showed a gradual increase of pressure until the desired flowrate of 2.5 µL/min was reached and remained constant over the course of the measurement. The values for the equilibrium pressures were in the range of activation pressure values: 24,890±760 Pa (a), 24,011±852 Pa (b), 30,007±266 Pa (c), 27,925±1248 Pa (d), 35,24±319 Pa (e), 25,991±451 Pa (f). Dark grey curve in the figure displayed the applied pressure, the blue curve showing the measured flowrate.

Part II:

Design and Investigation of a Model for Ocular Calcification

7 Introduction – Part II

7.1 Microfluidics

In the second part of this thesis, a microfluidic approach was used to develop a droplet-based mineralization model that simulates the biological mineral formation of CaP within MVs.
Over recent years, microfluidic technology has become a widely used approach for diverse applications at the microscale across various scientific and industrial fields [280]. It enables precise manipulation of extremely small volumes, reduces reaction times and costs and offers the ability to run multiple reactions simultaneously, thereby improving the efficiency and control of microscale operations and chemical reactions [280, 281].
The primary objective of microfluidics is to develop miniaturized versions of macroscale bulk systems, ultimately creating a lab-on-a-chip, that combines multiple biological, chemical and analytical functions on a single microchip [282, 283]. Such lab-on-a-chip system encompasses tools for chemical synthesis [282, 284], biological analysis [285, 286] and diagnostic applications for medicine [287-291]. In the realm of diagnostics, microfluidic devices have become essential in the development of point-of-care (POC) technologies [292]. Widely known established POC devices are for example pregnancy tests [293], glucometers [293, 294], or diagnostic tests for infectious diseases such as COVID [292] and HIV [295]. These devices have revolutionized patient monitoring by providing rapid, reliable results outside traditional laboratory settings [292].
For the integration of microfluidics in mineralization studies, it is essential to understand the physical principles that dominate at the microscale. The next section will give an overview of the key physical parameters.

7.1.1 Physics of Microscale Fluid Dynamics

For the design of microfluidic devices and approaches, it is important to understand the basic principles of fluid dynamics and the parameters and forces influencing fluid flow at the microscale.

Reynolds Number and Laminar Flow

In microchannels, flow patterns of fluids can be characterized by the Reynolds number (Re), a dimensionless quantity used to distinguish between turbulent and laminar flow regimes. The Reynolds number combines fluid properties, geometry properties and flow velocity [296] and is defined as:

$$Re = \frac{\rho v D_H}{\mu}$$

With ρ being the fluid density, v being the flow velocity and μ is the dynamic viscosity of the fluid.

D_H is the hydraulic diameter, a computed value that depends on the cross-sectional geometry of the channel:

$$D_H = \frac{4A}{P}$$

With A being the cross-sectional area and P the wetted perimeter of the channel.

Turbulent flow regimes occur at Re values >3000 [297] (figure 85a). They are inherently chaotic, making it extremely challenging to predict the exact position or trajectory of a particle within the fluid over time [280]. However, due to the small dimensions typical of microchannels, turbulent flow is rare in such systems and is almost always laminar [298].
Laminar flow, characterized by fluid movement in parallel layers without disruption, is the dominant flow regime at Re numbers <<2000 [297] (figure 85b). In the intermediate range (3000>Re>>2000), a transitional flow regime is expected, wherein the flow exhibits characteristics of both laminar and turbulent patterns [299].

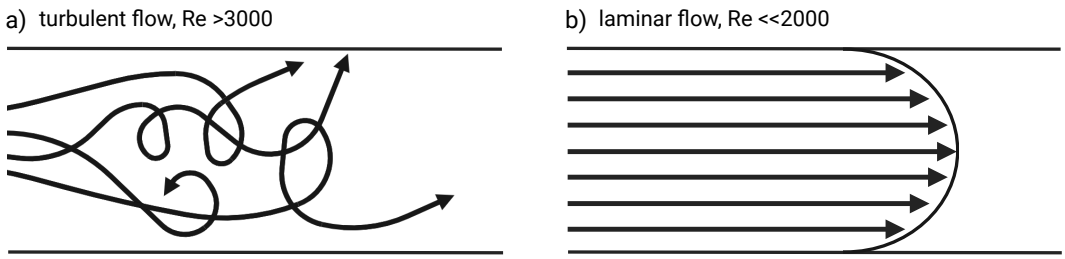

Figure 85: Schematic illustration of turbulent and laminar flow regime in microfluidic channel. The drawing was adapted from the literature [299, 300] and created with Biorender.com.

Diffusion

In microfluidic devices, the laminar co-flow of two (or more) fluids occurs without mixing, except by diffusion at the fluid interfaces, driven by the concentration gradient [280] (figure 86).
The mixing efficiency is determined by the diffusion coefficient D of the solutes and the dimensions of the channel [280]. The diffusion process can be expressed in one dimension by the equation [280]:

$$d^2 = 2Dt$$

Whereby d is the distance a particle moves in cm, in a time t in s, and D is the diffusion coefficient in cm^2/s. Since the distance varies to the square power, and due to the small dimensions in microfluidic channels, the diffusion becomes very important on the microscale [280]. Compared to macroscale systems, the diffusion timescale is relatively short and becomes the dominant mechanism for mixing [280].
When producing water-in-oil droplets for biomineralization studies, it is essential to ensure that the mixing of the fluids occurs within the droplets, rather than in the microfluidic channels, to

avoid clogging of the channel with mineralized particles. For this, our microfluidic channels are designed with very short cross-sectional dimensions. For a detailed overview of the droplet-based mineralization setup used in this study and exact dimensions of the channels refer to chapter 8.

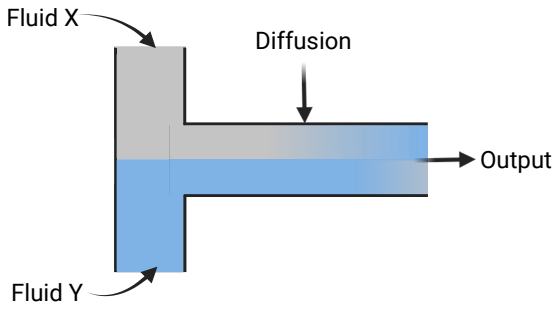

Figure 86: Illustration of diffusion in microfluidic channel. Mixing of two fluids (X and Y) occurs only by diffusion at fluid interfaces. The drawing was adapted from the literature [280] and created with BioRender.com.

Surface Tension

Another force at the microscale which significantly influences fluid behavior in microfluidic systems is the surface tension [280, 301]. Surface tension arises due to cohesive forces between liquid molecules at the liquid-gas or liquid-liquid interface of two immiscible fluids, like water and oil [280]. It can be quantitatively described by the surface free energy (γ) of a liquid, representing the amount of energy required to increase the surface area of the liquid [301]. To minimize the surface energy, liquids naturally tend to reduce their interface area, which explains the formation of droplets into spherical shapes [280], as seen in emulsions or droplets in microfluidic systems. The pressure difference across a curved liquid surface, known as the Laplace pressure ΔP, can be calculated using the Young-Laplace equation [302, 303]:

$$\Delta P = p_{in} - p_{out} = \gamma \left(\frac{1}{R_1} + \frac{1}{R_2} \right)$$

Whereby, R_1 and R_2 represent the perpendicular radii of curvature of the surface and γ being the surface free energy. For a perfectly spherical droplet (R_1=R_2), the equation simplifies to:

$$\Delta P = \frac{2\gamma}{R}$$

The reduced form shows that the internal pressure within a droplet increases as its radius decreases.

7.2 Droplet-Based Microfluidics

7.2.1 Emulsions

Droplet-based microfluidics uses emulsions to compartmentalize and manipulate fluids at the microscale [299]. Emulsions are dispersions or colloidal mixtures of one liquid phase within another immiscible phase, such as water-in-oil (W/O) or oil-in-water (O/W) systems, forming small droplets [304]. These systems are familiar in everyday life, such as milk or salad dressings.
In microfluidics, W/O emulsions are commonly used, where the oil acts as a continuous phase and the aqueous (dispersed) phase forms the droplets inside [305]. These systems are widely used because of their ability to isolate small volumes for biochemical reactions, drug synthesis and drug screening [306]. Beyond single emulsions, more complex systems are also possible as the formation of double or multiple emulsions, e.g. water-in-oil-in-water (W/O/W) systems [307, 308]. These double-layer emulsions can be used for controlled drug delivery, providing sustained release properties or protection of sensitive substances [306].

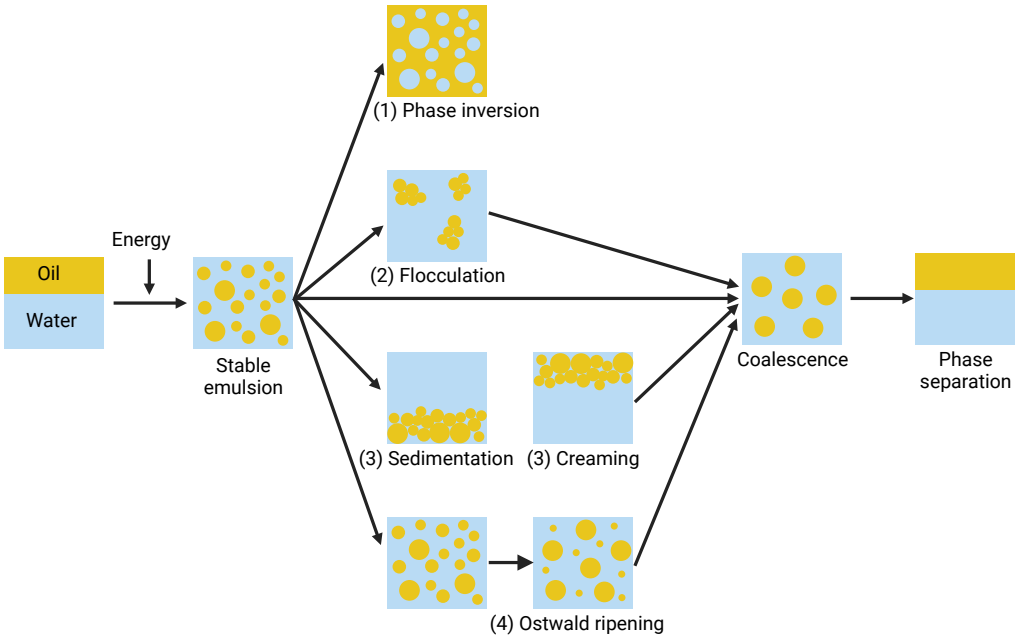

Figure 87: Schematic illustration of different mechanisms in emulsions. The Scheme was adapted from Hu et al. [305] and redrawn with Biorender.com.

The strong intermolecular forces between two immiscible phases, such as water and oil, prevent the spontaneous formation of emulsions due to their tendency to minimize the interfacial area which lowers the system's overall free energy [309]. Therefore, energy input is always required to separate the two phases and produce emulsions, a process also known as homogenization [299, 300, 310]. This energy can be applied mechanically, for example by vigorous shaking or stirring, or by using microfluidic systems [299, 310]. Emulsions are inherently unstable and without stabilizers, such as emulsifiers or surfactants, they tend to separate again over time, with different possible intermediate steps leading to coalescence (fusion of droplets) and finally to phase separation [307] (see figure 87). The instability mechanisms of emulsions include (1) phase inversion: the

continuous phases switches, turning oil droplets (continuous phase) into aqueous phase; (2) flocculation: droplets aggregate to grape-like structures as a result of attractive interactions between each other; (3) sedimentation or creaming: droplets either sink or rise, due to density differences between the phases; (4) Ostwald ripening: emulsion contains droplets of different sizes, as smaller droplets shrink, while larger droplets grow [303, 305]. It is therefore necessary to stabilize the droplets using emulsifiers or surfactants to counteract the phase separation.

7.2.2 Surfactants

Emulsions can be stabilized using surfactants (surface-active-agents). Due to their amphiphilic nature (hydrophilic head and hydrophobic tail), they are able to adsorb at the interface of two immiscible fluids, thereby reducing the surface tension of the interfacial region [311]. Surfactants form a protective monolayer around the droplets (figure 88a), preventing them from coalescing and stabilizing them for extended periods [304, 312-314].

The most commonly used surfactants for droplet stabilization, are fluorinated block copolymer surfactants [312]. In this thesis, a triblock copolymer was used, consisting of two hydrophobic perfluoropolyether (PFPE) chains attached to one hydrophilic PEG head, building a PFPE-PEG-PFPE block copolymer (figure 87b).

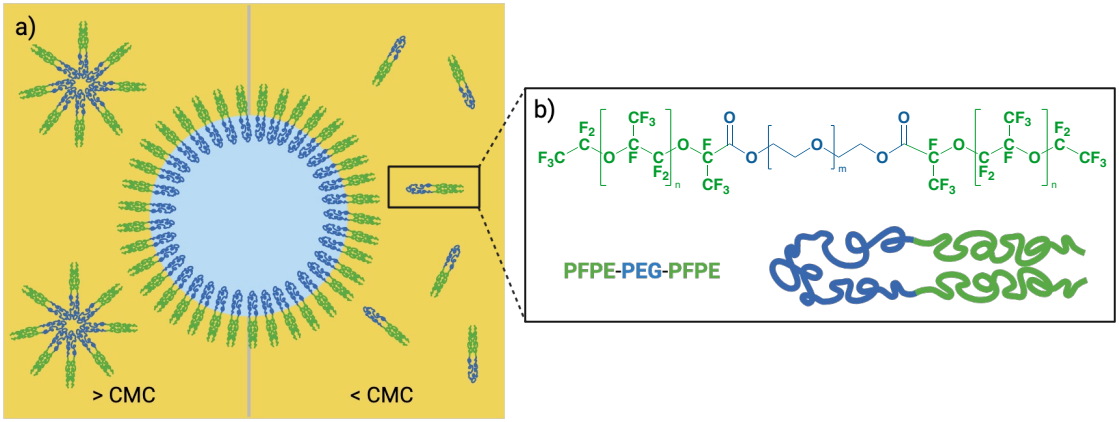

Figure 88: Schematic representation of droplet stabilization by surfactants at the interface of two immiscible fluids. Above the critical micellar concentration (CMC) the surfactant molecules begin to aggregate into micelles (a). Surfactant used in this study: perfluoropolyether-polyethylene glycol-perfluoropolyether (PFPE-PEG-PFPE), with two hydrophobic chains and one hydrophilic head (b). The drawing shown in a) was adapted from Haller [310] and redrawn using Biorender.com.

Surfactant Adsorption and Critical Micellar Concentration (CMC)

The adsorption of surfactants at the interface of two immiscible phases is mediated by the Gibbs free energy and can be calculated by the Gibbs adsorption equation [315]:

$$\Gamma = -\frac{c}{RT}\frac{d\gamma}{dc_b}$$

Whereby Γ being the surface concentration, R the ideal gas constant, T the absolute temperature, γ the surface tension and c_b the surfactant concentration in the bulk [315]. This equation shows,

that the surface tension directly depends on the amount of surfactant molecules adsorbed at the interface, which means the more surfactant molecules adsorbed, the lower the surface tension [315]. However, the Gibbs equation applies only for surfactant concentrations below a certain threshold [316]. Once the interface becomes fully saturated additional surfactant molecules do not further decrease the surface tension, instead, these molecules begin to aggregate into supramolecular structures, called micelles [317]. The concentration at which theses micelles begin to form is known as the critical micellar concentration (CMC) (figure 87b), and depends also on the solvents properties [317]. For fluorosurfactants at water-oil interfaces the typical CMC is 4 µM [309].

7.2.3 Droplet Production via Microfluidics

Droplet-based microfluidic technology is a highly versatile tool, that allows precise manipulation and production of surfactant-stabilized monodisperse emulsions in the femtoliter- to nanoliter-scale with controlled high throughout [318-321]. The main concept relies on encapsulating an aqueous phase into an immiscible continuous phase (oil) using microfluidic chips. A basic microfluidic chip design consists of two fluid channels (one for the aqueous, one for the oil phase), where the aqueous phase is cut by the oil phase producing uniform W/O droplets [322] (figure 89). Droplet size can be controlled and adjusted precisely in size (between few to hundreds of micrometers), depending on flowrates and channel geometries [281, 318, 323, 324].

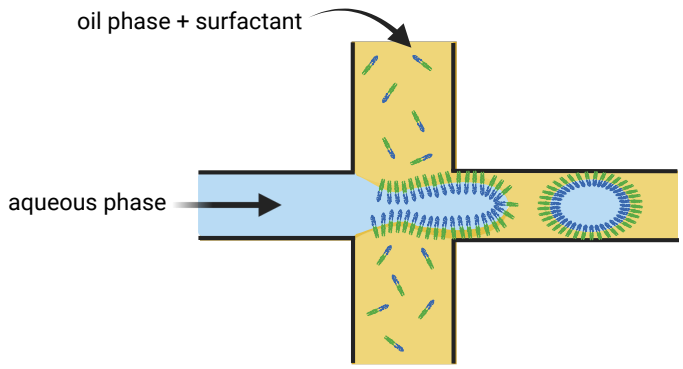

Figure 89: Schematic illustration of droplet production within a basic microfluidic device. On the cross section, the aqueous is cut by the oil phase into uniform droplets, stabilized by surfactants The drawing was created with BioRender.

Each droplet is an individual controllable reaction chamber, that can be used for high-throughput observations of chemical and biological reactions under well-defined conditions [325-327]. Droplet-based microfluidics allows a robust parallel processing of a large (unlimited) amount of uniform droplets, which enables the generation of statistically significant datasets, providing reliable and reproducible results. Within these droplets different components can be encapsulated, from single molecules or proteins to whole cells [328], and the droplets can be also further manipulated by techniques such as deformation, division, fusion, incubation or sorting [329]. The designs and geometries of microfluidic devices, droplet generation methods, such as flow focusing [320, 322, 330, 331] or T-junction devices [321] [332], as well as manipulation techniques are

manifold and can be adjusted for each experimental setup individually [333]. This flexibility makes droplet-based microfluidics suitable for diverse applications, and also for biomineralization studies, as shown in this thesis.

7.3 Droplet-Based Model for Mineralization Studies

In the second part of this thesis a new approach for mineralization studies of CaP was developed and investigated using droplet-based microfluidics. Current mineralization models present significant challenges and limitations: bulk systems are simple models but lack precise control [334], while models such as polymeric vesicles offer better control but are complex and labor-intensive [335]. This new droplet-based approach bridges the gap between these systems by combining simplicity with controllability. It mimics the spherical geometry of MVs, functioning as individual controllable reaction chambers, which allows an enhanced control over mineralization conditions and enables a more reproducible and efficient high-throughput analysis of CaP mineralization processes. The main concept of the droplet-based mineralization model is shown in figure 90.

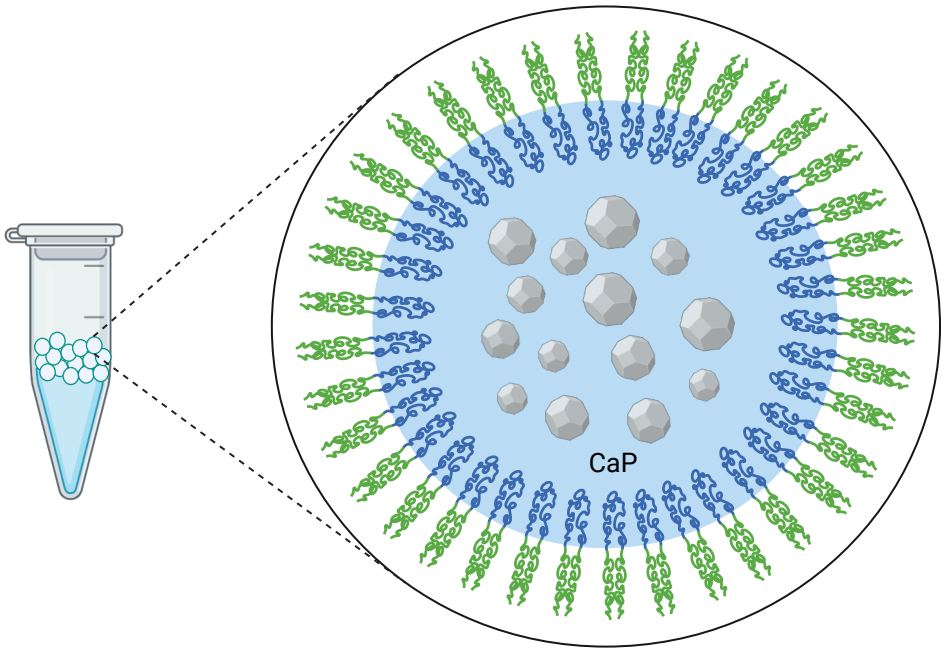

Figure 90: Schematic concept of the droplet-based mineralization model for CaP, developed and investigated in this study.

8 Materials and Methods – Part II

8.1 Microfluidic Device Production

The microfluidic device for droplet production was prepared according to a protocol adapted and modified from McDonald et al. [336]. The whole process for the production of the microfluidic devices is summarized in figure 91.

The negative master structure of the microfluidic two-channel-water system was designed by Dr. Lucia Benk using the software QCAD pro (Ribbonsoft, Switzerland) [337]. Dr. Christoph Frey transferred the design on a silicon master wafer by using photolithography as described in his Thesis [299].

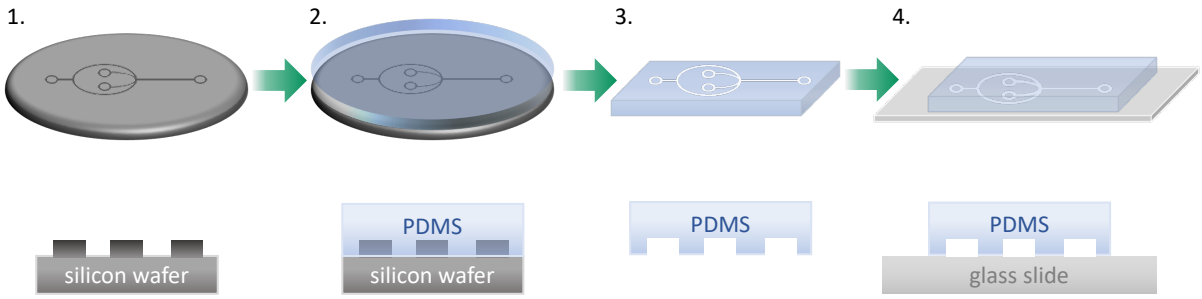

Figure 91: Schematic workflow for the production of microfluidic PDMS chips (top) with side view (bottom). 1. Silicon wafer with master structure produced by photolithography, 2. PDMS poured on the wafer and let polymerized, 3. PDMS mold was cut out, peeled off the wafer and outlet holes were punched in, 4. Chip assembly by O_2 plasma activation of PDMS mold and glass slide.

8.1.1 Materials

Chemicals, reagents, solutions and equipment	Source
Silicon wafer with the negative microfluidic channel system	Designed by Dr. Lucia Benk and prepared by Dr. Christoph Frey
Concentrated ethanol (EtOH), ROTIPURAN® (≥ 99.8%)	Carl Roth, 9065.1
SYLGARD™ 184 Silicone Elastomer Kit	Dow Silicones, 001002811545
Biopsy Puncher/Rapid Punch (Ø=0.5 mm)	WellTech, 0730K
2-Propanol/Isopropanol	VWR, 18D164006
Glass cover slides, 24 x 60 mm, #1.5 mm,	Carl Roth
O_2 Plasma	PVA TePla 100 Plasma System
SigmaCote®	Sigma Aldrich, #SLBZ2362
Novec 7500, FL-0004-HP-1000 (HFE-oil)	Ioltec, 21224

8.1.2 Preparation of Microfluidic Chips

For the preparation of the microfluidic polydimethoxysilane (PDMS) chips the following silicon wafer design as negative master structure was used, as shown in figure 92.

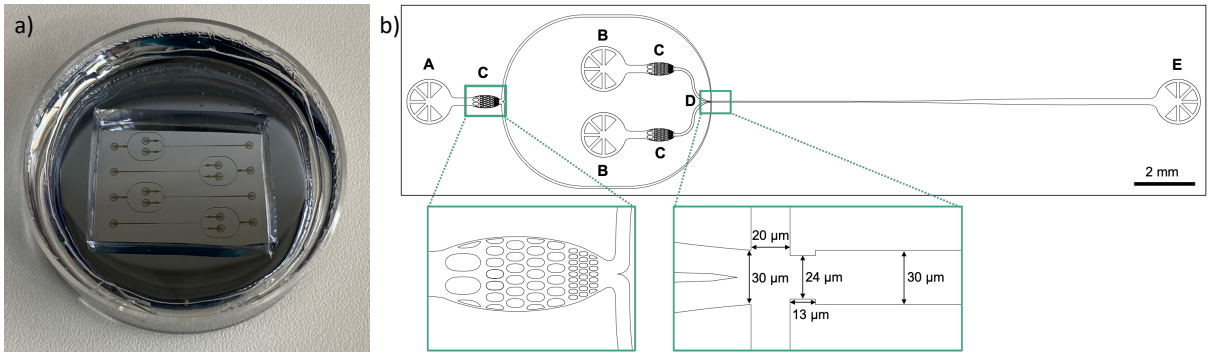

Figure 92: Picture of the silicon wafer with the negative master structure (a) and schematic drawing of the microfluidic channel system for droplet production (b). A: inlet channel for oil phase, B: inlet channels for water phases, C: filtering structure for fluids to prevent clogging, D: cross junction with corresponding channel diameters and E: droplet outlet.

The design consisted of three inlet channels, one for the oil phase (A) and the other two for the water phases (B). After inflow, the fluids were filtered by structure C to prevent clogging of the channels. On the cross junction (D), the two water phases were mixed before cutting by the oil phase and escaping as droplets to the outlet (E).

PDMS Mold Fabrication

The polydimethoxysilane (PDMS) was prepared by mixing the oligomer (siloxane base oligomer) with the polymerization catalyst (crosslinking oligomer) in a ratio of 9:1 (w/w). The silicon wafer with the structure of the microfluidic channel system was cleaned with 70 % EtOH and dried for 5 minutes at 65 °C. The PDMS was poured on the wafer and afterwards, the setup was placed in a desiccator and degassed for 30-60 minutes to avoid air bubbles in the channel structures. Full polymerization of the PDMS occurred at 65 °C for 2 h. After hardening, the PDMS mold was cut out generously by using a sharp scalpel and carefully removed from the wafer. Afterwards, the in- and outlet wholes were punched in the PDMS by using a biopsy puncher with ∅ 0.5 mm.

Chip Assembly by O_2 Plasma Treatment

For chip assembly the surfaces of PDMS molds and glass cover slides were activated by O_2 plasma treatment. Before the plasma treatment, the PDMS mold and the glass cover slide were both cleaned using 70% EtOH and nitrogen flow and dried for 5 min at 65°C. The plasma settings were 200 W, 0.45 mbar for 18 s. After the plasma treatment, the PDMS mold was strongly pressed onto the glass cover slide for covalently bonding and the chip was placed in the oven (65 °C) for 1 h to improve the sealing. Afterwards, the channels were rinsed with SigmaCote® for a hydrophobic coating and flushed with HFE-oil before the in- and outlet channels were sealed using a sellotape to avoid clogging due to dust until use.

8.2 Microfluidic Droplet Production for Calcium Phosphate Mineralization Model

For droplet-based mineralization studies of calcium phosphate two different approaches were explored (figure 93). The first one based on a bulk mineralization model of HAp as described by Jing Mao et al. [123]. In the second approach the droplet-based setup was further developed to an enzymatic mineralization model using the enzyme AP, according to bulk studies by Gungormus et al. [125, 338]. Both approaches were modified, transferred and investigated in our droplet-based setup.

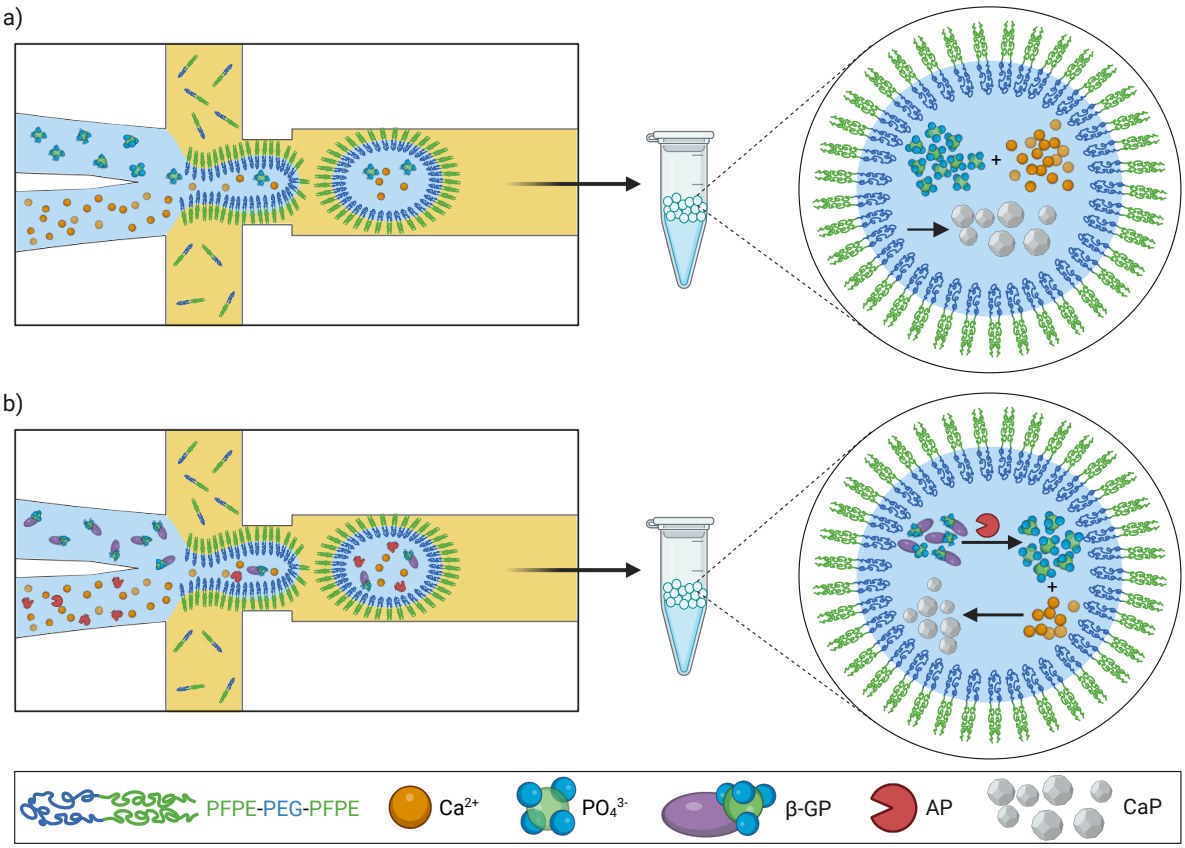

Figure 93: Schematic drawing of two different approaches for mineralization studies of CaP. Aqueous double-channel system for droplet production using two aqueous solutions ($CaCl_2$ and $NaHPO_4$) for mineralization of CaP (a). Enzymatic mineralization setup using alkaline phosphatase (AP) for controlled phosphate release from β-glycerophosphate (β-GP) and subsequent formation of CaP within the droplets (b). The picture was created using Biorender.com.

8.2.1 Materials

Chemicals, reagents, solutions and equipment	Source
Microfluidic PDMS chip with two-channel-water system	See section 8.1
Novec 7500, FL-0004-HP-1000 (HFE-oil)	Ioltec, 21224
1H, 1H, 2H, 2H-perfluoro-1-octanol (PFPE-PEG-PFPE)	Sigma-Aldrich, #MKCN8524
Calcium chloride dihydrate ($CaCl_2 * 2H_2O$)	Sigma-Aldrich, #041M00751V
Sodium di-hydrogen phosphate monohydrate ($NaH_2PO_4 * 2H_2O$)	Carl Roth, K300.1
Hydrochloric acid (HCl)	Sigma-Aldrich, 320331

Tris/HCl (TRIS), 25 mM, pH 7.4	Sigma-Aldrich, T6791
ß-Glycerophosphat (ß-GP)	Sigma-Aldrich, 154804-51-0
Alkaline phosphatase (AP)	Roche, 10713023001
Syringe pumps, Pump 11 Pico Plus Elite	Harvard Apparatus, D-303699
Plastic tubing ($\varnothing_{in}$ = 0.3 mm)	Bola, S1810-04
Syringes 1 ml ($\varnothing_{in}$ = 4.78 mm)	Henke-Ject, 0B02088
Syringe 0.5 ml ($\varnothing_{in}$ = 3.4 mm)	BD Micro-Fine, 123-I3 324825
MGP-peptides (see section 1.2.3)	Purchased from Genosphere Biotechnologies, France

8.2.2 Droplet-based Mineralization Setup with Aqueous Double-Channel System

A first and simple droplet mineralization model for CaP was investigated using two aqueous solutions for crystallization as described in previous bulk experiments by Mao et al. [123]. The approach was summarized in figure 93a, whereby the mineralization started when Ca^{2+} and PO_4^{3-} from both aqueous solutions converged at the cross-section of the microfluidic channel, shortly before they were encapsulated in droplets.

Aqueous stock-solutions of 5 mM $CaCl_2$ and 10 mM Na_2HPO_4 were prepared separately in a buffered solution of 25 mM TRIS/HCl, pH 7.4. and respectively transferred in a 0.5 ml syringe. The oil-phase consisted of a 2% PFPE-PEG-PFPE surfactant solution in HFE-oil and was transferred to a 1 ml syringe. The syringes were placed in the syringe pumps, connected with plastic tubings ($\varnothing_{in}$=0.3 mm) and plugged in the corresponding inlet holes of the microfluidic PDMS chip (see section, 8.1.2, figure 92b). The flowrates were 800 µl/min for the oil-phase and 200 µl/min for each aqueous phase, in order to produce droplets with 20-30 µm in diameter. When a constant flow was reached, the droplets were collected at the outlet into small plastic tubes.

8.2.3 Enzymatic Droplet-based Mineralization Setup

The second approach for mineralization studies of CaP was an adapted alkaline phosphatase-based bulk mineralization model described by Gungormus et al. [125, 338] which was further developed to an enzymatic droplet-based mineralization setup as shown in figure 93b. With this approach the mineralization started by hydrolysis of β-glycerophosphate (β-GP) by AP within the droplets, releasing inorganic phosphate (P_i) and facilitating the mineralization process of CaP.

Two mineralization solutions were prepared from scratch in Tris/HCl buffer (25 mM, pH 7.4): one solution with 28,8 mM β-GP; the second solution composed of $CaCl_2$ (48,8 mM) and the enzyme AP at a concentration 0.1 U/µl. Both solutions were transferred to a 0.5 ml syringe which were connected to plastic tubings ($\varnothing_{in}$=0.3 mm) and plugged in each to an inlet channel for the aqueous phases.

For the oil-phase a solution of 2 % PFPE-PEG-PFPE surfactant in HFE-oil was prepared and transferred to a 1 ml syringe, which was connected to the oil-phase-inlet of the microfluidic PDMS chip. In order to produce droplets with 20-30 µm in diameter, the flowrate settings were 200 µl/min for each aqueous phase and 800 µm for the oil-surfactant phase. When a constant flow was reached (after 1-2 min), the droplets were collected at the outlet into small plastic tubes and the samples were incubated at 37°C for 0.5 h, 1 h, 2 h and 4 h while soft orbital shaking (150 rmp). At the different time points, the AP was inactivated by heating the sample up to 90°C for 10 min and subsequent cooling down and storing the mineral-containing droplets at 4°C to prevent further phosphate release.

Droplet-based Mineralization Studies with Matrix Gla Protein (MGP)-Peptides

A further object of this thesis was to investigate the anti-calcification properties of MGP in our droplet-based setup. Since the 84-amino acid protein was known to be poorly soluble, especially the C-terminal end of MGP, it was divided into peptides with each 14 amino acids in length (figure 94a), according to previous bulk studies from O' Young et al. [109].

For our studies four peptides were chosen, varying in their amount and position of γE (gla residues), which were believed to be the main functional groups for the anti-calcification activities of MGP: YGlaS – with one γE residue, FIN – without γE residue, and QR-Gla and SK-gla, both with two γE residues. Thereby, each peptide with a functional group was investigated in its uncarboxylated=inactive state with the glu residue and in its carboxylated=active state with the gla residue (figure 94b).

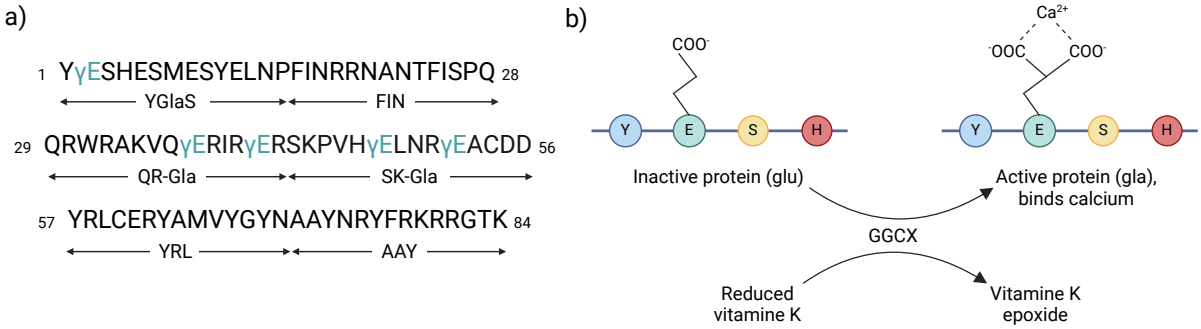

Figure 94: Amino-acid sequence of matrix gla protein (MGP) and peptides used in this thesis (a) and activation mechanism of MGP (b).

The peptides at the C-terminal end of the protein, YRL and AAY, were not investigated, since both were poorly soluble. It also has to be noted, that one these peptides YGLAS normally contains also three phosphate groups at the three serine residues. In our study we did not use the phosphorylated variant, since the enzyme AP would dephosphorylate these groups.

An additional peptide, MPP3, was chosen as a positive control, since this peptide was shown to accelerate the mineralization of CaP in bulk experiments [125]. MPP3 is a 14-amino-acid peptide comprising four pairs of oppositely charged residues, separated by alanine residues [125].

The peptides used in this study were listed in table 9, summarizing the position of MGP peptides within the protein, their sequences and their molecular weigth (M_n) in g/mol. All peptides were purchased from the company Genosphere Biotechnologies with a purity of >90%.

To test the influence of these peptides on the nucleation and mineralization of CaP the AP-based approach was used, as described before (see section 8.2.3). For this, the peptides were added to the ß-GP solution at final concentrations of 5 µM and 500 µM; as a control sample, no peptide was added to the ß-GP solution.
In first experiments, the samples were incubated for different time intervals: 0 min, 0.5 h, 1h, 2h and 4 h. Whereby, the 0 min samples were collected for 2 min and subsequently heated up to 90°C for 10 min to deactivate the AP. The other samples were collected for 8 min and inactivated at the corresponding time points.

Table 9: Overview of peptides used in this study with amino acid position within the matrix gla protein (MGP), amino acid sequence with γE = gamma-carboxyglutamic acid (gla) residues, and molecular weight (M_n) of each peptide in [g/mol].

Peptide name	Amino acid position	Sequence	M_n [g/mol]
YGLAS	1-14	YγESHESMESYELNP	1759
YGLUS	1-14	YESHESMESYELNP	1715
FIN	15-28	FINRRNANTFISPQ	1678
QR-GLA	29-42	QRWRAKVQγERIRγER	2007
QR-GLU	29-42	QRWRAKVQERIRER	1911
SK-GLA	43-56	SKPVHγELNRγEACDD	1701
SK-GLU	43-56	SKPVHELNREACDD	1613
MPP3	-	PGEKADRAEKADRA	1514

8.3 Imaging Analysis of Calcium Phosphate (CaP) Minerals

The mineralized particles of CaP were first imaged within the droplets using light scanning microscopy (LSM) and additionally the minerals were isolated and purified from the droplets to investigate their morphological properties more closely via scanning electron microscopy (SEM).

8.3.1 Materials

Chemicals, reagents, solutions and equipment	**Source**
Glass cover slips, #1 or #1.5, 24x50 mm and 18x24 mm	Carl Roth, 1871
Concentrated ethanol (EtOH), ROTIPURAN® (≥ 99.8%)	Carl Roth, 9065.1
Two-component dental glue, picodent twinsil® speed	Dental Produktions- und Vertriebs GmbH, 270125
Novec 7500, FL-0004-HP-1000 (HFE-oil)	Ioltec, 21224
1H, 1H, 2H, 2H-perfluoro-1-octanol (PFPE-PEG-PFPE)	Sigma-Aldrich, #MKCN8524
Sterile filter flask, max. 0.5 l	Sarstedt, 60U2412
Filter membrane, Ø=47 mm, pore size: 0.45 µm,	Merck Millipore, FHLC04700
Petri dish, Ø=5 cm	Greiner BioOne
Ultrasonicator, 60/240 W; 35 kHz	Bandelin electronic, Berlin
Si-wafer, 1x1 cm	
Acetone	VWR,
2-Propanol/Isopropanol	VWR, 18D164006
Laser scanning microscope	
Scanning electron microscope (SEM)	Zeiss, Ultra™ 55

8.3.2 Light Scanning Microscopy (LSM) Imaging

After the droplet samples were collected at the outlet, they were imaged using LSM. For this, an observation chamber was assembled to prevent evaporation of the samples during imaging. The protocol for the construction of the observation chamber was adapted from Dr. Lucia Benk [337].

Construction of Observation Chamber

The workflow for the preparation of the observation chamber was summarized in figure 95. First, the glass cover slips (24x50 mm and 18x24 mm) were cleaned using EtOH (70 %) and let dry for 5 min at 65 °C. Then, two thin pieces of double sticky tape (l=1.5-2 cm), serving as spacer, were adhered in the middle of the large glass cover slip (24x50 mm), as shown in the figure (1.), and a small glass cover slip (18x24 mm) was carefully pressed on top of these sticky tapes (2.). The droplet-containing emulsion was pipetted in the small space between both glass cover slips (3.), so that approx. 2/3 of the area building a monolayer of droplets, the remaining air in the chamber was removed by inserting oil-surfactant solution. In the last step, the chamber was sealed using two-component dental glue (4.), to prevent evaporation of the samples. The observation chamber was stored at 4 °C until use for max. 2 days, then the oil was evaporated.

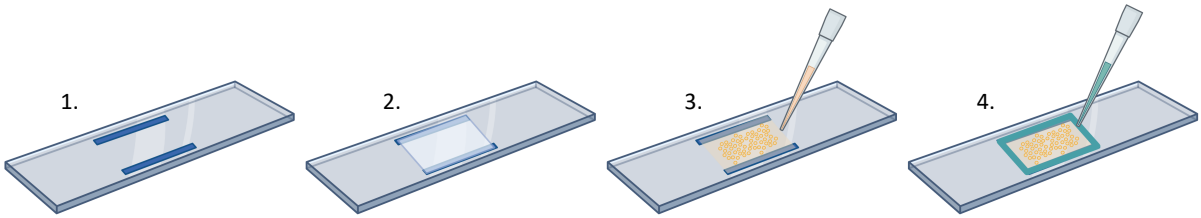

Figure 95: Schematic drawing of the observation chamber preparation for droplet imaging *via* light scanning microscope (LSM). Two thin pieces of double sticky tape (blue) were adhered in the middle of the large glass cover slide (1.) and a small glass cover slide was pressed on top of these tapes (2.). The droplet-containing emulsion was pipetted in the small space between the glass cover slides (3.) and the chamber was sealed using two-component dental glue (4.). The picture was adapted from Dr. Lucia Benk and created using BioRender.com.

8.3.3 Scanning Electron Microscopy (SEM) Imaging

For SEM analysis, the mineralized particles were isolated and purified from the droplets and afterwards prepared for imaging. The protocols were adapted from previous studies by Dr. Lucia Benk for mineralized particles of calcium carbonate ($CaCO_3$) and they were transferred and modified for our samples.

Isolation and Purification of Mineralized Particles

In order to obtain sufficient amounts of mineralized particles for SEM analysis, the droplet emulsion of 4 to 5 samples was merged and filtered through a filter membrane (0.45 µm). The particles were washed twice on the filter using 1-2 ml of pure EtOH and then transferred to a petri dish by flushing the particles off the membrane several times using 1-2 ml EtOH. The sample was transferred to a 2 ml small plastic tube and then centrifuged for 5 min at 500 g. The supernatant was removed and the particles were resuspended in 1 ml EtOH. After a second centrifugation step (5 min, 500 g), the supernatant was again discarded except of ~20 µl and the sample was transferred on a silicium (si)-wafer for SEM analysis, as described in the following.

Sample Preparation for SEM Imaging

First, the si-wafer were cleaned by ultrasonication (240 W, 35 kHz) in MilliQ, followed by sonication in acetone-isopropanol (1:1) and again in MilliQ, for 10 min each. The si wafer were dryed in a N_2 stream and the isolated and purified particles were pipetted on the cleaned wafer and let dry at 80 °C over night. The next day, the samples were sputtered with carbon (8 nm) and imaged via SEM (3-5 kV).

9 Results and Discussion – Part II

9.1 Biomimetic Droplet-Based Mineralization Model

In the second part of this thesis a new biomimetic approach for biomineralization studies of CaP was developed and investigated.

It is known, that the physiological and pathological mineralization of CaP takes place in small spherical structures – the MVs [82, 339]. Simplified the whole mineralization process can be divided in two phases: the intake and accumulation of Ca^{2+} and PO_4^{3-} in the MVs and the formation of first HAp crystals within the vesicles (phase I), followed by MV disruption, crystal release and mineral propagation on collagen fibrils in the ECM (phase II) [92]. (For detailed description refer to section 1.2.1).

Our approach focused on phase I and the design of small spherical structures in order to mimic the biological mineral formation in MVs. Therefore, a microfluidic droplet-based model was chosen and different microfluidic devices were designed, prepared and tested. Moreover, different types of surfactants were investigated and flowrates of aqueous and oil phases were varied.

In the following two different approaches were explored, summarizing the best conditions (concentrations, surfactant, flowrates) for stable and uniform droplets.

9.1.1 Aqueous Double-Channel System

The first approach based on previous bulk mineralization studies of HAp as described by Mao et al. [123]. Outgoing from this bulk system, a simple droplet-based setup was developed, consisting of an aqueous double-channel system, with two aqueous solutions ($CaCl_2$ and Na_2HPO_4) used for crystallization of CaP. As continuous (oil) phase a 2 % PFPE-PEG-PFPE solution in HFE-oil was used.

In general, the results with this setup showed stable and uniform droplets (~30 µm) harboring small mineralized particles of calcium phosphate (figure 96a and 96a').

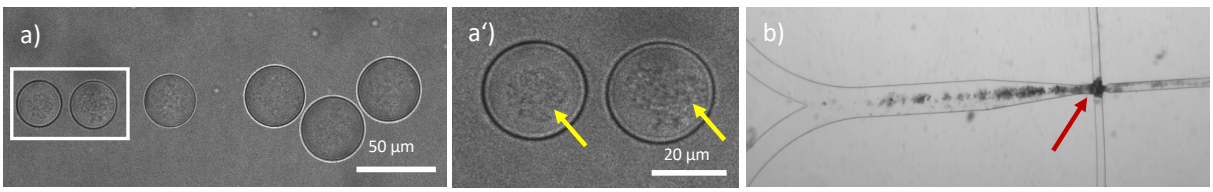

Figure 96: Aqueous double-channel system for droplet mineralization of calcium phosphate. The system consisted of two aqueous solutions, $CaCl_2$ (5 mM) and $NaHPO_4$ (10 mM), both in 25 mM TRIS/HCl buffer, pH 7.4. Mineralization started when Ca^{2+} and PO_4^{3-} from both solutions converged at the cross-section of the microfluidic channel, shortly before they were encapsulated in droplets. For the oil phase a solution of 2 % PFPE-PEG-PFPE surfactant in HFE-oil was used. The flowrates were 800 µl/min (oil-phase) and 200 µl/min (aqueous phases). The droplets were stable and uniform, with approx. 30 µm in diameter (a), showing mineralized particles inside each droplet (yellow arrows in a', enlarged droplets from a). Within few minutes, the channels clogged at the cross-section where the solutions converged (red arrow in b), showing that mineralization occurred very fast.

However, the results also showed that the number of droplets was really small and furthermore the channels of the microfluidic chips clogged within few minutes at the cross-section where the solutions merged (figure 94b), making them unusable afterwards. This rapid clogging suggested that the mineralization occurred at a high rate, necessitating further optimization of the process, ultimately leading to the discontinuation of this approach.

9.1.2 Enzymatic Droplet-Based Mineralization Setup

The second approach for studying CaP mineralization involved a modified bulk mineralization model based on the enzyme alkaline AP, as described by Gungormus et al. [124, 125]. This bulk system was further refined into an enzymatic droplet-based mineralization setup. Thereby, mineralization is initiated by hydrolysis of β-GP by AP within the droplets, leading to the release of inorganic phosphate (Pi) and promoting HAp formation. With this, each droplet is an individual controllable reaction chamber, similar to the biological MV-mediated biomineralization.
In addition to the enzymatically controlled approach, further design improvements of the microfluidic chip were made, by shortening the channel in which the two aqueous solutions meet, in order to prevent clogging of the channel.

Figure 97 shows the successful mineralization of CaP in the enzymatic droplet-based system. The mineralization was observed over a period of 4 hours, with samples being taken at different time points (0 min, 0.5 h, 1 h, 2 h and 4 h).

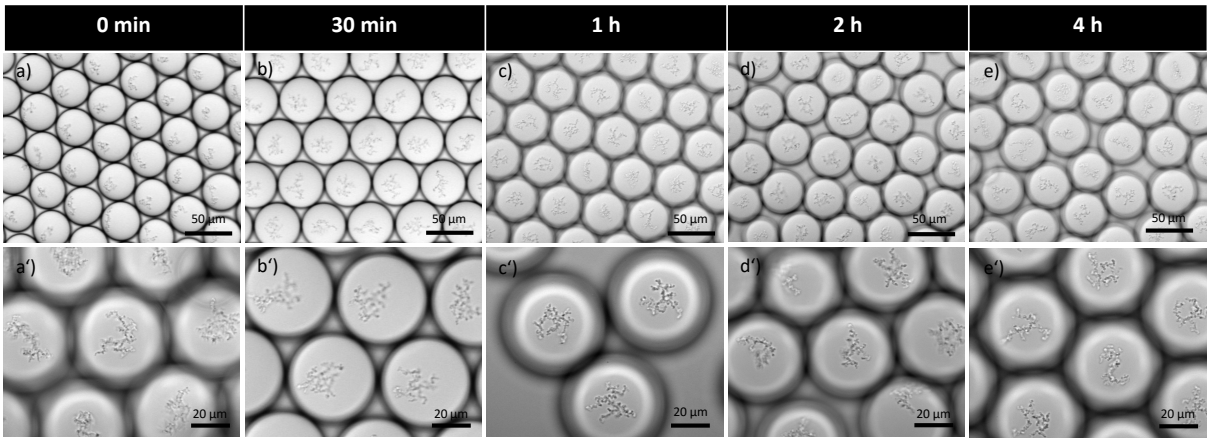

Figure 97: Successful mineralization of calcium phosphate (CaP) in an enzymatic droplet-based setup. The setup involved the controlled release of phosphate from β-glycerophosphate (β-GP) by alkaline phosphatase (AP). Two aqueous solutions were prepared in 25 mM TRIS/HCl buffer, pH 7.4: 1.) $CaCl_2$ (24.4 mM) + AP (0.1 U/µl); 2. β-GP (14.4 mM). For the oil phase a solution of 2 % PFPE-PEG-PFPE surfactant in HFE-oil was used. The flowrates were 800 µl/min for the oil-phase and 200 µl/min for each aqueous phase. Droplets were collected at the outlet into small plastic tubes for 5 min and incubated at 37°C for 0 min (a/a'), 0.5 h (b/b'), 1 h (c/c'), 2 h (d/d') and 4 h (e/e'). At the different time points the enzyme was inactivated by heating the sample up to 90 °C for 10 min and subsequent cooling down and storing at 4 °C. Pictures in a', b', c', d' and e' showing enlarged droplets from a, b, c, d and e.

All samples showed uniform and stable droplets (~30 µm) with mineralized particles inside each; a time-dependent particle growth inside the droplets could not be observed. These findings, and the

fact that mineralization was also present in the samples at 0 min, where the AP was directly inactivated after sample collection (5 min), showed again that mineralization proceeds very fast. Control samples without AP showed no mineralization inside the droplets after 4 h of incubation (see appendix, section 11.1.1).

Comparison of Droplet-based Mineralization Model vs. Natural and Biomimetic Mineralisation Systems

One major difference between our droplet-based mineralization model and the natural system is the larger size of the droplets compared to MVs, which typically range between 10 nm to 400 nm in diameter [90, 92-94]. To better replicate natural conditions, the droplet size in our model has to be reduced in the future, and this can be achieved in different ways.

In microfluidic systems the droplet size is mainly determined by the balance between interfacial tension and shear forces [340, 341]. The surface tension between the continuous (oil) and the dispersed phase (water) is crucial, as lower interfacial tension generally results in smaller droplets [340]. The shape and size of droplets can also be controlled by adjusting flowrates of continuous and dispersed phases, as higher flowrates of continuous phase combined with lower flow rates of dispersed phase result in smaller droplets [331]. The viscosity of continuous phase also impacts droplet size, with lower viscosity enhancing shear forces/flow at the droplet formation site and leading to smaller droplets [332]. Smaller droplet sizes can also be achieved by modifying the channel width, length, geometry and entry angle in the microfluidic chip, for instance, by tapering the droplet formation area [331]. Factors, such as temperature, type of surfactant or surfactant concentration can modulate both viscosity and interfacial tension [332].

Overall, by adjusting these parameters it should be possible, to reduce the size of the droplets to few micrometers, as known from previous studies [281, 318]. Although this is still larger than natural MVs, they are in a similar volumetric range on the femtoliter scale.

Another difference from natural MV-mediated mineralization is the presence of the enzyme AP within the droplets. As outlined in section 1.2.1, AP functions as a membrane ectoprotein of MVs with a GPI anchor, connected to the C-terminus of the protein by an amide linkage [96-98]. However, in addition to AP another enzyme, Phopho-1, was known to be present within MVs, releasing phosphate ions from PC or PEA, and therefore has the same function as AP that was used in our study.

In addition, prior bulk studies conducted by Golub et al., demonstrated that, the mineral produced by AP exhibited characteristics more closely aligned with mineral formed *in vivo*, in contrast to the outcomes observed when mixing calcium and phosphate solutions directly [342]. Furthermore, the use of AP resulted in the formation of a greater amount of mineral [342]. They proposed that the generation of phosphate from β-GP by AP could alter the physicochemical state of nascent Pi, thereby leading to a crystallization pathway distinct from that occuring in bulk systems without AP [342].

Further differences between droplets and MVs are related to the overall structural composition of MVs, which incorporate various different enzymes and proteins, important for their function as initial sites of mineral formation.
Compared to our droplet-based model other MV analogues better mimic the composition of MVs, such as proteoliposomes, which are modified with different enzymes and proteins linked to MV-mediated mineralization [93, 96, 97]. However, the incorporation of all these components is quite difficult since previous studies showed, that the stability of the proteoliposomes and the activity of incorporated AP decreases with higher complexity of the proteoliposomes [136]. Furthermore, the proteins and enzymes within natural MVs are not randomly distributed, but are organized in microdomains and their composition also changes during the mineralization process [136, 137]. Therefore, proteoliposomes are quite complex mineralization systems and they require a methodological standardization for the insertion of each specific protein or enzyme for a correct protein orientation and functionality [96].
Polymeric vesicles are another example for biomimetic MVs, but they mainly focus on studies of phase II of the mineralization process, the mineral release from MVs and mineral propagation on collagen fibrils, as demonstrated by Shen et al. [141]. With our droplet-based setup it is possible to investigate both phases of the mineralization process, as mineralized particles formed within droplets can be released by using destabilizing surfactants.
The bulk mineralization models share more similarity with the droplet-based system, as they are quite simple mineralization models focusing on the produced mineral itself as primary objective in material science [123-126]. However, in bulk systems, parameters like pH or ion concentrations can be less precisely controlled and gradients that can form within the solution that can lead to e.g. inhomogeneous mineral growth [334]. The open nature of bulk systems makes them also prone to side reactions, which can influence the desired mineralization process and lead to impurities and undesired byproducts [334]. Furthermore, as outlined before, the initial biomineralization of HAp expires in MVs, for that reason the bulk mineralization model represents only partially the biological formation of hard tissues and ectopic mineralization processes. For comprehensive descriptions of common mineralization models for CaP, refer to section 1.2.3

Despite differences from natural MVs, the droplet-based approach offers major advantages compared to the other MV-mimicking systems. It bridges the simplicity of bulk systems and the spherical geometry of MVs as discrete, individual reaction chambers, similar to proteoliposomes or polymeric vesicles, but less complicated and time-consuming. Within the droplets, the chemical microenvironment is highly controlled, including pH or ion concentration, and this allows the mineralization process to proceed more uniform, compared to bulk systems. The small reaction volumes within droplets allow mineralization studies under mild conditions and enable the formation of nanomaterials that are difficult to achieve in bulk. Droplets also minimize side reactions, by isolating the reaction components from the external environment, and by this preventing unwanted reactions and stabilizing intermediates within the confide space.

9.1.3 Scanning Electron Microscopy (SEM) of Isolated Minerals

For the mineralized particles inside the droplets shown in section 9.1.2, an isolation and purification protocol were developed (see section 8.3.3). The morphological properties of the particles were analyzed by SEM and compared to the AP-mediated bulk mineralization model, which was carried out as described by Gungormus et al. [124, 125].

Isolated Particles from Bulk Mineralization

The results of the bulk mineralization (figure 98) showed a time-wise morphological development in the first hour of mineralization.

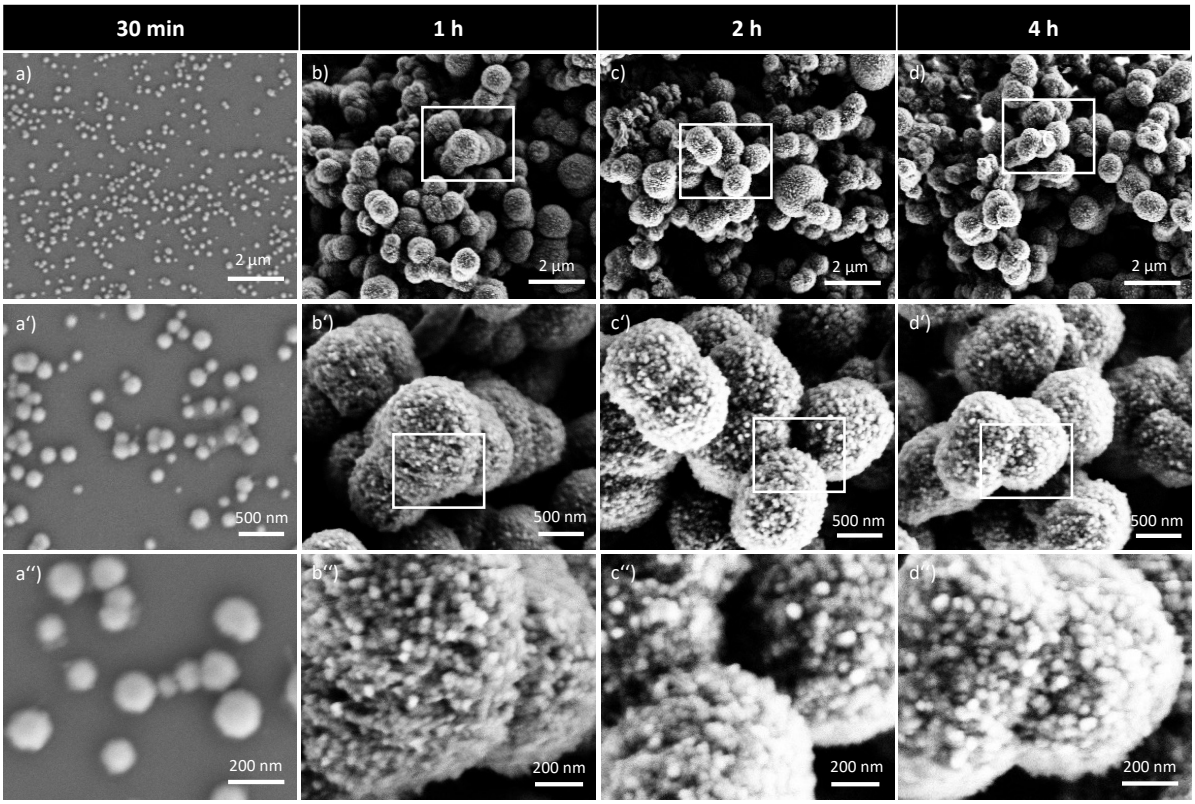

Figure 98: Bulk mineralization of calcium phosphate in an enzymatic-based setup according to Gungormus et al. [124, 125]. The setup involved the release of phosphate by enzymatic hydrolysis of ß-glycerophosphate (ß-GP). The mineralization solution consisted of $CaCl_2$ (24.4 mM) and β-GP (14.4 mM) in a TRIS/HCl buffer (25 mM, pH 7.4). Aliquots of 300 µl were transferred to a 96-well plate and mineralization was started by adding AP (0.1 U/µl). Mineralization was carried out for different time intervals (30 min, 1 h, 2 h, 4 h) at 37°C. Reaction was stopped by deactivation of AP (heating up to 90°C for 10 min and cooling down and storing at 4°C). For SEM analysis, mineralized particles were transferred to a si-wafer, dried and coated with carbon (8 nm).

After 30 minutes single, small spherical structures were observed ranging in size between ~50 nm and ~200 nm (figure 98a/a'/a''). Samples after 1 h, 2 h and 4 h of mineralization showed larger spherical structures, organized in aggregates (figure 98b/b'/b'', 98c/c'/c'' and 98d/d'/d''). The particle size of single spherical structures ranged between ~500 nm and ~1.5 µm, whereby the size of individual particles seemed to remain the same after 1 h and only the amount of mineralized material increased afterwards. Enlarged regions of the round particles shown in figure 98b, 98c and 98d displayed a structured surface with small spots.

Previous studies utilizing the AP-mediated bulk mineralization setup reported different phases of CaP formed *in vitro* [342-344]. The three major forms are amorphous ACP ($Ca_9(PO_4)_6$) and the crystalline phases OCP ($Ca_8(HPO_4)_2(PO_4)_4*5\ H_2O$) and HAp ($Ca_5(OH(PO_4)_3)$) [124, 342-344].
In literature and several studies, the morphological characteristics of each form are already well documented and described, insofar our samples can be roughly categorized visually into the individual phases of CaP.

In the case of the bulk-mineralized particles in figure 98, the morphological characteristics fit to those described for ACP by Gungormus et al. [124] and Qi et al. [345]. Similar to our observations, Qi et al. reported small spherical structures with a smooth surface in the first 30 min, but slightly larger diameter compared to ours (1 μm to 5 μm) [345]. Nonetheless, particle dimensions of ACP can vary due to several factors, as pH and concentration of the mineralization solution or the temperature during the mineralization process [346]. Therefore, variations in particle size were attributed to different mineralization setups used. Similar to our results Qi et al. further reported a noticeable change in morphology after 1 h, by the emergence of small spots on the surface of the spherical particles and accumulation of particles [345].

Isolated Particles from Droplet-Based Mineralization

The mineral crystallinity of particles formed within droplets showed significant differences compared to the bulk system (figure 99). The microspheres exhibited bundled needle-like particles (∅=1-2 μm) with nano-'whiskers' (approximately 200–500 nm in length), similar to small dandelions. Morphological differences between the samples, regarding a time-wise manner, were not observed, only the amount of mineralized material increased over time.
These morphological characteristics of our minerals fit to those reported by Qi et al. for the crystalline phase HAp [345], whereby differences to our minerals were observed in regard of the mineralization rate. In the bulk setup from Qi et al [345], the transformation from ACP to HAp started after ~3 h and was completed after 8 h [345]. In our droplet-based setup this transformation seemed to progress faster, as no ACP minerals were observed after 30 min, instead only morphological HAp-characteristics were present.
However, an in-depth element analysis of the samples, for instance by x-ray diffraction (XRD) and/or Fourier transform infrared (FTIR) spectroscopy, would be necessary in future studies to confirm the phases or phase compositions in our samples.
Nonetheless, the results of morphological differences between mineralized particles in bulk and droplets clearly showed, that in our droplet-based mineralization setup the crystallization pathway was clearly distinct from that occuring in bulk systems.

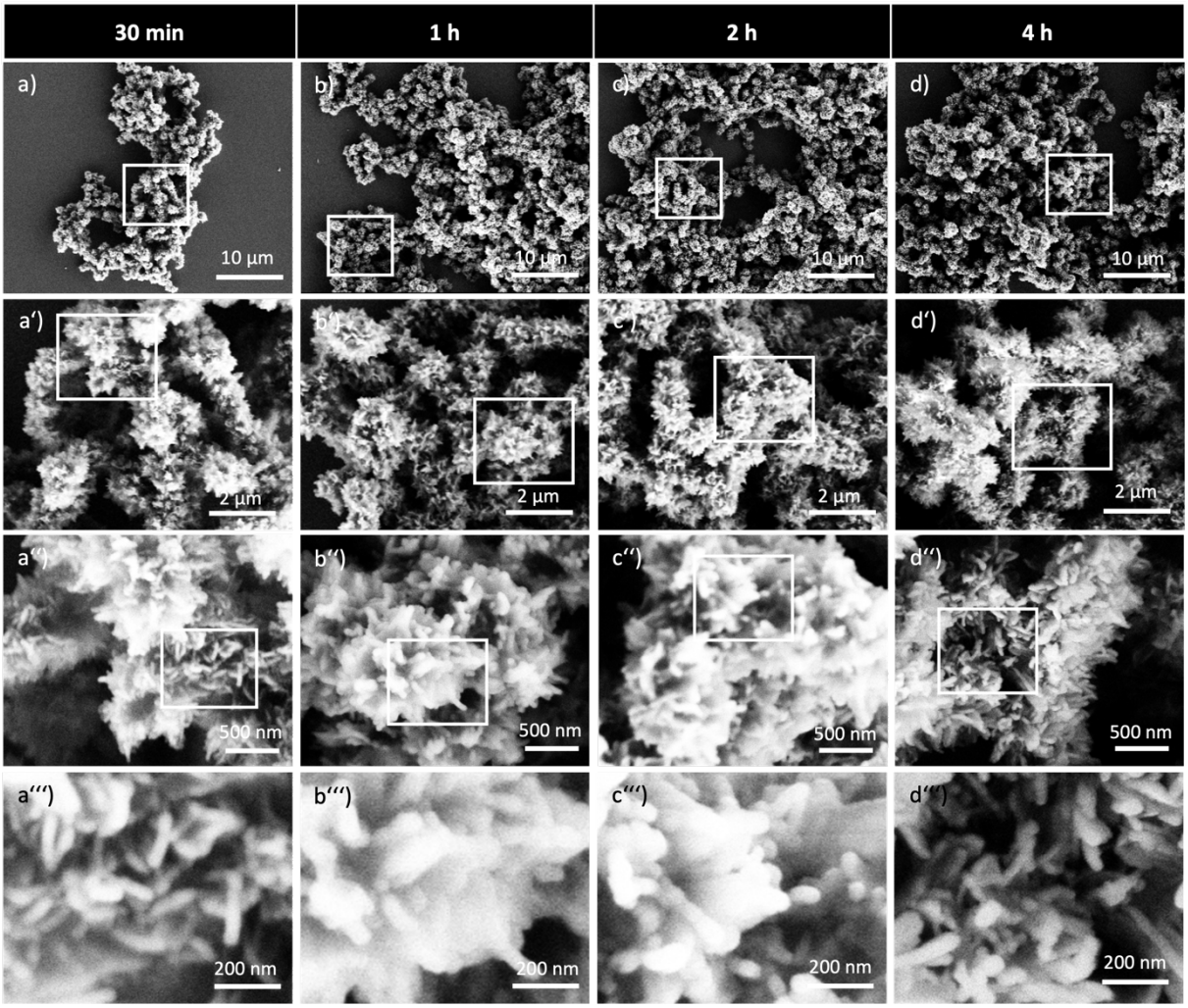

Figure 99: Isolated and purified particles of calcium phosphate from enzymatic, droplet-based mineralization setup shown in figure 2. The minerals were formed in droplets, using two aqueous solutions (in 25 mM TRIS/HCl buffer, pH 7.4): 1.) $CaCl_2$ (24.4 mM)+AP (0.1 U/µl); 2.) β-GP (14.4 mM). Oil phase: 2% PFPE-PEG-PFPE surfactant in HFE-oil. The flowrates were 800 µl/min (oil-phase) and 200 µl/min (aqueous phases). Droplets were incubated at 37 °C for 30 min (a/a'/a"/a'"), 1 h (b/b'/b"/b'"), 2 h (c/c'/c"/c'"), 4 h (d/d'/d"/d'"). AP was inactivated by heating up to 90 °C for 10 min and subsequent cooling down and storing at 4 °C. For SEM analysis, mineralized particles were isolated and transferred to a si-wafer, dried and coated with carbon (8 nm).

9.2 Enzymatic Droplet-based Mineralization with Peptides of Matrix Gla Protein (MGP)

After successful development of a droplet-based mineralization model, another objective in the second part of this thesis was to investigate anti-calcification properties of MGP.
Current knowledge and research suggests two possible ways in which MGP might inhibit calcification of e.g. blood vessels or cartilage [109].
The primarily mechanism describes a direct binding of MGP to calcium and early-stage crystals by the acidic γ-E (gla) residues in MGP and thereby blocking further crystal growth, similar to osteocalcin or phosphoproteins [347, 348]. The second mechanism of MGP describes the inhibition of cell differentation as seen in atherosclerosis, where MGP act as inhibitor of bone morphogenetic protein 2 (BMP2), which helps stop cells from turning into bone-forming cells [349].
In previous bulk mineralization studies by O'Young et al. it was demonstrated that peptides of MGP attached to and slowed down formation of HAp minerals [109]. The aim of our study was to investigate whether similar effects can be observed in our biomimetic droplet-based mineralization model. According to previous studies by O'Young et al. MGP was divided into peptides, with each 14 amino-acids in length [109]. For our studies, four peptides were selected that differ in the number and position of gla residues, which are believed to be the primary functional groups responsible for the anti-calcification activity of MGP. The peptides chosen include YGLAS, which contains one gla residue; FIN, with no gla residue; and QR-GLA and SKA-GLA, both of which contain two gla residues. In addition, each peptide with a functional group was also examined in its uncarboxylated state, where gla was replaced by glu, representing the inactive form of the peptide.
An additional peptide, MPP3, was selected as a positive control, as it has been shown in previous bulk experiments to accelerate the mineralization of CaP [125].
All peptides were investigated at low and high concentration of 5 μM and 500 μM. First experiments with peptide additives, showed no further difference in morphology after 1 h, similar to the control sample without peptide (see section 9.1.3). Therefore, the following results of the SEM analysis summarized only the mineralized particles after 4 h.

9.2.1 Analysis of Droplet Characteristics

After collecting the droplet samples, they were directly imaged via LSM to analyze differences in droplet morphology, size and characteristics of mineralized particles within the droplets. The results after 4 h of mineralization are summarized in figure 100 and figure 101, displaying representative data for each peptide at concentrations of 5 μM and 500 μM, respectively.
Overall, no big differences were observed regarding droplet size or amount and morphology of mineralized particles within the droplets, for both peptide concentrations.

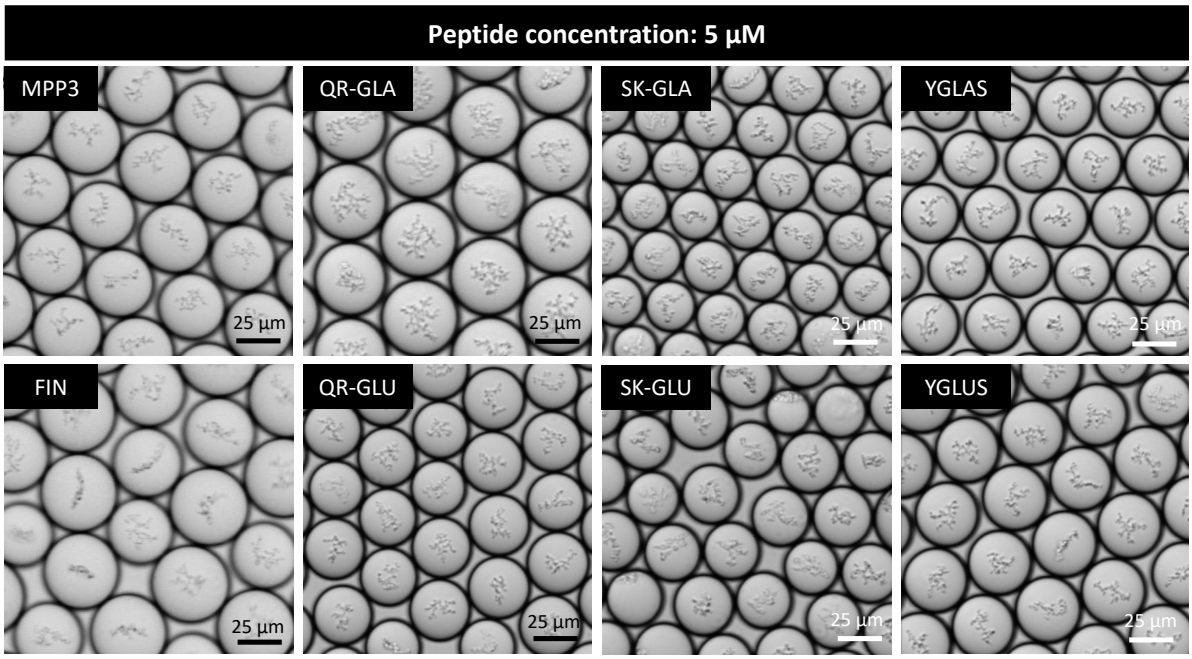

Figure 100: Mineralization of calcium phosphate in an enzymatic droplet-based setup with different peptides concentration of 5 µM. The setup involved the controlled release of phosphate from ß-glycerophosphate (β-GP) by alkaline phosphatase (AP). Two aqueous solutions were prepared in 25 mM TRIS/HCl buffer, pH 7.4: 1.) $CaCl_2$ (24.4 mM)+AP (0.1 U/µl); 2.) β-GP (14.4 mM)+peptide (5 µM). Peptides used: MPP3 as positive control; FIN without gla residue; YGLAS with one gla residue; QR-GLA and SK-GLA both with two gla residues and inactive forms of peptides with glu residues: QR-GLU, SK-GLU and YGLUS. The oil phase was a solution of 2 % PFPE-PEG-PFPE surfactant in HFE-oil. The flowrates were: 800 µl/min (oil-phase) and 200 µl/min (aqueous phases). Droplets were collected at the outlet into small plastic tubes for 5 min and incubated at 37 °C for 4 h. At the different time points the enzyme was inactivated by heating the sample up to 90°C for 10 min and subsequent cooling down and storing at 4°C.

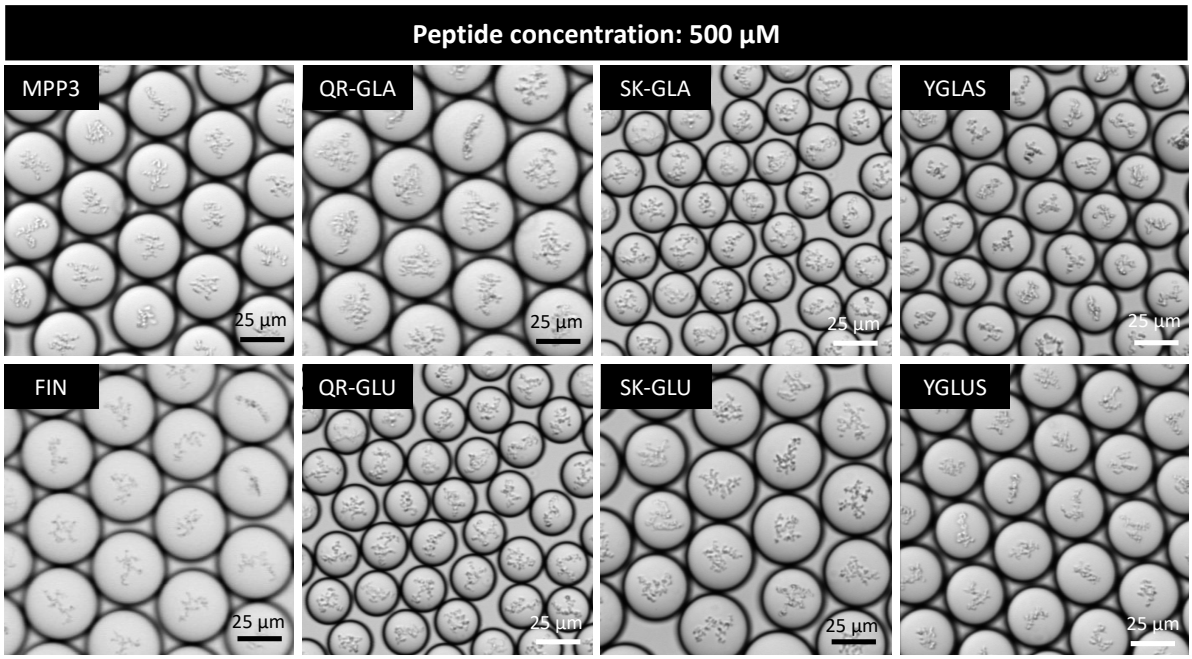

Figure 101: Mineralization of calcium phosphate in an enzymatic droplet-based setup with different peptides at a concentration of 500 µM. The setup involved the controlled release of phosphate from β-glycerophosphate (ß-GP) by alkaline phosphatase (AP). Two aqueous solutions were prepared in 25 mM TRIS/HCl buffer, pH 7.4: 1.) $CaCl_2$ (24.4 mM) + AP (0.1 U/µl); 2.) β-GP (14.4 mM)+peptide (500 µM). Peptides used: MPP3 as positive control; FIN without gla residue; YGLAS with one gla residue; QR-GLA and SK-GLA both with two gla residues and inactive forms of peptides with glu residues: QR-GLU, SK-GLU and YGLUS. For the oil phase a solution of 2 % PFPE-PEG-PFPE surfactant in HFE-oil was used. The flowrates were: 800 µl/min (oil-phase) and 200 µl/min (aqueous phases). Droplets were collected at the outlet into small plastic tubes for 5 min and incubated at 37 °C for 4 h. At the different time points the enzyme was inactivated by heating the sample up to 90 °C for 10 min and subsequent cooling down and storing at 4 °C.

It was assumed that gla-peptides (QR-GLA, SK-GLA and Y-GLAS) would visibly influence the mineral formation within the droplets, due to their functional groups which were believed to be responsible for the anti-calcification properties of MGP [102, 107, 110].
For MPP3 a visible effect was also expected, since in previous bulk experiments it accelerated CaP precipitation significantly [125].
In some samples, a reduced droplet size was observed, as illustrated in figure 101 for SK-GLA and QR-GLU. However, detailed analysis and measurements of droplet diameters across three independent experiments (see appendix, section 11.1.2) demonstrated that, overall, droplet sizes were consistent across samples, with only minor variations in size. In summation, the diameter of droplets ranged between ~32 μm and ~38 μm.

9.2.2 SEM-Analysis of Minerals Formed in the Presence of MGP-Peptides

For in-depth morphological analysis the mineralized particles formed within the droplets were isolated and analyzed by SEM. Some isolated CaP particles exhibited distinct structural characteristics compared to the control sample shown in section 9.1.3. The results for all peptides are displayed separately for the concentrations 5 μM and 500 μM in figure 102 and figure 103. Detailed SEM-images for each peptide are summarized in the appendix (see section 11.2).

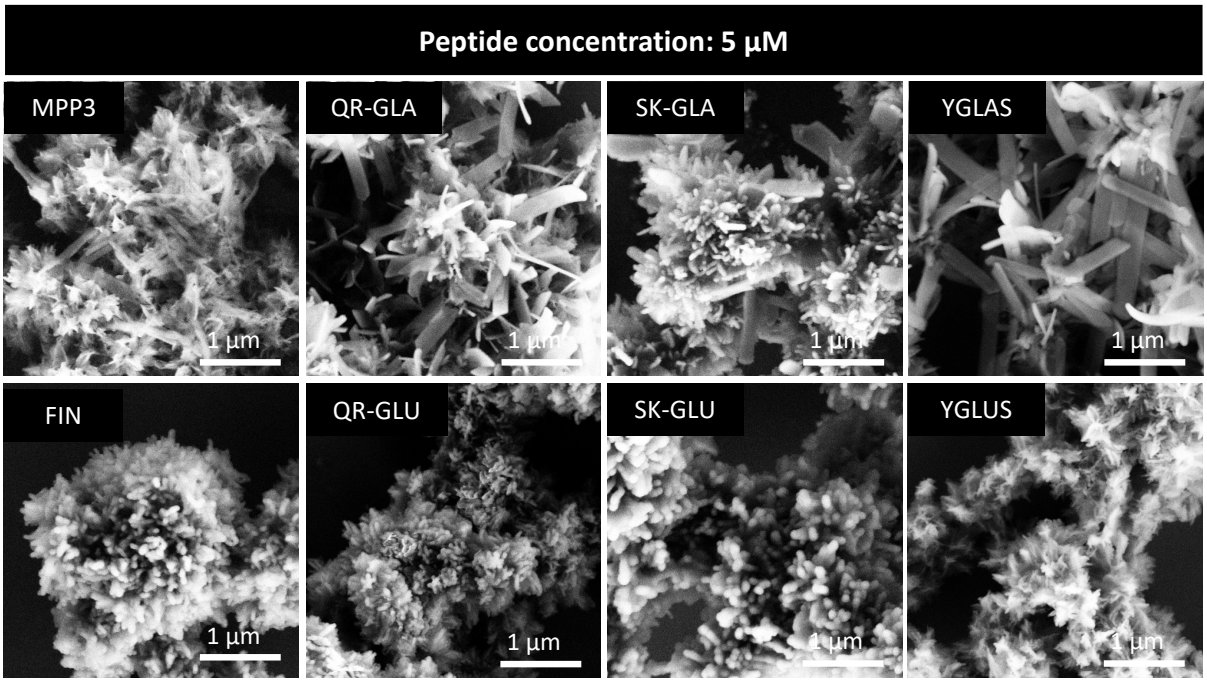

Figure 102: Overview of mineralized calcium phosphate particles formed within droplets in presence of different peptides at a concentration of 5 μM. Different structural characteristics were visible for the different peptide additives. Aggregates of bundled, fiber-like structures/nanostrips mixed with nano-'whiskers' were observed for the peptides MPP3 and active gla-containing MGP-peptides QR-GLA, SK-GLA and YGLAS. For the glu-variants less effect was visible; similar to sample control these peptides exhibited aggregated spheres coated with nano-needles/'whiskers'. Particles formed in presence of FIN also produced morphologies resembling the control. Pictures were taken at 3 kV.

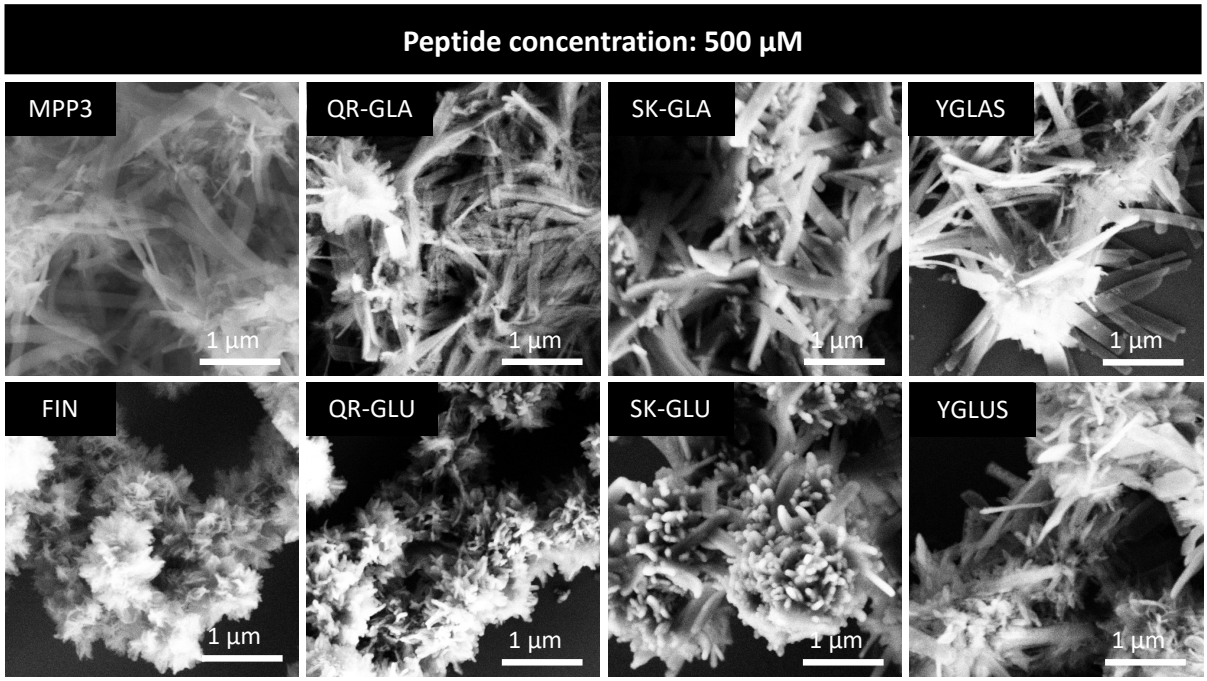

Figure 103: Overview of mineralized calcium phosphate particles formed within droplets in presence of different peptides at a concentration of 500 µM. At high concentrations significant differences were visible for the different peptide additives. Particles formed in the presence of MPP3 and gla-containing MGP-peptides (QR-GLA, SK-GLA and YGLAS) produced aggregates of bundled, fiber-like structures/nanostrips. For the glu-variants less effect was visible; similar to sample control these peptides exhibited aggregated spheres coated with nano-needles/'whiskers mixed with nanostrips. Particles formed in presence of FIN also produced morphologies similar to the control, but with refined nano-needles, similar to dandelions. Pictures were taken at 3 kV.

For the peptide MPP3, used as positive control due to its acceleration effect on CaP mineralization in bulk systems [125], significant morphological characteristics were evident. At both peptide concentrations (5 µM and 500 µM), CaP minerals appeared as aggregates of bundled fiber-like structures or nanostrips, whereby the effect was more pronounced with higher peptide concentration.

These results were significantly different to those of the bulk mineralization obtained by Gungormus et al., where MPP3 produced a mixture of spherulites and needle-like particles [125], more similar to our control sample. In the bulk system, MPP3 resulted in a significant increase in the mineralization kinetics and Gungormus et al. concluded that differences in the mineral morphology may be the result of a kinetics effect, rather than the interaction of the peptide with the mineral surface [125].

Further unique morphologies were observed in samples with the MGP-peptides containing the gla-residues: QR-GLA, SK-GLA and YGLAS. At low concentration of 5 µM the peptides produced a mixture of nanostrips and aggregated spheres, coated with small nano-'whiskers', similar to the control sample. At high concentration (500 µM) the amount of the nanostrips and bundled fibers was markedly increased.

In contrast, the inactive variants of the peptides with the glu residue, QR-GLU, SK-GLU and YGLUS showed less effects on crystal morphology. Especially at low concentration (5 µM), the particles exhibited similar characteristics to those of the control samples with aggregated spheres

coated with nano-needles. At 500 µM, these peptides induced a mixture of dandelions and nanostrips, especially for YGLUS.
For the peptide FIN at 5 µM, similar mineral characteristics were observed as for the glu-variants at low concentration and for the control; whereas for higher concentration (500 µM), the 'whiskers' were significantly more refined and thinner compared to others, similar to dandelions.

In summation, the greatest influence on mineral morphology was observed for MPP3 and the MGP-peptides with the gla-residues (QR-GLA, YGLAS and SK-GLA), especially for high peptide concentrations. No effect was observed for the non-modified peptide variants FIN, QR-GLU, for SK-GLU and YGLUS low effects were visible. The results of the morphological characteristics are summarized in figure 104. Conclusions regarding the anti-calcification properties of the peptides, particularly those containing gla-groups, cannot be drawn, as no reduction in mineral quantity was observed.

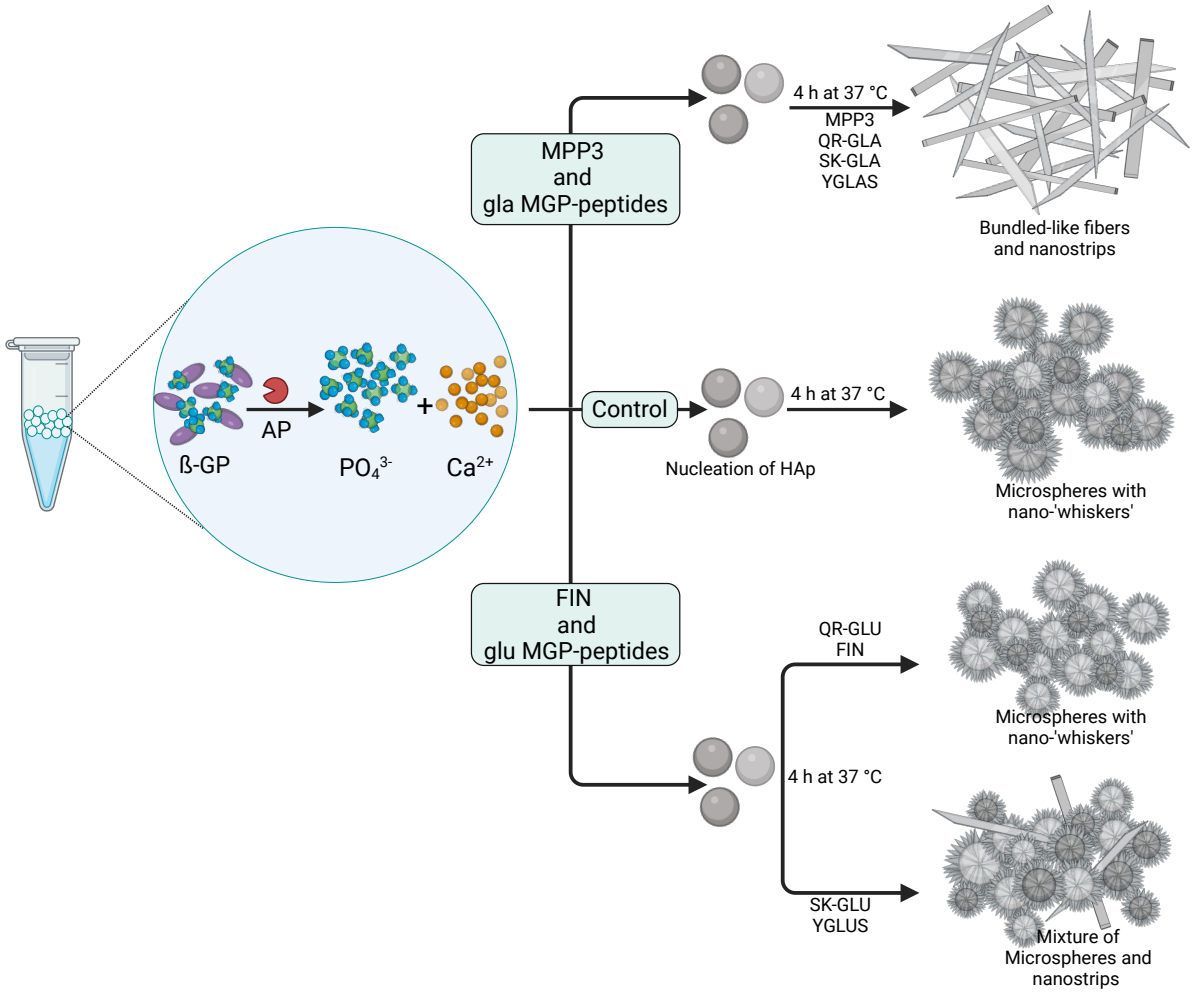

Figure 104: Overview of morphological characteristics for mineralized particles formed within droplets in presence of different peptide additives. The drawing was created with BioRender.com.

Our results partly overlapped with the findings published by O'Young et al. [109] and Goiko et al. [350], although no morphological SEM-analyses were available for comparison. Instead, dynamic

light scattering (DLS) [350] and *in vitro* growth rates [109] were used to study the inhibition effects of MGP peptides on HAp crystal growth.
However, the results matched in the fact that gla-peptides (YGLAS, QR-GLA and SK-GLA) had a greater impact on HAp crystallization than the glu-variants (YGLUS, QR-GLU and SK-GLU).
Overall, there was found to be a lack regarding morphological SEM-analyses of bulk mineralization studies with MGP peptides, for comparison with our observations.
Therefore, in the following, a deeper insight into morphological and structural characteristics of our samples were made with respect to the different mineral phases of CaP.

Phases and Properties of Calcium Phosphate (CaP) Minerals formed in Droplets

CaP exists in several different mineral phases, whereby HAp is the most stable form [84, 87, 91]. Further CaP phases, such as ACP or OCP and others are precursors, or sub-precursors, that transform into HAp *in vivo* or in aqueous environments with elevated pH [85-87].
As already mentioned, the three major phases of CaP formed *in vitro* are ACP, OCP and HAp [124, 342-344]. Over the past decade, several studies have reported a wide variety of CaP morphologies and characteristics of each form, including particles, spheres, needles, rods, sheets, flakes, wires, strips, flowers, porous structures and hollow forms [87, 351, 352]. These structures can vary in size, from nanoscale to macroscale, exhibiting differences in their physical and mechanical properties and capabilities [87].
When comparing our findings from the droplet-mineralized particles with literature data, it became clear that the morphological characteristics of our CaP minerals closely matched those of HAp, despite structural differences across all samples. For example, the aggregates of bundled fiber-like structures and nanostrips observed in samples with MPP3, and the gla-containing MGP-peptides (QR-GLA, SK-GLA and YGLAS) were comparable to those published by Lin et al. [352], Viswanath et al. [353] or Xiao et al. for HAp [354].
These nanostrips can be assigned to the group of 2-D shaped CaP crystals, exhibiting excellent molecular adsorption capabilities and mechanical properties [87]. It is well established that the physical characteristics of inorganic components, including their size and morphology, significantly influence the mechanical properties of organic-inorganic composites [355, 356].
This is why 2-D shape crystals of CaP are often used as raw materials to enhance the mechanical strength of bio-composites, where there are generally regarded as highly effective reinforcement agents in isotropic composite materials, as in dental or bone composites [357].

The aggregated microspheres coated with nano-needles/'whiskers' produced by glu-containing MGP-peptides and control, or dandelion-like structures, as observed for FIN, were similar to HAp-structures reported by Qi et al. and Zhang et al. [358].
These structures match to the 3-D group of CaP materials, which in recent years have gained considerable attention due to their excellent biological performance and wide range of biomedical applications [352]. Three-dimensional grafts and scaffolds with nano- or micro-structured surfaces exhibit improved biological properties due to their resemblance to natural bone and tooth

structures [359-361]. This similarity promoted osteointegration and supported subsequent bone tissue regeneration [359-361].

Overall, CaP materials hold significant promise for different applications, such as bone repair, due to their unique properties, closely resembling those of natural minerals [87]. With advancements in understanding biomimetic principles, biomimetic CaP materials have attracted increased attention. Investigating the mechanisms of biomineralization is essential and advantageous for the development and applications of CaP-based biomaterials [87].
Various methods have been already explored to produce CaP materials in diverse sizes and morphologies. However, techniques for precisely controlling particle size remain limited [87].

Droplet-based microfluidics offers a promising tool and several advantages for studying the formation of biominerals within small spherical structures, similar to the natural biomineralization in MVs, instead of e.g. conventional bulk systems. It enables a tight control over droplet size and distribution, leading to a high-throughput of uniform and stable droplets. Within the droplets, the chemical microenvironment is highly controlled, including parameters such as pH and ion concentrations. This enables reaction processes to proceed more uniform and isolated from other components in the external environment, which minimizes unwanted side reactions and furthermore stabilizes intermediates of minerals within a confined space. The small reaction volumes within droplets allow the formation of nanomaterials that are difficult to achieve in bulk. Another notable advantage is the increased reaction rate within droplets, as in the confided environment of droplets the nucleation process proceeds much faster and more efficient, as in bulk, as shown for the control sample in section 9.1.3. From an environmental and cost perspective, the droplet-based system contributes to sustainability by reducing reagent consumption and minimizing waste.
In conclusion, our droplet-based system provides a unique combination of simplicity, uniform and controllable reaction chambers, enhanced reaction efficiency and sustainability. These advantages make droplet-based systems an attractive platform for advancing research and applications in material science.

10 Summary and Outlook – Part II

10.1 Design of a Droplet-Based Mineralization Model

In the second part of this thesis a novel biomimetic approach for studying the biomineralization of CaP was created and explored using a microfluidic droplet-based model.
This model was designed to replicate the initial stages of mineral formation within MVs, which naturally involve two phases: 1.) ion accumulation and initial crystal formation within the vesicles, and 2.) vesicle rupture followed by mineral propagation in the ECM.
The developed system aimed on mimicking the first phase by creating spherical micro-droplets to simulate ion accumulation and mineralization within MVs. For this, two different microfluidic droplet-based approaches were explored. The initial setup, which combined calcium and phosphate ions directly, yielded uniform droplets but suffered from rapid clogging of microfluidic channels. This issue was resolved in the second setup by introducing an enzymatic reaction using the enzyme AP to hydrolyze β-GP, thereby controlling phosphate release and initiating mineralization. This AP-mediated setup successfully produced stable, uniform droplets containing mineralized CaP particles.

10.1.1 Morphological Analysis of Calcium Phosphate (CaP) Minerals Formed within Droplets

For mineralized particles formed within droplets an isolation protocol was established and morphological properties were analyzed by SEM. The droplet-isolated CaP minerals were compared to those formed in a bulk mineralization setup, which was carried out according to previous studies [124, 125].
In the bulk setup, the particles displayed spherical structures with increasing aggregate size over time and with morphological characteristics similar to those described for ACP [124, 345].
In contrast, particles formed within droplets showed distinct morphologies, including nanosized 'whiskers' or needles indicative of crystalline HAp [345]. These morphological differences suggest that the droplet-based mineralization model follows a distinct crystallization pathway compared to bulk mineralization.
In conclusion, these results demonstrate the potential of an enzymatic droplet-based model for controlled biomineralization of CaP. The model brides the simplicity of bulk mineralization studies and the discrete, controllable environment of MV-mediated biomineralization. Although further optimizations are required, the enzymatic droplet-based model holds promise as a versatile platform for *in vitro* studies of biomineralization. This approach not only improves the understanding of CaP formation but also provides a valuable tool for future research into bone tissue engineering and the development of biomimetic materials.

10.2 Enzymatic Droplet-Based Mineralization with Peptides of Matrix Gla Protein (MGP)

Another objective in the second part of this thesis was to investigate the anti-calcification properties of MGP, which was believed to be primarily mediated by its post-translationally activated gla residues.

For our studies MGP was divided into smaller peptides, with each 14 amino-acids in length. Four peptides were selected, that differed in number and position of gla residues.

The peptides included YGLAS, which contain a single gla residue; FIN which lacks gla residues; and QR-GLA and SK-GLA, each containing two glas residues. Additionally, the uncarboxylated versions of these peptides were analyzed, where gla residues were replaced by glutamic acid (glu) residues, representing the inactive form of the peptides. As positive control the peptide MPP3 was used, since it accelerated the mineralization of CaP in previous bulk studies [125]. All peptides were analyzed at low and high concentration of 5 μM and 500 μM.

10.2.1 Imaging Analysis of Droplets and Mineralized Particles

First the droplets were imaged via LSM to analyze variations in droplet morphology and characteristics of mineralized particles formed within droplets.

No significant differences were observed in droplet size (ranging between 32 and 38 μm) or morphology of particles formed within the droplets across all peptides and peptide concentrations. Furthermore, despite the expectations that gla-containing peptides would impact mineral formation, the results showed no significant reduction in the quantity of minerals formed. While some peptides, particularly at high concentrations, influenced mineral morphology, no clear anti-calcification effects were observed in terms of mineral reduction.

SEM-analysis revealed distinctive morphological changes of crystals formed in presence of certain peptides, particularly MPP3 and the gla-containing peptides (QR-GLA, SK-GLA and YGLAS), but these did not necessarily correlate with anti-calcification properties. Instead, these changes seemed to affect the structure of CaP minerals, with differences in their morphology, as aggregated nano-spheres and fiber-like bundles or nanostrips, compared to the control. In addition, the properties of mineralized CaP particle were explored, noting that they exhibited characteristics similar to HAp, a stable biologically relevant mineral phase. These CaP minerals could be valuable for applications in biomaterials.

In conclusion, while the investigations into the anti-calcification properties of MGP peptides in the droplet-based mineralization model did not reveal clear reduction in mineral formation, it did provide important insights into the influence of MGP peptides on the morphology of CaP crystals. It was demonstrated, that gla-containing peptides had an impact on the mineral structure, with high concentrations leading to unique crystal morphologies. However, the lack of a significant reduction in mineral quantity suggests that these peptides did not directly inhibit calcification in this model, contrary to what was expected based on their known functions *in vivo*. Further studies are needed

to fully understand the mechanisms by which MGP peptides may influence mineralization processes and their potential for preventing calcification in biological systems.

10.3 Outlook and Perspectives for Future Work

One major difference between our droplet-based model and the natural system is the larger size of the droplets compared to MVs. Our droplets are ranging around 30 µm in diameter, while MVs typically range between 10 to 400 nm [82, 92-94].

Future experiments may focus on droplet size reduction to further refine the model and better replicate natural conditions. As already discussed in section… there are two main factors influencing the droplet size: interfacial tension and shear forces [340, 341]. These factors can be influenced by different variables as flowrates of continous (oil) and dispersed phase (water), type and concentration of surfactant, temperature or by modifying the channel geometry, width, length and angle of the microfluidic chip [331, 332].

The force balance between these factors can be described by the capillary number (C_a), a dimensionless number, expressing the ration between viscous forces and interfacial tension [341] [331]:

$$C_a = \frac{\mu_C * u_C}{\sigma} = \frac{\mu_C * F_C}{s * \sigma}$$

Whereby, μ_C and u_C are the dynamic viscosity and velocity of the continuous phase in Pa*s and mm/s; Fc is the continuous volumetric flow rate in µl/s; s is the microchannel surface area in mm^2 and σ is the surface tension at the rupturing trice in Nm/m [331].

The balance of these factors requires careful optimization to achieve the desired droplet size and production efficiency. Overall, it should be possible to reduce the size of the droplets to few micrometers, as known from previous studies [281, 318]. Although this is still larger than natural MVs, they are in a similar volumetric range on the femtoliter scale.

Another important aspect for future experiments should focus on an in-depth analysis of mineralized particles, for instance by FTIR and/or XRD, to confirm the phases or phase compositions in our samples.

Furthermore, the setup could be optimized in terms of that MGP-peptides are added in a later stage of the mineralization process, since in the natural system MGP is an extracellular protein and not within MVs [100]. For instance, droplets could be produced without peptide additive, as the control, and after certain mineralization time destabilizing surfactants could be added, to release the crystals in a solution of the peptide(s), as in the natural system.

With our approach of droplet-based mineralization and destabilizing surfactants for crystal release the first and second phase of the mineralization process can be investigated in one. In recent studies, the phases of the mineralization process were investigated separately, as e.g. shown by Shen et al. [141]. They used polymeric vesicles as Biomimetic MVs, encapsulated ACP within these vesicles and afterwards released ACP again to study mineral propagation on collagen.

With our setup, intermediated steps can be eliminated, which is not only time saving but also much more similar to the natural system.

In summation, droplet-based microfluidics represents a powerful and versatile tool for studying biomineralization within small, spherical structures that closely mimic natural biomineralization processes occuring in MVs. Droplet-based microfluidics offer precise control of uniform and stable droplets at high throughput. This uniformity ensures reproducibility across experiments and provides an ideal platform for investigating biomineralization under well-defined conditions.
One of the most significant advantages of the droplet-based system is the ability to tightly regulate the chemical environment within each droplet, including parameters such as pH or ion concentrations. This enables reaction processes to proceed uniformly and isolates them from external influences, thereby minimizing unwanted side reactions. Additionally, the confined environment stabilizes intermediates of biominerals, ensuring greater precision and reliability in the mineralization process.
Another key benefit of the droplet-based approach is the enhance reaction efficiency. The small reaction volumes within droplets provide a confined space that accelerates the nucleation process, making it faster and more efficient compared to bulk systems. This phenomenon is particularly evident in the control samples discussed in section 9.1.3, where the confined space of droplets significantly improved reaction kinetics.
These advantages are complemented by the system's sustainability, as droplet-based approaches require minimal reagent consumption and generate less waste.
In conclusion, despite differences from natural MVs, such as size and complexity, the enzymatic droplet-based system established here represents a step forward. It provides an attractive and innovative platform for advancing biomineralization research and material science. By bridging the gap between natural or other biomimetic MVs (e.g. polymeric vesicles) and conventional bulk systems, this approach opens new possibilities for the development of biomimetic nanomaterials for bone tissue engineering and can gain deeper insights into biomineralization processes.

11 Appendix – Part II

11.1 Additional Results for Droplet Mineralization

11.1.1 Droplet Control without Alkaline Phosphatase (AP)

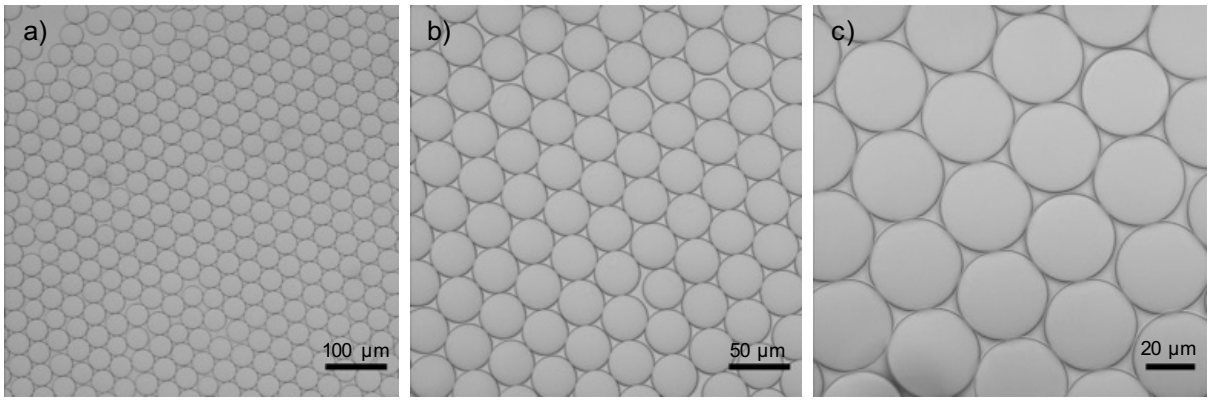

Figure 105: Control sample without AP. As control sample the two aqueous solutions were used, $CaCl_2$ (24.4 mM) and β-glycerophosphate (β-GP, 14.4 mM), both in a TRIS/HCl buffer (25 mM, pH 7.4), without the addition of the enzyme AP. For the oil phase a solution of 2 °C for 4 h. As expected, the results showed no mineralization within the droplets.

11.1.2 Droplet Size in Controls and in Presence of Peptides

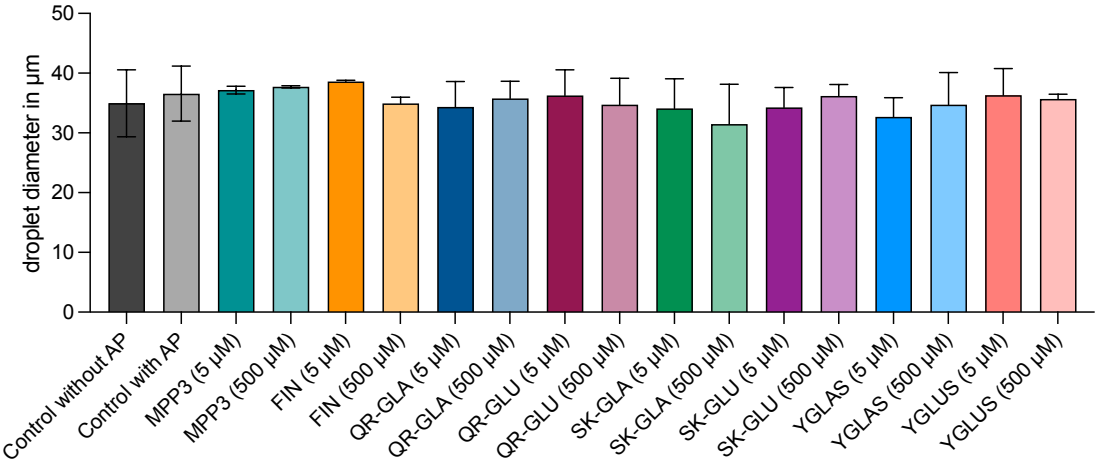

Figure 106: Overview of droplet size in controls and in presence of different peptides. Control without AP: 34.96±5.62 µm (n=366); control with AP: 36.57±4.60 µm (n=499); MPP3 (5 µM): 37.17 ±0.66 µm (n=185); MPP3 (500 µM): 37.71±0.17 µm (n=186); FIN (5 µM): 38.59±0.21 µm (n=144); FIN (500 µM): 34.92±1.05 µm (n=158); QR-GLA (5 µM): 34.35±4.27 µm (n=171); QR-GLA (500 µM): 35.75±2.90 µm (n=189); QR-GLU (5 µM): 36.25±4.31 µm (n=131); QR-GLU (500 µM): 34.73±4.43 µm (n=133); SK-GLA (5 µM): 34.11±4.94 µm (n=117); SK-GLA (500 µM): 31.48±6.66 µm (n=101); SK-GLU (5 µM): 34.27±3.32 µm (n=105); SK-GLU (500 µM): 36.18±1.93 µm (n=145); YGLAS (5 µM): 32.69±3.22 µm (n=121); YGLAS (500 µM): 34.72±5.39 µm (n=168); YGLUS (5 µM): 36.31±4.48 µm (n=115); YGLUS (500 µM): 35.68±0.81 µm (n=138). For each sample, droplet diameter was measured using ImageJ2 (version 2.3.0/1.53f) and calculated from three individual experiments with the standard deviation as error bar.

11.2 Additional SEM-Images of Isolated Particles

11.2.1 Calcium Phosphate Particles Formed within Droplets in Presence of MGP-Peptides

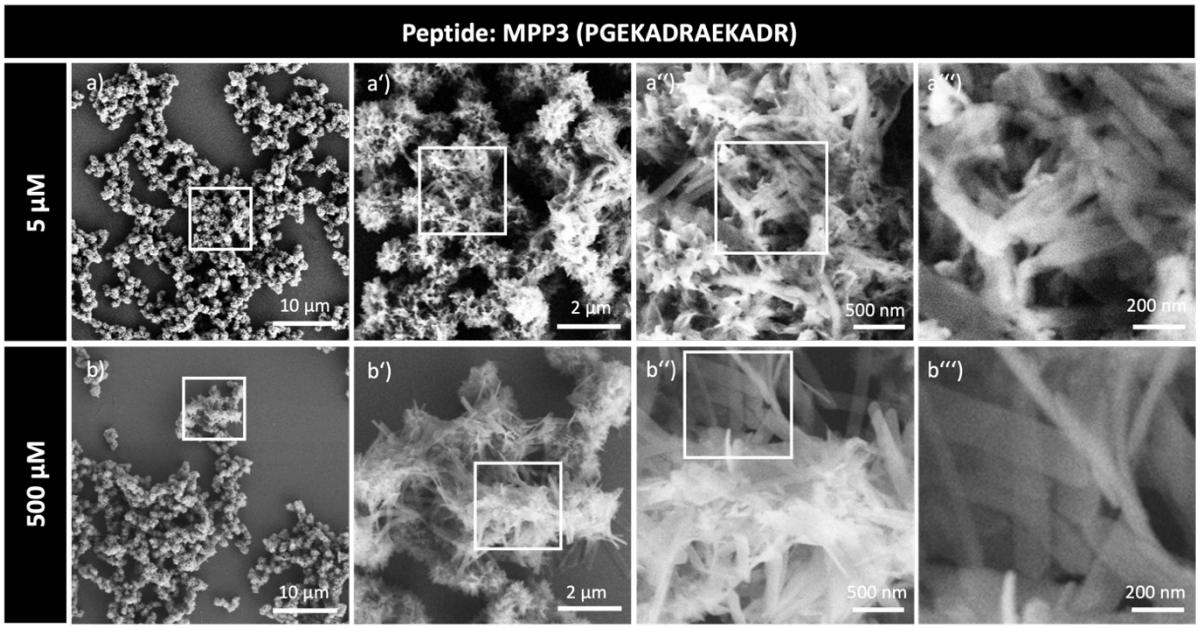

Figure 107: Isolated particles of calcium phosphate formed within droplets in presence of peptide MPP3 at low and high concentration (5 µM and 500 µM). At both peptide concentrations MPP3 produced CaP minerals with a bundled fibre-like structure, but more pronounced at higher concentration. The minerals, formed within droplets, were isolated and transferred to a si-wafer, dried and coated with carbon (8 nm). Pictures were taken at 3 kV.

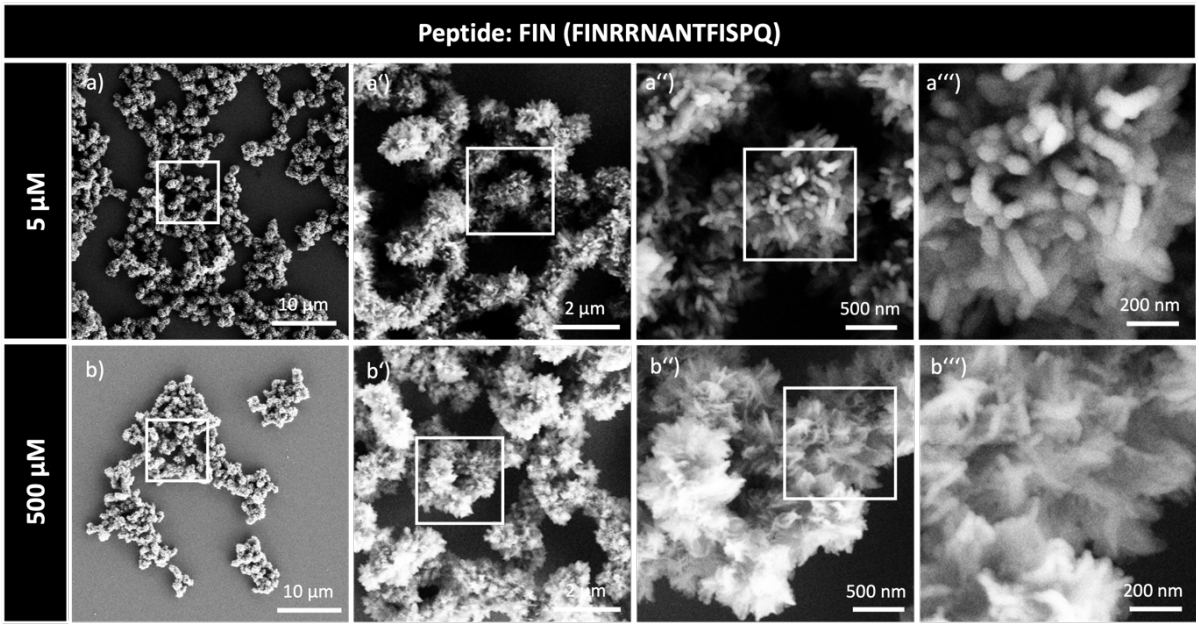

Figure 108: Isolated particles of calcium phosphate formed within droplets in presence of peptide FIN at low and high concentration (5 µM and 500 µM). The particles exhibited similar characteristics as those observed in control samples, with small nano-needles/'whiskers' on the surface of spherical particles, similar to dandelions. The minerals were formed in droplets. For SEM analysis, mineralized particles were isolated and transferred to a si-wafer, dried and coated with carbon (8 nm). Pictures were taken at 3 kV.

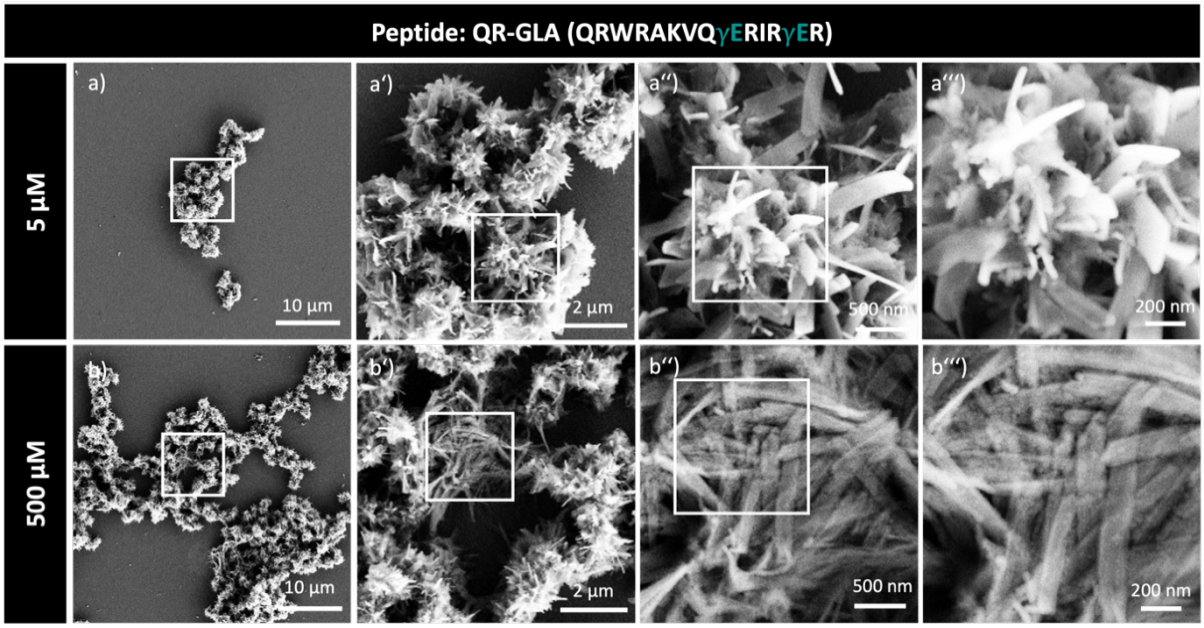

Figure 109: Isolated particles of calcium phosphate formed within droplets in presence of peptide QR-GLA at low and high concentration (5 µM and 500 µM). CaP minerals appeared as bundled fibre-like structures or nanosheets. The minerals were formed in droplets. For SEM analysis, mineralized particles were isolated and transferred to a si-wafer, dried and coated with carbon (8 nm). Pictures were taken at 3 kV.

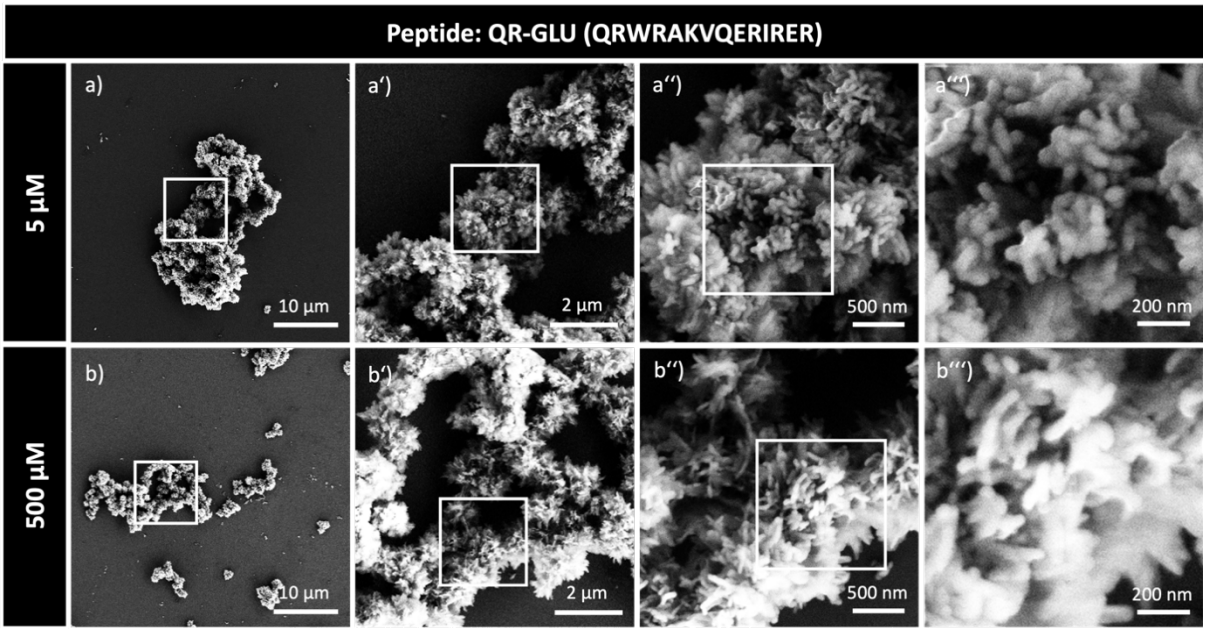

Figure 110: Isolated particles of calcium phosphate formed within droplets in presence of peptide QR-GLU at low and high concentration (5 µM and 500 µM). The particles exhibited similar characteristics as those observed in control samples, with small nano-needles/'whiskers' on the surface of spherical particles. The minerals were formed in droplets. For SEM analysis, mineralized particles were isolated and transferred to a si-wafer, dried and coated with carbon (8 nm). Pictures were taken at 3 kV.

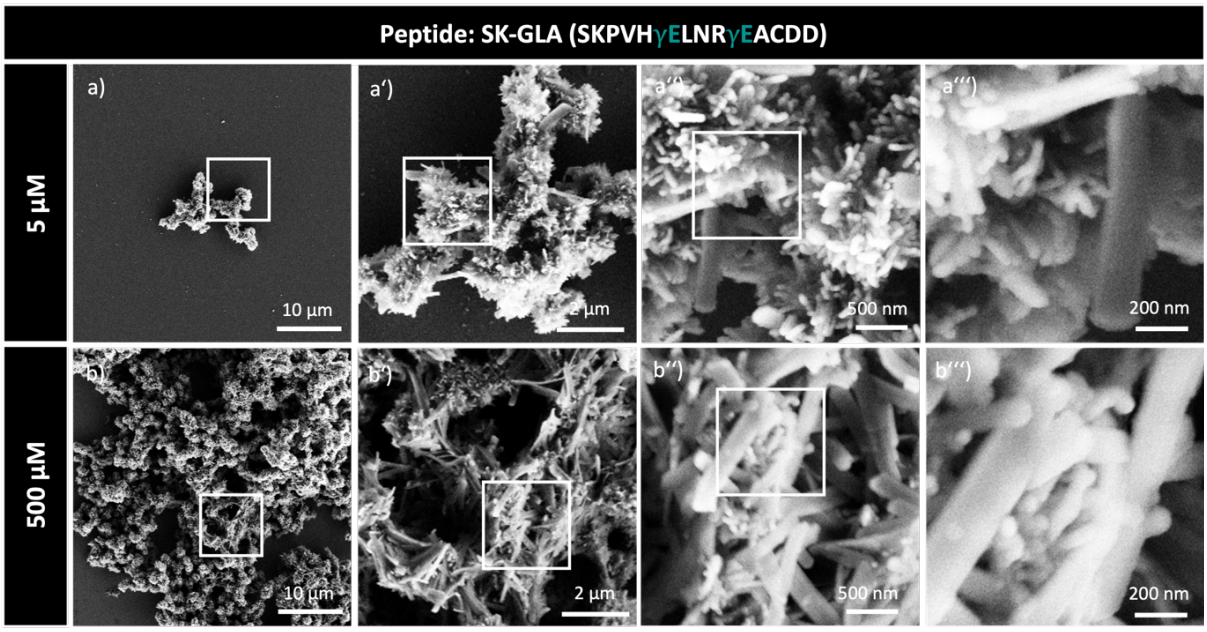

Figure 111: Isolated particles of calcium phosphate formed within droplets in presence of peptide SK-GLA at low and high concentration (5 µM and 500 µM). At low concentration (5 µM) similar characteristics were observed as in control samples, with small nano-needles/'whiskers' on the surface of spherical particles. At high peptide concentration (500 µM) fibre-like nano sheets were formed. The minerals were formed in droplets. For SEM analysis, mineralized particles were isolated and transferred to a si-wafer, dried and coated with carbon (8 nm). Pictures were taken at 3 kV.

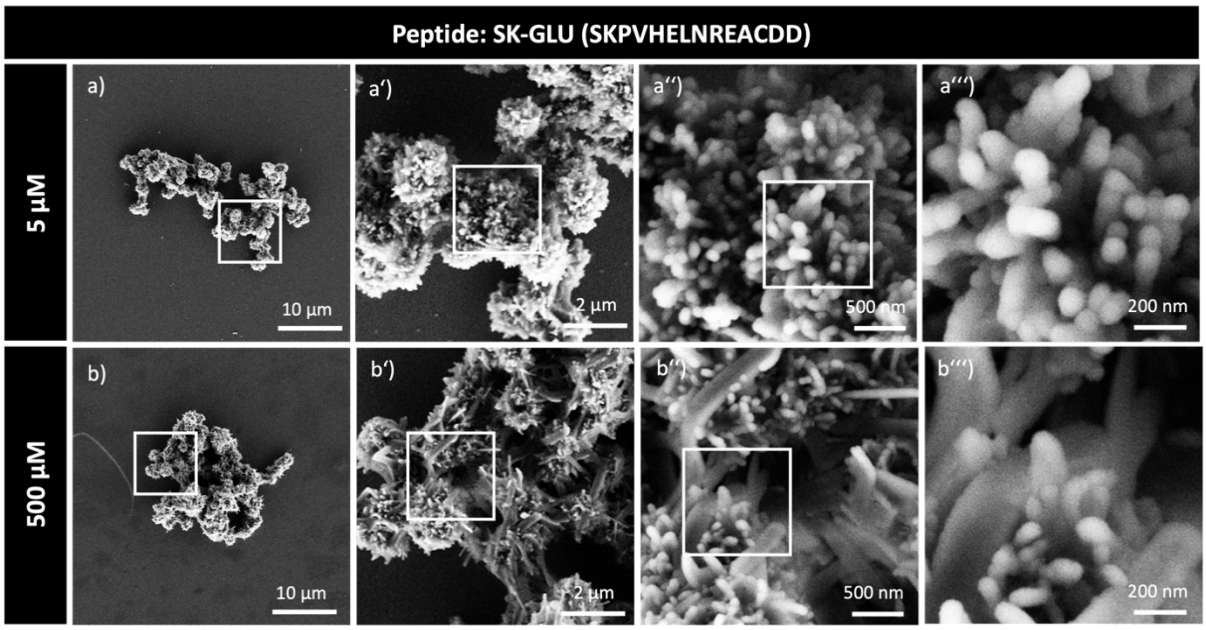

Figure 112: Isolated particles of calcium phosphate formed within droplets in presence of peptide SK-GLU at low and high concentration (5 µM and 500 µM). At low concentration (5 µM) small nano-needles/'whiskers' on the surface of spherical particles were observed. At high peptide concentration (500 µM) additional fibre-like nano sheets were formed mixed with small nano-'whiskers'. The minerals were formed in droplets. For SEM analysis, mineralized particles were isolated transferred to a si-wafer, dried and coated with carbon (8 nm). Pictures were taken at 3 kV.

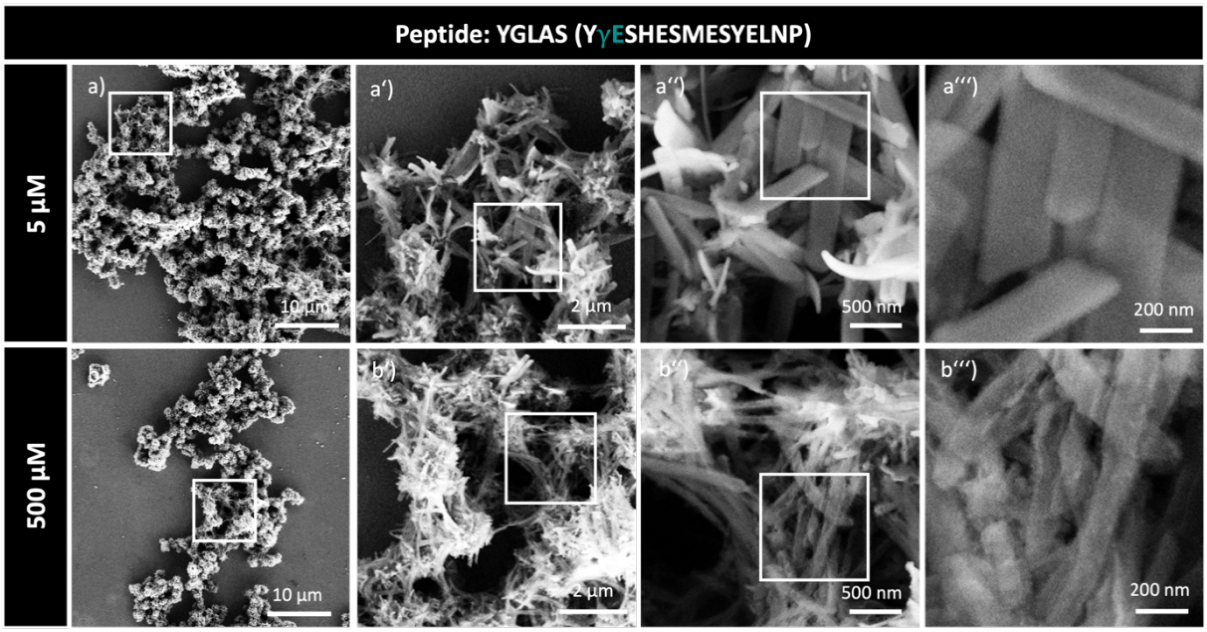

Figure 113: Isolated particles of calcium phosphate formed within droplets in presence of peptide YGLAS at low and high concentration (5 µM and 500 µM). At both concentrations, CaP minerals appeared as bundled fibre-like structures or nanosheets. The minerals, formed within droplets, were isolated and transferred to a si-wafer, dried and coated with carbon (8 nm). Pictures were taken at 3 kV.

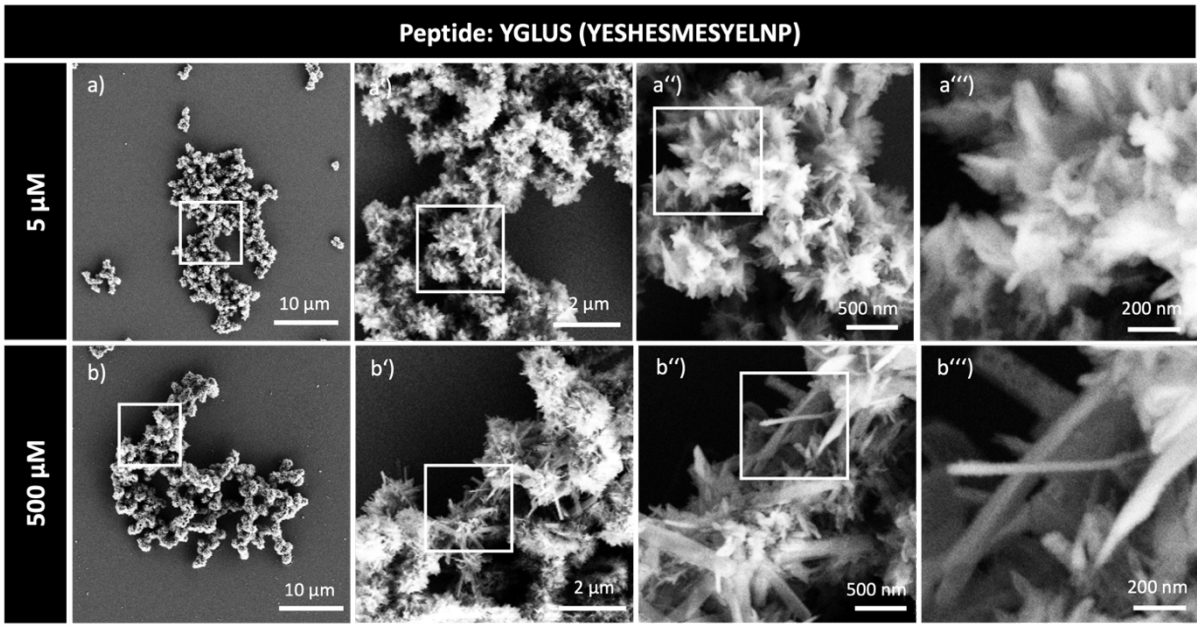

Figure 114: Isolated particles of calcium phosphate formed within droplets in presence of peptide YGLUS at low and high concentration (5 µM and 500 µM). At low concentration (5 µM) YGLUS induced dandelion-like structures. At high peptide concentration (500 µM) additional fibre-like mainly nano needles were formed. The minerals formed within droplets, were isolated and transferred to a si-wafer, dried and coated with carbon (8 nm). Pictures were taken at 3 kV.

Scientific Contribution

Conferences, Presentations and Publications

Contribution at the International Congress on Glaucoma Surgery (ICGS), Montreal, Canada, September 6-8, 2018

'*Pressure Measurements and Cell Studies on Hyaluronan Hydrogel-Modified Implants for Glaucoma Treatment'*, Oral Presentation at the Annual Symposium, Antholz, Italy, April 2019

'*Hyaluronan Hydrogels for Pressure Regulation in Glaucoma Therapy'*, Oral and Poster Presentation at the International Society of Hyaluronan Science (ISHAS) conference, Cardiff, Wales, June 9-13, 2019

'*Glaucoma Nano-Technology'*, Oral Presentation at the 15th Projekthaus NanoBioMater workshop, Stuttgart, Germany, October 9, 2019

Völkle (nee Evgrafov) E., Schulz F., Kanold J. M., Michaelis M., Wissel K., Brümmer F., Schenk A. S., Ludwigs S., Bill J., Rothenstein D, *'Functional mimicry of sea urchin biomineralization proteins with $CaCO_3$-binding peptides selected by phage display'*, Journal of Materials Chemistry B, **2023** 11(42): p. 10174-10188. DOI: https://doi.org/10.1039/D3TB01584J

Elke Völkle, Joachim P. Spatz, Fania Geiger, *'Customizable hyaluronan hydrogel-based glaucoma drainage devices (GDDs) for intraocular pressure (IOP) management'*, in preparation.

Elke Völkle, Joachim P. Spatz, Fania Geiger, *'Enzymatic droplet-based model for biomineralization studies of CaP*, in preparation.

Literature

1. Lim, R. and I. Goldberg, *Glaucoma in the twenty-first century*, in *The glaucoma book: a practical, evidence-based approach to patient care*, P.N. Schacknow and J.R. Samples, Editors. 2010, Springer. p. 1-21. ISBN: 978-0-387-76699-7
2. Tham, Y.C., et al., *Global prevalence of glaucoma and projections of glaucoma burden through 2040.* Ophthalmology, 2014. **121**: p. 2081-2090. https://doi.org/10.1016/j.ophtha.2014.05.013
3. Weinreb, R.N., T. Aung, and F.A. Medeiros, *The pathophysiology and treatment of glaucoma: a review.* JAMA, 2014. **311**(18): p. 1901-11. https://doi.org/10.1001/jama.2014.3192
4. Grehn, F. and R. Stamper, *Glaucoma.* Essentials in Ophthalmology, ed. G.K. Krieglstein and R.N. Weinreb. 2006, Berlin Heidelberg: Springer. ISBN: 3-540-26220-2
5. Weinreb, R.N. and P.T. Khaw, *Primary open-angle glaucoma.* The Lancet, 2004. **363**(9422): p. 1711-1720. https://doi.org/10.1016/s0140-6736(04)16257-0
6. Pascolini, D. and S.P. Mariotti, *Global estimates of visual impairment: 2010.* British Journal of Ophthalmology, 2012. **96**(5): p. 614-8. https://doi.org/10.1136/bjophthalmol-2011-300539
7. Quigley, H.A. and A.T. Broman, *The number of people with glaucoma worldwide in 2010 and 2020.* British Journal of Ophthalmology, 2006. **90**(3): p. 262-7. https://doi.org/10.1136/bjo.2005.081224
8. organization, W.h. *World report on vision.* 2019. 180 DOI: https://www.who.int/publications/i/item/9789241516570.
9. McMenemy, M.G., *Primary open angle glaucoma*, in *The glaucoma book: a practical, evidence-based approach to patient care*, P.N. Schacknow and J.R. Samples, Editors. 2010, Springer. p. 399-419.
10. Abu-Hassan, D.W., T.S. Acott, and M.J. Kelley, *The trabecular meshwork: a basic review of form and function.* Journal of Ocular Biology, 2014. https://doi.org/10.13188/2334-2838.1000017
11. Zhang, N., et al., *Prevalence of primary open angle glaucoma in the last 20 years: a meta-analysis and systematic review.* Science Reports, 2021. **11**(1): p. 13762. https://doi.org/10.1038/s41598-021-92971-w
12. Fechtner, R.D. and R.N. Weinreb, *Mechanisms of optic nerve damage in primary open angle glaucoma.* Survey of Ophthalmology, 1994. **39**(1): p. 23-42. https://doi.org/10.1016/s0039-6257(05)80042-6
13. Naumann, G.O.H. and D.J. Apple, *Pathology of the eye.* 1986: Springer. ISBN: 978-1-4613-8527-1
14. Bellezza, A.J., et al., *Deformation of the lamina cribrosa and anterior scleral canal wall in early experimental glaucoma.* Investigative Ophthalmology & Visual Science, 2003. **44**(2): p. 623-37. https://doi.org/10.1167/iovs.01-1282
15. Pena, J.D.O., et al., *Increased elastin expression in astrocytes of the lamina cribrosa in response to elevated intraocular pressure.* Investigative Ophthalmology & Visual Science, 2001. **42**: p. 2303-2314. PMID: 11527944
16. Quigley, H.A., et al., *Retrograde axonal transport of BDNF in retinal ganglion cells Is blocked by acute IOP elevation in rats.* Investigative Ophthalmology & Visual Science, 2000. **41**: p. 3460-3466. PMID: 11006239
17. Cioffi, G.A. and L. Wang, *Optic nerve blood flow in glaucoma.* Seminars in Ophthalmology, 1999. **14**(3): p. 164-70. https://doi.org/10.3109/08820539909061470
18. Loewen, N.A. and A.P. Tanna, *Glaucoma risk factors: intraocular pressure*, in *The glaucoma book: a practical, evidence-based approach to patient care*, P.N. Schacknow and J.R. Samples, Editors. 2010, Springer. p. 35-49. ISBN: 978-0-387-76699-7

19. Goldmann, H., *Abflussdruck, Minutenvolumen und Widerstand der Kammerwasserströmung des Menschen.* Documenta Ophthalmologica, 1951. **5**: p. 278-356. https://doi.org/10.1007/BF00143664
20. Schappert-Kimmijser, J., *A five-year follow-up of subjects with intra-ocular pressure of 22-30 mmHg without anomalies of optic nerve and visual field typical for glaucoma at first investigation.* Ophthalmologica, 1971. **162**: p. 289-295. https://doi.org/10.1159/000306295
21. Sun, Y., et al., *Time trends, associations and prevalence of blindness and vision loss due to glaucoma: an analysis of observational data from the Global Burden of Disease Study 2017*. BMJ Open, 2022. **12**(1): p. e053805. https://doi.org/10.1136/bmjopen-2021-053805
22. Reiss, G.R., et al., *Aqueous humor flow during sleep.* Investigative Ophthalmology & Visual Science, 1984. **25**: p. 776-778. PMID: 6724850
23. Qureshi, I.A., et al., *Seasonal and diurnal variation of ocular pressure in ocular hypertensive subjects in pakistan.* Singapore Medical Journal, 1999. **40**: p. 345-348. PMID: 10489493
24. Liu, J.H.K., et al., *Twenty-four–hour pattern of intraocular pressure in the aging population.* Investigative Ophthalmology & Visual Science, 1999. **40**: p. 2912-2917. PMID: 10549652
25. Liu, J.H., et al., *Twenty-four-hour intraocular pressure pattern associated with early glaucomatous changes.* Investigative Ophthalmology & Visual Science, 2003. **44**(4): p. 1586-90. https://doi.org/10.1167/iovs.02-0666
26. Realini, T., *Monocular drug trials for glaucoma therapy in the community setting*, in *The glaucoma book: a practical evidence-based approach to patient care*, P.N. Schacknow and J.R. Samples, Editors. 2010, Springer. p. 643-646. ISBN: 978-0-387-76699-7
27. Schacknow, P.N. and J.R. Samples, *Medications used to treat Glaucoma*, in *The glaucoma book: a practical, evidence-based approach to patient care*, P.N. Schacknow and J.R. Samples, Editors. 2010, Springer. p. 583-628. ISBN: 978-0-387-76699-7
28. Buffault, J., et al., *The trabecular meshwork: structure, function and clinical implications. A review of the literature.* Journal Francais d'Ophthalmologie, 2020. **43**: p. e217-e230. https://doi.org/10.1016/j.jfo.2020.05.002
29. Knepper, P.A., M.J. Nolan, and B.Y.J.T. Yue, *How the revolution in cell biology will affect glaucoma: biomarkers*, in *The glaucoma book: a practical, evidence-based approach to patient care*, P.N. Schacknow and J.R. Samples, Editors. 2010, Springer. p. 933-938. ISBN: 978-0-387-76699-7
30. Acott, T.S. and M.J. Kelley, *Extracellular matrix in the trabecular meshwork.* Experimental Eye Research, 2008. **86**(4): p. 543-61. https://doi.org/10.1016/j.exer.2008.01.013
31. Tamm, E.R., *The trabecular meshwork outflow pathways: structural and functional aspects.* Experimental Eye Research, 2009. **88**(4): p. 648-55. https://doi.org/10.1016/j.exer.2009.02.007
32. Lennarz, W.J., *The biochemistry of glycoproteins and proteoglycans*. 1980: Plenum Press New York. ISBN: 978-1-4684-1008-2
33. Faralli, J.A., et al., *Cytoskeletal active agents for glaucoma therapy*, in *The glaucoma book: a practical, evidence-based approach to patient care*, P.N. Schacknow and J.R. Samples, Editors. 2010, Springer. p. 955-959. ISBN: 978-0-387-76699-7
34. Stamer, W.D. and A.F. Clark, *The many faces of the trabecular meshwork cell.* Exp Eye Res, 2017. **158**: p. 112-123. https://doi.org/10.1016/j.exer.2016.07.009
35. Tam, D.Y. and I.K. Ahmed, *Incisional therapies: canaloplasty and new implant devices*, in *The glaucoma book: a practical, evidence-based approach to patient care*, P.N. Schacknow and J.R. Samples, Editors. 2010, Springer. p. 795-812. ISBN: 978-0-387-76699-7
36. Borras, T., *Gene expression in the trabecular meshwork and the influence of intraocular pressure.* Progress in Retinal and Eye Research, 2003. **22**(4): p. 435-463. 10.1016/s1350-9462(03)00018-1
37. Vranka, J.A., et al., *Extracellular matrix in the trabecular meshwork: intraocular pressure regulation and dysregulation in glaucoma.* Experimental Eye Research, 2015. **133**: p. 112-25. https://doi.org/10.1016/j.exer.2014.07.014

38. Knepper, P.A., et al., *Glycosaminoglycans of the human trabecular meshwork in primary open-angle glaucoma.* Investigative Ophthalmology & Visual Science, 1996. **37**: p. 1360-1367. PMID: 8641839
39. Sun, Y.Y. and K.E. Keller, *Hyaluronan cable formation by ocular trabecular meshwork cells.* Experimental Eye Research, 2015. **139**: p. 97-107. https://doi.org/10.1016/j.exer.2015.07.018
40. Lütjen-Drecoll, E., et al., *Quantitative analysis of ‚plaque material' in the inner- and outer wall of Schlemm's canal in normal and glaucomatous eyes.* Experimental Eye Research, 1986. **42**: p. 443-455. https://doi.org/10.1016/0014-4835(86)90004-7
41. Lütjen-Drecoll, E., *Functional morpholoy of the trabecular meshwork in primate eyes.* Progress in Retinal and Eye Research, 1998. **18**: p. 91-119. 10.1016/s1350-9462(98)00011-1
42. Tripathi, R.C., et al., *Trabecular cells express the TGF-0ß2 gene and secrete the cytokine.* Experimental Eye Research, 1994. **58**: p. 523-528. https://doi.org/10.1006/exer.1994.1046
43. Vittal, V., et al., *Changes in gene expression by trabecular meshwork cells in response to mechanical stretching.* Investigative Ophthalmology & Visual Science, 2005. **46**(8): p. 2857-68. https:/doi.org/10.1167/iovs.05-0075
44. Johnstone, M.A., *A new model describes an aqueous outflow pump and explores causes of pump failure in glaucoma*, in *Glaucoma*, F. Grehn and R. Stamper, Editors. 2006, Springer. ISBN: 3-540-26220-2
45. Tane, N., et al., *Effect of excess synthesis of extracellular matrix components by trabecular meshwork cells: possible consequence on aqueous outflow.* Experimental Eye Research, 2007. **84**(5): p. 832-42. https://doi.org/10.1016/j.exer.2007.01.002
46. Whitson, J.T., *Choosing adjunctive glaucoma therapy*, in *The glaucoma book: a practical, evidence-based approach to patient care*, P.N. Schacknow and J.R. Samples, Editors. 2010, Springer. p. 629-641. ISBN: 978-0-387-76699-7
47. Weinreb, R.N., et al., *Prostaglandins increase matrix metalloproteinase release from human ciliary smooth muscle cells.* Investigative Ophthalmology & Visual Science, 1997. **38**: p. 2772-2780. PMID: 9418730
48. Gabelt, B.T. and P.I. Kaufman, *Prostanglandin F2alpha increases uveoscleral outflow in the cynomolgus monkey.* Experimental Eye Research, 1989. **49**: p. 389-402. https://doi.org/10.1016/0014-4835(89)90049-3
49. Villumsen, J., A. Alm, and M. Söderström, *Prostaglandin F2-isopropylester eye drops: effect on intraocular pressure in open-angle glaucoma.* British Journal of Ophthalmology, 1989. **73**: p. 975-979. https://doi.org/0.1136/bjo.73.12.975
50. Rasmussen, C.A., P.L. Kaufman, and J.A. Kiland, *Benzalkonium chloride and glaucoma.* Journal of Ocular Pharmacology and Therapeutics, 2014. **30**: p. 163-169. https://doi.org/10.1089/jop.2013.0174
51. Stjernschantz, J.W., et al., *Mechanism and clinical significance of prostaglandin-induced iris pigmentation.* Survey of Opthalmology, 2002. **47**: p. S162-S175. https://doi.org/10.1016/s0039-6257(02)00292-8
52. Bito, L.Z., et al., *Neoinvasive observations on eyes of cats after long-term maintenance of reduced intraocular pressure by topical application of prostaglandin E2.* Investigative Ophthalmology & Visual Science, 1983. **24**: p. 376-380. PMID: 6572618
53. Friedman, D.S.e.a., *Using pharmacy claims data to study adherence to glaucoma medications: methodology and findings of the glaucoma adherence and persistency study (GAPS).* Investigative Ophthalmology & Visual Science, 2007. **48**: p. 5052-5057. https://doi.org/0.1167/iovs.07-0290
54. Gaasterland, D., *Laser therapies: iridotomy, iridoplasty and trabeculectomy*, in *The glauoma book: a practical, evidence-based approach to patient care*, P.N. Schacknow and J.R. Samples, Editors. 2010, Springer. p. 713-739. ISBN: 978-0-387-76699-7

55. The-AGIS-investigators, *The advanced glacoma intervention study (AGIS): 11. risk factors for failure of trabeculectomy and argon laser trabeculoplasty.* American Journal of Ophthalmology, 2002. **134**(4): p. 481-498. https://doi.org/10.1016/S0002-9394(02)01658-6
56. The-AGIS-investigators, *The advanced glaucoma intervention study (AGIS): 13. comparison of treatment outcomes within race: 10 year-result.* Ophthalmology, 2004. **111**(4): p. 651-664. https://doi.org/10.1016/j.ophtha.2003.09.025.
57. Melamed, S. and D. Cotlear, *Incisional therapies: trabeculectomy surgery*, in *The glaucoma book: a practical, evidence-based approach to patient care*, P.N. Schacknow and J.R. Samples, Editors. 2010. p. 765-787. ISBN: 978-0-387-76699-7
58. Riva, I., et al., *Canaloplasty in the treatment of open-Angle glaucoma: a review of patient selection and outcomes.* Advances in Therapy, 2019. **36**(1): p. 31-43. https://doi.org/10.1007/s12325-018-0842-6
59. Jay, J. and S. Murray, *Early trabeculectomy versus convetional management in primary open angle glaucoma.* British Journal of Ophthalmology, 1988. **72**: p. 881-889. https://doi.org/10.1136/bjo.72.12.881
60. Greenfield, D.S., et al., *Late-onset bleb leaks after glaucoma filtering surgery.* Archives of Ophthalmology, 1998. **116**(4): p. 443-7. https://doi.org/10.1001/archopht.116.4.443
61. Patel, H.Y. and H.V. Danesh-Meyer, *Incidence and management of cataract after glaucoma surgery.* Current Opinion in Ophthalmology, 2013. **24**(1): p. 15-20. https://doi.org/10.1097/ICU.0b013e32835ab55f
62. Molteno, A.C.B., *New implant for drainage in glaucoma.* British Journal of Ophthalmology, 1969. **53**: p. 606-615. https://doi.org/10.1136/bjo.53.9.606
63. Molteno, A.C.B., J. Strachan, and E. Ancker, *Long tube implants in the management of glaucoma.* South Africa Medical Journal, 1976. **50**: p. 1062–1066. PMID: 951630
64. Boyle, J.W. and P.A. Netland, *Incisional therapies: shunts and valved implants*, in *The glaucoma book: a practical, evidence-based approach to patient care*, P.N. Schacknow and J.R. Samples, Editors. 2010, Springer. p. 813-830. ISBN: 978-0-387-76699-7
65. Krupin, T., et al., *Valve implants in filtering surgery.* American Journal of Ophthalmology, 1976. **81**(2): p. 232-5. https://doi.org/10.1016/0002-9394(76)90737-6
66. Minckler, D., et al., *Experimental studies of aqueous filtration using the molteno implant.* Transactions of the Amercian Ophthalmological Society, 1987. **85**: p. 368-392. PMID: 3447338
67. Roy, S., E. Ravinet, and A. Mermoud, *Baerveldt implant in refractory glaucoma: long-term results and factors influencing outcome.* International Ophthalmology, 2002. **24**: p. 93-100. https://doi.org/10.1023/a:1016335313035
68. Chen, D.Z. and C.C.A. Sng, *Safety and efficacy of microinvasive glaucoma surgery.* Journal of Ophthalmology, 2017. **2017**: p. 3182935. https://doi.org/10.1155/2017/3182935
69. Hill, R. and D. Minckler, *Incisional therapies. what's on the horizon?*, in *The glaucoma book: a practical, evidence-based approach to patient care*, P.N. Schacknow and J.R. Samples, Editors. 2010, Springer. p. 831-840. ISBN: 978-0-387-76699-7
70. Gabbay, I.E. and S. Ruben, *CyPass micro-stent safety and efficacy at one year: what have we learned?* Journal of Current Glaucoma Practice, 2019. **13**: p. 99-103. https://doi.org/10.5005/jp-journals-10078-1264
71. Pinchuk, L., et al., *The development of a micro-shunt made from poly(styrene-block-isobutylene-block-styrene) to treat glaucoma.* Journal of Biomedical Materials Research A, 2017. **105**(1): p. 211-221. 10.1002/jbm.b.33525
72. Ansari, E., *An update on implants for minimally invasive glaucoma surgery (MIGS).* Ophthalmology and Therapy, 2017. **6**(2): p. 233-241. https://doi.org/10.1007/s40123-017-0098-2
73. Yaswanth, T.S., et al., *Outcomes of reimplantation of a new Glaucoma Drainage Device after explantation of an older implant from exposure-related complications.* Indian Journal of Ophthalmology, 2023. **71**(10): p. 3352-3356. https://doi.org/10.4103/IJO.IJO_3105_22

74. Nguyen, Q.H., *Primary surgical management refractory glaucoma: tubes as initial surgery.* Current Opinion in Ophthalmology, 2009. **20**(2): p. 122-5. https://doi.org/10.1097/ICU.0b013e32831da828
75. Gedde, S.J., et al., *Postoperative complications in the Tube Versus Trabeculectomy (TVT) study during five years of follow-up.* American Journal of Ophthalmology, 2012. **153**: p. 804–814. https://doi.org/10.1016/j.ajo.2011.10.024
76. Souza, C., et al., *Long-term outcomes of Ahmed glaucoma valve implantation in refractory glaucomas.* American Journal of Ophthalmology, 2007. **144**(6): p. 893-900. https://doi.org/10.1016/j.ajo.2007.07.035
77. Budenz, D.L., et al., *Postoperative complications in the Ahmed Baerveldt comparison study during five years of follow-up.* American Journal of Ophthalmology, 2016. **163**: p. 75-82 e3. https://doi.org/10.1016/j.ajo.2015.11.023
78. Wishart, P.K., A. Choudhary, and D. Wong, *Ahmed glaucoma valves in refractory glaucoma: a 7-year audit.* British Journal of Ophthalmology, 2010. **94**(9): p. 1174-9. https://doi.org/10.1136/bjo.2009.165357
79. Byun, Y.S., N.Y. Lee, and C.K. Park, *Risk factors of implant exposure outside the conjunctiva after Ahmed glaucoma valve implantation.* Japanese Journal of Ophthalmology, 2009. **53**(2): p. 114-119. https://doi.org/10.1007/s10384-008-0630-y
80. Smith, M., Y.M. Buys, and G.E. Trope, *Replacement of Ahmed aqueous drainage devices in eyes with device-related complications.* Journal of Glaucoma, 2009. **18**(6): p. 484-7. https://doi.org/10.1097/IJG.0b013e31818fa73b
81. Luo, G., et al., *Spontaneous calcification of arteries and cartilage in mice lacking matrix GLA protein.* Nature, 1997. **386**: p. 78-81. https://doi.org/10.1038/386078a0
82. Anderson, H.C., *Matrix vesicles and calcification.* Current Rheumatology Reports, 2003. **5**: p. 222-226. https://doi.org/10.1007/s11926-003-0071-z
83. Anderson, H.C., *Electron microscopic studies of induced cartilage development and calcification.* Journal of Cell Biology, 1967. **35**: p. 81-101. https://doi.org/10.1083/jcb.35.1.81
84. Ehrlich, H., *Biocomposites and mineralized tissues*, in *Biological materials of marine origin*. 2015, Springer. p. 91-210. ISBN: 978-94-007-5729-5
85. Jeong, J., et al., *Bioactive calcium phosphate materials and applications in bone regeneration.* Biomaterials Research, 2019. **23**: p. 4. https://doi.org/10.1186/s40824-018-0149-3
86. Eliaz, N. and N. Metoki, *Calcium Phosphate Bioceramics: A Review of Their History, Structure, Properties, Coating Technologies and Biomedical Applications.* Materials (Basel), 2017. **10**(4). https://doi.org/10.3390/ma10040334
87. Hou, X., et al., *Calcium phosphate-based biomaterials for bone repair.* Journal of Functional Biomaterials, 2022. **13**(4). https://doi.org/10.3390/jfb13040187
88. Bonucci, E., *Fine structure of early cartilage calcification.* Journal of Ultrastructure Research, 1967. **20**: p. 33-50. https://doi.org/10.1016/S0022-5320(67)80034-0
89. Wuthier, R.E., *Matrix vesicles: structure, composition, formation and function in calcification.* Frontiers in Biosience, 2011. **16**: p. 2812-2902. https://doi.org/10.2741/3887
90. Anderson, H.C., *Molecular biology of matrix vesicles.* Clinical Orthopaedics and Related Research, 1995. **314**: p. 266-280. PMID: 7634645
91. Sadat-Shojai, M., et al., *Synthesis methods for nanosized hydroxyapatite with diverse structures.* Acta Biomateriala, 2013. **9**(8): p. 7591-621. 1https://doi.org/0.1016/j.actbio.2013.04.012
92. Golub, E.E., *Role of matrix vesicles in biomineralization.* Biochimica et Biophysica Acta, 2009. **1790**(12): p. 1592-8. https://doi.org/10.1016/j.bbagen.2009.09.006
93. Bottini, M., et al., *Matrix vesicles from chondrocytes and osteoblasts: Their biogenesis, properties, functions and biomimetic models.* Biochimica et Biophysica Acta, 2018. **1862**(3): p. 532-546. https://doi.org/0.1016/j.bbagen.2017.11.005
94. Ansari, S., et al., *Matrix vesicles: role in bone mineralization and potential use as therapeutics.* Pharmaceuticals (Basel), 2021. **14**(4). https://doi.org/10.3390/ph14040289

95. Xiao, Z., et al., *Proteomic analysis of extracellular matrix and vesicles.* Journal of Proteomics, 2009. **72**(1): p. 34-45. https://doi.org/10.1016/j.jprot.2008.11.011
96. Ciancaglini, P., et al., *Proteoliposomes in nanobiotechnology.* Biophysical Reviews, 2012. **4**(1): p. 67-81. https://doi.org/10.1007/s12551-011-0065-4
97. Simao, A.M., et al., *Proteoliposomes harboring alkaline phosphatase and nucleotide pyrophosphatase as matrix vesicle biomimetics.* Journal of Biological Chemistry, 2010. **285**(10): p. 7598-609. https://doi.org/10.1074/jbc.M109.079830
98. Camolezi, F.L., et al., *Construction of an alkaline phosphatase-liposome system: a tool for biomineralization study.* The International Journal of Biochemistry & Cell Biology, 2002. **34**: p. 1091-1101. https://doi.org/10.1016/S1357-2725(02)00029-8
99. Dillon, S., et al., *How tobBuild a bone: PHOSPHO1, biomineralization, and beyond.* JBMR Plus, 2019. **3**(7): p. e10202. https://doi.org/10.1002/jbm4.10202
100. Borras, T. and N. Comes, *Evidence for a calcification process in the trabecular meshwork.* Experimental Eye Research, 2009. **88**(4): p. 738-46. https://doi.org/10.1016/j.exer.2008.11.027
101. Wu, L.N., et al., *Collagen-binding proteins in collagenase-released matrix vesicles from cartilage. Interaction between matrix vesicle proteins and different types of collagen.* Journal of Biological Chemistry, 1991. **266**(2): p. 1195-1203. https://doi.org/10.1016/s0021-9258(17)35301-2
102. Schurgers, L.J., J. Uitto, and C.P. Reutelingsperger, *Vitamin K-dependent carboxylation of matrix Gla-protein: a crucial switch to control ectopic mineralization.* Trends in Molecular Medicine, 2013. **19**(4): p. 217-26. https://doi.org/10.1016/j.molmed.2012.12.008
103. Rohen, J.W., *Presence of matrix vesicles in the trabecular meshwork of gluacomatous eyes.* Graefes Archives of Clinical and Experimental Ophthalmology, 1981. **218**: p. 171-176. https://doi.org/10.1007/BF02150090
104. Xue, W., et al., *Matrix GLA protein function in trabecular meshwork cells: inhibition of BMP2-induced calcification process.* Investigative Ophthalmology & Visual Science, 2006. **47**: p. 997-1007. https://doi.org/10.1167/iovs.05-1106
105. Xue, W., N. Comes, and T. Borrás, *Presence of an established calcification marker in trabecular meshwork tissue of glaucoma donors.* Investigative Ophthalmology & Visual Science, 2007. **48**: p. 3184-3194. https://doi.org/10.1167/iovs.06-1403
106. Vittitow, J. and T. Borras, *Genes expressed in the human trabecular meshwork during pressure-induced homeostatic response.* Journal of Cellular Physiology, 2004. **201**(1): p. 126-37. https://doi.org/10.1002/jcp.20030
107. Price, P.A., J.D. Fraser, and G. Metz-Virca, *Molecular cloning of matrix Gla protein: implications for substrate recognition by the vitamin K-dependent gamma-carboxylase.* PNAS, 1984. **84**: p. 8335-8339. https://doi.org/10.1073/pnas.84.23.8335
108. Fraser, J.D. and P.A. Price, *Lung, heart, and kidney express high levels of mRNA for the vitamin K-dependent matrix Gla protein. Implications for the possible functions of matrix Gla protein and for the tissue distribution of the gamma-carboxylase.* Journal of Biological Chemistry, 1988. **263**(23): p. 11033-11036. https://doi.org/10.1016/s0021-9258(18)37912-2
109. O'Young, J., et al., *Matrix gla protein inhibits ectopic calcification by a direct interaction with hydroxyapatite crystals.* Journal of the American Chemical Society, 2011. **133**(45): p. 18406-12. https://doi.org/10.1021/ja207628k
110. Hackeng, T.M., et al., *Total chemical synthesis of human matrix Gla protein.* Protein Science, 2001. **10**(4): p. 864-70. https://doi.org/10.1110/ps.44701
111. Price, P.A., D. Toroian, and J.E. Lim, *Mineralization by inhibitor exclusion: the calcification of collagen with fetuin.* Journal of Biological Chemistry, 2009. **284**(25): p. 17092-17101. https://doi.org/10.1074/jbc.M109.007013
112. Price, P.A., J.S. Rice, and M.K. Williamson, *Conserved phosphorylationof serines in the Ser-X-Glu/Ser(P) sequences of the vitamin K- dependent matrix Gla protein from shark, lamb, rat, cow, and human.* Protein Science, 1994. **3**: p. 822-830. https://doi.org/10.1002/pro.5560030511

113. Wajih, N., et al., *Processing and transport of matrix gamma-carboxyglutamic acid protein and bone morphogenetic protein-2 in cultured human vascular smooth muscle cells: evidence for an uptake mechanism for serum fetuin.* Journal of Biological Chemistry, 2004. **279**(41): p. 43052-60. https://doi.org/10.1074/jbc.M407180200
114. Munroe, P.B., et al., *Mutations in the gene encoding the human matrix Gla protein cause Keutel syndrome.* Nature Genetics, 1999. **21**. https://doi.org/10.1038/5102
115. Ali, S.Y., S.W. Sajdera, and H.C. Anderson, *Isolation and characterization of calcifying matrix vesicles from epiphyseal catrilage.* PNAS, 1970. **67**: p. 1513-1520. https://doi.org/10.1073/pnas.67.3.1513
116. Cui, L., et al., *Characterisation of matrix vesicles in skeletal and soft tissue mineralisation.* Bone, 2016. **87**: p. 147-58. https://doi.org/10.1016/j.bone.2016.04.007
117. Buchet, R., et al., *Isolation and characteristics of matrix vesicles.* Methods of Molecula Biology, 2013. **1053**: p. 115-24. https://doi.org/10.1007/978-1-62703-562-0_7
118. Veschi, E.A., et al., *Localization of Annexin A6 in Matrix Vesicles During Physiological Mineralization.* International Journal for Molecular Science, 2020. **21**(4). https://doi.org/10.3390/ijms21041367
119. Wu, L.N., et al., *Physicochemical characterization of the nucleational core of matrix vesicles.* Journal of Biological Chemistry, 1997. **272**(7): p. 4404-11. https://doi.org/10.1074/jbc.272.7.4404
120. Qiao, Z., et al., *Fracture healing and the underexposed role of extracellular vesicle-based cross talk.* Shock, 2018. **49**(5): p. 486-496. https://doi.org/10.1097/SHK.0000000000001002
121. Swanson, W.B., et al., *Scaffolds with controlled release of pro-mineralization exosomes to promote craniofacial bone healing without cell transplantation.* Acta Biomaterialia, 2020. **118**: p. 215-232. https://doi.org/10.1016/j.actbio.2020.09.052
122. Simao, A.M.S., et al., *Proteoliposomes as matrix vesicles' biomimetics to study the initiation of skeletal mineralization.* Brazilian Journal of Medical and Biologcal Research, 2010. **43**: p. 234-241.
123. Mao, J., et al., *Identification of specific hydroxyapatite binding heptapeptide by phage display and its nucleation effect.* Materials (Basel), 2016. **9**(8). https://doi.org/10.3390/ma9080700
124. Gungormus, M., et al., *Regulation of in vitro calcium phosphate mineralization by combinatorially selected hydroxyapatite-binding peptides.* Biomacromolecules, 2008. **9**: p. 966-973. https://doi.org/10.1021/bm701037x
125. Gungormus, M., et al., *Accelerated calcium phosphate mineralization by peptides with adjacent oppositely charged residues.* ACS Biomaterials Science & Engineering, 2020. **6**(7): p. 3791-3798. https://doi.org/10.1021/acsbiomaterials.0c00194
126. Völkle nee Evgrafov, E., et al., *Functional mimicry of sea urchin biomineralization proteins with CaCO(3)-binding peptides selected by phage display.* Journal of Materials Chemistry B, 2023. **11**(42): p. 10174-10188. https://doi.org/10.1039/d3tb01584j
127. Reggi, M., et al., *Biomineralization in mediterranean corals: the role of the intraskeletal organic matrix.* Crystal Growth & Design, 2014. **14**(9): p. 4310-4320. https://doi.org/10.1021/cg5003572
128. Albeck, S., I. Addadi, and S. Weiner, *Regulation of calcite crystal morphology by intracrystalline acidic proteins and glycoproteins.* Connective Tissue Research, 1996. **35**(1-4): p. 365-70. https://doi.org/10.3109/03008209609029213
129. Kanold, J.M., et al., *Spine and test skeletal matrices of the Mediterranean sea urchin Arbacia lixula--a comparative characterization of their sugar signature.* FEBS Journal, 2015. **282**(10): p. 1891-905. https://doi.org/10.1111/febs.13242
130. Kanold, J.M., et al., *The test skeletal matrix of the black sea urchin Arbacia lixula.* Comparative Biochemistry and Physiology Part D Genomics Proteomics, 2015. **13**: p. 24-34. https://doi.org/10.1016/j.cbd.2014.12.002
131. Blandford, N.R., et al., *Modeling of matrix vesicle biomineralization using large unilamellar vesicles.* Journal of Inorganic Biochemistry, 2003. **94**(1-2): p. 14-27. https://doi.org/10.1016/s0162-0134(02)00629-3

132. Mu, X., et al., *Stimulus-responsive vesicular polymer nano-integrators for drug and gene delivery.* International Journal of Nanomedicine, 2019. **14**: p. 5415-5434. https://doi.org/10.2147/IJN.S203555
133. Shen, H.H., T. Lithgow, and L. Martin, *Reconstitution of membrane proteins into model membranes: seeking better ways to retain protein activities.* International Journal for Molecular Science, 2013. **14**(1): p. 1589-607. https://doi.org/10.3390/ijms14011589
134. Lee, S.J., I.K. Lee, and J.H. Jeon, *Vascular calcification - new insights into its mechanism.* International Journal of Molecular Sciences, 2020. **21**(8). https://doi.org/10.3390/ijms21082685
135. Duer, M.J., et al., *Mineral surface in calcified plaque is like that of bone: further evidence for regulated mineralization.* Arteriosclerosclerosis, Thrombosis and Vascular Biology, 2008. **28**(11): p. 2030-4. https://doi.org/10.1161/ATVBAHA.108.172387
136. Bolean, M., et al., *Thermodynamic properties and characterization of proteoliposomes rich in microdomains carrying alkaline phosphatase.* Biophysical Chemistry, 2011. **158**(2-3): p. 111-8. https://doi.org/10.1016/j.bpc.2011.05.019
137. Wu, L.N., et al., *Transport of inorganic phosphate in primary cultures of chondrocytes isolated from the tibial growth plate of normal adolescent chickens.* Journal of Cellular Biochemistry, 2002. **86**(3): p. 475-89. https://doi.org/10.1002/jcb.10240
138. Discher, D.E. and A. Eisenberg, *Polymer vesicles.* Science, 2002. **297**: p. 967-973. https://doi.org/10.1126/science.1074972
139. Discher, B.M., et al., *Polymerosomes: tough vesicles made from diblock copolymers.* Science, 1999. **284**: p. 1143-1145. https://doi.org/10.1126/science.284.5417.1143
140. Discher, D.E., et al., *Emerging Applications of Polymersomes in Delivery: from Molecular Dynamics to Shrinkage of Tumors.* Progress in Polymer Science, 2007. **32**(8-9): p. 838-857. https://doi.org/10.1016/j.progpolymsci.2007.05.011
141. Shen, M., et al., *MV-mimicking micelles loaded with PEG-serine-ACP nanoparticles to achieve biomimetic intra/extra fibrillar mineralization of collagen in vitro.* Biochimica et Biophysica Acta, 2019. **1863**(1): p. 167-181. https://doi.org/10.1016/j.bbagen.2018.10.005
142. Wang, Y., et al., *Bioinspired extracellular vesicles embedded with black phosphorus for molecular recognition-guided biomineralization.* Nature Communications, 2019. **10**(1): p. 2829. https://doi.org/10.1038/s41467-019-10761-5
143. Shi, S., et al., *Bioinspired matrix vesicles based on platelet membrane for biomineralization of dentin tubules.* Industrial & Engineering Chemistry Research, 2023. **62**(22): p. 8611-8620. https://doi.org/10.1021/acs.iecr.3c00188
144. Brinkhuis, R.P., F.P.J.T. Rutjes, and J.C.M. van Hest, *Polymeric vesicles in biomedical applications.* Polymer Chemistry, 2011. **2**(7). https://doi.org/10.1039/c1py00061f
145. Thaller, M., *Hyaluronan hydrogel modified intraocular implants for glaucoma treatment.*, in *Institute for Physical Chemistry*. 2016, Ruperto-Carola Univeristy of Heidelberg. p. 157.
146. Thaller, M., et al., *Hyaluronsäuregele zur Druckregulierung in der Glaukomtherapie.* Ophthalmologe, 2017. **115**: p. 195-201. https://doi.org/10.1007/s00347-017-0602-z
147. Völkle nee Evgrafov, E., *Pressure measurements and cell studies on hyaluronan hydrogel-modified implants for glaucoma treatment*, in *Department of Molecular Biology and Plant Virology*. 2018, University of Stuttgart, Institute for Biomaterials and Biomolecular Systems. p. 102.
148. Ullah, F., et al., *Classification, processing and application of hydrogels: A review.* Mater Sci Eng C Mater Biol Appl, 2015. **57**: p. 414-33. 10.1016/j.msec.2015.07.053
149. Corkhill, P., C. Hamilton, and B. Tighe, *Synthetic hydrogels VI. Hydrogel composites as wound dressings and implant materials.* Biomaterials, 1989. **10**: p. 3-10. https://doi.org/10.1016/0142-9612(89)90002-1
150. Kamoun, E.A., et al., *Crosslinked poly(vinyl alcohol) hydrogels for wound dressing applications: A review of remarkably blended polymers.* Arabian Journal of Chemistry, 2015. **8**(1): p. 1-14. https://doi.org/10.1016/j.arabjc.2014.07.005

151. Caló, E. and V.V. Khutoryanskiy, *Biomedical applications of hydrogels: A review of patents and commercial products.* European polymer journal, 2015. **65**: p. 252-267. https://doi.org/10.1016/j.eurpolymj.2014.11.024
152. Einerson, N., K. Stevens, and W. Kao, *Synthesis and physiochemical analysis of gelatin-based hydrogels for drug carrier matrices.* Biomaterials, 2002. **24**: p. 509-523. https://doi.org/10.1016/s0142-9612(02)00369-1
153. Song, Y., et al., *In situ formation of injectable chitosan-gelatin hydrogels through double crosslinking for sustained intraocular drug delivery.* Materials Science & Engineering C: Materials for Biological Applications, 2018. **88**: p. 1-12. https://doi.org/10.1016/j.msec.2018.02.022
154. Cavallaro, G., et al., *Alginate gel beads filled with halloysite nanotubes.* Applied Clay Science, 2013. **72**: p. 132-137. https://doi.org/10.1016/j.clay.2012.12.001
155. Pouyani, T., G.S. Harbison, and G.D. Prestwich, *Novel hydrogels of hyaluronic acid: Synthesis, surface morphology, and solid state NMR.* Journal of the American Chemical Society, 1994. **116**: p. 7515-7522. https://doi.org/10.1021/ja00096a007
156. Manzi, G., et al., *"Click" hyaluronan based nanohydrogels as multifunctionalizable carriers for hydrophobic drugs.* Carbohydrate Polymers, 2017. **174**: p. 706-715. https://doi.org/10.1016/j.carbpol.2017.07.003
157. Hagel, V., et al., *Desmosine-inspired cross-linkers for hyaluronan hydrogels.* Scientific Reports, 2013. **3**: p. 2043. https://doi.org/10.1038/srep02043
158. Liu, Y., et al., *Crosslinked hyaluronan hydrogels containing mitomycin C reduce postoperative abdominal adhesions.* Fertil Steril, 2005. **83 Suppl 1**: p. 1275-83. 10.1016/j.fertnstert.2004.09.038
159. Shu, X.Z., et al., *In situ crosslinkable hyaluronan hydrogels for tissue engineering.* Biomaterials, 2004. **25**: p. 1339-48. https://doi.org/10.1016/j.biomaterials.2003.08.014
160. Son, K.H. and J.W. Lee, *Synthesis and characterization of poly(ethylene glycol) based thermo responsive hydrogels for cell sheet engineering.* Materials, 2016. **9**. https://doi.org/10.3390/ma9100854
161. Lin, C.C., *Recent advances in crosslinking chemistry of biomimetic poly(ethylene glycol) hydrogels.* RSC Advances, 2015. **5**(50): p. 39844-398583. https://doi.org/10.1039/C5RA05734E
162. Zhang, Z., et al., *Synthesis of poly(ethylene glycol)-based hydrogels via amine-Michael type addition with tunable stiffness and postgelation chemical functionality.* Chemistry of Materials, 2014. **26**: p. 3624-3630. https://doi.org/10.1021/cm500203j
163. Benedetto, F.D., Biasco, A., Pisignano, D. & Cingolani, R., *Patterning polyacrylamide hydrogels by soft lithography.* Nanotechnology, 2005. **16**: p. 165-170. https://doi.org/10.1088/0957-4484/16/5/006
164. Ahmed, E.M., *Hydrogel: Preparation, characterization, and applications: A review.* Journal of advanced research, 2015. **6**(2): p. 105-121. 10.1016/j.jare.2013.07.006
165. Drury, J.L. and D.J. Mooney, *Hydrogels for tissue engineering: scaffold design variables and applications.* Biomaterials, 2003. **24**: p. 4337-4351. https://doi.org/10.1016/S0142-9612(03)00340-5
166. Qiu, J. and K. Park, *Environment-sensitive hydrogels for drug delivery.* Advanced Drug Delivery Reviews, 2001. **53**: p. 321-339. 10.1016/s0169-409x(01)00203-4
167. Jen, A., C. Wake, and A. Mikos, *Review: hydrogels for cell immobilization.* Biotechnology and bioengineering, 1996. **50**: p. 357-364. https://doi.org/10.1002/(SICI)1097-0290(19960520)50:4<357::AID-BIT2>3.0.CO;2-K
168. Neethu, T.M., P.K. Dubey, and A.R. Kaswala, *Prospects and applications of hydrogel technology in agriculture.* International Journal of Current Microbiology and Applied Sciences, 2018. **7**(05): p. 3155-3162. https://doi.org/10.20546/ijcmas.2018.705.369
169. Walimbe, T., A. Panitch, and P.M. Sivasankar, *A review of hyaluronic acid and hyaluronic acid-based hydrogels for vocal fold tissue engineering.* Journal of Voice, 2017. **31**(4): p. 416-423. https://doi.org/10.1016/j.jvoice.2016.11.014
170. Meiring, J.E., et al., *Hydrogel biosensor array platform indexed by shape.* Chemistry of materials, 2004. **16**: p. 5574-5580. https://doi.org/10.1021/cm049488j

171. Jamnongkan, T. and S. Kaewpirom, *Potassium release kinetics and water retention of controlled-release fertilizers based on chitosan hydrogels.* Journal of Polymers and the Environment, 2010. **18**: p. 413-421. https://doi.org/10.1007/s10924-010-0228-6
172. Demitri, C., et al., *Potential of cellulose-based superabsorbent hydrogels as water reservoir in agriculture.* International Journal of Polymer Science, 2013: p. 1-6. https://doi.org/10.1155/2013/435073
173. Ligon, S.C., et al., *Polymers for 3D printing and customized additive manufacturing.* Chemical Reviews, 2017. **117**(15): p. 10212-10290. https://doi.org/10.1021/acs.chemrev.7b00074
174. Eshel-Green, T., et al., *PEGDA hydrogels as a replacement for animal tissues in mucoadhesion testing.* International Journal of Pharmaceutics, 2016. **506**(1-2): p. 25-34. https://doi.org/10.1016/j.ijpharm.2016.04.019
175. Seidlits, S.K., et al., *Fibronectin-hyaluronic acid composite hydrogels for three-dimensional endothelial cell culture.* Acta Biomaterialia, 2011. **7**(6): p. 2401-9. https://doi.org/10.1016/j.actbio.2011.03.024
176. Shikanov, A., et al., *Hydrogel network design using multifunctional macromers to coordinate tissue maturation in ovarian follicle culture.* Biomaterials, 2011. **32**(10): p. 2524-31. https://doi.org/10.1016/j.biomaterials.2010.12.027
177. Durst, C.A., et al., *Flexural characterization of cell encapsulated PEGDA hydrogels with applications for tissue engineered heart valves.* Acta Biomaterialia, 2011. **7**(6): p. 2467-76. https://doi.org/10.1016/j.actbio.2011.02.018
178. Kreuz, T., *Hyaluronic acid/poly(ethylene glycol) gradient hydrogels for intraocular pressure regulation in glaucoma therapy*. 2019, Univerisity of Stuttgart. p. 119.
179. Hegger, P.S., *Hyaluronan based ECM-mimetics with tunable charge densities*. 2017, Ruperto-Carola Univeristy of Heidelberg.
180. Hoffman, A.S., *Hydrogels for biomedical applications.* Advanced Drug Delivery Review, 2012. **64**: p. 3-12. https://doi.org/10.1016/j.addr.2012.09.010
181. Billiet, T., et al., *A review of trends and limitations in hydrogel-rapid prototyping for tissue engineering.* Biomaterials, 2012. **33**(26): p. 6020-41. https://doi.org/10.1016/j.biomaterials.2012.04.050
182. Lin, Y.H., et al., *Physically crosslinked alginate/N,O-carboxymethyl chitosan hydrogels with calcium for oral delivery of protein drugs.* Biomaterials, 2005. **26**(14): p. 2105-13. https://doi.org/10.1016/j.biomaterials.2004.06.011
183. Boucard, N., et al., *The use of physical hydrogels of chitosan for skin regeneration following third-degree burns.* Biomaterials, 2007. **28**(24): p. 3478-88. https://doi.org/10.1016/j.biomaterials.2007.04.021
184. Hu, W., et al., *Advances in crosslinking strategies of biomedical hydrogels.* Biomaterial Sciences, 2019. **7**(3): p. 843-855. https://doi.org/10.1039/c8bm01246f
185. Parhi, R., *Cross-LInked hydrogel for pharmaceutical applications: a review.* Advanced Pharmaceutical Bulletin, 2017. **7**(4): p. 515-530. https://doi.org/10.15171/apb.2017.064
186. Gholamali, I., et al., *Exploring the progress of hyaluronic acid hydrogels: synthesis, characteristics, and wide-ranging applications.* Materials (Basel), 2024. **17**(10). https://doi.org/10.3390/ma17102439
187. Ozturk, T. and B. Amna, *Click chemistry: a fascinating method of connecting organic groups.* Organic Communications, 2021(2): p. 97-120. https://doi.org/10.25135/acg.oc.100.21.03.2006
188. Hoyle, C.E., A.B. Lowe, and C.N. Bowman, *Thiol-click chemistry: a multifaceted toolbox for small molecule and polymer synthesis.* Chemical Society Reviews, 2010. **39**(4): p. 1355-87. https://doi.org/10.1039/b901979k
189. Michael, A., *On the addition of sodium acetoacetic ether and analogous sodium compounds to unsaturated organic ethers.* American Chemical Journal, 1887. **9**: p. 115.
190. Lowe, A.B., C.E. Hoyle, and C.N. Bowman, *Thiol-yne click chemistry: A powerful and versatile methodology for materials synthesis.* Journal of Materials Chemistry, 2010. **20**(23). 10.1039/b917102a

191. Hoyle, C.E., T.Y. Lee, and T. Roper, *Thiol–enes: Chemistry of the past with promise for the future.* Journal of Polymer Science Part A: Polymer Chemistry, 2004. **42**(21): p. 5301-5338. https://doi.org/10.1002/pola.20366
192. Nair, D.P., et al., *The thiol-Michael addition click reaction: a powerful and widely used tool in materials chemistry.* Chemistry of Materials, 2013. **26**(1): p. 724-744. https://doi.org/10.1021/cm402180t
193. Mather, B.D., et al., *Michael addition reactions in macromolecular design for emerging technologies.* Progress in Polymer Science, 2006. **31**(5): p. 487-531. https://doi.org/10.1016/j.progpolymsci.2006.03.001
194. Chen, W.-Q. and J.-A. Ma, *Additions to and substitutions at C-C pi bonds*, in *Comprehensive Organic Synthesis*. 2014, Elsevier. 978-0-08-097743-0
195. Fraser, J.R.E., T.C. Laurent, and U.B.G. Laurent, *Hyaluronan: its nature, distribution, functions and turnover.* Journal of Internal Medicine, 1997. **242**: p. 27–33. https://doi.org/10.1046/j.1365-2796.1997.00170.x
196. Laurent, T.C., U.B.G. Laurent, and J.R.E. Fraser, *The structure and function of hyaluronan: An overview.* Immunology and Cell Biology, 1996. **74**: p. 1-7. https://doi.org/10.1038/icb.1996.32
197. Meyer, L. and R. Stern, *Age-dependent changes of hyaluronan in human skin.* Journal of Investigative Dermatology, 1994. **102**: p. 385-389. https://doi.org/10.1111/1523-1747.ep12371800
198. Laurent, U.B.G., *Hyaluronate in aqueous humour.* Experimental Eye Research, 1981. **33**: p. 147-155. https://doi.org/10.1016/S0014-4835(81)80063-2
199. Hargittai, I. and M. Hargittai, *Molecular structure of hyaluronan: an introduction.* Structural Chemistry, 2008. **19**: p. 697-717. https://doi.org/10.1007/s11224-008-9370-3
200. Anseth, K.S., C.N. Bowman, and L. Brannon-Peppas, *Mechanical properties of hydrogels and their experimental determination.* Biomaterials, 1996. **17**: p. 1647-1657. https://doi.org/10.1016/0142-9612(96)87644-7
201. Zhu, W., et al., *Determination of kinetic changes of aggrecan-hyaluronan interactions in solution from its rheological properties.* Elsevier Science Inc., 1994. **27**: p. 571-579. https://doi.org/10.1016/0021-9290(94)90066-3
202. Xu, X., et al., *Hyaluronic acid-based hydrogels: from a natural polysaccharide to complex networks.* Soft Matter, 2012. **8**(12): p. 3280-3294. https://doi.org/10.1039/C2SM06463D
203. Hintze, V., M. Schnabelrauch, and S. Rother, *Chemical modification of hyaluronan and their biomedical applications.* Frontiers in Chemistry, 2022. **10**: p. 830671. https://doi.org/10.3389/fchem.2022.830671
204. Kim, K.S., et al., *Injectable hyaluronic acid-tyramine hydrogels for the treatment of rheumatoid arthritis.* Acta Biomaterialia, 2011. **7**(2): p. 666-74. https://doi.org/10.1016/j.actbio.2010.09.030
205. Frenkel, J.S., *The role of hyaluronan in wound healing.* International Wound Journal, 2014. **11**: p. 159-163. https://doi.org/10.1111/j.1742-481X.2012.01057.x
206. Wu, K.Y., et al., *Hydrogels in ophthalmology: novel strategies for overcoming therapeutic challenges.* Materials (Basel), 2023. **17**(1). https://doi.org/10.3390/ma17010086
207. Liesegang, T.J., *Viscoelastic substances in ophthalmology.* Survey of Opthalmology, 1990. **34**: p. 268-293. htpps://doi.org/10.1016/0039-6257(90)90027-s
208. Zarembinski, T.I., et al., *Thiolated hyaluronan-based hydrogels crosslinked using oxidized glutathione: an injectable matrix designed for ophthalmic applications.* Acta Biomaterialia, 2014. **10**(1): p. 94-103. https://doi.org/10.1016/j.actbio.2013.09.029
209. Jin, R., et al., *Synthesis and characterization of hyaluronic acid-poly(ethylene glycol) hydrogels via Michael addition: An injectable biomaterial for cartilage repair.* Acta Biomater, 2010. **6**(6): p. 1968-77. 10.1016/j.actbio.2009.12.024
210. Lin, C.C. and K.S. Anseth, *PEG hydrogels for the controlled release of biomolecules in regenerative medicine.* Pharmaceutical Research, 2009. **26**(3): p. 631-43. https://doi.org/10.1007/s11095-008-9801-2

211. Jeong, C.G., et al., *Screening of hyaluronic acid-poly(ethylene glycol) composite hydrogels to support intervertebral disc cell biosynthesis using artificial neural network analysis.* Acta Biomaterialia, 2014. **10**(8): p. 3421-30. https://doi.org/10.1016/j.actbio.2014.05.012
212. Fea, A.M., et al., *Glaucoma treatment and hydrogel: current insights and state of the art.* Gels, 2022. **8**(8). https://doi.org/10.3390/gels8080510
213. Wang, J., et al., *Mildly Cross-Linked Dendrimer Hydrogel Prepared via Aza-Michael Addition Reaction for Topical Brimonidine Delivery.* J Biomed Nanotechnol, 2017. **13**(9): p. 1089-1096. 10.1166/jbn.2017.2436
214. Wang, J., G.S. Williamson, and H. Yang, *Branched polyrotaxane hydrogels consisting of alpha-cyclodextrin and low-molecular-weight four-arm polyethylene glycol and the utility of their thixotropic property for controlled drug release.* Colloids Surf B Biointerfaces, 2018. **165**: p. 144-149. 10.1016/j.colsurfb.2018.02.032
215. Bellotti, E., et al., *Tuning of thermoresponsive pNIPAAm hydrogels for the topical retention of controlled release ocular therapeutics.* Journal of Materials Chemistry B, 2019. **7**(8): p. 1276-1283. https://doi.org/10.1039/C8TB02976H
216. Shehata, A.E.M., et al., *Burst pressures in eyes with clear corneal incisions treated with ReSure glue.* Journal of Ophthalmology, 2021. **2021**: p. 6691489. https://doi.org/10.1155/2021/6691489
217. Lin, K.T., et al., *Recent advances in hydrogels: ophthalmic applications in cell delivery, vitreous substitutes, and ocular adhesives.* Biomedicines, 2021. **9**(9). https://doi.org/10.3390/biomedicines9091203
218. Ozcelik, B., et al., *Biodegradable and biocompatible poly(ethylene glycol)-based hydrogel films for the regeneration of corneal endothelium.* Advanced Healthcare Materials, 2014. **3**(9): p. 1496-507. https://doi.org/10.1002/adhm.201400045
219. Blümmel, J., et al., *Protein repellent properties of covalently attached PEG coatings on nanostructured SiO(2)-based interfaces.* Biomaterials, 2007. **28**: p. 4739-4747. https://doi.org/10.1016/j.biomaterials.2007.07.038
220. Rolli, C.G., et al., *Switchable adhesive substrates: revealing geometry dependence in collective cell behavior.* Biomaterials, 2012. **33**(8): p. 2409-18. https://doi.org/10.1016/j.biomaterials.2011.12.012
221. Pal, K. and I. Banerjee, *Polymeric gels: characterization, properties and biomedical applications*. 1 ed. 2018: Elsevier. 9780081021804
222. Holback, H., Y. Yeo, and K. Park, *Hydrogel swelling behavior and its biomedical applications.* Biochemistry, manufacture & medical applications, 2011: p. 3-24. https://doi.org/10.1533/9780857091383.1.3
223. Flory, P.J. and J. Rehner, *Statistical mechanics of cross-linked polymer networks II. swelling.* The Journal of Chemical Physics, 1943. **11**(11): p. 521-526. https://doi.org/10.1063/1.1723792
224. Peppas, N.A., et al., *Hydrogels in biology and medicine: from molecular principles to bionanotechnology.* Advanced Materials, 2006. **18**(11): p. 1345-1360. https://doi.org/10.1002/adma.200501612
225. Yang, T., *Mechanical and swelling properties of hydrogels.* 2012: p. 77. ISBN: 978-91-7501-471-5
226. Jiang, D., J. Liang, and P.W. Noble, *Hyaluronan in tissue injury and repair.* Annual Review of Cell and Developmental Biology, 2007. **23**: p. 435-61. https://doi.org/10.1146/annurev.cellbio.23.090506.123337
227. Kim, M.-H., D.-T. Nguyen, and D.-D. Kim, *Recent studies on modulating hyaluronic acid-based hydrogels for controlled drug delivery.* Journal of Pharmaceutical Investigation, 2022. **52**(4): p. 397-413. https://doi.org/10.1007/s40005-022-00568-w
228. Dobner, S., et al., *A synthetic non-degradable polyethylene glycol hydrogel retards adverse post-infarct left ventricular remodeling.* Journal of Cardiac Failure, 2009. **15**(7): p. 629-36. https://doi.org/10.1016/j.cardfail.2009.03.003
229. Pandala, N., et al., *Finding the sweet spot: a library of hydrogels with tunable degradation for tissue model development.* Journal of Materials Chemistry B, 2022. **10**(13): p. 2194-2203. https://doi.org/10.1039/d1tb02436a

230. Vercruysse, K.P., et al., *Synthesis and in vitro degradation of new polyvalent hydrazide cross-linked hydrogels of hyaluronic acid.* Bioconjugate Chemistry, 1997. **8**: p. 686-694. https://doi.org/10.1021/bc9701095
231. Shu, X.Z., et al., *Disulfide cross-linked hyaluronan hydrogels.* Biomacromolecules, 2002. **3**: p. 1304-1311. https://doi.org/10.1021/bm025603c
232. Brunette, D.M., et al., *Titanium in Medicine*. 2001, Berlin Heidelberg: Springer. ISBN: 978-3-642-63119-1
233. Halliwell, C.M. and A.E.G. Cass, *A factorial analysis of silanization conditions for the immobilizations of oligonucleoties on glass surfaces.* Analytical Chemistry, 2001. **73**: p. 2476-2483. https://doi.org/10.1021/ac0010633
234. Nanci, A., et al., *Chemical modification of titanium surfaces for covalent attachment of biological molecules.* Journal of Biomedical Materials Research, 1998. **40**: p. 324-335. https://doi.org/10.1002/(sici)1097-4636(199805)40:2<324::aid-jbm18>3.0.co;2-l
235. Günther, H., *NMR spectroscopy. Basic principles, concepts and applications in chemistry*. 3 ed. 2013. ISBN: 978-3-527-67477-0
236. Claridge, T.D.W., *High-resolution NMR techniques in organic chemistry*. 2016. 541. ISBN: 978-0-08-099986-9
237. Olofsson, G., *The equilibrium constant and enthalpy change for the acid ionization of tris(hydroxymethyl)aminoethane, tris, in water.* Journal of Chemical Thermodynamics, 1971. **3**: p. 217-220. https://doi.org/10.1016/S0021-9614(71)80105-2
238. SigmaAldrich, p.i., *Tris(hydroxymethyl)aminomethane, TRIS*. 2012.
239. Segura, T., et al., *Crosslinked hyaluronic acid hydrogels: a strategy to functionalize and pattern.* Biomaterials, 2005. **26**(4): p. 359-71. https://doi.org/10.1016/j.biomaterials.2004.02.067
240. Smith, J.G., *Synthetically useful reactions of epoxides.* Synthesis, 1984. **8**: p. 629-656. https://doi.org/10.1055/s-1984-30921
241. Parker, R.E. and N.S. Isaacs, *Mechanisms of epoxide reactions.* Chemical Reviews, 1959. **59**: p. 737-799. https://doi.org/10.1021/cr50028a006
242. Pinchuk, L., et al., *The use of poly(styrene-block-isobutylene-block-styrene) as a microshunt to treat glaucoma.* Regenerative Biomaterials, 2016. **3**(2): p. 137-42. https://doi.org/10.1093/rb/rbw005
243. Beamish, J.A., et al., *The effects of monoacrylated poly(ethylene glycol) on the properties of poly(ethylene glycol) diacrylate hydrogels used for tissue engineering.* Journal of Biomedical Materials Research A, 2010. **92**(2): p. 441-50. https://doi.org/10.1002/jbm.a.32353
244. Quesada-Pérez, M., et al., *Gel swelling theories: the classical formalism and recent approaches.* Soft Matter, 2011. **7**(22). https://doi.org/10.1039/c1sm06031g
245. Erickson, H.P., *Size and shape of protein molecules at the nanometer level determined by sedimentation, gel filtration, and electron microscopy.* Biological Procedures Online, 2009. **11**: p. 32-51. https://doi.org/10.1007/s12575-009-9008-x
246. Cheng, J., et al., *Priming the Ahmed glaucoma valve: pressure required and effect of overpriming.* Journal of Glaucoma, 2015. **24**: p. 34-35.
247. Albis-Donado, O., *The Ahmed valve*, in *Atlas of Glaucoma Surgery*. 2006. p. 58-58. 9788180616518
248. Jones, E., et al., *Preimplantation flow testing of Ahmed Glaucoma Valve and the early postoperative clinical outcome.* Journal of Current Glaucoma Practice, 2013. **7**(1): p. 1-5. 10.5005/jp-journals-10008-1128
249. Choudhari, N.S., et al., *Is Ahmed glaucoma valve consistent in performance?* Translational Vision Science & Technology, 2018. **7**(3): p. 19. https://doi.org/10.1167/tvst.7.3.19
250. Sarkisian, S.R., Jr., *Tube shunt complications and their prevention.* Current Opinion in Ophthalmology, 2009. **20**(2): p. 126-30. https://doi.org/10.1097/ICU.0b013e328323d519
251. Infeld, D.A. and J.G. O'Shea, *Glaucoma: diagnosis and managment.* Journal of Postgraduate Medicine, 1998. **74**: p. 709-715. https://doi.org/10.1136/pgmj.74.878.709
252. Bergua, A., *Das menschliche Auge in Zahlen*. 2017: Springer. ISBN: 978-3-662-47283-5

253. Sheybani, A., H. Reitsamer, and I.I.K. Ahmed, *Fluid dynamics of a novel micro-fistula implant for the surgical treatment of glaucoma.* Investigative Ophthalmology & Visual Science, 2015. **56**: p. 4789–4795. https://doi.org/10.1167/iovs.15-16625
254. Bochmann, F., et al., *Intraoperative testing of opening and closing pressure predicts risk of low intraocular pressure after Ahmed glaucoma valve implantation.* Eye (Lond), 2014. **28**(10): p. 1184-9. https://doi.org/10.1038/eye.2014.168
255. Moss, E.B. and G.E. Trope, *Assessment of closing pressure in silicone ahmed glaucoma valves.* Journal of Glaucoma, 2008. **17**: p. 489-493. https://doi.org/10.1097/IJG.0b013e3181622532
256. Porter, J.M., C.H. Krawczyk, and R.F. Carey, *In vitro flow testing of glaucoma drainage devices.* Ophthalmology, 1997. **104**(10): p. 1701-7. 10.1016/s0161-6420(97)30077-3
257. Asrani, S., et al., *Large diurnal fluctuations in intraocular pressure are an independent risk factor in patients with glaucoma.* Journal of Glaucoma, 2000. **9**: p. 134-142. https://doi.org/10.1097/00061198-200004000-00002
258. Konstas, A.G., et al., *Diurnal and 24-h intraocular pressures in glaucoma: monitoring strategies and impact on prognosis and treatment.* Advances in Therapy, 2018. **35**(11): p. 1775-1804. https://doi.org/10.1007/s12325-018-0812-z
259. Nouri-Mahdavi, K., et al., *Predictive factors for glaucomatous visual field progression in the Advanced Glaucoma Intervention Study.* Ophthalmology, 2004. **111**(9): p. 1627-35. https://doi.org/10.1016/j.ophtha.2004.02.017
260. Gordon, M.O., et al., *The ocular hypertension treatment study.* Archives of Ophthalmology, 2002. **120**: p. 714-720. https://doi.org/10.1001/archopht.120.6.714
261. Oyen, M.L., *Mechanical characterisation of hydrogel materials.* International Materials Reviews, 2013. **59**(1): p. 44-59. https://doi,org/10.1179/1743280413y.0000000022
262. Normand, V., et al., *New insight into agarose gel mechanical properties.* Biomacromolecules, 2000. **1**: p. 730-738. https://doi.org/10.1021/bm005583j
263. Lee, D., H. Zhang, and S. Ryu, *Elastic modulus measurement of hydrogels*, in *Cellulose-Based Superabsorbent Hydrogels*. 2018. p. 1-21.
264. Iwasaki, K., et al., *Prospective cohort study of corneal endothelial cell loss after Baerveldt glaucoma implantation.* PLoS One, 2018. **13**. https://doi.org/10.1371/journal.pone.0201342
265. Tan, A.N., et al., *Corneal endothelial cell loss after Baerveldt glaucoma drainage device implantation in the anterior chamber.* Acta Ophthalmologica, 2017. **95**(1): p. 91-96. https://doi.org/10.1111/aos.13161
266. Omatsu, S., et al., *Changes in corneal endothelial cells after trabeculectomy and EX-PRESS shunt: 2-year follow-up.* BMC Ophthalmology, 2018. **18**(1): p. 243. https://doi.org/10.1186/s12886-018-0913-0
267. Mendrinos, E., et al., *Coupling of HRT II and AS-OCT to evaluate corneal endothelial cell loss and in vivo visualization of the Ahmed glaucoma valve implant.* Eye, 2008. **23**(9): p. 1836-1844. https://doi.org/10.1038/eye.2008.321
268. Kim, M.S., K.N. Kim, and C.S. Kim, *Changes in corneal endothelial cell after Ahmed glaucoma valve implantation and trabeculectomy: 1-year follow-up.* Korean J Ophthalmol, 2016. **30**(6): p. 416-425. https://doi.org/10.3341/kjo.2016.30.6.416
269. Lee, E.K., et al., *Changes in corneal endothelial cells after Ahmed glaucoma valve implantation: 2-year follow-up.* American Journal of Ophthalmology, 2009. **148**(3): p. 361-7. https://doi.org/10.1016/j.ajo.2009.04.016
270. Shin, D.B., S.B. Lee, and C.S. Kim, *Effects of viscoelastic material on the corneal endothelial cells in trabeculectomy with adjunctive mitomycin-C.* Korean Journal of Ophthalmology, 2003. **17**: p. 83-90. https://doi.org/10.3341/kjo.2003.17.2.83
271. Sihota, R., T. Sharma, and H.C. Agarwal, *Intraoperative mitomycin C and the corneal endothelium.* Acta Ophthalmologica Scandinavia, 1998. **76**(1): p. 80-2. https://doi.org/10.1034/j.1600-0420.1998.760115.x
272. Miron, A., et al., *Early and late-onset cell migration from peripheral corneal endothelium.* PLoS One, 2023. **18**(5): p. e0285609. https://doi.org/10.1371/journal.pone.0285609

273. Meekins, L.C., et al., *Corneal endothelial cell migration and proliferation enhanced by Rho kinase (ROCK) inhibitors in in vitro and in vivo models.* Investigative Ophthalmology & Visual Science, 2016. **57**(15): p. 6731-6738. https://doi.org/10.1167/iovs.16-20414
274. Desai, E.S., et al., *Critical factors affecting cell encapsulation in superporous hydrogels.* Biomedical materials, 2012. **7**. 10.1088/1748-6041/7/2/024108
275. Shu, X.Z., et al., *Attachment and spreading of fibroblasts on an RGD peptide–modified injectable hyaluronan hydrogel.* Journal of Biomedical Materials Research, 2004. **68A**: p. 365-375. https://doi.org/10.1002/jbm.a.20002
276. Choritz, L., et al., *Surface topographies of glaucoma drainage devices and their influence on human tenon fibroblast adhesion.* Investigative Ophthalmology & Visual Science, 2010. **51**: p. 4047-5053.
277. Hersel, U., C. Dahmen, and H. Kessler, *RGD modified polymers: biomaterials for stimulated cell adhesion and beyond.* Biomaterials, 2003. **24**(24): p. 4385-4415. https://doi.org/10.1016/s0142-9612(03)00343-0
278. Karel, S., et al., *Stabilization of hyaluronan-based materials by peptide conjugation and its use as a cell-seeded scaffold in tissue engineering.* Carbohydrate Polymers, 2018. **201**: p. 300-307. https://doi.org/10.1016/j.carbpol.2018.08.082
279. Cheng, J., et al., *Priming the Ahmed glaucoma valve. Pressure required and effect of overpriming.* Journal of Glaucoma, 2015. **24**(4): p. 34-35. https://doi.org/10.1097/IJG.0000000000000099
280. Beebe, D.J., G.A. Mensing, and G.M. Walker, *Physics and applications of microfluidics in biology.* Annual Review of Biomedocal Engineering, 2002. **4**: p. 261-86. https://doi.org/10.1146/annurev.bioeng.4.112601.125916
281. Teh, S.Y., et al., *Droplet microfluidics.* Lab Chip, 2008. **8**(2): p. 198-220. https://doi.org/10.1039/b715524g
282. Ohno, K., K. Tachikawa, and A. Manz, *Microfluidics: applications for analytical purposes in chemistry and biochemistry.* Electrophoresis, 2008. **29**(22): p. 4443-53. https://doi.org/10.1002/elps.200800121
283. Figeys, D. and D. Pinto, *Lab-on-a-chip: a revolution in biological and medcial sciences.* Analytical Chemistry, 2000. **72**(9): p. 309 A-2181. https://doi.org/10.1021/ac002800y
284. Song, H., J.D. Tice, and R.F. Ismagilov, *A microfluidic system for controlling reaction networks in time.* Angewandte Chemie International Edition, 2003. **42**(7): p. 768-72. https://doi.org/10.1002/anie.200390203
285. Breslauer, D.N., P.J. Lee, and L.P. Lee, *Microfluidics-based systems biology.* Molecular Biosystems, 2006. **2**(2): p. 97-112. https://doi.org/10.1039/b515632g
286. Pearce, T.M. and J.C. Williams, *Microtechnology: meet neurobiology.* Lab Chip, 2007. **7**(1): p. 30-40. https://doi.org/10.1039/b612856b
287. Huang, Y., et al., *Microfluidics-based devices: New tools for studying cancer and cancer stem cell migration.* Biomicrofluidics, 2011. **5**: p. 013412. https://doi.org/10.1063/1.3555195
288. Yager, P., et al., *Microfluidic diagnostic technologies for global public health.* Nature, 2006. **442**(7101): p. 412-8. https://doi.org/10.1038/nature05064
289. Rivet, C., et al., *Microfluidics for medical diagnostics and biosensors.* Chemical Engineering Science, 2011. **66**(7): p. 1490-1507. https://doi.org/10.1016/j.ces.2010.08.015
290. Chin, C.D., et al., *Microfluidics-based diagnostics of infectious diseases in the developing world.* Nat Med, 2011. **17**(8): p. 1015-9. https://doi.org/10.1038/nm.2408
291. Nosrati, R., *Lab on a chip devices for fertility: from proof-of-concept to clinical impact.* Lab Chip, 2022. **22**(9): p. 1680-1689. https://doi.org/10.1039/d1lc01144h
292. Yang, S.M., et al., *Microfluidic point-of-care (POC) devices in early diagnosis: A review of opportunities and challenges.* Sensors (Basel), 2022. **22**(4). https://doi.org/10.3390/s22041620
293. Park, H.D., *Current Status of Clinical Application of Point-of-Care Testing.* Arch Pathol Lab Med, 2021. **145**(2): p. 168-175. 10.5858/arpa.2020-0112-RA
294. Choi, S., et al., *What we should consider in point of care blood glucose Test; current quality management status of a single institution.* Medicina (Kaunas), 2021. **57**(3). https://doi.org/10.3390/medicina57030238

295. Yang, W., et al., *An immunoassay cassette with a handheld reader for HIV urine testing in point-of-care diagnostics*. Biomed Microdevices, 2020. **22**(2): p. 39. https://doi.org/10.1007/s10544-020-00494-4
296. Stone, H.A., *Introduction to fluid dynamicsfor microfluidic flows*, in *CMOS Biotechnology*. 2007, Spriger US. p. 5-30.
297. Hardt, S. and F. Schönfeld, *Chapter 1 microfluidics: fundamentals and engineering concepts*, in *Microfluidic technologies for miniaturized analysis systems*. 2007, Springer. p. 1-58.
298. White, F.M., *Viscous fluid flow*. 2nd ed. 1991: McGraw-Hill. 0-07-069712-4
299. Frey, C., *Development of functional droplet based microfluidic systems for synthetic biology and biomedical high-troughput applications*. 2020, Ruperto-Carola University of Heidelberg, Germany.
300. Pashapour, S., *Generation of extracellular matrix protein-based microcapsules for investigating single cells*. 2021, Ruperto-Carola University of Heidelberg, Germany.
301. Atencia, J. and D.J. Beebe, *Controlled microfluidic interfaces.* Nature, 2005. **437**(7059): p. 648-55. https://doi.org/10.1038/nature04163
302. Siqveland, L.M. and S.M. Sjjæveland, *Derivations of the Young-Laplace equation.* 2ß14: p. 1-20. https://doi.org/10.13140/RG.2.1.4485.5768
303. Adamson, A.W. and A.P. Gast, *Physical chemistry of surfaces*. 6th ed. 1993: Wiley.
304. Bibette, J., et al., *Stability criteria for emulsions.* Physical Review Letters, 1992. **69**(16): p. 2439-2442. https://doi.org/10.1103/PhysRevLett.69.2439
305. Hu, Y.T., et al., *Techniques and methods to study functional characteristics of emulsion systems.* Journal of Food & Drug Analysis, 2017. **25**(1): p. 16-26. https://doi.org/10.1016/j.jfda.2016.10.021
306. Trinh, T.N.D., et al., *Droplet-based microfluidics: applications in pharmaceuticals.* Pharmaceuticals (Basel), 2023. **16**(7). https://doi.org/10.3390/ph16070937
307. Utada, A.S., et al., *Monodisperse double emulsions generated from a microcapillary device.* Science, 2005. **308**(5721): p. 537-541. https://doi.org/10.1126/science.1109164
308. Abate, A.R., J. Thiele, and D.A. Weitz, *One-step formation of multiple emulsions in microfluidics.* Lab Chip, 2011. **11**(2): p. 253-8. https://doi.org/10.1039/c0lc00236d
309. Riechers, B., et al., *Surfactant adsorption kinetics in microfluidics.* PNAS, 2016. **113**(41): p. 11465-11470. https://doi.org/10.1073/pnas.1604307113
310. Haller, B., *The reconstitution of eukaryotic architecture and motility via microfludic technology*. 2018, Ruperto-Carola University of Heidelberg, Germany.
311. Dai, B. and G. Leal, *The mechanism of surfactant effects on drop coalescence.* Physics of Fluids, 2008. **20**: p. 040802. https://doi,org/10.1063/1.2911700
312. Hu, Z., et al., *Formation of vesicles in block copolymer-fluorinated surfactant complexes.* Langmuir, 2007. **23**: p. 116-122. https://doi.org/10.1021/la061532h
313. Bibette, J., F. Leal Calderon, and P. Poulin, *Emulsions: basic principles.* Reports on Progress in Physics, 1999. **62**: p. 969-1033. https://doi.org/10.1088/0034-4885/62/6/203
314. Baret, J.C., et al., *Kinetic aspects of emulsion stabilization by surfactants: a microfluidic analysis.* Langmuir, 2009. **25**(11): p. 6088-93. https://doi.org/10.1021/la9000472
315. Baret, J.C., *Surfactants in droplet-based microfluidics.* Lab Chip, 2012. **12**(3): p. 422-33. https://doi.org/10.1039/c1lc20582j
316. Tadros, T.F., *Applied surfactants: principles and applications*. 2006.
317. Ruckenstein, E. and R. Nagarajan, *Critical micelle concentration. A transition point for micellar size distribution.* Journal for Physical Chemistry, 1975. **79**: p. 2622-2626. https://doi.org/10.1007/978-1-4419-1415-6_3
318. Shim, J.U., et al., *Ultrarapid generation of femtoliter microfluidic droplets for single-molecule-counting immunoassay.* ACS Nano, 2013. **7**(7): p. 5955-5964. https://doi.org/10.1021/nn401661d
319. Theberge, A.B., et al., *Microdroplets in microfluidics: an evolving platform for discoveries in chemistry and biology.* Angewandte Chemie International Edition, 2010. **49**(34): p. 5846-68. https://doi.org/10.1002/anie.200906653

320. Anna, S.L. and H.C. Mayer, *Microscale tipstreaming in a microfluidic flow focusing device.* Physics of Fluids, 2006. **18**: p. 121512. https://doi.org/10.1063/1.2397023
321. Garstecki, P., et al., *Formation of droplets and bubbles in a microfluidic T-junction-scaling and mechanism of break-up.* Lab Chip, 2006. **6**(3): p. 437-46. https://doi.org/10.1039/b510841a
322. Anna, S.L., N. Bontoux, and H.A. Stone, *Formation of dispersions using „flow focusing" in microchannels.* Applied Physics Letters, 2003. **82**(3): p. 364-366. https://doi.org/10.1063/1.1537519#
323. Siltanen, C., et al., *Microfluidic fabrication of bioactive microgels for rapid formation and enhanced differentiation of stem cell spheroids.* Acta Biomaterialia, 2016. **34**: p. 125-132. https://doi.org/10.1016/j.actbio.2016.01.012
324. Vyawahare, S., A.D. Griffiths, and C.A. Merten, *Miniaturization and parallelization of biological and chemical assays in microfluidic devices.* Chemical Biology, 2010. **17**(10): p. 1052-65. https://doi.org/10.1016/j.chembiol.2010.09.007
325. Tawfik, D.S. and A.D. Griffiths, *Man-made cell-like compartments for molecular evolution.* Nature Biotechnology, 1998. **16**: p. 652-656. https://doi.org/10.1038/nbt0798-652
326. Elvira, K.S., et al., *The past, present and potential for microfluidic reactor technology in chemical synthesis.* Nature Chemistry, 2013. **5**(11): p. 905-15. https://doi.org/10.1038/nchem.1753
327. Brouzes, E., et al., *Droplet microfluidic technology for single-cell high-throughput screening.* PNAS, 2009. **106**(34): p. 14195-14200. https://doi.org/10.1073/pnas.0903542106
328. Edd, J.F., et al., *Controlled encapsulation of single-cells into monodisperse picolitre drops.* Lab Chip, 2008. **8**(8): p. 1262-4. https://doi.org/10.1039/b805456h
329. Göpfrich, K., I. Platzman, and J.P. Spatz, *Mastering Complexity: Towards Bottom-up Construction of Multifunctional Eukaryotic Synthetic Cells.* Trends in Biotechnology, 2018. **36**(9): p. 938-951. https://doi,org/10.1016/j.tibtech.2018.03.008
330. Moon, B.U., et al., *Water-in-water droplets by passive microfluidic flow focusing.* Analytical Chemistry, 2016. **88**(7): p. 3982-9. https://doi.org/10.1021/acs.analchem.6b00225
331. Sartipzadeh, O., et al., *Controllable size and form of droplets in microfluidic-assisted devices: Effects of channel geometry and fluid velocity on droplet size.* Materials Science & Engineering C: Materials for Biological Applications, 2020. **109**: p. 110606. https://doi.org/10.1016/j.msec.2019.110606
332. Yao, J., et al., *The effect of oil viscosity on droplet generation rate and droplet size in a T-junction microfluidic droplet generator.* Micromachines (Basel), 2019. **10**(12). https://doi.org/10.3390/mi10120808
333. Zhu, P. and L. Wang, *Passive and active droplet generation with microfluidics: a review.* Lab Chip, 2016. **17**(1): p. 34-75. https://doi.org/10.1039/c6lc01018k
334. Chen, Y., et al., *Biomineralization forming process and bio-inspired nanomaterials for biomedical application: a review.* Minerals, 2019. **9**(2). https://doi.org/10.3390/min9020068
335. Veschi, E.A., et al., *Mineralization profile of annexin A6-harbouring proteoliposomes: shedding light on the role of annexin A6 on matrix vesicle-mediated mineralization.* International Journal for Molecular Science, 2022. **23**(16). https://doi.org/10.3390/ijms23168945
336. McDonald, J.C. and G.M. Whitesides, *Poly(dimethylsiloxane) as a material for fabricating microfluidic devices.* Accounts of Chemical Research, 2002. **35**: p. 481-499. https://doi.org/10.1021/ar010110q
337. Benk, L., *Adhesive synthetic cells based on microfluidics.* 2019, Ruperto Carola University Heidelberg.
338. Gungormus, M., et al., *Regulation of in vitro calcium phosphate mineralization by combinatorially selected hydroxyapatite-binding peptides.* Biomacromolecules, 2008. **9**: p. 966-973.
339. Golub, E.E., *Biomineralization and matrix vesicles in biology and pathology.* Seminars in Immunopathology, 2011. **33**(5): p. 409-17. https://doi.org/10.1007/s00281-010-0230-z
340. Wang, K., et al., *Determination of dynamic interfacial tension and its effect on droplet formation in the T-shaped microdispersion process.* Langmuir, 2009. **25**: p. 2152-2158. https://doi.org/10.1021/la803049s

341. Cristini, V. and Y.C. Tan, *Theory and numerical simulation of droplet dynamics in complex flows-a review*. Lab Chip, 2004. **4**(4): p. 257-64. https://doi.org/10.1039/b403226h
342. Golub, E.E., et al., *The role of alkaline phosphatase in cartilage mineralization*. Bone and Mineral, 1992. **17**: p. 273-278. https://doi.org/10.1097/BCO.0B013E3282630851
343. Bellows, C.G., J.N.M. Heersche, and J.E. Aubin, *Inorganic phosphate added exogenously or released from ß-glycerophosphate initiates mineralization of osteoid nodules in vitro*. Bone and Mineral, 1992. **17**: p. 15-29. https://doi.org/10.1016/0169-6009(92)90707-K
344. Hamade, E., et al., *Chick embryo anchored alkaline phosphatase and mineralization process in vitro*. European Journal of Biochemistry, 2003. **270**(9): p. 2082-90. https://doi.org/10.1046/j.1432-1033.2003.03585.x
345. Qi, M.L., et al., *Crystallization of smooth amorphous calcium phosphate microspheres to core-shell hydroxyapatite microspheres*. RSC Advances, 2024. **14**(35): p. 25369-25377. https://doi.org/10.1039/d4ra04078c
346. Blumenthal, N.C., A.S. Posner, and J.M. Holmes, *Effect of preparation conditions on the properties and transformation of amorphous calcium phosphate*. Journal of Materials Research Bulletin, 1972. **7**: p. 1181-1190. https://doi.org/10.1016/0025-5408(72)90097-9
347. Romberg, R.W., et al., *Inhibition of hydroxyapatite crystal growth by bone-specific and other calcium-binding proteins*. Biochemistry, 1986. **25**(5): p. 1176-80. https://doi.org/10.1021/bi00353a035
348. Hunter, G.K., et al., *Nucleation and inhibition of hydroxyapatite formation by mineralized tissue proteins*. Biochem J, 1996. **317**: p. 59-64.
349. Doherty, T., et al., *Calcification in atherosclerosis: Bone biology and chronic inflammation at the arterial crossroadsmgp*. PNAS, 2003. **100**: p. 11201-11206. https://doi.org/10.1073/pnas.1932554100
350. Goiko, M., et al., *Peptides of matrix gla protein inhibit nucleation and growth of hydroxyapatite and calcium oxalate monohydrate crystals*. PLoS One, 2013. **8**(11): p. e80344. https://doi.org/10.1371/journal.pone.0080344
351. Mohd Pu'ad, N.A.S., et al., *Syntheses of hydroxyapatite from natural sources*. Heliyon, 2019. **5**(5): p. e01588. https://doi.org/10.1016/j.heliyon.2019.e01588
352. Lin, K., C. Wu, and J. Chang, *Advances in synthesis of calcium phosphate crystals with controlled size and shape*. Acta Biomaterialia, 2014. **10**(10): p. 4071-102. https://doi.org/10.1016/j.actbio.2014.06.017
353. Viswanath, B. and N. Ravishankar, *Controlled synthesis of plate-shaped hydroxyapatite and implications for the morphology of the apatite phase in bone*. Biomaterials, 2008. **29**(36): p. 4855-63. https://doi.org/10.1016/j.biomaterials.2008.09.001
354. Xiao, J., et al., *Biomacromolecule and Surfactant Complex Matrix for Oriented Stack of 2-Dimensional Carbonated Hydroxyapatite Nanosheets as Alignment in Calcified Tissues*. Crystal Growth & Design, 2010. **10**(4): p. 1492-1499. 10.1021/cg9001016
355. Lezaja, M., et al., *Effect of hydroxyapatite spheres, whiskers, and nanoparticles on mechanical properties of a model BisGMA/TEGDMA composite initially and after storage*. Journal of Biomedical Materials Research, 2013. **101**(8): p. 1469-76. https://doi.org/10.1002/jbm.b.32967
356. Dou, Y., K. Lin, and J. Chang, *Polymer nanocomposites with controllable distribution and arrangement of inorganic nanocomponents*. Nanoscale, 2011. **3**(4): p. 1508-11. https://doi.org/10.1039/c1nr10028a
357. Neira, I.S., et al., *Reinforcing of a calcium phosphate cement with hydroxyapatite crystals of various morphologies*. ACS Applied Material Interfaces, 2010. **2**(11): p. 3276-84. https://doi.org/10.1021/am100710b
358. Zhang, C., et al., *Hydroxyapatite nano- and microcrystals with multiform morphologies: controllable synthesis and luminescence properties*. Crystal Growth & Design, 2009. **9**(6): p. 2725-2733. https://doi.org/10.1021/cg801353n

359. Xia, L., et al., *Enhanced osteogenesis through nano-structured surface design of macroporous hydroxyapatite bioceramic scaffolds via activation of ERK and p38 MAPK signaling pathways*. Journal of Materials Chemistry B, 2013. **1**(40): p. 5403-5416. https://doi.org/10.1039/c3tb20945h
360. Lin, K., et al., *Tailoring the nanostructured surfaces of hydroxyapatite bioceramics to promote protein adsorption, osteoblast growth, and osteogenic differentiation.* ACS Applied Material Interfaces, 2013. **5**(16): p. 8008-17. https://doi.org/10.1021/am402089w
361. Liu, X., et al., *3D-printed bioactive ceramic scaffolds with biomimetic micro/nano-HAp surfaces mediated cell fate and promoted bone augmentation of the bone-implant interface in vivo*. Bioactive Materials, 2022. **12**: p. 120-132. https://doi.org/10.1016/j.bioactmat.2021.10.016